Assessing the robust impacts of land use change on the climate of the past 150 years and on the projected climate of the 21st century.

Juan Pablo Boisier

To cite this version:

Juan Pablo Boisier. Assessing the robust impacts of land use change on the climate of the past 150 years and on the projected climate of the 21st century.. Earth Sciences. Ecole Polytechnique X, 2012. English. NNT : . pastel-00787972

HAL Id: pastel-00787972
https://pastel.hal.science/pastel-00787972v1

Submitted on 13 Feb 2013

THÈSE DE DOCTORAT DE L'ÉCOLE POLYTECHNIQUE

Filière Mécanique
Spécialité Sciences du Climat

Presentée par

Juan Pablo BOISIER

pour obtenir le grade de

Docteur de l'École Polytechnique

Assessing the robust impacts of land-use change on the climate of the past 150 years and on the projected climate of the 21st century

Efectuée au Laboratoire des Sciences du Climat et de l'Envirronnement
(CEA/CNRS/UVSQ)

Présentée et soutenue le 9 Novembre 2012 devant le jury composé de

Hervé LE TREUT, Lab. de Météorologie Dynamique, École Polythecnique	*Président du Jury*
Richard A. BETTS, Met Office Hadley Centre	*Rapporteur*
Gerhard KRINNER, Lab. de Glaciologie et Géophysique de l'Environnement	*Rapporteur*
Sonia I. SENEVIRATNE, Institute for Atmospheric and Climate Science, ETH	*Examinateur*
Stephen SITCH, University of Exeter	*Examinateur*
Bart J. J. M. VAN DEN HURK, Royal Netherlands Meteorological Institute	*Examinateur*
Nathalie DE NOBLET-DUCOUDRÉ, LSCE, Institut Pierre Simon Laplace	*Directrice de thèse*

Remerciements

Cette thèse fut le résultat d'une recherche de plus de trois ans qui n'aurait pas été possible sans le soutien de nombreuses personnes. Je voudrais en premier temps remercier ma directrice de thèse, Nathalie de Noblet, qui a accepté de m'encadrer sans connaissance de mon expérience précédente et qui a dirigé cette étude avec un grand enthousiasme. Merci beaucoup de cette confiance et énergie, qui fut très encourageante pour aboutir les différentes étapes de ce parcours. De ma part, le sujet de l'interaction végétation-atmosphère a été abordé pour la première fois au début de cette thèse. En plus de l'expérience transmise le long de ces années dans ce domaine spécifique, Nathalie m'a rapidement introduit dans la dynamique de la recherche scientifique, notamment dans ce qui concerne le travail en collaboration, la façon de synthétiser les résultats, ainsi que la divulgation des ceux-ci.

Je tiens à remercier tous les participants du projet LUCID qui ont vu leurs boîtes émail encombrées des questions et demandes de données, lesquelles ont été opportunément répondues. Je voudrais remercier particulièrement Andy Pitman et sa disposition pour travailler à distance et à n'importe quelle heure. Les discussions avec Andy, Nathalie, Sonia Seneviratne et Bart van den Hurk ont été également très motivantes.

Je voudrais remercier Philippe Ciais pour son grand appui, fondamental pour le bon déroulement de la partie finale de cette thèse. Je tiens aussi à remercier les rapporteurs de ce manuscrit, Richard Betts et Gerhard Krinner, ainsi qu'à l'ensemble du jury, par leurs commentaires constructifs et valorisants, et leurs recommandations pour les études en prospectives.

Un grand merci aussi à toutes les personnes qui font du LSCE un endroit très agréable et accueillant, idéal pour un étudiant s'embarquant dans une thèse. Merci Aude, collègue de bureau, de ta compagnie et aussi de répondre mes incessantes questions linguistiques. Merci Arnaud, Juliette, Patricia et tout le bâtiment 712, de vôtre bon esprit et disposition.

La réussite de cette aventure fut possible grâce au soutien et affection infinie de ma petite famille en France, laquelle a pris forme au cours de ces années et qui m'a accompagné chaleureusement. Merci Amarí et José Nahuel. Tous mes sentiments aussi aux proches, famille et amis, en France et dans l'autre bout du globe, qui ont été toujours présents.

Cette thèse a été partiellement financée par des bourses d'études issues de la Commission Nationale d'investigation scientifique et Technologique du Chili (CONICYT) et de l'association ÉGIDE, et par le projet européen FP7-AMAZALERT.

Résumé

A ce jour, les hommes ont modifié plus de la moitié des surfaces habitables pour leurs activités agricoles. Le changement de l'occupation des sols qui en résulte a une influence importante sur le climat à l'échelle du continent de par les modifications des propriétés physiques de la surface. Le niveau de connaissance de ces impacts biogéophysiques est cependant insuffisant, en raison notamment des nombreux processus impliqués. Via l'intercomparaison de modèles de climat et d'autres outils développés, cette thèse vise à identifier les signaux climatiques robustes liés au changement d'occupation des sols, ainsi qu'à évaluer les incertitudes associées. Depuis l'époque préindustrielle, le changement d'usage des sols a résulté en une déforestation extensive dans les régions tempérées de l'hémisphère Nord, où l'augmentation de l'albédo de surface a sûrement induit un refroidissement durant l'hiver et le printemps. Les rétroactions atmosphériques et les effets non radiatifs, comme par exemple la perturbation du cycle hydrologique, ont très probablement amorti ce refroidissement. L'amplitude des effets climatiques en hiver ainsi que le rôle des effets non radiatifs en été (et le changement résultant de températures) reste pourtant très incertain parmi les modèles. Ces incertitudes répondent (1) à la façon dont le changement de l'occupation des sols est représenté dans les modèles de surface et (2) aux sensibilités intrinsèques des modèles de climat aux perturbations de la couverture végétale. Nous avons démontré que le deuxième point explique plus de 50% de la dispersion inter-modèle dans des variables clés au climat de surface comme l'évapotranspiration. Suite à cette incertitude, des outils statistiques ont été développés pour reconstruire les impacts du changement d'occupation des sols dans certaines variables à partir d'observations contemporaines. L'évolution passée de l'albédo de surface a été inférée à partir de données satellites et les cartes de végétation prescrites dans les modèles de surface ici évalués. Cette technique a permis non seulement de faire une estimation réaliste des changements d'albédo, mais aussi d'avoir une référence à laquelle comparer les résultats simulés. Bien que l'ensemble des modèles ne montre pas un biais systématique par rapport aux estimations, les simulations de chaque modèle diffèrent largement des leurs estimations. Une analyse similaire a été faite pour l'évapotranspiration à partir de produits globaux issus d'observations. L'ensemble de ces analyses montre que les incertitudes actuelles des effets sur le climat du changement d'occupation des sols sont en grande partie liées aux paramétrisations de surface des modèles de climat, et peuvent donc être réduites par une évaluation plus rigoureuse des modèles de surface.

Abstract

Humans, through land-use activities, have modified more than half of the global habitable landscapes. Land-use induced land cover change (LULCC) is an important climate forcing at the continental scale due to the underlying alterations of the properties of the soil-vegetation system. However, the knowledge of these biogeophysical impacts of LULCC is middling, notably due to the large number of processes involved. By means of model intercomparison and other approaches specifically developed, this study aims to identify the robust climate signals of LULCC as well as to assess the associated uncertainties. LULCC since the preindustrial period has led to extensive deforestation in the northern temperate regions and therefore to increases in surface albedo. This radiative effect has very likely cooled down the surface during the winter and spring. Atmospheric feedbacks and non-radiative effects of LULCC, such as perturbations in the hydrological cycle, tend to dampen this cooling. The amplitude of the winter impacts and the role of the non-radiative effect in summer (and the resulting changes in temperature) are still quite uncertain within the model results. These uncertainties respond (1) to the way LULCC is implemented in land surface models (LSMs) and (2) to the inherent model sensitivities to land-cover perturbations and the resulting changes in both the surface radiation budget and turbulent exchanges. We show that the second point could explain more than 50% of the inter-model dispersion in key variables for the surface climate such as the evapotranspiration. We therefore developed statistical tools to reconstruct the impacts of LULCC in some variables from present-day observations. Satellite surface albedo data were projected to the past based on the same land-cover maps prescribed in the LSMs here assessed. This technique, besides representing a realistic estimation of the past albedo changes, brings a benchmark for model results. Although there is no systematic bias in the simulated changes in albedo with respect to those estimated, there are large differences between the individual model results and the observations-based ones. A similar analysis was performed for evapotranspiration, based on global products of this variable derived from observations. The analyses carried out here show that current uncertainties in the climate impacts of LULCC are in major part the result of the land-surface parameterizations used in climate models and, hence, could be reduced with a more thoroughly evaluation of LSMs.

Table of contents

Chapter 1 General introduction

Chapter 2 Impacts of LULCC on climate between the preindustrial period and present-day: Results from the LUCID intercomparison project

Chapter 3 Surface albedo and evapotranspiration changes due to past LULCC estimated from global observations

Chapter 4 Land-use and climate changes from the preindustrial period to the end of the 21st century

Symbols and acronyms

Symbols	
α	Surface albedo
ε	Surface emissivity
E	Evaporation
EF	Evaporative fraction
ET	Evapotranspiration
G	Ground heat flux
H, Q_H	Sensible heat flux
L	Latent heat of vaporization
LE, Q_{LE}	Latent heat flux
L_D	Downward longwave radiation at the surface
L_U	Upward longwave radiation at the surface
P	Precipitation
Q_A	Available energy at the surface ($S_N + L_D$)
Q_T	Total turbulent energy flux ($Q_{LE} + Q_H$)
R_N	Net radiation at the surface
S_D	Downward shortwave radiation at the surface
S_N	Net shortwave radiation at the surface
S_U	Upward shortwave radiation at the surface
T_{2m}	2-meter temperature
T_S	Surface temperature
Z_0	Surface roughness

Acronyms	
AVHRR	Advanced Very High Resolution Radiometer
CMIP5	Coupled Model Intercomparison Project – Phase 5
GCM	Global Climate Model
GEWEX	Global Energy and Water Cycle Experiment
GLASS	Global Land/Atmosphere System Study
GPCP	Global Precipitation Climatology Project
IGBP	International Geosphere-Biosphere Programme
iLEAPS	Integrated Land Ecosystem-Atmosphere Processes Study
IPCC	Intergovernmental panel on Climate Change
IPSL	Institut Pierre Simon Laplace
LAI	Leaf Area Index
LCC	Land Cover Change
LSM	Land Surface Model
LUCID	Land-Use and climate, IDentification of robust impacts (project)
LULCC	Land-Use induced Land-Cover Change
MODIS	Moderate resolution imaging spectroradiometer
NH	Northern Hemisphere
PFT	Plant Functional Type
RF	Radiative Forcing
SH	Southern Hemisphere
SEB	Surface Energy Budget
SIC	Sea-Ice Concentration
SST	Sea-Surface Temperature
SWE	Snow Water Equivalent

Chapter 1

General introduction

Land-use change has been one of the major and more visible ways in which humans have modified the Earth and its climate. It has likely been the major anthropogenic climate forcing before the industrial revolution and has continued to be a leading driver of climate change since then. Nowadays, more than half of the ice-free lands are occupied by human settlements and agricultural activities. This study addresses the physical impacts on climate of large-scale land-use induced land-cover change (LULCC). In this introduction, a general background on the interactions between land-surface and the atmosphere is given, as well as a review of past research on the historical and potential effects on climate of land-use changes. Since a major part of the results described in the following chapters involve climate simulations with a particular emphasis on land-atmosphere interactions, an overview of the land surface modeling is also presented here.

1.1 Vegetation in the climate system

1.1.1 Role of terrestrial ecosystems in the global biogeochemical and hydrological cycles

Plants are the main engines of the global carbon cycle. About 120 gigatons of carbon (GtC) –equivalent to 15% of the carbon dioxide (CO_2) contained in the atmosphere– are allocated in terrestrial ecosystems every year through plant photosynthesis (biomass production). The same amount of carbon is sent back to the atmosphere by means of plant respiration and litter decomposition (in approximately equal parts; Denman et al., 2007). These values are higher but of the same order than the annual carbon exchanges between the ocean and the atmosphere. Hence, terrestrial ecosystems and the ocean regulate the bulk of the carbon balance between the various components of the climate system at short (biological) times scales. Particularly, the seasonal variation in the net ecosystem exchange (NEE) of terrestrial biosphere explains the distinct seasonal cycle of the Northern Hemisphere (NH) atmospheric CO_2 concentration. Terrestrial ecosystems are also responsible for a major part of the interannual variability in CO_2 concentration (e.g., Bousquet et al., 2000; Buermann et al., 2007).

At long time scales (years-to-centuries), the biosphere has carried out an important ecological service in mitigating the anthropogenic alterations of the global carbon cycle. Between the preindustrial period and the present, terrestrial plants have taken up the equivalent of about 30% of the atmospheric carbon surplus resulting from fossil fuel emissions and land-use changes (Canadell et al., 2007; Denman et al., 2007). Changes in land cover have significantly contributed to the net anthropogenic carbon emissions and have therefore influenced the global climate trends. A review of the biogeochemical effects on climate of LULCC is presented in Section 1.4.2.

Vegetation is also fundamental in regulating the global water cycle. Total precipitation over lands (~10^5 km^3 yr^{-1}) is in its major part (~70%) sent back to the atmosphere throughout evaporation and plant transpiration (evapotranspiration). In turn, an important fraction of the atmospheric moisture that precipitates over lands comes from the evapotranspiration itself (water recycling). Therefore, although the primary source of water is the ocean, vegetation plays a fundamental role in increasing the water recycling strength over the continents and, then, on the availability of fresh water. Modeling experiments have shown that the total land evapotranspiration and precipitation are respectively reduced by 65% and 50% when a completely vegetated planet is converted to a desert one (Kleidon et al., 2000). Vegetated lands and their high evapotranspiration rates also modulate the surface climate, maintaining moderate temperatures and a heating contrast between the continents and the oceans (Shukla and Mintz, 1982). The global circulation is also in part regulated by vegetation, notably by tropical forest convection hot spot such as the Amazon.

1.1.2 Water and energy budget in vegetated surfaces

The hydrology of the soil-canopy system may be characterized by different water reservoirs and fluxes (Figure 1.1). Precipitation has a component that reaches the ground (directly or as stemflow) and another that is intercepted by the foliage. The latter represents a small reservoir of water that is rapidly evaporated (interception loss). The water reaching the ground by precipitation or by snow melt may in part infiltrate the soil, run off or evaporate. The soil represents a water pool from which the plants' roots uptake moisture. How the available water by precipitation is distributed between these different compounds will depend on the amount of vegetation, and on the plant's morphological (e.g., foliage density, root length, leaf water holding capacity) and physiological (stomatal conductance) properties.

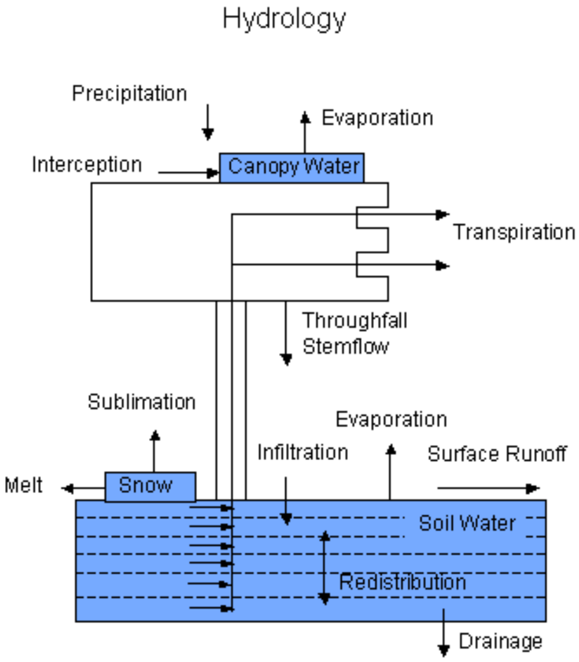

Figure 1.1
Land surface hydrology as represented in land surface models. (Reprinted from Bonan, 2008a)

The surface energy balance varies widely following the geographical location, in part due to the atmospheric forcings (momentum, radiation and precipitation), but also according to the properties of the different land-cover and soil types. As commented above, the amount of vegetation, the plant type and canopy density will drive the hydrologic processes at the surface and the resulting flux of latent heat (evapotranspiration). Vegetation also determines the aerodynamic properties of the surface (surface roughness), regulating the ensemble of turbulent exchanges between the land and the atmosphere.

The surface energy balance is regulated by the surface radiation budget, which also depend on the type of land cover. For instance, the optical properties of the soil (soil color) and plants (e.g., leaf/stem albedo) will determine the amount of solar radiation sent back to the atmosphere. Dense forest has low albedos (~12%) compared to, e.g., dry barren soils (~30%). Under snow-covered conditions, the albedo difference between forest and barren or herbaceous lands is still larger because the trees' canopy masks the very high albedo of the snow lying at the surface (Bonan, 2008b).

Looking at the ground-vegetation system as a whole, the surface energy balance may be described as follows:

$$(1-\alpha)\, S_D + L_N = LE + H + G \qquad (1.1)$$

where S_D and L_N are the solar radiation incoming the surface and the net (downward minus upward) longwave radiation, respectively. *LE*, *H* and *G* are respectively the latent, sensible and ground heat fluxes. The surface albedo (α) results from the combined soil and canopy reflectance. *H* and *LE* may, in this case, be represented in a simplified way with bulk relations of heat and moisture transfer between the surface (including vegetation) and a reference level in the atmosphere, formulation usually used to solve Equation (1.1) and the surface temperature in land surface models (described in the following section).

1.2 Modeling the land surface

Climate models have been systematically developed since the 1960s' and have quickly become powerful tools for climate studies and weather forecasting. The early global climate models (GCMs) only simulated the atmospheric motions (Global Circulation Models) and used very simple parameterizations of the surface. Besides the systematic improvements of the dynamics and physics of the atmosphere, the development of GCMs has been characterized by a more complete representation of the complexity of the climate system, by adding different components of it. An early improvement was the more explicit description of the continents and its biogeography. The modern schemes that solve land surface processes, referred to as land surface models (LSMs), are usually distinct modules that can be used either coupled to a GCM or forced with prescribed near surface variables and atmospheric fluxes.

During the early stage of climate modeling, the water and energy exchanges between the continental surfaces and the atmosphere were represented by simple bucket/surface energy balance schemes (e.g., Manabe, 1969). In a limited set of equations and parameterizations, usually referred to as LSMs of first generation (Sellers et al, 1997), the soil water content is represented as a simple reservoir (i.e., a single soil layer) that fills up with precipitation and snow melt, and empties with evaporation and runoff (typically the surplus water when a prescribed reservoir level is reached). *H* and *LE* are calculated with their corresponding bulk transfer equations, which respectively depend on the temperature and water vapor pressure gradient between the surface and the first layer in the atmosphere. That is,

$$H = \rho\, c_p\, (T_s - T_a) / r_H \tag{1.2}$$

$$LE = \beta\, \rho\, c_p\, \gamma\, (e^*(T_s) - e_a) / r_W \tag{1.3}$$

where ρ, c_p and γ are the air density, the specific heat capacity of the air and the psychrometric constant, respectively. In this case, both resistances to transfer of heat (r_H) and to water exchange (r_W) correspond to the aerodynamic one. LE is also limited by the soil moisture availability (β), which depends linearly on the reservoir water level. In these models, different land-cover types may be taken in account through prescribed parameters for the water holding capacity, surface albedo and roughness. The scheme described in Manabe (1969) was the first and common reference for this kind of land surface parameterization.

A thorough evolution of LSMs included the multilayer representation of the soil processes (hydrology and heat conduction) and the explicit representation of the energy, water and momentum exchanges between the vegetation and the atmosphere. These second-generation LSMs simulate the water fluxes in a more realistic way than previous approaches, because the total land evaporation is partitioned between plant transpiration, interception loss and soil evaporation components (Figure 1.1). In these models, leaf transpiration is regulated by stomatal conductance, defined empirically as function of environmental factors (photosynthetic active radiation, air humidity and air CO_2 concentration) and the properties of plants. r_W in Equation (1.3) integrates, in this case, more barriers in the soils and plants' canopy to evaporation and transpiration (e.g., aerodynamic resistance, stomatal resistance or soil moisture deficit). The inclusion of two or more layers in the soil allows combining processes acting at different time scales. While the near surface layer accounts for fast variability (e.g., diurnal), the deeper soil layers relate with slower processes (e.g., seasonal cycle).

The processes described by the leaf biophysics are scaled up to the canopy level through the foliage density, which is usually characterized with the Leaf Area Index (LAI), the cumulated foliage area of the canopy projected in a unit of ground surface. The common way to derive the fluxes between the canopy and the atmosphere is the simple extension of the leaf processes. In this case, the canopy conductance is equal to the stomatal conductance pondered by LAI. This approach, usually known as 'big leaf canopy', contrasts with more complex representations in which the ground-canopy system is divided into multiple layers. The mean fluxes in a grid-cell depend then on its fractional vegetation cover and LAI, both quantities prescribed in second-generation models (usually based on satellite observations). Several LSMs also prescribe different vegetation classes within a cell. Such models used biomes classes or Plant Functional Types (PFTs) to describe the sub-grid land cover heterogeneity. The latter is a plant classification based on their functions, physical characteristics, life form, etc. Depending on the model, different processes –at least the water balance calculations– are independently computed over each PFT and then aggregated to the grid level following the relative grid fractions of each of them.

Based on the original work of Deardorff (1978), the Biosphere Atmosphere Transfer Scheme (Dickinson et al., 1986) and Simple Biosphere model (Sellers et al., 1986) are earlier LSMs of enhanced complexity, from which several other second-generation LSMs were developed.

During the last two decades, a number of LSMs have evolved and others have been developed in order to include the biochemical processes within the land surface in a comprehensive way along with its biophysical counterpart. These models are recognized as of third generation or ‘green’ LSMs because they explicitly simulate photosynthesis (usually based on Farquhar et al., 1980) and stomatal conductance (typically following the semi-empirical relation by Collatz et al., 1992), allowing representing key aspects of plants’ life such as the phenology. Given that these LSMs simulate the carbon exchange between plants, the soil and the atmosphere, a large field in vegetation-climate interactions studies was opened. For instance, these models allow estimating the change in the global carbon cycle due to anthropogenic forcings (emissions from fossil-fuel combustion and derived from land-use changes; e.g., Brovkin et al., 2004), or account in climate simulations for the plants’ physiological response to environmental changes (either in climate or CO_2 concentration; e.g., Betts et al., 1997, 2007a; Schimel et al., 2000).

In addition to the biogeochemistry, some modern LSMs also include natural disturbances (e.g., wildfires), land management or schemes of plant competition for light, water and nutrients, allowing simulating of the natural evolution of biogeography (e.g., Sitch et al., 2003; Cox et al., 2004). The latter are known as Dynamics Global Vegetation Models (DGVM).

ORCHIDEE (ORganizing Carbon and Hydrology in Dynamic EcosystEms; Krinner et al., 2005) is an example of state-of-the-art LSM, which is used in the IPSL global modeling framework (Marti et al., 2006). ORCHIDEE builds on the energy and hydrologic transfer model SECHIBA (Ducoudré et al., 1993) and on two other schemes that respectively simulate plant biogeochemistry (STOMATE) and vegetation dynamics (LPJ; Sitch et al., 2003). Hence, this model has a modular architecture that allows using it in a SECHIBA configuration alone, in a SECHIBA-STOMATE configuration or in a fully coupled configuration, in which ORCHIDEE works as a DGVM. When STOMATE is activated, the carbon cycle is integrated to the biophysical component in a coherent manner; the model simulates photosynthesis, stomatal conductance and autotrophic respiration following Ball et al. (1987), Farquhar et al. (1980), Collatz et al. (1992) and Ruimy (1996). STOMATE also accounts for carbon allocation into the different vegetation pools (and into the litter and soil ones in regard with leaf senescence and tree mortality), plant phenology, litter decomposition and the soil carbon dynamics. The global biogeography and the sub-grid land-cover distribution are characterized through thirteen PFTs living within a grid-cell: two pairs (C3 and C4) of grasses and crops, six tree classes, and a bare soil class.

An in depth review of LSMs is described in Sellers et al. (1997), Pitman (2003) and Bonan (2008a).

1.3 Historical land-use induced land-cover change

The rapid human expansion during the Holocene has been characterized by the transition from hunter-gathering to sedentary cultures that developed agriculture, food storage and livestock techniques. The early phase of this societal transition, the so-called Neolithic revolution, and the associated first signals of systematic land-use did not happen until the last climate shift at the end of the Pleistocene. This occurred in the Near Easter Fertile Crescent (region surrounding the Syrian desert from Egypt to Iran) and in Guinea somewhat before ten thousand years ago (Diamond, 1999). During the next 5000 years, food production has spread eastward and westward across Eurasia. Land-use practices have also emerged (independently) in other parts of the globe such as in east China (~9500 yr BP) and Mesoamerica (~5500 yr BP).

Forest clearing was already a common land-use practice during the earlier agricultural societies (Williams, 2000). From the deep past to the preindustrial period (18th century), land-use has been raising more or less monotonically following human population (that reached ~1 billion in 1800). Land conversion during this period was accompanied by moderate cropland expansion (~+2.6 million km^2) and deforestation (~-2 million km^2), particularly affecting Europe, India, and southeastern Asia (Pongratz et al., 2008; Figure 1.2). The industrial revolution has introduced novel techniques for agriculture, notably boosted by the use of fossil fuels and fertilizers (Nitrogen). Along with human population, the expansion of the agriculture accelerated dramatically in the last 300 years (Ramankutty and Foley, 1999; Klein Goldewick 2001). Croplands increased strongly in North America, west Eurasia, India and China during the 18th and 19th centuries. Land-cover changes have then stabilized during the 20th century in some regions such as in Europe, and accelerated in tropical regions and in South America.

Nowadays more than half of the global habitable lands (excluding Greenland and Antarctica) are occupied by croplands, rangelands and other human settlements (Ellis and Ramankutty, 2008). Forests, particularly the tropical ones, will likely be under strong pressure during the next decades due to the population demand for food and energy (e.g., biofuel industry).

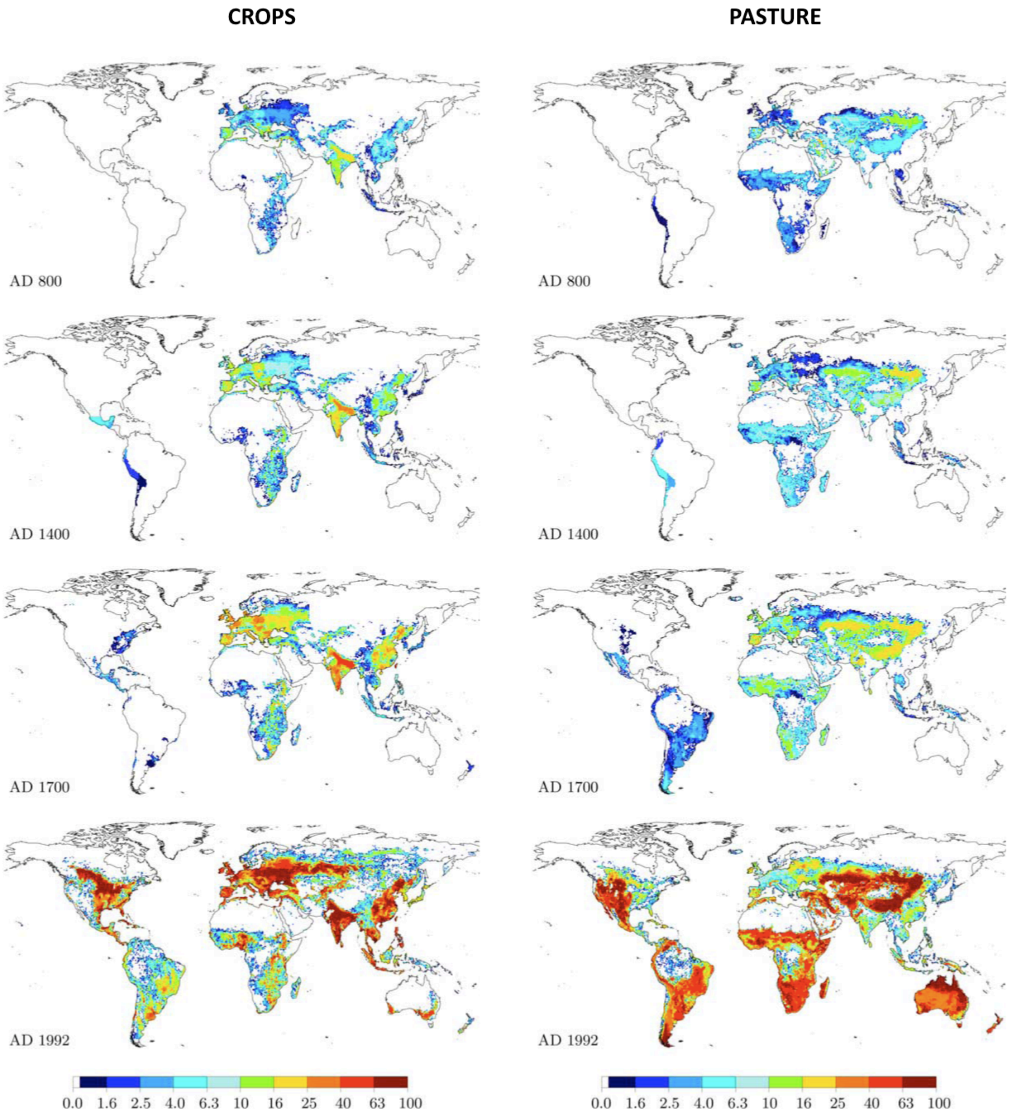

Figure 1.2
Global historical cropland (left) and pasture (right) area. Units are percent of grid cell. Values smaller than 1% are colored white. Note the logarithmic scale. (Reprinted from Pongratz et al., 2008)

1.4 LULCC-induced changes in climate

Land-use and land-cover changes affect climate by means of different mechanisms. These are conveniently divided into those that perturb the biogeochemical cycle (biogeochemical impacts) and those that affect the climate through changes in physical properties of the surface (biogeophysical impacts). Both cases are reviewed next.

1.4.1 Biogeophysical impacts

1.4.1.1. Radiative effects

As mentioned in Section 1.1.2, the surface radiation budget over lands varies widely from region to region, in part because of the different radiative properties of the various land-cover types. Forest canopy is generally more opaque to sunlight than herbaceous vegetation and bare soil. This difference is much larger if snow is present because forest masks the snow-covered surfaces lying under its tall canopy, maintaining a relatively low albedo. Current estimates based on satellite observations report snow-free albedo values of around 0.12 and 0.17 for forests and grasslands, respectively (e.g., Gao et al., 2002; Myhre et al., 2005). Under snowy conditions, the albedo of the same two vegetation classes increases to near 0.26 and 0.57, respectively (Jin et al., 2002). That is, the albedo difference between forest and grassland is ~0.05 in absence of snow, and reaches ~0.30 under snow.

The climate is very sensitive to surface albedo changes. Without considering any feedback within the climate system and using an incoming solar radiation at the surface of 200 W m^{-2} (~ global average), an increase in surface albedo of 0.01 will reduce the energy absorbed at the surface by 2 W m^{-2}. This is quite a significant difference and of the same order than the radiative forcing exerted at the top of the troposphere by the change in atmospheric greenhouse gases concentration since the preindustrial period (Forster et al., 2007). Manifestly, the potential global impact of LULCC-induced surface albedo changes is quite weaker because land conversion is constrained to a minor fraction of earth surface. On the contrary, the radiative effects of LULCC could be very important at the continental scale, considering notably that a local albedo change due to e.g. deforestation is often larger than 0.01.

Since the late 1990s, several studies using global climate simulation have investigated the biogeophysical impacts of the past large-scale LULCC. Most of them have shown a predominantly cooling effect driven by strong albedo increases in NH temperate regions (Hansen et al., 1998; Brovkin et al., 1999, 2004, 2006; Betts, 2001; Gowindassamy et al., 2001; Matthews et al., 2003, 2004; Feddema et al., 2005a; Betts et al., 2007b). Hansen et al. (1998) show a clear cooling in the NH as response to LULCC between the preindustrial period and present-day (Figure 1.3b). This cooling is in clear relation with higher surface albedo and decreases in net radiation over the regions of intense deforestation, in eastern North America, in mid-western Eurasia and in southeastern Asia (Figure 1.3a). Given the major role of albedo, some of the mentioned references and others studies have quantified the effects of the past LULCC in terms of radiative forcing (RF). The use of this metric has further allowed direct comparisons with other natural and human-induced climate forcings, despite it does not account for non-radiative effects of LULCC (Davin et al., 2007). The global mean RF induced by surface albedo changes since the pre-agricultural period have a typical value of –0.2 W m^{-2} but vary widely within different estimates, ranging from –0.66 to +0.02 W m^{-2} (see Forster et al., 2007, and references therein). This uncertainty has been in part attributed to different crop albedo values prescribed in LSMs (Matthews et al, 2003; Myhre and Myhre, 2003). Other studies show little global impacts and regionally warming responses to LULCC (e.g., Pitman and Zhao, 2000; Findell et al., 2007).

Idealized modeling experiments have been very helpful to evaluate the potential impact of LULCC in regions other than the NH temperate and boreal ones. A number of studies have carried out simulations encompassing large-scale reforestation or deforestation (e.g., Clausen et al., 2001; Gibbard et al., 2005; Bala et al., 2007). Most of them, in accordance with the simulated climate responses to the historical LULCC, show that forest tends to warm the surface at high latitudes because of its comparatively low albedo, particularly during the winter and spring, when the snow-masking effect is maximized. During the warm season at mid/high latitudes or through the year at lower latitudes, the effects of deforestation and land-use in general are more intricate because of the major role of turbulent energy fluxes.

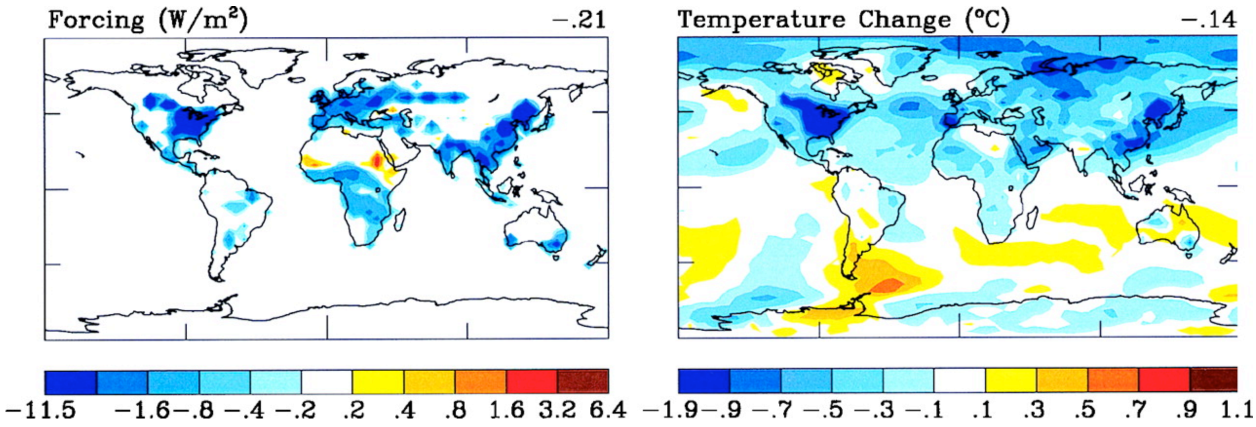

Figure 1.3
Climate forcing and simulated surface air temperature response for land-use change between the pre-industrial era and the present. (Reprinted from Hansen et al. 1998)

1.4.1.2. Non-radiative effects

In addition to the radiative impacts, LULCC affects the surface climate by altering the hydrology and the aerodynamic drag of the surface on the atmosphere and, therefore, the turbulent exchanges within the boundary layer. We can recognize three mechanisms in which the turbulent heat fluxes could respond to LULCC. Two of them will occur through direct modification of the surface resistances to water and heat exchanges (see Equations 1.2 and 1.3).

On one hand, a change in surface roughness and thereby in the aerodynamic resistance, will affect both *H* and *LE* in the same direction. On the other hand, the relative strength of one flux with respect to the other (i.e., a change in the Bowen ratio) will be affected by changes in the evaporative efficiency. The latter is notably controlled by the plants' morphology (e.g., the root depth), physiology (stomatal conductance) and the foliage density, affecting the evapotranspiration (ET) partitioning (transpiration vs. interception loss vs. soil evaporation; Figure 1.1). A third way in which *H* and *LE* will be modified is throughout changes in available energy by radiation. Radiation will directly affect plant transpiration through changes in the photosynthetic active radiation (PAR). Turbulent fluxes will also respond to changes in the surface radiation following (and modifying) the surface and air temperature in a way that the surface energy balance must be maintained.

Several modeling studies have shown decreases in ET as responses to large-scale deforestation in the tropics, overwhelming the albedo-induced cooling and producing a net warming (e.g., Claussen 2001, Gibbard et al., 2005), although the opposite effect has also been reported (Snyder et al., 2004). The particular question of the climate response to a hypothetical Amazon deforestation has been addressed in a number of modeling studies since the 1980's (see D'Almeida et al., 2007; Sampaio et al., 2007; Bonan, 2008a; and references therein). Most of these studies, as well as other simulations prescribing historical LULCC (e.g., Bounoua et al., 2002), agree that Amazonian clearing leads to a warmer and dryer regional climate. Some observations-based studies have shown consistent differences between the hydrologic properties of rainforest and deforested areas in the Amazon (Gash and Nobre, 1997; von Randow et al., 2004). Others studies based on observations or mesoscale simulations have shown an opposite pattern, with enhanced convection and water recycling over local forest clearing (e.g., Baidya Roy and Avissar, 2002; Negri et al., 2004), highlighting that the question of how deforestation affects the water cycle in tropical areas is highly dependent on the scale of the perturbation (D'Almeida et al., 2007).

Changes in ET due to land conversions are even more uncertain in temperate latitudes. Crops have associated higher canopy conductance than natural vegetation (Baldocci et al., 1997) and, under well-watered conditions, could evaporate more than forest. Cropland expansion at expense of grassland or forest could then cool the surface in summer due to increases in both ET and surface albedo. Such LULCC signals have been simulated in North America (Bonan, 1999; Bounoua et al., 2002; Oleson et al., 2004) and are consistent with observations (Bonan, 2001). Other modeling studies have shown the opposite effect due to the past deforestation in North America (Baidya Roy et al., 2003) and in other regions (Betts, 2001; Findell et al., 2007).

In addition to changes in land cover, land use also affects the climate through irrigation. During the 20th century, this technique has been used to develop agriculture in arid and semi-arid regions, notably in northern India, in eastern China and in the great plains of North America. Most studies have shown that irrigation has significantly increased ET and cooled the surface in those and other regions (e.g., Douglas et al., 2006; Mahmood et al, 2006, Adegoke et al., 2007; Lobell and Bonfils, 2008). Global-scale studies have also shown increasing ET and cooling due to irrigation (Boucher et al., 2004; Gordon et al., 2005; Haddeland et al., 2007).

1.4.1.2. Indirect impacts and feedbacks

Direct modifications of the surface properties affect energy, momentum and water exchanges within the boundary layer, inducing changes in the upper air temperature, moisture, convection and cloud cover. The surface climate is therefore indirectly affected by LULCC through changes in precipitation, in the wind stress or in the incoming (downward) radiation.

There are many mechanisms by which the atmosphere can feedback the surface perturbations, as described in Pitman (2003). How the surface affects the boundary layer processes will also depend on the surface-atmosphere coupling strength (Koster et al., 2006). For instance, increases in precipitation will likely enhance soil moisture and ET, notably in arid or semi-arid regions. In turn, the way in which ET affects precipitation is complex and not necessarily one-sided. Increasing ET could enhance convection and supply moisture to the atmosphere inducing more precipitation. This mechanism results in a positive feedback between ET and precipitation (e.g., Koster et al., 2006). On the contrary, the surface cooling due to increasing ET may make the boundary layer more stable. In this case more ET inhibits convection and precipitation, producing a negative feedback (e.g., Cook et al., 2006). The atmosphere could also produce a negative feedback to changes in ET through changes in air water vapour. An increase in the latter due to increases in ET will reduce the evaporative demand and, then, inhibit ET.

As commented before, a large number of studies using GCMs show large decreases in precipitation and ET due to tropical deforestation, notably for the Amazon case. It is noteworthy that most of these studies show larger decreases in precipitation than evaporation in term of water flux (see D'Almeida et al., 2007, and references therein). This footprint highlights that, more than a pure water vapor recycling effect, changes in turbulence and convection play a leading role in explaining the precipitation responses to LULCC in the tropic.

The radiative effects of LULCC induced by changes in surface albedo may be amplified due to a positive feedback along with the surface temperature and the snow cover (in the same way than the ice-albedo feedback). In turn, the albedo-induced decrease in net shortwave radiation may be dampened from decreases in the incoming solar radiation. This may occur if the less energy absorbed at the surface inhibits convection and, therefore, reduces cloud cover (Pitman, 2003). Such impacts of LULCC, although observed in numerical experiments (e.g., Bala et al., 2007; Findell et al., 2007), have not been particularly addressed and remain quite uncertain. Result from, e.g., Oleson et al. (2004) show different directions in the changes of incoming shortwave radiation when simulated with different LSMs.

In addition to the local impacts, land-cover changes may also affect the climate of remote areas through changes in the atmospheric circulation. Some studies have shown that historical LULCC could affect the climate in regions far away (Chase et al., 2000; Zhao et al., 2001). These studies and others that have prescribed intense deforestation scenarios have shown that changes in global circulation and teleconnections are particularly sensible to tropical disturbances (e.g, Gedney and Valdes, 2000; Werth and Avissar, 2005).

1.4.2 Biogeochemical impacts

The leading role of terrestrial ecosystems in the global biogeochemical cycle makes them particularly vulnerable to changes in biogeography. Historical deforestation has released about 150 GtC of CO_2 since the preindustrial times, which has contributed to an increase of ~20 ppm in atmospheric CO_2 concentration (Houghton, 2003; Brovkin et al., 2004).

In contrast to the biogeophysical effects, changes in the carbon cycle affect climate at the global scale by modifying the radiative properties of the atmosphere. Claussen et al. (2001) performed ad-hoc simulations to investigate both the biophysical and the biogeochemical impact of large-scale deforestation scenarios using a climate model of intermediate complexity. They show that the albedo-induced cooling due to deforestation at high latitudes overwhelms the corresponding biogeochemical-induced warming. In contrast, in a tropical forest clearing scenario, the biogeochemical effect dominates leading to a net warming. Bala et al. (2007) show similar results based on a GCM. Most studies addressing the impact of land-use in a historical perspective show counteracting climatic responses due to biogeophysical (cooling) and biogeochemical (warming) effects. The latter dominates since 1850 in the modeling experiences of Mathews et al. (2004), resulting in a net global warming of ~0.15 C. Brovkin et al. (2004) show the opposite pattern in a similar experience, where the biophysical effect dominates and leads to weak cooling.

1.5 Thesis outlook: motivation, objectives and structure

Almost all the studies mentioned in the precedent sections and others omitted agree in that LULCC affects significantly the climate, at least at the regional scale. However, there are large uncertainties regarding the amplitude and, in some cases, the direction of these impacts. The biogeophysical effects of land-cover change have actually been assessed in a very shallow manner in the last report of the Intergovernmental Panel of Climate Change (IPCC; Forster et al., 2007). The impacts of LULCC have been evaluated mainly in terms of the albedo-related radiative forcing and, pertinently, have been qualified with a low-to-medium level of scientific understanding.

Given the direct impact in the global carbon cycle of reforestation and afforestation, such strategies have been proposed to mitigate the GHG-induced global warming. In spite of the clear ecological services of forest (e.g., carbon sequestration or biodiversity preservation), the net effect of reforestation in climate is likely to be misleading if the biogeophysical effects are not accounted for.

Land-use is nowadays rapidly evolving and will play a major role in the near future following the mentioned ecological demand as well as the energy and food necessities of a sharply increasing global population.

It is clear that the ensemble of modeling and other studies does not bring a regionally and seasonally consistent climate signal of land-use changes. There are many reasons that could explain the differences in the simulated effect of LULCC. For instance, many LSMs used in climate models are very novel, and vary among them in their complexities (processes involved) and the philosophies adopted to represent the land surface. The simulation strategies as well as the land-surface forcing dataset are also very different.

The main goal of this thesis is to identify the robust biogeophysical impacts of LULCC. The following questions are particularly suggested:

- How strong are these impacts at both the global and regional scale?
- Have been the local impacts of past LULCC in, e.g., surface temperature comparable to those induced by the increasing atmospheric GHGs?
- Which are the relative impacts of radiative and non-radiative effects?
- How large are the uncertainties, in which variables in particular, and which are the main

reasons explaining these uncertainties?

A straightforward strategy to address these points is the model intercomparison analysis of simulations carried out with a coherent protocol to assess the impacts of LULCC. The Land-Use and Climate: IDentifications of robust impacts (LUCID) project was conceived with this motivation (de Noblet-Ducoudré and Pitman, 2007). This thesis is done within the framework of LUCID. The first set of simulations of this project was carried out by seven GCMs in order to assess the impact of LULCC between the preindustrial period and present-day. To constrain the uncertainties between model results, the protocol includes a common agricultural dataset and all GCMs were run forced at the ocean with a unique sea surface temperature data. The ensemble of analyses associated to this modeling initiative is described in Chapter 2.

This thesis also explores the impacts of past LULCC based on present-day observations-based datasets. This study was done for two key variables of the surface climate: the surface albedo and the evapotranspiration. The two approaches developed here, besides bringing novel estimations in the changes of these variables, were used to evaluate the model outputs from LUCID. These results are described in Chapter 3.

Chapter 4 describes the results from a set of simulations carried out with the IPSL Earth System Model in the context of LUCID and the Coupled Model Intercomparison Project Phase 5 (CMIP5) to evaluate both the historical and future impacts on climate due to LULCC. Simulations of the 21st century, including land-cover change scenarios from corresponding RCPs (Representative Concentration Pathways), were compared to simulations with fixed land cover.

General conclusions are provided at the end.

Chapter 2

Impacts of LULCC on climate between the preindustrial period and present-day: Results from the LUCID intercomparison project

This chapter presents a model intercomparison analysis of the biogeophysical effects of LULCC from a set of global simulations carried out within the first phase of the LUCID project. The objective of LUCID is to identify those impacts on climate of LULCC that are coherently simulated by the various models assessed and, then, appear as robust signals. This is tried to be addressed here, as well as to understand and identify the sources of model divergences.

This chapter is organized as follows: an overview of LUCID, the set of simulations assessed and the global climate models (GCMs) involved are presented in Section 2.1. Section 2.2 presents the general methodology and flux conventions. Results are then presented in two parts. An overview of the simulated LULCC-induced changes in the surface climate is first shown at global scale in Section 2.3. Results described in Section 2.4 focus on the temperate regions of the Northern Hemisphere, particularly on two regions where large land-cover conversions occurred between the ends of the 19th and 20th centuries, defined respectively in North America and Eurasia. Part of these results, which a particular focus on the model differences and the causes behind the simulated responses LULCC, are described in two published papers by de Noblet-Ducoudré et al. (2012) and Boisier et al. (2012), included in sections 2.4.4 and 2.4.5. Although some results presented in these two papers repeat those described in the precedent sections, they show in most cases independent analyses. A chapter summary and conclusions are provided in Section 2.5.

2.1 LUCID project

Land-Use and Climate, IDentification of robust impacts (LUCID) is an international initiative conceived under the auspices of IGBP-iLEAPS and GEWEX-GLASS bearing as main objectives the identification and quantification of the robust impacts of human-induced land-cover changes (see de Noblet-Ducoudré and Pitman, 2007). To address this, the strategy of

LUCID includes the analysis of a large ensemble of climate simulations, including multiple models.

Seven climate modeling groups participated in the first phase of LUCID, which performed a set of simulations designed to assess the biogeophysical impacts on climate induced by LULCC between the preindustrial epoch and present-day. A number of studies have been carried out using this set of simulations. Pitman et al. (2009) described the very first results of the project, focusing on the northern summer (JJA) climate responses to LULCC at the global-scale. This study shows that models simulate significant changes in near surface temperatures and in latent heat flux (LE), but constrained to those regions with significant changes in land cover. While most models simulate cooling, the changes in LE are quite uneven within them. Van der Molen et al. (2011) detect, for one GCM participating in LUCID (EC-Earth), a negative feedback on the impact of LULCC in the tropics. Increases in the incoming solar radiation oppose the direct radiative effect (decrease in net shortwave radiation) resulting from increases in surface albedo. De Noblet-Ducoudré et al. (2012) and Boisier et al. (2012), studies describing the major results of this chapter, explore the mechanisms behind the climate responses to LULCC in the Northern Hemisphere temperate regions.

2.1.1 Experimental setup and models

Seven GCMs participated in the first LUCID experiment (see below), all of them conducting four types of simulations. These consisted of ensembles of five realizations of 30-year simulations at equilibrium, constrained by the choice of the imposed vegetation and large-scale climate forcings. The latter were determined by both the boundary conditions at the ocean –all the models were forced with the monthly varying sea surface temperature (SST) and sea-ice concentration (SIC) dataset of Rayner et al. (2003)– and the prescribed atmospheric carbon dioxide concentrations ([CO_2]). The various land surface models (LSMs) embedded in each GCMs also incorporated a common global agricultural dataset in their native land-cover maps. The SAGE (Ramankutty et al., 1999) and HYDE (Klein Goldewith, 2001) datasets were respectively used for cropland and pastureland areal fractions.

The combination of the forcing dataset defined the four modeling experiences carried out (Table 2.1). Then, the 'Present-Day' simulations (PD) used the SST/SIC data from 1970 to 1999, [CO_2] set to 375 ppm, and the vegetation distribution of 1992. Another set of present-day simulations were forced with the same SST/SIC and [CO_2] than that of PD runs, but with the land cover of 1870 (PDv). In the two other experiments, the models (except one of them; Table

2.1) prescribed preindustrial values of SST/SIC (the 1870-1999 period was used in this case) and [CO_2] (set to 280 ppm), and the land-cover distribution of 1870 in one case (PI), and that of 1992 in the other (PIv).

Therefore, the experimental design allows assessing the effects of large-scale changes in climate and in land-use. The biogeophysical effects of LULCC between 1870 and 1992 may be explored trough the difference resulting from the experiments PD and PDv, or/and between PIv and PI. These two different responses to LULCC could also be compared to studying synergisms between LULCC and climate, aspect not explored here, as we found in preliminary analyses that both diagnostics show quite similar results for most variables.

Table 2.1. LUCID set of simulations summary.

Experiment	PD	PDv	PI	PIv
SST/SIC period	1970–1999	1970–1999	1870–1899*	1870–1899*
[CO_2] (ppm)	375	375	280	280
Land-cover year	1992	1870	1870	1992

* Model SPEEDY/LPJmL prescribes present-day SST/SIC in their PI and PIv simulations.

The seven GCMs participating in LUCID are listed in Table 2.2. The land-surface component of these GCMs are all LSMs that, following Pitman et al. (2003), may be categorized as second generation in the case of ISBA (ARPEGE) and TESSEL (ECEARTH), since they do not integrate canopy transpiration and photosynthesis in a common framework, and as third generation for the other cases. The GCM/LSMs references along with a number of key land-surface features concerning this study are included in Table 2.2.

The various LSMs used different strategies to characterize the subgrid land-cover heterogeneity. Most of them define plant functional types (PFTs) to parameterize specific vegetation types, but share different number of them within the grid-cell. This feature will affect the way in which the areal fraction of crops or pasture is set within a cell and, then, the final character of the imposed land-cover conversion. One extreme case occurs with CABLE, which uses a unique PFT per cell and, subsequently, must adopt a rule that should prescribe either 0 or 100% of an agricultural unit within the concerned pixel.

Table 2.2. GCM/LSMs used to perform the LUCID simulations. A list of features relevant to this study is indicated.

GCM	**ARPEGE** **Salas et al. (2005)**	**CCAM** **McGregor and Dix (2008)**	**CCSM** **Collins et al. (2006)**	**EC-Earth** **www.ecmwf.int/research/ifsdocs/CY31r1/**	**ECHAM5** **Roeckner et al. (2003)**	**IPSL** **Marti et al. (2005)**	**SPEEDY** **Strengers et al. (submitted)**
LSM	**ISBA** **Voldoire (2006)**	**CABLE** **Wang et al. (2007); A-bramowitz et al. (2008)**	**CLM** **Oleson et al. (2008)**	**TESSEL** **Van den Hurk et al. (2000)**	**JSBACH** **Raddatz et al. (2007)**	**ORCHIDEE** **Krinner et al. (2005)**	**LPJmL** **Bondeau et al. (2007)**
Resolution	2.8 x 2.8	2.5 x 2.5	1.875 x 2.5	1.8 x 1.8	3.75 x 3.75	2.5 x 3.75	3.75 x 3.75
Background land-cover	ECOCLIMAP (Masson et al., 2003)		Potential (Lawrence and Chase, 2010)	AVHRR (Loveland et al., 2000)	Potential (Pongratz et al., 2008)	AVHRR (Loveland et al., 2000)	Potential (computed)
Total PFT number	12	12	15	16	12	12	11
PFTs per grid cell	No tiles. Aggregated parameters from PFTs	1	4	2	6	12	6
Crops representation	3 specifics PFTs (C3, C4 and irrigated)	1 PFT (C3)	1 PFT (C3)	1 PFT	1 PFT	2 PFTs (C3 and C4)	2 PFTs (C3 and C4)
Pastures representation	As natural grass	As crop	As C3/C4 natural grass	As crop	As C3/C4 natural grass	As C3/C4 natural grass	Managed C3/C4 grassland with intensive cutting cycles
Crops integration strategy	Proportional reduction of natural vegetation	Grid-cell filled up with crop if the combined crop and pasture fraction > 50%	Proportional reduction of natural vegetation	Reduction of low vegetation first and of forest secondarily	Reduction of low vegetation first and of forest secondarily	Proportional reduction of natural vegetation	Proportional reduction of natural vegetation
Leaf/steam albedo							
Soil color	From ECOCLIMAP (satellite)	From ISLSCP2 (Sellers et al., 1996a, 1996b)	MODIS-derived 20 soil color classes (Lawrence and Chase, T.N. 2007)	Vegetation-specific values derived from AVHRR	Derived from MODIS (Rechid, Raddatz, Jacob 2009)	From Wilson and Henderson-Sellers (1985)	0ne general value (0.3), based on Gallimore et al. (2005)
Temperature Layers	2	6 (soil); 3 (snowpack)	10 (soil); 5 (snowpack)	4	5	7	5
Water reservoirs	soil reservoir, surface and snowpack	6 soil layers	10 soil layers	4 soil layers, surface and snowpack	soil reservoir, surface, snowpack on soil and canopy	soil reservoir, surface and snowpack	soil reservoir, surface and snowpack
Soil scheme type	Force-Restore	Diffusion		Diffusion	Single bucket	Single bucket	Single bucket
Canopy resistance	Jarvis	Ball et al. (1987), Leuning (1995), Wang and Leuning (1998), Wang (2000)	Two-leaf (sunlit and shaded) photosynthesis-conductance model (Ball et al., 1987)	Jarvis	Knorr & Heimann (2001)	Ball et al. (1987)	Gerten et al. (2004) modified as described by Strengers et al. (in revision)
Photosynthesis	None	Farquhar et al. (1980), von Caemmerer and Farquhar (1981), Leuning (1995), Wang and Leuning (1998), Wang (2000)	Collatz et al. (1991, 1992)	None	Farquhar et al. (1980), Collatz et al. (1992)	Farqhar et al. (1980), Collatz et al. (1992)	Farqhar et al. (1980), Collatz et al. (1992)
Phenology traitement	Prescribed LAI seasonal cycle	Prescribed LAI seasonal cycle	Prescribed LAI seasonal cycle	Fixed LAI (no seasonal cycle)	Computed LAI	Computed LAI	Computed LAI
Harvesting	Implicit (from observed LAI imposed)	Implicit (from observed LAI imposed)	Implicit (from observed LAI imposed)	None	Implicit in crop phenology scheme	Implicit (from duration of leaf cycle that is shorter than with natural vegetation)	Computed harvest @ maturity, based on temperature sum concept

Another aspect that will affect the climate responses to LULCC is how LSMs parameterize the various land-cover types, particularly in the case of crops and pastures. Depending on the LSM, one to three specifics crop PFTs are defined, while pastures may be represented as crops (CABLE and TESSEL) or natural grass (all the others). The phenological cycle is also described in different ways within the various LSMs. JSBACH, LPJmL and ORCHIDEE, simulated LAI cycle based on the seasonal carbon allocation and the local climate. The other LSMs prescribe a LAI cycle based on satellite observations (ISBA, CABLE, CLM), or use a fixed value year-round (TESSEL).

Given that the processes behind the effets of LULCC are primarily dependent on the land-surface parameterizations and since this study focuses on the surface climate, the models will usually be referred with both the names of the GCM and/or the LSM in which it is embedded.

The global crop and pasture distribution from respectively SAGE and HYDE datasets are illustrated in Figure 2.1. Croplands are nowadays (1992) particularly extensive in the Northern Hemisphere, notably in North America, Eurasia, India and southeast China. Pasturelands are more localized and dense in some regions as the Middle East. From this dataset, crops or pastures covered together more than 20% of the global ice-free land surface in 1992, half of which has been added since 1870. The expansion of cropland from 1870 to 1992 is particularly large in the North American continent, and moderate in other regions that were already highly perturbed in 1870 (e.g., Eurasia, India and China; Figure 2.1c).

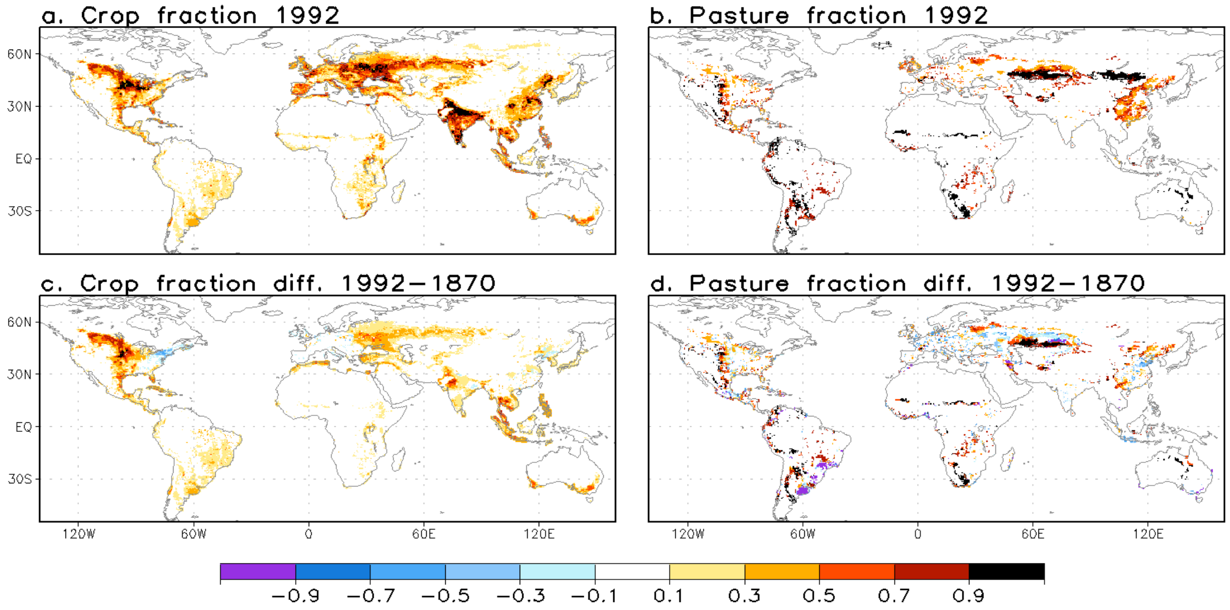

Figure 2.1
Areal fraction of cropland (a) and pastureland (b) in 1992 and the corresponding differences between 1992 and 1870 (c, d).

Even if all the LUCID modeling groups used the same sources of global crop and pasture distribution, the imposed land-cover maps and the resulting differences between 1870 and 1992 were not the same across the various LSMs. As commented above, the land-cover distribution depends both on the original (built-in) maps of each LSM and on the strategy adopted to incorporate the agricultural data.

The resulting changes in the global land area covered by crops, grasses, trees and bare soil in each LSM are summarized in Table 2.3. Most models (excepting CCAM/CABLE) show increases in cropland area from 1870 to 1992 similar or lower than that prescribed in the SAGE dataset (around +8 million km^2). Part of the models differences comes from their specific map projections and the resulting land masks. However, the resulting changes in the other land-cover groups are very different within the models, mainly reflecting their uneven natural vegetation maps and methods used to integrate the agricultural datasets. The change in total forest area is representative of these differences, ranging from −4 to −10 million km^2 in the case ECHAM5/JSBACH and ECEARTH/TESSEL, respectively. The global distribution of the resulting forest fracton change between 1870 and 1992 in each model is provided in Appendix A2.

Hence, the models did not prescribe the same land-cover forcing between 1870 and 1992 that, logically, will affect the simulated responses to LULCC and add an important source of uncertainty on the model intercomparison analyses. The character of the imposed land-cover change (e.g., the resulting deforestation strength) is then addressed continuously in the results presented in the following sections, and its role on the resulting responses to LULCC and on the inter-model dispersion is particularly explored in Section 2.4.

Table 2.3. Change in global land area covered by different vegetation types and bare soil between 1870 and 1992 (in million km^2).

GCM LSM	ARPEGE ISBA	CCAM CABLE	CCSM CLM	EC-Earth TESSEL	ECHAM5 JSBACH	IPSL ORCH.	SPEEDY LPJmL
Crops	6.1	13.0	6.1	5.9	5.1	8.1	7.5
Grasses	1.1	−8.4	−1.1	3.3	−1.1	1.6	0.7
Everg. trees	−4.1	−3.0	−2.1	−2.3	−1.8	−4.5	−4.3
Decid. trees	−1.0	−1.4	−2.9	−7.7	−2.2	−5.0	−2.9
Total forest	−5.1	−4.4	−5.0	−10.0	−4.0	−9.5	−7.2
Bare soil	−2.1	−0.2	0.0	0.5	0.0	−0.2	−1.0

2.2 General methodology and flux convention

The analyses presented in this chapter focus on the surface climate and, particularly, on the various components of the surface energy budget (SEB). This is considered in the following way:

$$Q_A = Q_T + L_U + G \qquad (2.1)$$

$$Q_A = L_D + S_N \qquad (2.2)$$

$$Q_T = LE + H \qquad (2.3)$$

$$S_N = S_D - S_U = (1 - \alpha)\, S_D \qquad (2.4)$$

The energy flux Q_A, the sum of the downward longwave radiation (L_D) and the net shortwave radiation (S_N), will be referred to as available energy. It is positive when incoming the surface and provide an estimate of the total radiation absorbed at the surface (i.e., the surface emissivity is considered to be 1.0). The total turbulent energy flux (Q_T) –the sum of latent (LE) and sensible (H) heat fluxes–, the emitted longwave radiation (L_U) and the ground heat flux (G) are positive when outgoing the surface (downward direction in the latter case).

The surface albedo (α), although explicitly diagnosed in the various LSMs assessed, is here computed from upward (S_U) and downward (S_D) shortwave radiation (i.e., $\alpha = S_U/S_D$), fluxes that are positive when outgoing and incoming the ground, respectively. The resulting net shortwave radiation (S_N) is then positive incoming the surface. The simulated G values are not evaluated in this study.

As described in the precedent section, the impacts of LULCC can be diagnosed from the LUCID experiences (Table 2.1) from both difference *PD–PDv* and *PIv–PI*. In most cases, the LULCC-induced anomaly of a generic variable *V* will be referred as 'mean' impact on *V* resulting from the vegetation change between 1870 and 1992, i.e.,

$$\Delta V = 1/2\, (V|_{PD} - V|_{PDv} + V|_{PIv} - V|_{PI}) \qquad (2.5)$$

where $V|_E$ represents the climatological mean value of *V* for the ensemble of simulations *E* (5 × 30 = 150 years). In some cases, the LULCC-induced anomalies are compared to those resulting from the changes in the ocean boundary condition (i.e., SST/SICs) and in [CO_2] (thereafter ΔSST/CO2). The resulting climate response to the change in those large-scale drivers is used here as an estimation of the GHG-induced impacts between the two periods studied. The ensembles of used diagnostics are summarized in Table 2.4.

Table 2.4. Set of diagnostic used to evaluate the effect of changes in land cover and in the large-scale climate drivers (ΔSST/CO2) between 1870 and 1992.

ΔL1	LULCC –induced change (present-day global-scale conditions)	*PD – PDv*
ΔL2	LULCC –induced change (preindustrial global-scale conditions)	*PIv – PI*
ΔLm	LULCC –induced change (mean)	*0.5 (PD – PDv + PIv – PI)*
ΔC1	ΔSST/CO2 –induced change (vegetation fixed to 1992)	*PD – PIv*
ΔC2	ΔSST/CO2 –induced change (vegetation fixed to 1870)	*PDv – PI*
ΔCm	ΔSST/CO2 –induced change (mean)	*0.5 (PD – PIv + PDv – PI)*
ΔLC	Net impact	*PD – PI*

All the model data were linearly interpolated to a common rectangular grid of 2.0×2.0 degree, in order to allow point-to-point statistics among the various GCMs and coherent regional comparisons. Maps showing differences in a selected variable illustrate, in most cases, the anomalies that are significantly different from zero. This is evaluated by means of Student's hypothesis tests (t-test), applied to the complete time-series of each grid-point in a single model, without assuming equal variances between the various LUCID experiences.

2.3 Large-scale changes on surface climate

This section describes the global patterns of the simulated climate responses to LULCC. Changes in the temperature, precipitation and surface energy fluxes are calculated from the ensemble of LUCID simulations following Equation (2.5). The results shown here are principally multi-model statistics, while the corresponding individual model responses are given in Appendix 2.1.

2.3.1 Temperature and precipitation

Figure 2.2 illustrates the model mean and the inter-model mean deviation (MD) of the 2-m temperature (T_{2m}) responses to LULCC in Northern Hemisphere (NH) winter (December-January-February; DJF) and summer (June-July-August; JJA).

In both DJF and JJA, the ensemble mean of LUCID simulations shows cooling around the hot spots of intense LULCC in the NH temperate regions (see Figure 2.1), with anomalies of up to around -1.0 K. The MD statistic indicates the model average of the absolute departures of the individual responses to LULCC from the model-mean one. In the T_{2m} case, the MDs are of the same order than the model-mean response, enlightening quite large differences between the model results (Figure 2.2[c-d]). ARPEGE and ECEARTH simulate strong cooling compared to the other models in both DJF and JJA, while CCSM and ECHAM5 show very weak signals (see figures A2.2 and A2.3). As is described in the following sections, non-radiative effects of LULCC become critical in summer and may conduct to a net warming, as the IPSL model shows (Figure A2.3).

The model mean LULCC-induced precipitation changes do not show significant signals in most part the globe (Figure 2.3). As the MDs suggest, in the NH temperate regions and in the corresponding winter (DJF), the almost inexistent mean precipitation signal results from weak responses to LULCC systematic simulated by most models (Figure A2.4). In turn, the precipitation changes in JJA show significant anomalies, but with irregular patterns and of different signs within the models (Figure A2.5). For instance, CCSM and ECEARTH show clear summer precipitation increases in North America, while IPSL simulated decreases in this variable.

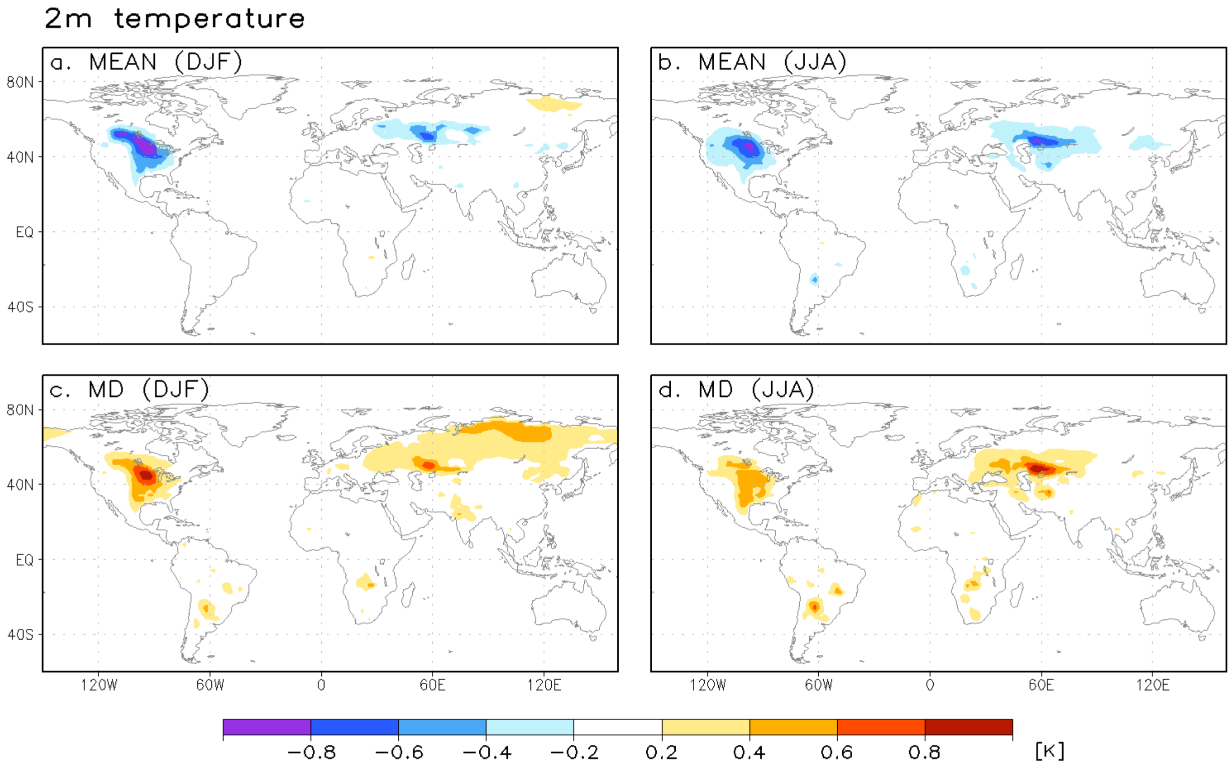

Figure 2.2
LULCC-induced 2-m temperature anomaly in DJF (a, c) and JJA (b, d). Top and bottom panels indicate respectively the model mean anomalies and the mean deviations between the individual model responses.

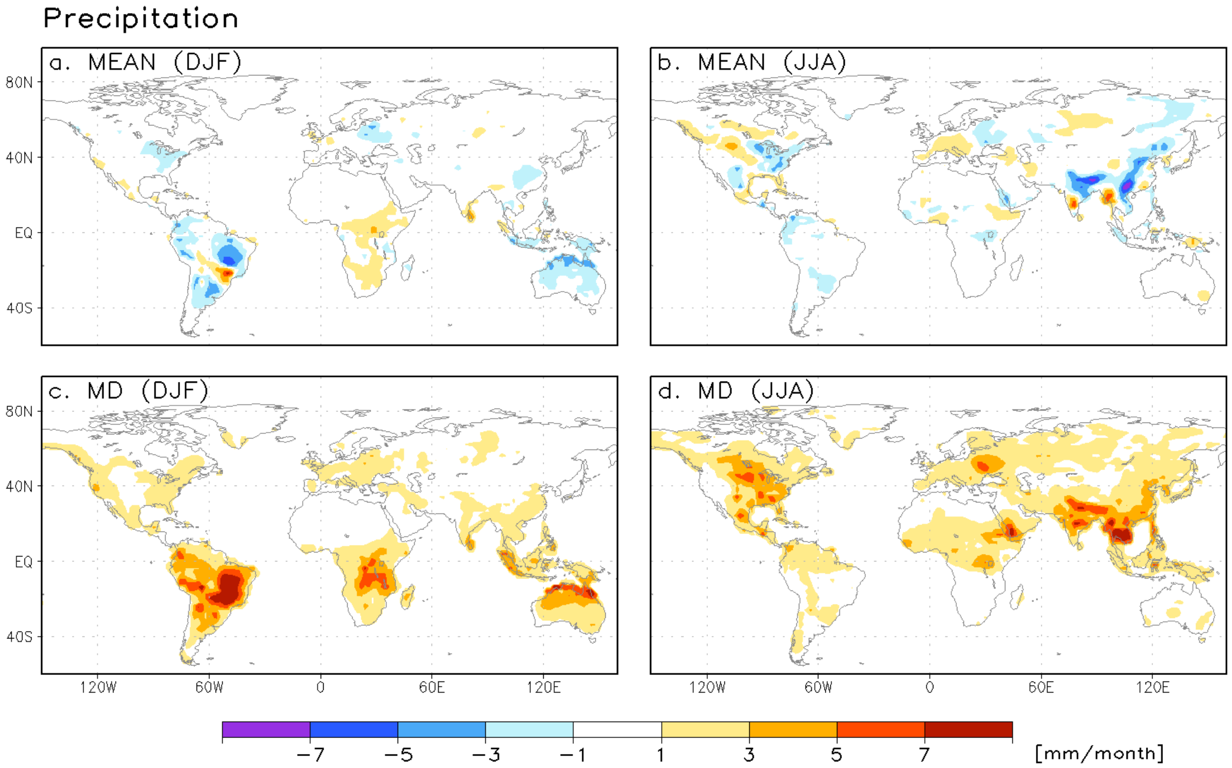

Figure 2.3
As for Figure 2.2, except for changes in precipitation.

2.3.2 Surface energy fluxes

Figures 2.4 and 2.5 illustrate the model mean and inter-model MDs of the LULCC-induced net shortwave radiation (S_N) and latent heat flux (*LE*) changes between the preindustrial period and present-day. A first view to these components of the surface energy budget (SEB) is presented here because they are supposed to be directly perturbed by land-cover conversions. The simulated changes in surface albedo (α) are also illustrated in Figure 2.4 (indicated by contour lines).

In accordance to what is expected from previous studies assessing the climate responses to deforestation in temperate regions (e.g., review by Bonan, 2008b), the ensemble of LUCID models shows α increases and S_N reductions in the most perturbed areas of the NH in the corresponding winter (DJF; Figure 2.4a). S_N anomalies are mainly (but not entirely; see Section 2.4) driven by the changes in α, which are particularly strong under snow-covered surfaces. The model-mean S_N reduction in DJF is coherent with the simulated cooling in this season, and also shows significant differences between individual responses, particularly in North America (Figure 2.4c and Figure A2.6). The LULCC-induced S_N anomalies in JJA are also predominantly negative (Figure 2.4b). Although the summer α responses in the NH temperate regions are quite weaker than that simulated in winter, the larger incoming solar radiation in JJA results on S_N

anomalies of similar amplitude to those of DJF. The inter-model MD is also quite large in this season (Figure 2.4d).

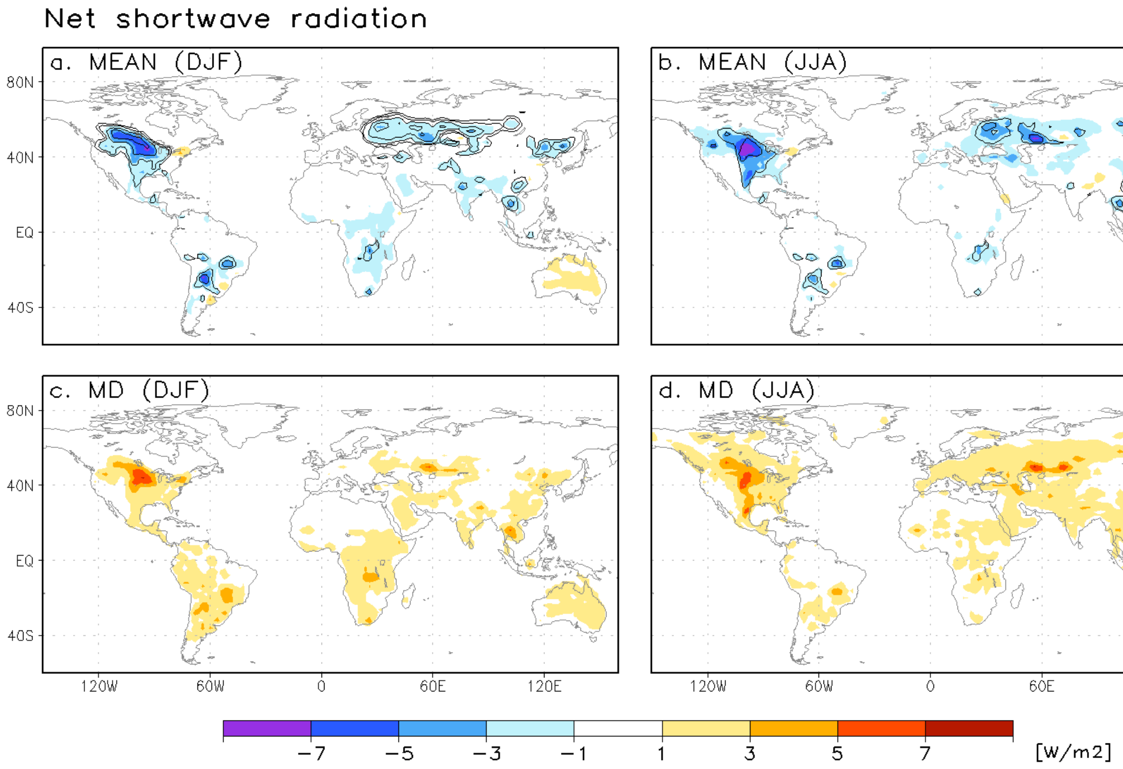

Figure 2.4
As for Figure 2.2, except for changes in net shortwave radiation. Contour lines in upper panels indicate the LULCC-induced surface albedo changes of +0.01, +0.02, +0.05 and +0.1.

The model-mean *LE* changes in the NH temperate regions show weak negative anomalies in DJF (with amplitudes of around 1 W m^{-2}; Figure 2.5a). The model-mean *LE* response is also weak in JJA if compared to the absolute values (not shown), and with a quite irregular pattern (Figure 2.5b). The feeble mean *LE* signal in the NH winter and the weak MD associated (Figure 2.5c) results from weak individual responses (Figure A2.6), coherent with the low available energy by radiation and *LE* (absolute) values during this season. In turn, the weak model-mean *LE* change in JJA results from quite large individual responses, but diverse in amplitude and sign, as the MD of this variable and season clearly illustrates (Figure 2.5d). Two GCMs show clear *LE* decreases in this season (IPSL, SPEEDY), three of them show clear *LE* increases (CCSM, ECEARTH, ECHAM5) and the other two models have irregular responses (Figure A2.7).

The large MD associated to changes in *LE* in the tropical and southern subtropical areas result from quite large *LE* responses simulated by two models: CCAM and SPEEDY (figure A2.6 and A2.7).

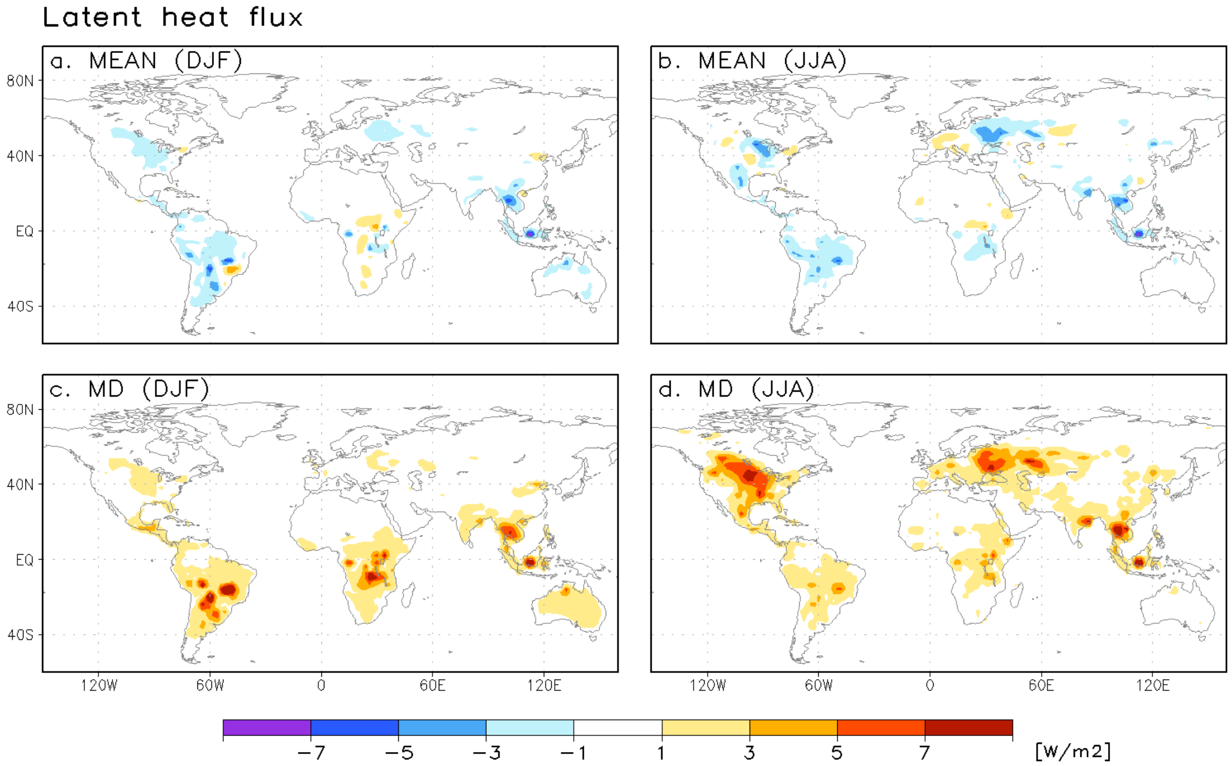

Figure 2.5
As for Figure 2.2, but for changes in latent heat flux.

The annual mean responses to LULCC averaged over the global ice-free lands are summarized in Table 2.5 for a number of variables, including all the SEB components studied here. All models show negative T_{2m} anomalies, but of quite weak amplitude (up to 0.19 K and below 0.05 K in four out the seven models). The model-mean cooling of –0.09 K over lands and of –0.02 K globally is lower in amplitude than earlier estimates of, e.g., –0.14 K (globally) by Hansen et al. (1998) or of –0.05 K by Davin et al. (2007). However, since LUCID simulations used the fixed SST/SIC, the resulting global temperature responses to LULCC are likely constrained and, probably, underestimated, due to suppressed feedbacks from the ocean (Davin et de Noblet-Ducoudré, 2010).

The models also show systematic global mean decreases in S_N and in net radiation (R_N) at the surface. The model-mean change in S_N averages –0.8 W m^{-2} over lands and near –0.14 W m^{-2} ± 0.08 W m^{-2} (model range) globally. Considering this value as an estimate (roughly) of the LULCC-induced radiative forcing since the preindustrial period, the results from LUCID models are lower than the best radiative forcing (RF) estimated reported in the IPCC's Fourth Assessment Report (Forster et al., 2007) of –0.2 W m^{-2} but within the uncertainties associated (± 0.2 W m^{-2}).

Consistent with the LULCC-induced R_N perturbation, the changes in turbulent heat fluxes are mostly negatives. The latent (*LE*) and sensible (*H*) heat flux anomalies are quite more heterogeneous within the models. Changes in *LE* range from –1.95 (SPEEDY) to 0.36 (CCAM) W m^{-2}. These two models, however, also simulate different changes in R_N and in the total turbulent energy flux (Q_T), difference that implies a change in other SEB terms not considered here (i.e., a change in the soil and/or in the snowpack heat storage) or a surface energy imbalance in their the simulations.

Table 2.5. Annual mean LULCC-induced changes in different variables and components of the surface energy budget averaged over the global lands excluding Greenland and Antarctica.

GCM	T_{2m} [K]	P [mm/y]	S_N [W/m^2]	L_N [W/m^2]	R_N [W/m^2]	LE [W/m^2]	H [W/m^2]	Q_T [W/m^2]
ARPEGE	–0.19	–4.6	–0.78	0.48	–0.30	–0.18	–0.12	–0.30
CCAM	–0.02	10.3	–1.29	1.14	–0.15	0.36	–0.40	–0.04
CCSM	–0.03	1.0	–0.40	0.04	–0.36	–0.02	–0.36	–0.38
ECEARTH	–0.19	–5.0	–1.27	0.05	–1.22	–0.33	–0.89	–1.22
ECHAM5	–0.03	–3.1	–0.27	0.03	–0.24	–0.1	–0.12	–0.23
IPSL	–0.03	–7.5	–0.51	–0.41	–0.92	–0.59	–0.33	–0.92
SPEEDY	–0.13	–12.9	–1.11	0.60	–0.51	–1.95	0.10	–1.85
MEAN	–0.09	–3.1	–0.80	0.28	–0.52	–0.40	–0.30	–0.70

2.4 Impacts of LULCC in the Northern Hemisphere temperate regions

The results described in the precedent section show that the impacts of LULCC simulated by the LUCID models are confined to the regions where large land-cover perturbations were prescribed. The analyses presented here focus on the temperate regions of the Northern Hemisphere and, particularly, in two regions defined in respectively North America (NA) and West Eurasia (EA). These two regions were chosen because of their associated extensive and continuous areas LULCC between 1870 and 1992. Within a fixed domain, each region was defined by the grid-cells showing absolute differences in crop or in pasture fraction higher than 5% between 1870 and 1992. Region NA encompasses those grid-cells within 30°N and 60°N and within 120°W and 80°W, while EA those within 45°N and 60°N and within 0°E and 90°E (Figure 2.6). The resulting areas totalize 4.5 and 5.9 million km^2 in NA and EA, respectively.

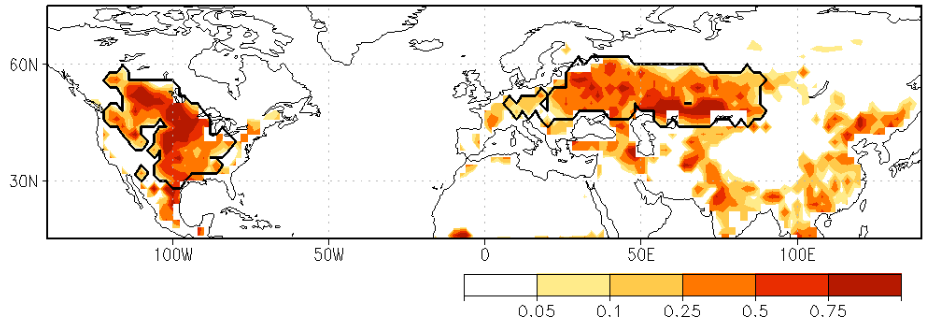

Figure 2.6
Absolute changes in crop and pasture fractions between 1870 and 1992. Solid contours indicate areas with changes larger than 5% in crop or pasture fractions confined to North America and west Eurasia, regions that will be further used in the analyses.

2.4.1 How large are the land-use effects at the regional scale? The problem of attributing climate changes to GHGs without taking in account LULCC

The changes in the surface energy fluxes due to LULCC between the preindustrial period and the present-day and the resulting temperature responses simulated by the LUCID models are weak when averaged over the global lands (Table 2.5), and remain almost insignificant when averaged globally (not shown). Actually, the impacts on the surface climate, following the LUCID simulations, are mainly constrained to those regions where the land-cover change is imposed, as figures 2.2 to 2.5 show and Pitman et al. (2009) stated. Remote impacts of LULCC or teleconnections are probably limited by the fact that SST/SICs is prescribed, as discussed by van der Molen et al. (2011). Davin and de Noblet-Ducoudré (2010) using the IPSL model in its fully coupled configuration (i.e., with interactive ocean), show that the radiative effects of deforestation are transferred to the ocean, resulting on a stronger global cooling than those obtained in simulations with prescribed SST/SIC. Even so, the historical impact of LULCC on the global temperature is weak compared to other human-induced climate perturbations, notably to the one induced by changes in the atmospheric greenhouse gases (GHGs) concentrations (Forster et al., 2007).

The effects of LULCC increase when moving from large to regional scale, in which the large land-conversion occurs. As Figure 2.7 illustrates, LUCID simulations show that the amplitude of the LULCC-induced temperature changes at the regional scale could be similar or higher than the one induced by the global-scale climate forcing (ΔSST/CO2; Table 2.4). In this figure, the NH winter (DJF) T_{2m} responses to both LULCC (green line) and ΔSST/CO2 (red line) in the NH extratropical areas are plotted against the change in the net herbaceous fraction ΔF_H (i.e., crops plus grasses; changes in pasturelands are implicitly accounted for in one of these two types of vegetation; see Table 2.2). The net impact resulting from both climate drivers is also plotted in black lines. Four out of the seven GCMs show clear LULCC-induced cooling in DJF, with amplitudes roughly proportional to ΔF_H (this measure is equal to the magnitude of deforestation when there is no changes in bare soil fraction). Since there is no a direct geographical dependence on the T_{2m} effects due to changes in SST/CO2, the models show an approximately constant positive T_{2m} response to ΔSST/CO2 (SPEEDY do not show such feature because the same SST/SIC period were prescribed in their preindustrial and present-day simulations). The SST/CO2-induced T_{2m} anomalies are within +0.5 and +1.0 K, in accordance to the global warming of around +0.8 K estimated since the preindustrial period (Trenberth et al., 2007).

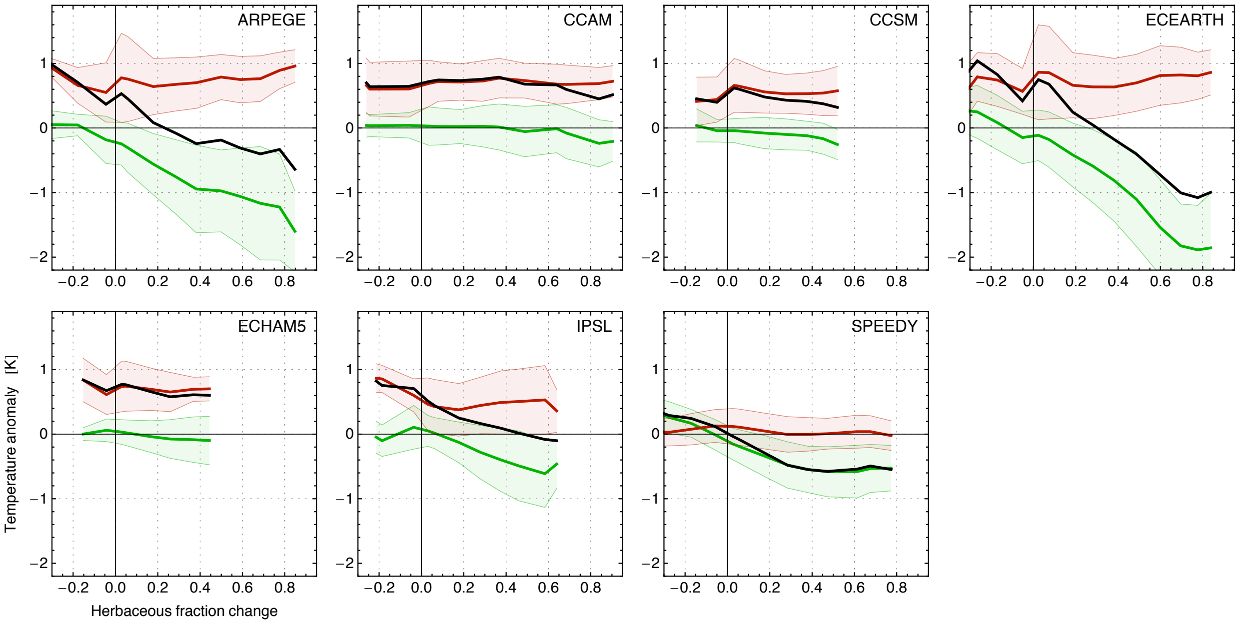

Figure 2.7
Winter mean (DJF) 2-meter temperature anomalies in northern extratropical areas (north of 25N) plotted against the changes in net herbaceous fraction between 1870 and 1992 (crops plus grasses; ΔF_H). Green, red and black lines respectively illustrate the anomalies induced by LULCC (ΔLm), by $\Delta SST/CO_2$ (ΔCm) and by both drivers (ΔLC) (see Table 2.4). Solid lines and shaded areas indicate the mean ±1 standard deviation from grid-cells showing ΔF_H within a range of 0.1 centered on the values indicated in x-axis.

It is easy to appreciate from Figure 2.7 the minimum level of deforestation in which the winter LULCC-induced (regional) cooling could offset the SST/CO2-induced (large-scale) warming. This level ranges from around 20% in the case of ARPEGE to 50% in the case of IPSL. As Figure 2.8 illustrates, within the NH extratropical lands (beyond 25°N), the surface area showing 20% of deforestation or larger range from ~3 million km^2, in the case of ECHAM5, to ~10 million km^2, in the case of ECEARTH. Meanwhile, pixels showing minimum fraction of deforestation of 50% totalizes less than half a million km^2 in thee models (CCSM, ECHAM5 and IPSL) and more than a million in the rest of the models. Although these values vary widely within models, it can be concluded that the surface climate could have been quite significantly disturbed by past LULCC over areas of the order of millions km^2, with temperature responses of the same order than those induced by changes the atmospheric GHGs; i.e., a regional to continental scale.

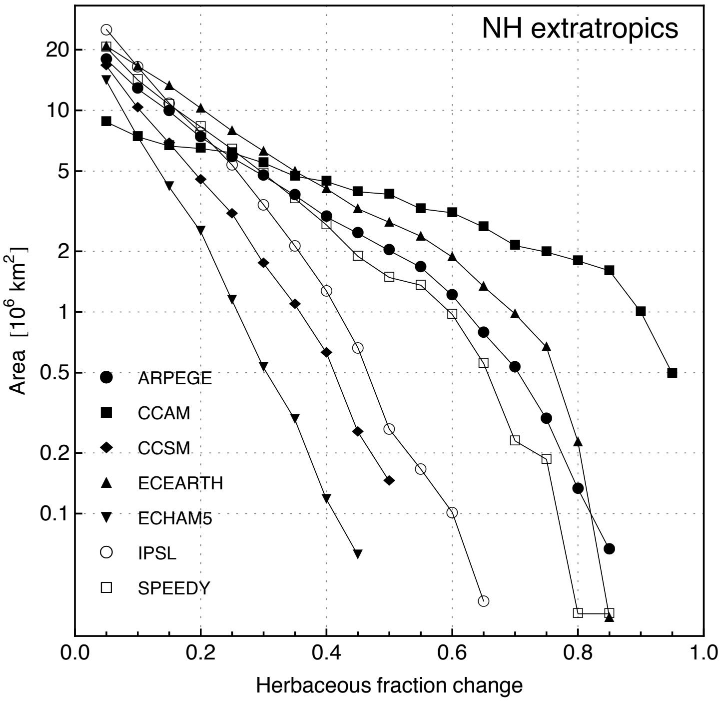

Figure 2.8
Total land area within the Northern Hemisphere extratropics (beyond 25N) with ΔF_H equal or greater than the values indicated in the x-axis. Results from the various LUCID models are shown.

In the specific case of northern winter shown in Figure 2.7, the model T_{2m} responses to LULCC are mostly negatives, offsetting the ΔSST/CO2-induced warming. In other seasons, particularly during the northern summer, the models results are more uncertain. The effects of LULCC and those of SST/CO2 could actually be additive. Despite these uncertainties, the message from figures 2.7 and 2.8 is that past LULCC have likely induced changes in temperature over quite extensive areas with amplitudes as large that may produce misleading interpretation of the regional temperature changes due to large-scale climate trends (e.g., GHG-induced).

The comparison between the simulated regional climate changes induced by LULCC and the ones induced by ΔSST/CO2 is more clearly illustrated in Figure 2.9. This figure shows the seasonal changes in available energy Q_A (Eq. 2.2) and T_{2m} averaged over NA and EA, resulting from both drivers. The multiple responses from the various models and different anomaly calculations (ΔL1, ΔL2 by one side, and ΔC1, ΔC2 by the other; Table 2.4) are illustrated as box-whisker plots, showing the extremes values, the inter-quartile range and the median.

The LULCC-induced Q_A and T_{2m} changes in NA and EA shown by the ensemble of LUCID simulations are of the same order but opposite in sign than the estimated responses to the historical change in the atmospheric concentration of GHG (ΔSST/CO2) over the same regions. The changes in Q_A highlight the radiative impacts on the surface induced by both climate drivers. These are notably directed by decreases in net solar radiation (S_N) in the case of LULCC, and by increases in downward longwave radiation (L_D) in the case of the ΔSST/CO2 (not shown). Following the changes in Q_A, the near surface if the regions assessed cools and warms as response to LULCC and ΔSST/CO2, respectively, with amplitudes of about 0.5 K in both cases. It is also evident from Figure 2.9 that the uncertainties associated to the impacts of LULCC are larger than those related to changes in SST/CO2.

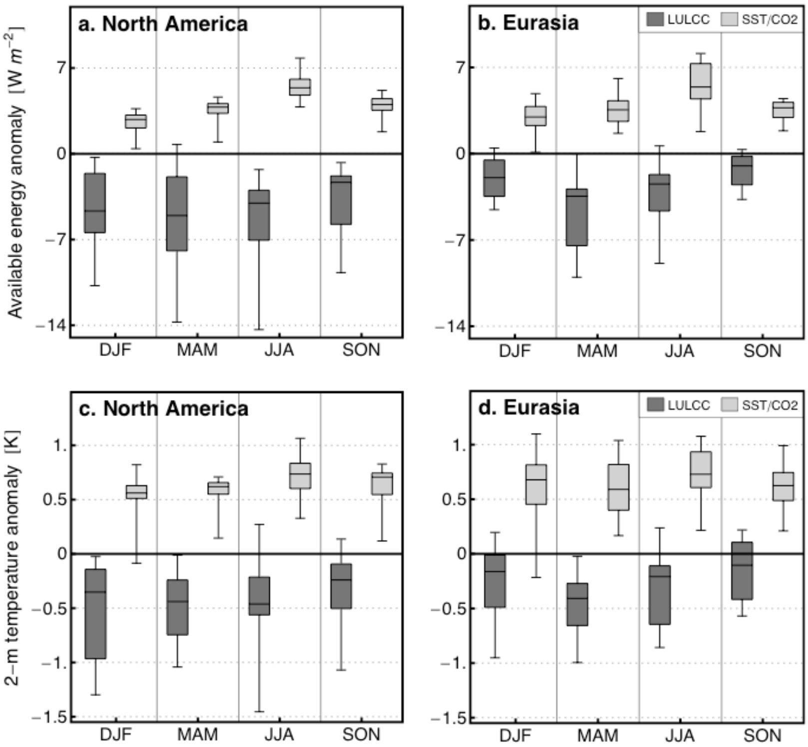

Figure 2.9
Changes in available energy (sum of downward longwave and net shortwave radiation; a, b) and in 2-m temperature (c, d) induced by LULCC (dark gray boxes) and by changes in SST/CO2 (light gray) between preindustrial period and present day. The anomalies are calculated for the two regions defined in North America (NA; a, c) and Eurasia (EA; b, d). Box-whisker plots indicate the extremes, the inter-quartile range and the median values of the individual model results and both anomalies of each climate driver (see Table 2.4).

2.4.2 Differences in the imposed LULCC and resulting inter-model dispersion

Figure 2.10 illustrates the seasonal T_{2m} anomalies induced by LULCC in NA and EA simulated by each of the seven LUCID GCM/LSMs. Most models simulate cooling during the whole year with anomalies of around -0.5 K. The amplitudes of the T_{2m} changes are slightly stronger in NA than in EA, pattern expected given the different intensities of land-use changes between both regions (Figure 2.11).

Two GCMs, ARPEGE and ECEARTH, show clear stronger responses than the other models, both cases showing winter cooling with amplitudes larger than 1 K in NA. Results from IPSL are exceptions, showing near surface warming in both regions during the northern summer and fall. CCSM also simulates warming in EA in SON. The models do not show a systematic seasonal pattern in their temperature responses, as well as they neither show coherent seasonal responses within the two regions. A further description on the seasonal responses to LULCC and a more complete comparison within the results in NA and EA is described in Section 2.4.4 (de Noblet-Ducoudré et al., 2012).

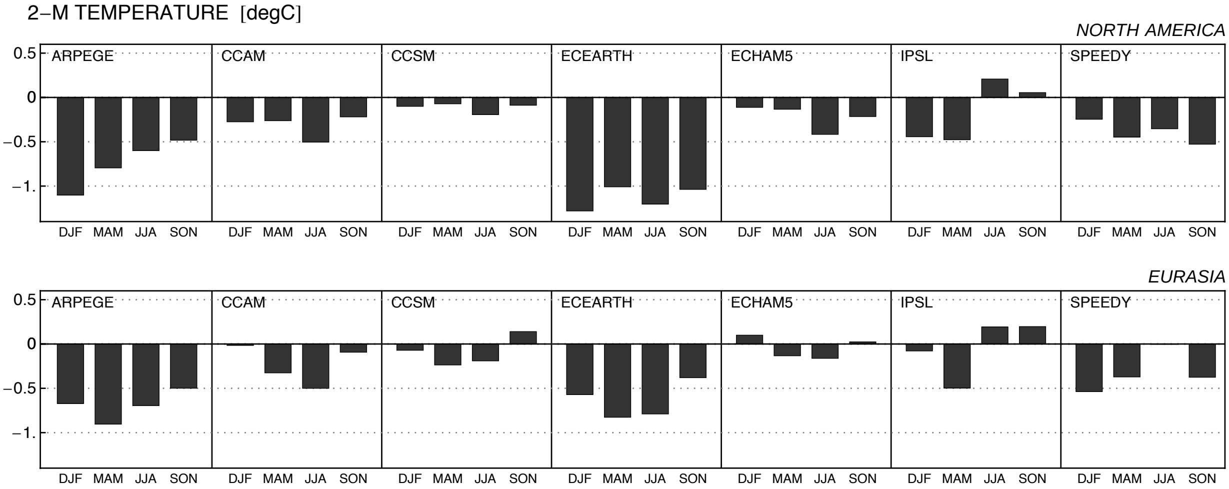

Figure 2.10
LULCC-induced seasonal 2-m temperature changes in NA (top) and EA (bottom).

Besides those climatic signals of LULCC that are systematically simulated by LUCID models in NA and EA (e.g., winter and spring cooling), the results show a remarkable dispersion among the various models here assessed. The first logical factor that should contribute to this dispersion is the land-surface forcing itself.

As highlighted in Section 2.1, although all the modeling groups used the same crop/pasture dataset, the land-cover distribution of 1870 and 1992, and the resulting difference between the two periods are quite model-dependant (Table 2.3). These differences result from

1) the strategies used to incorporate the agricultural data in the native LSM's land-cover maps –aspect that is also constrained by the LSM's structure (Table 2.2)– and

2) the native land-cover maps themselves (a discussion on this subject is found in de Noblet-Ducoudré et al., 2012).

With the exception of CABLE (LSM constrained by the option of a unique PFT per pixel), in most LSMs were adopted a similar strategy to prescribe the vegetation distributions of 1870 and 1992, which proportionally modify their respective background natural vegetation to allocate crops and pastures. Then, the resulting land-cover differences within the LUCID LSMs reside principally on their native vegetation distribution.

Figure 2.11 illustrates the mean land-cover partitioning in NA and EA for 1870, and the vegetation differences between 1870 and 1992. The various LSM's land cover distributions are compared here through four groups of vegetation: crops, grasses, evergreen trees and deciduous trees; in addition to bare soil. Since the various LSMs have their specific PFTs, which are not necessarily equivalent between them, the choice of these general land-cover groups allows performing coherent comparisons between the models.

The various LSMs show a quite different partitioning of vegetation in 1870 in the two studied regions. These differences are related to both the relative presence of herbaceous plants vs. that of forest and the forest type partitioning (evergreen vs. deciduous). For instance, the grass fraction in NA ranges from nearly 0% in TESSEL (ECEARTH) to around 50% in CABLE (CCAM), CLM (CCSM) and JSBACH (RCHAM5) (Figure 2.11a). Further, most LSMs show a higher fraction of evergreen trees than that of deciduous trees, with the clear exception of TESSEL (ECEARTH).

The land-cover differences between 1870 and 1992 are, consequently, heterogeneous within the models (Figure 2.11b). Those models having comparatively large portions of grass in 1870 show an increase in crop fraction in detriment of grass and forest in similar rates (e.g., CCSM/CLM in NA). In turn, ISBA (ARPEGE), TESSEL (ECEARTH), ORCHIDEE (IPSL) and LPJmL (SPEEDY) show clear higher rates of deforestation in NA. The difference in crop fraction between 1870 and 1992 is similar in most models, holding all of them the change done by the SAGE dataset of ~0.3 in NA and ~0.2 in EA (dashed lines in Figure 2.11b). CCAM/CABLE is a clear exception. This model used a specific crops incorporation strategy forced by the CABLE land-cover representation (Table 2.2), resulting in a noticeable larger increase in crop fraction between 1870 and 1992.

The resulting deforested areas within NA and EA between 1870 and 1992 in NA and EA are summarized in Table 2.5. The different land-cover partitioning prescribed in the various LUCID LSMs results in deforestation rates ranging from ~0.6 (ECHAM5, CCSM) to ~1.8 million km^2 (ECEARTH) in NA, and from ~0.6 (CCSM) to ~1.4 million km^2 (CCAM) in EA.

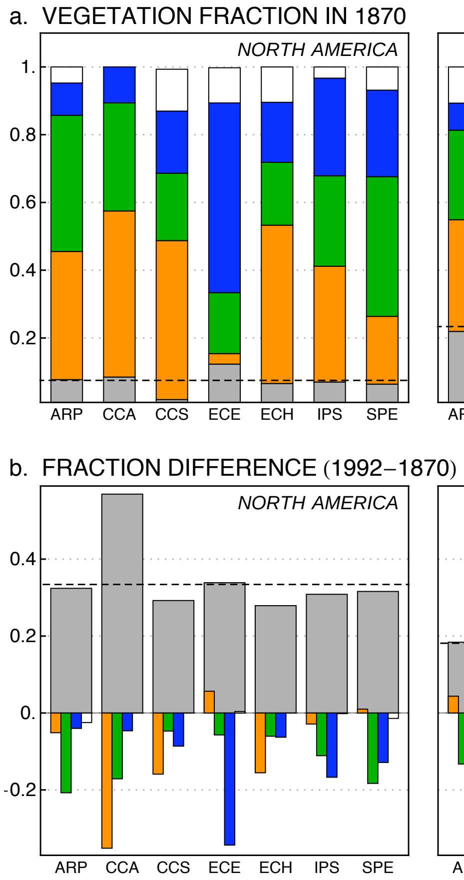

Figure 2.11
Land-cover partitioning in 1870 (a) over the regions defined in North America (NA) and Eurasia (EA), and the land cover change between 1870 and 1992 (b). Color bars illustrate the fraction of the surface occupied by crops (gray), grasses (orange), evergreen trees (green), deciduous trees (blue) and bare soil (white). Dashed lines indicate the corresponding crop fraction in 1870 (a) and the fraction differences (1992-1870) from the SAGE dataset. ARP, CCA, CCS, ECE, ECH, IPS, and SPE are the GCM acronyms for respectively ARPEGE/ISBA, CCAM/CABLE, CCSM/CLM, ECEARTH/TESSEL, ECHAM5/JSBACH, IPSL/ ORCHIDEE and SPEEDY/LPJmL.

Table 2.5
Forest area change between 1870 and 1992 within two selected regions in North America (NA) and Eurasia (EA) (in million km^2).

Region	ARPEGE ISBA	CCAM CABLE	CCSM CLM	EC-Earth TESSEL	ECHAM5 JSBACH	IPSL ORCH.	SPEEDY LPJmL
NA	−1.13	−0.99	−0.61	−1.82	−0.56	−1.27	−1.42
EA	−0.95	−1.75	−0.58	−1.37	−0.64	−1.07	−0.82

A rate of deforestation does not define a land-cover perturbation as a whole, but remains a good metric for assessing the LULCC-induced change in those variables or properties of the surface that are highly dependant on the tree density of the surface (e.g., surface roughness and albedo). Figure 2.12 illustrates how the change in forest fraction relates with the response to LULCC of different variables during the NH summer in NA and EA.

Excepting CCAM/CABLE, the LULCC-induced surface albedo (α) anomalies simulated by the various models correlates well with the corresponding change in forest fraction (Figure 2.12a). All the models simulate summer α increases because of the higher snow-free leaf/stem albedo of herbaceous plants (natural grasses and crops) than that of forest parameterized in the various LSMs. The version of CABLE used in this study makes no differences in leaf albedo between PFTs, which result on a roughly null α response to LULCC in JJA. Consistent with what is expected from α changes, the various models simulate S_N decreases of amplitudes, at first order, proportional to the deforestation strength (Figure 2.12b). However, more dispersion is appreciated within the models in this case, suggesting that other factors than α are playing a major role, such as perturbations in incoming solar radiation (S_D) or in the snow-cover. The contribution of S_D to ΔS_N is quantified in the section that follows.

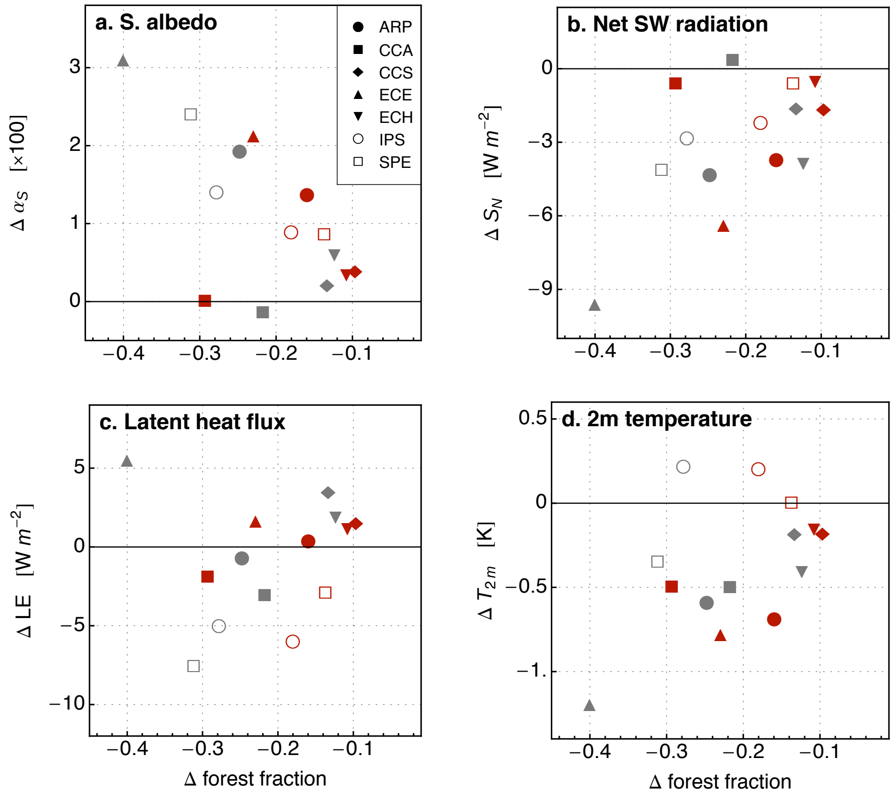

Figure 2.12
LULCC-induced NH summer (JJA) changes in surface albedo (a), net shortwave radiation (b), latent heat flux (c) and 2-m temperature (d), plotted against the forest fraction change between 1870 and 1992. Plot markers indicate the model results averaged over NA (gray) and EA (red). Model acronyms are the same as in Figure 2.11.

It is not possible to establish a clear relationship within the LULCC-induced *LE* and T_{2m} anomalies and the amplitude of deforestation (Figure 2.12c-d). The *LE* anomalies exhibit different signs and, in some models, have associated comparatively large amplitudes for moderate rates of deforestation (e.g., IPSL in EA). *LE* and T_{2m} responses to land-cover perturbations depend on several surface processes and on the land-atmosphere coupling in a more complex way than for α or S_N. Then, the various GCM/LSMs express quite different sensitivities in their *LE* and T_{2m} anomalies. These inherent sensitivities to LULCC and the strength of the land-cover changes themselves contribute by their own to the resulting final inter-model dispersion. The relative role of these two factors in the simulated responses to LULCC is one the main questions of this Chapter that is particularly addressed and quantified in Section 2.4.5 (Boisier et al., 2012).

2.4.3 Related changes in surface properties, energy fluxes and temperature

The seasonal patterns of changes in a number of variables and land-surface properties are compared here in order to probe those mechanisms that could conduct the simulated surface energy fluxes and temperature responses to LULCC. In many cases, coherent LULCC-induced signals are interpreted through simple comparison, results that will complement the more formal attribution analyses presented in Section 2.4.5. The anomalies of the different variables are here averaged over the total area composed by both NA and EA (hereafter NAEA).

2.4.3.1. Changes in surface albedo and radiative effects

Surface albedo (α) is a key element regarding the effects of land-use on the surface climate because it is very sensitive to land-cover perturbations and lead the impact on the surface radiation balance. The NH winter and summer LULCC-induced T_{2m} changes simulated by the LUCID models in NAEA plotted against the corresponding changes in S_N are illustrated in Figure 2.13. The anomalies of these two variables closely follow each other in DJF, while a less clear relation is observed in JJA. These patterns highlight the leading role of the radiative effects of LULCC during the winter, and suggest a major role of non-radiative effects during the summer. The simulated S_N responses to LULCC are examined next, along with the changes in α and in the incoming solar radiation (S_D).

Figure 2.14 illustrates the monthly mean LULCC-induced changes in NAEA in cloud cover fraction, in α, and in shortwave radiation. All models show a similar annual pattern in their α anomalies, characterized by positives changes yearlong and a marked seasonal cycle with maximum anomalies during the winter. This cycle is consistent the seasonal variation of the extension of the snow-covered areas in NAEA (not shown), on which the LULCC-induced α

changes are amplified trough canopy-masking effect reduction (the role of the snow on the α responses to LULCC is more deeply studied in sections 2.4.5 and 3.2).

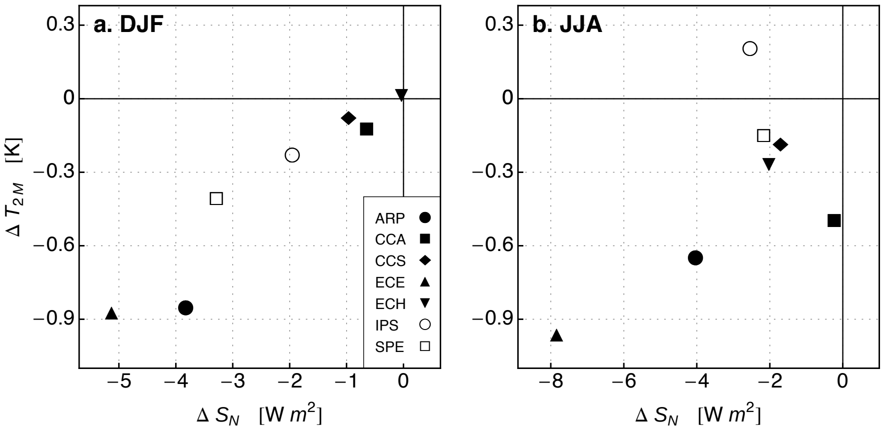

Figure 2.13
LULCC-induced 2m-temperature anomalies in DJF (a) and JJA (b) plotted against the corresponding changes in net shortwave radiation. Model acronyms are the same as in Figure 2.11.

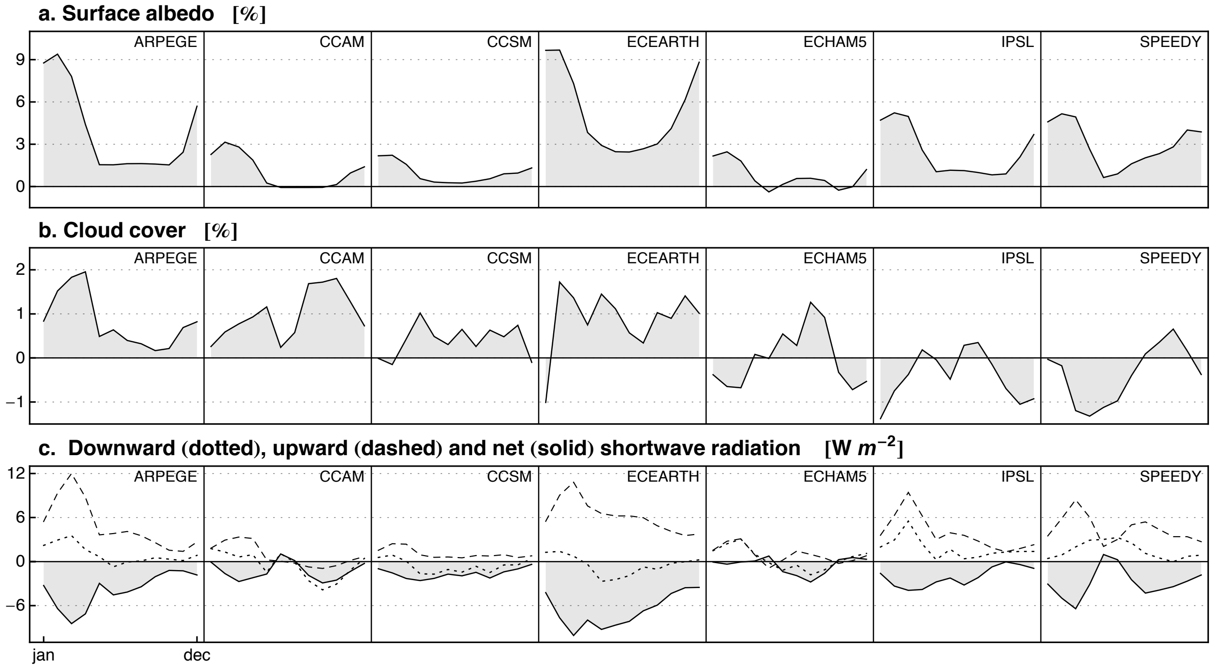

Figure 2.14
LULCC-induced monthly anomalies in NAEA. Surface albedo (a), cloud cover (b) and surface shortwave radiation (c; ΔS_D, ΔS_U and ΔS_N are respectively indicate by dotted, dashed and solid lines).

Although similar in shape, $\Delta\alpha$ varies in magnitude from model to model following, at first order, the intensity of forest fraction changes, as Figure 2.12a illustrates for JJA. In the case of CCSM and ECHAM5, the winter α responses do not exceed +3% (absolute difference), while ARPEGE and ECEARTH simulate changes of near +10% during this season.

The S_N responses to LULCC are all negative during most part of the year, with anomalies consistent in magnitude with those of $\Delta\alpha$ if compared across the models (Figure 2.14c). Since the available solar radiation is larger during the summer (not shown), cycle opposing that of $\Delta\alpha$, ΔS_N does not shows a clear annual cycle. For its part, S_D exhibits some substantial changes, leading to S_N anomalies of similar magnitude than that induced by $\Delta\alpha_S$. The relative contribution of ΔS_D and $\Delta\alpha$ to the LULCC-induced S_N changes is calculated as follow and illustrated in Figure 2.15 for DJF and JJA.

Following Equation (2.4), a change in S_N may be expressed in terms of perturbation in incoming solar radiation (ΔS_D) and in surface albedo ($\Delta\alpha$), i.e.,

$$\Delta S_N = -\Delta\alpha S_D + (1 - \alpha)\,\Delta S_D - \Delta\alpha\Delta S_D \qquad (2.6)$$

The first and second term in the right-hand side of equation (2.6) represent the fraction of the S_N change induced by respectively $\Delta\alpha$ and ΔS_D. The third term is an anomaly of second order that is expected to be weak compared to the other terms if the perturbations are small fractions of the net values. In this case, we use this decomposition to attribute the changes in S_N due to LULCC from preindustrial period to present-day. Hence, the net quantities in Equation (2.6) (i.e., S_D and α in respectively the first and second terms in the right-hand side) correspond to its preindustrial means.

The expected LULCC-induced S_N anomalies computed from the first two components of equation (2.6), the resulting net ΔS_N from both components and the simulated S_N anomalies are shown in Figure 2.15 for NAEA and each GCM in DJF and JJA. The simulated ΔS_N are almost completely explained by these two terms and clearly led by the changes in α. Nevertheless, ΔS_D play a secondary but quite significant role in explaining the simulated ΔS_N. In DJF, all the models simulate increases in S_D (Figure 2.14c) dampening the negative S_N anomalies induced by the –also systematic– increase in α (Figure 2.15a). This offsetting effect ranges from around 12%, in the case of ECEARTH, to 100%, in the case of ECHAM5. The latter simulates a very weak winter response to LULCC in NAEA, not only in terms of S_N, but also in all the other surface energy fluxes and in T_{2M} (see Figures A2.2 and A2.6).

The changes in S_D in JJA are also significant but show different direction across the models, amplifying (CCSM, ECEARTH and ECHAM5) or dampening (IPSL and SPEEDY) the negative α–induced S_N anomalies (Figure 2.15b).

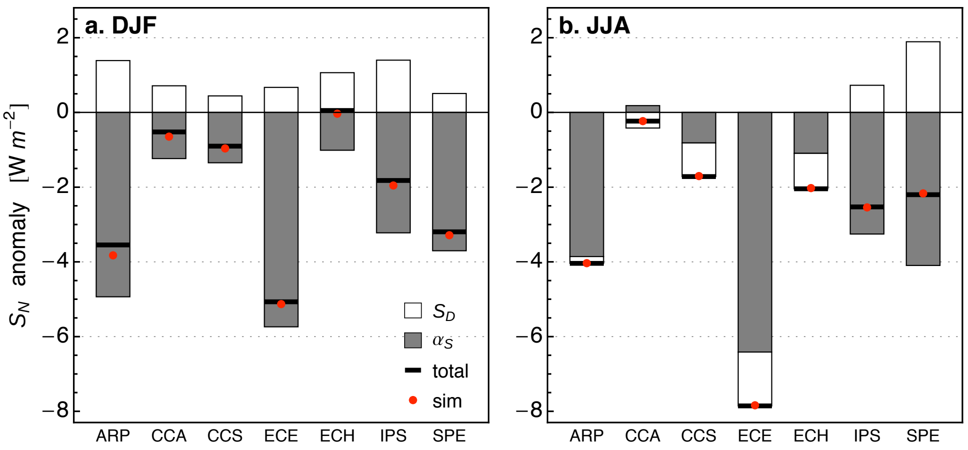

Figure 2.15
Expected LULCC-induced changes in net shortwave radiation changes (ΔS_N) in DJF (a) and JJA (b) induced by changes in surface albedo (grey bars) and by changes in incoming solar radiation (white bars). Black lines and red dots indicate the net ΔS_N expected from both drivers and the simulated ΔS_N, respectively. Model acronyms are the same as in Figure 2.11.

Changes in S_D could result from indirect impacts of LULCC that, by means of perturbations in e.g. surface heating or water supply to the atmosphere (evapotranspiration), may induce changes in convection and cloud cover. Changes in cloud cover were actually reported as a leading factor inducing a negative feedback in the radiative effect of LULCC for the particular case of ECEARTH/TESSEL (van der Molen et al., 2011). However, the changes in cloud cover and S_D are not coherently related in NAEA (i.e., cloud cover increase/decrease and S_D decrease/increase) across the different models (figures 2.14b and 2.14c). For instance, ARPEGE/ISBA simulated clear increases in both cloud-cover fraction and S_D during the first part of the year.

In addition to changes in cloud cover, S_D should respond to changes in surface albedo in those regions partially covered by clouds. Since S_U is partially reflected back to the surface by the cloud deck, an α–induced increase in S_U will, in turn, produce an increase in S_D if cloud cover is relatively large. This mechanism is not quantified here but should represent and 'inherent' negative feedback of the direct (α–driven) changes in S_N, which should be more intense in regions with larger climatological cloud cover fraction.

2.4.3.2 Changes in canopy density, surface roughness and turbulent heat fluxes

Figure 2.16 illustrates the monthly mean LULCC-induced changes in surface roughness (z_0), leaf area index (LAI), precipitation and in the turbulent heat fluxes, averaged over the NAEA region. As expected, given the net deforestation prescribed in LSMs (Table 2.5), all the models simulate decreases in z_0. Four out of the seven models do not parameterize seasonal cycles in z_0 and therefore show a fixed change along the year. The amplitudes of Δz_0 are related to the deforestation strength, but some models show particular strong decreases (e.g., ARPEGE/ISBA).

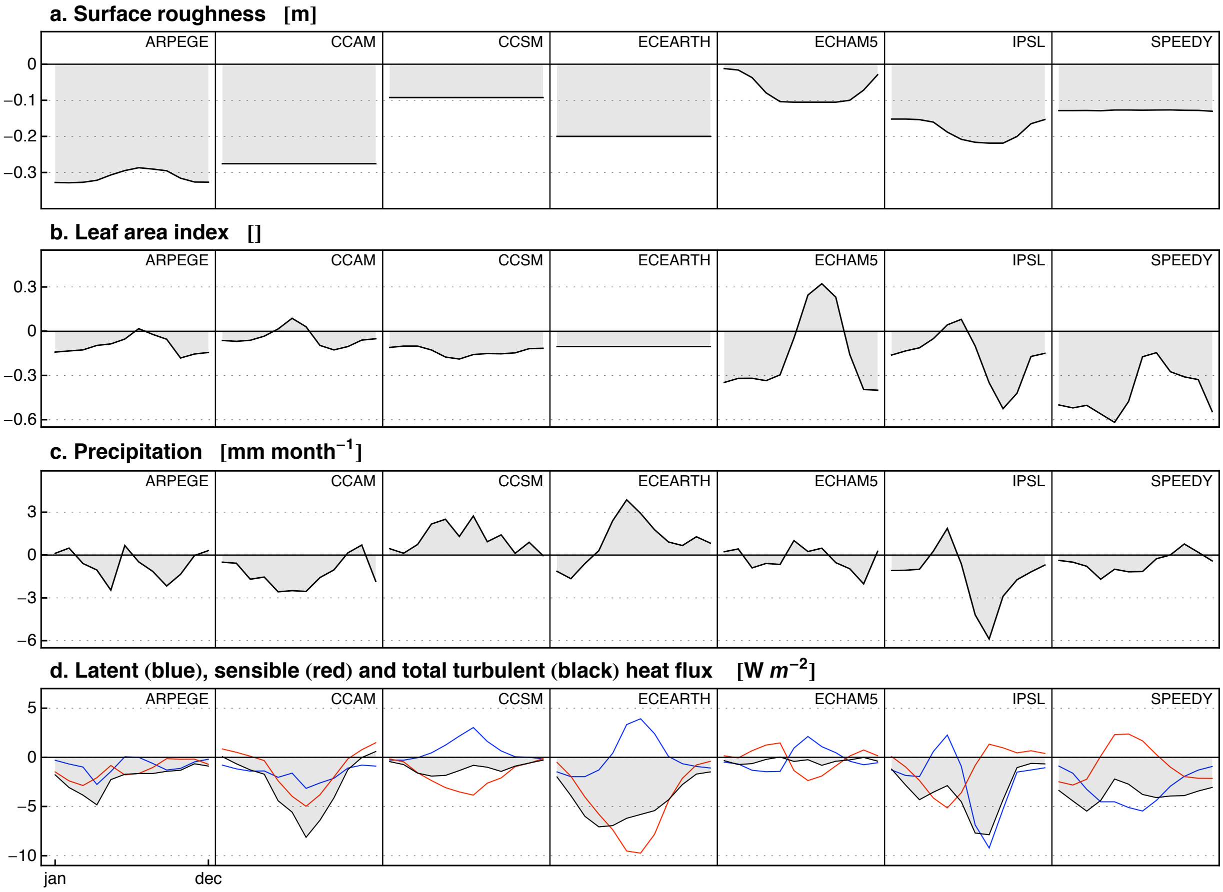

Figure 2.16
LULCC-induced monthly anomalies in surface roughness (a), LAI (a), precipitation (c) and turbulent heat fluxes (d; LE, H and Q_T=LE+H indicated respectively by blue, red and black lines) in NAEA.

All models also show LAI decreases during most part of the year (Figure 2.16b). It is noteworthy that those GCM/LSMs that explicitly calculate LAI (ECHAM5/JSBACH, IPSL/ORCHDEE and SPEEDY/LPJmL; see Table 2.2) clearly exhibit larger changes with regard to the other models. The annual patterns of LAI changes respond to the particular phenological cycles prescribed or diagnosed in the various LSMs. For instance, the growing season of crops simulated by JSBACH (ECHAM5) in NAEA is centered in the late summer. In this season, crops reach very high foliage density with LAI values even higher than that of temperate forest, while in winter crop's LAI goes to 0. This cycle results on net positive LULCC-induced LAI anomalies during the growing season and negatives values the rest of the year. LPJmL (SPEEDY) has similar LAI seasonal cycle than JSBACH, but with a lower crop's LAI in summer. In turn, the crop seasonal cycle simulated by ORCHIDEE (IPSL) has associated an earlier growing season in NAEA than that of JSBACH and LPJmL. The resulting LULCC-induced LAI anomalies in this model show a positive maximum in the late spring, and a marked minimum in fall.

As commented previously and discussed in Pitman et al. (2009), the LULCC-induced changes in latent heat flux (*LE*) are particularly heterogeneous within the LUCID models, with anomalies of different amplitudes and sign (blue lines in Figure 2.16d). CCSM, ECEARTH and ECHAM5 simulate *LE* increases during the NH summer, as do the IPSL model in spring. SPEEDY simulates comparatively large *LE* decreases along the year. The IPSL model shows a clear seasonal pattern of ΔLE, with a marked decrease at the end of the summer and during the fall, resulting in an annual shape closely similar to that of ΔLAI. This is no surprising given that surface flux calculations in ORCHIDEE depend directly on foliage density (Krinner et al., 2005). A coherent pattern between *LE* and LAI can also be appreciated in the ECHAM5 case, but with *LE* anomalies weaker than that of IPSL.

The LULCC-induced precipitation change shown by the IPSL model also has a remarkable similar annual pattern than that of *LE* (Figure 2.16c). Although less clear than for the IPSL case, the other models also suggest coherent monthly changes in precipitation and *LE*. Actually, with the exception of SPEEDY, the summer LULCC-induced changes in precipitation simulated by the various GCM/LSMs reveal a quite positive correlation within them when plotted against their corresponding *LE* changes (Figure 2.17). This relation does not ensure any causality but suggests a positive coupling between these variables or a water-recycling ratio of similar amplitude within the models when averaged over NAEA. Precipitation and *LE* are related through soil moisture. A positive precipitation-soil moisture coupling (i.e., when a perturbation in the former affects the latter in the same direction) is expected in most regions as well as a positive soil moisture-*LE* coupling. Hence, a positive feedback between LE and precipitation will occur when there is also a positive soil moisture-precipitation coupling (Seneviratne et al., 2010). The latter is not a relation clearly one-sided, but GCMs usually show a positive coupling instead a negative one (Koster et al., 2004). What is surprising from Figure 2.17 is that LUCID models seem to show a quite similar coupling strength, agreement not expected in climate models (Koster et al., 2004).

Since the primarily perturbations occur at the surface, and given that summer *LE* changes in NAEA are clearly more significant than the precipitation ones (see Figures A2.5 and A2.7), it is reasonable to interpret the summer changes in precipitation depicted in Figure 2.17 as responses to the *LE* ones, and not vice-versa. Indeed, as Boisier et al. (2012) show, the changes in precipitation explain only a fraction of the *LE* anomalies, fraction that further amplify the *LE* signals directly induced by LULCC (see Figure 7 in Boisier et al., 2012).

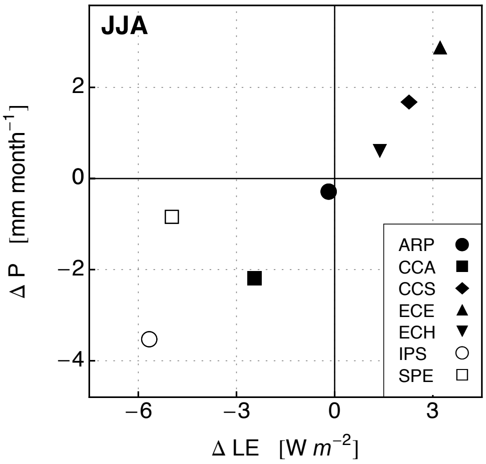

Figure 2.17
Northern Hemisphere summer (JJA) LULCC-induced changes in precipitation (P) in NAEA plotted against the changes in latent heat flux (LE). Model acronyms are the same than in Figure 2.11.

Most models (excepting CCAM/CABLE) show opposite patterns between their monthly *LE* and *H* responses to LULCC (Figure 2.16d). All of them also show the ensemble of both *LE* and *H* anomalies shifting to negatives values. That is, all models simulate net decreases in the total turbulent energy flux (Q_T). This is consistent with the fact that less energy is available at the surface due to the radiative impacts of LULCC (Figure 2.14c). Decreases in Q_T could also be expected as a direct non-radiative response to land-surface perturbations. For instance, the comparatively large decrease in Q_T simulated by IPSL during the late summer, seems to be conducted by changes in *LE*. Q_T reductions are also expected as responses to decreases in z_0 and the resulting increases in the aerodynamic resistance of the surface (Figure 2.16a).

2.4.3.3. Changes in available energy, in turbulent energy flux and temperature responses

Figures 2.14 and 2.16 illustrate both the radiative and non-radiative effect of LULCC in NAEA. The first one is characterized through changes in S_N and, then, in the available energy Q_A; the second, through changes in the *LE*/*H* partitioning and in the total turbulent heat flux Q_T. Although with different amplitudes, the models are systematic in their Q_A and Q_T changes, both flux anomalies being negative during most part of the year. In order to maintain the surface energy balance (Equation 2.1), the negative anomalies of these variables should act in opposite ways regarding the changes in surface temperatures. That is, in absence of other perturbations, decreases in Q_A should induce surface cooling, while decreases in Q_T should produce warming. Beside these effects on surface temperature, the changes in Q_A should also affect Q_T.

Figure 2.18 illustrates the monthly LULCC changes in Q_A (black lines), in Q_T (blue) and in the infrared radiation emitted by the surface (L_U; red). ARPEGE, ECEARTH and SPEEDY show that their negative anomalies of Q_A are accompanied with decreases in Q_T and L_U of similar amplitudes (of about half of ΔQ_A). CCAM and IPSL show clear larger decreases in Q_T than in Q_A during the summer-fall. In the latter case, the strong negative Q_T response to LULCC is balanced with positive L_U changes (i.e., surface warming). Model CCAM as well as SPEEDY show clear energy imbalances between Q_A, Q_T and L_U ($\Delta Q_T + \Delta L_U$ is expected to be equal to ΔQ_A if there is no changes in G or in the snowpack heat storage; Equation 2.1), implying a change in other SEB component not considered here or a surface energy closure problem.

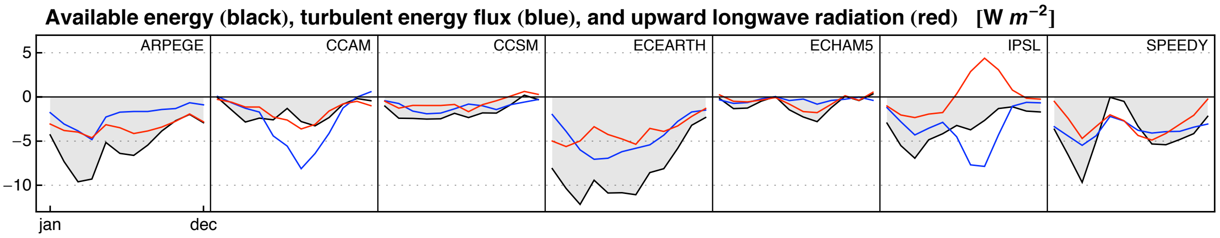

Figure 2.18
Monthly mean LULCC-induced changes in available energy (black), total turbulent energy flux (blue) and outgoing longwave radiation (red).

It is not evident from Figure 2.18 the relative role that Q_A and Q_T play in the surface temperature responses. In order to better assess that, the summer (JJA) LULCC-induced changes in these two variables are plotted one against the other in Figure 2.19. The corresponding changes induced by the large scale forcing (ΔSST/CO2) are also plotted for comparison (indicated by red markers). The grey shaded area represents the expected changes in Q_T induced by ΔQ_A if the climatological Q_T/Q_A ratios remain constant within the different simulation experience (in the region studied the simulated summer Q_T/Q_A ratios by the various models are similar and about 0.25). In other words, the grey area represents estimates of the Q_T changes in absence of direct non-radiative impacts of LULCC (e.g., that driven by aerodynamics effects).

Figure 2.19 illustrates that these very simplistic radiative-induced ΔQ_T estimates match relatively well the simulated ΔSST/CO2-induced Q_T changes. This is somehow expected since this forcing is mainly radiative and characterized by increases in the incoming longwave radiation at the surface (L_D). In turn, in the case of LULCC, four models show negative Q_T anomalies clearly larger in amplitude than those expected by the sole radiative effect (CCAM, ECEARTH, IPSL and SPEEDY). Supposing that the SEB fluxes were balanced by Q_T, Q_A, and L_U, the 'extra' Q_T reduction simulated by these four models should dampen the radiative cooling induced by decreases in Q_A, as occur in the ECEARTH case. In the more extreme case in which the amplitude of a negative Q_T anomaly was higher than that of ΔQ_A, the surface should respond with a net warming (the $\Delta Q_T = \Delta Q_A$ curve is indicated by a dashed line in Figure 2.19). That is what happens in the IPSL case. Models CCAM and SPEEDY do not hold in this statement because they do not show an energy closure between Q_A, Q_T and L_U.

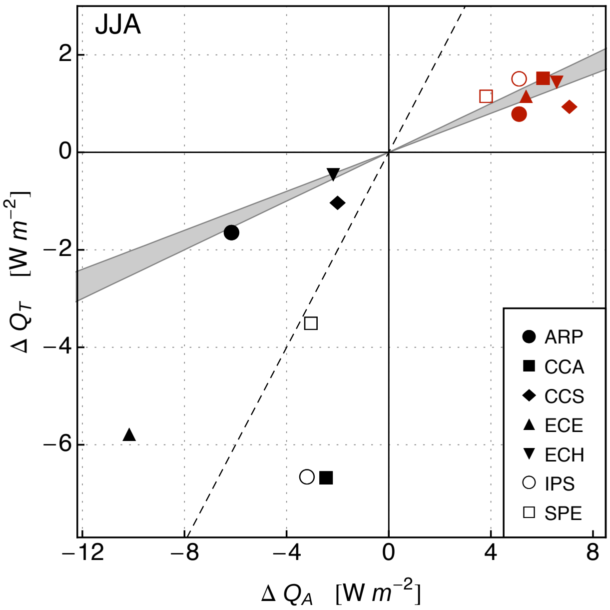

Figure 2.19
Northern Hemisphere summer (JJA) changes in total turbulent heat flux (ΔQ_T) plotted against the changes in available energy (ΔQ_A) averaged over NAEA. Plot markers indicate the models responses to LULCC (black) and to ΔSST/CO2 (red). Gray area encompass the model range of their climatological ratios between Q_T and Q_A [i.e., $y = (Q_T/Q_A)\ x$]. Dashed line indicate the $y = x$ relation. Model acronyms are the same as in Figure 2.11.

2.4.4 Paper: Determining robust impacts of land-use-induced land cover changes on surface climate over North America and Eurasia: results from the first set of LUCID experiments

By N. de Noblet-Ducoudré, J. P. Boisier, A. Pitman, G. B. Bonan, V. Brovkin, F. T. Cruz, C. Delire, V. Gayler, B. J. J. M. van den Hurk, P. J. Lawrence, M. K. van der Molen, C. Müller, C. H. Reick, B. J. Strengers, and A. Voldoire

Reference: Journal of Climate, Vol. 25, pp. 3261–3281, 2012. doi:
http://dx.doi.org/10.1175/JCLI-D-11-00338.1

Determining Robust Impacts of Land-Use-Induced Land Cover Changes on Surface Climate over North America and Eurasia: Results from the First Set of LUCID Experiments

NATHALIE DE NOBLET-DUCOUDRÉ,* JUAN-PABLO BOISIER,* ANDY PITMAN,+ G. B. BONAN,#
V. BROVKIN,@ FAYE CRUZ,+,@@ C. DELIRE,& V. GAYLER,@ B. J. J. M. VAN DEN HURK,** P. J. LAWRENCE,#
M. K. VAN DER MOLEN,** C. MÜLLER,++ C. H. REICK,@ B. J. STRENGERS,## AND A. VOLDOIRE&

** Laboratoire des Sciences du Climat et de l'Environnement, Gif-sur-Yvette, France*
+ Centre of Excellence for Climate System Science, University of New South Wales, Sydney, New South Wales, Australia
 # National Center for Atmospheric Research, Boulder, Colorado
@ Max Planck Institute for Meteorology, Hamburg, Germany
& Groupe d'Étude de l'Atmosphère Météorologique, Toulouse, France
*** Royal Netherlands Meteorological Institute, De Bilt, Netherlands*
++ Earth System Analysis, Potsdam Institute for Climate Impact Research, Potsdam, Germany
PBL Netherlands Environmental Assessment Agency, Bilthoven, Netherlands

(Manuscript received 17 June 2011, in final form 26 October 2011)

ABSTRACT

The project Land-Use and Climate, Identification of Robust Impacts (LUCID) was conceived to address the robustness of biogeophysical impacts of historical land use–land cover change (LULCC). LUCID used seven atmosphere–land models with a common experimental design to explore those impacts of LULCC that are robust and consistent across the climate models. The biogeophysical impacts of LULCC were also compared to the impact of elevated greenhouse gases and resulting changes in sea surface temperatures and sea ice extent (CO2SST). Focusing the analysis on Eurasia and North America, this study shows that for a number of variables LULCC has an impact of similar magnitude but of an opposite sign, to increased greenhouse gases and warmer oceans. However, the variability among the individual models' response to LULCC is larger than that found from the increase in CO2SST. The results of the study show that although the dispersion among the models' response to LULCC is large, there are a number of robust common features shared by all models: the amount of available energy used for turbulent fluxes is consistent between the models and the changes in response to LULCC depend almost linearly on the amount of trees removed. However, less encouraging is the conclusion that there is no consistency among the various models regarding how LULCC affects the partitioning of available energy between latent and sensible heat fluxes at a specific time. The results therefore highlight the urgent need to evaluate land surface models more thoroughly, particularly how they respond to a perturbation in addition to how they simulate an observed average state.

1. Introduction

Land use–land cover change (LULCC) via deforestation, or via conversion of natural grasslands, occurs principally for urbanization and agriculture. It is a process that probably began with human's systematic use of fire ~400 000 yr ago (Williams 2003). There is no doubt that LULCC has been geographically extensive (Defries et al. 1995; Ramankutty and Foley 1999; Klein Goldewijk 2001; Hurtt et al. 2006; Pongratz et al. 2008; Klein Goldewijk et al. 2011; Kaplan et al. 2011). LULCC affects the nature of the land surface in ways strongly determined by the type of change. The impact of removing forests for agriculture depends on the spatial scale of the change. It also depends on the type of natural vegetation removed, since a coniferous forest interacts with the atmosphere differently than a deciduous

---

@@ Current affiliation: Manila Observatory, Quezon City, Philippines.

Corresponding author address: Nathalie de Noblet-Ducoudré, Laboratoire des Sciences du Climat et de l'Environnement, Bâtiment 712, Orme des Merisiers, Point Courrier 132, F-91191 Gif-sur-Yvette CEDEX, France.
E-mail: nathalie.de-noblet@lsce.ipsl.fr

DOI: 10.1175/JCLI-D-11-00338.1

forest, and both differ significantly from a native grassland or savanna system. The impact of LULCC also depends on the type of crops implemented, whether the crops are irrigated, and whether the croplands revert back to something similar to the original vegetation over time or are maintained as crops or are transformed to urban landscapes. Large-scale LULCC affects the mean regional climate (e.g., Bonan 1997; Gallo et al. 1999; Zhou et al. 2004; Oleson et al. 2004; Hale et al. 2006; Lobell and Bonfils 2008; Mahmood et al. 2008; Fall et al. 2010) but also the likelihood of extremes (Zhao and Pitman 2002; Deo et al. 2009; Teuling et al. 2010), carbon and other trace gas emissions (Denman et al. 2007), fluxes of biologically active volatile organic compounds (Arneth et al. 2010), and the direct heating of the atmosphere through anthropogenic heat input (McCarthy et al. 2010). LULCC has also had a substantial biogeochemical effect on global climate through emission of CO_2 and other greenhouse gases (GHGs), such as CH_4 and N_2O (Denman et al. 2007), although such impacts and exchanges are not within the scope of this paper.

The biogeochemical effect of historical LULCC on climate is reasonably well established. LULCC releases CO_2, and therefore increases radiative forcing, although the magnitude of this increase still requires accurate quantification. In contrast, the impact of the biogeophysical effects of LULCC is more uncertain. While the land surface modeling community would basically agree that LULCC is a significant driver of climate through physical effects, there is no consensus on what this statement means. The community would agree that LULCC affects the albedo and through the albedo the energy to drive the surface energy balance. LULCC also affects how that energy is partitioned into sensible and latent heat fluxes, the turbulent energy fluxes that transfer water and heat into the atmosphere. There is a general consensus that provided LULCC is spatially coherent and on a spatial scale that is large enough, this would change the regional-scale climate significantly. However, the community could not define the scale of LULCC required to be "large enough," how large the resulting change in the regional climate might be expected to be, or how the nature of the existing climate over a region might suppress or amplify the initial impacts of LULCC. Most contentious is the unresolved question of whether an LULCC-induced regional climate change teleconnects to trigger significant remote (in space) changes in climate. Some climate modeling evidence suggests that it can (Henderson-Sellers et al. 1993; Zhang et al. 1996; Gedney and Valdes 2000; Werth and Avissar 2002, 2005) and other climate modeling evidence suggests it cannot (Findell et al. 2007, 2009; Pitman et al. 2009), and this is not a problem easily resolved using observational evidence. Another complication arises from the type of climate model used in the LULCC experiments. Experiments with prescribed sea surface temperatures (SSTs) and sea ice cover could underestimate the global effects of LULCC because air temperature over ocean, which covers 71% of the planet, is constrained to the observed state.

The global-scale impact of historical LULCC on radiative forcing through land surface albedo changes estimated as -0.2 ± 0.2 W m^{-2} is small relative to the CO_2 radiative forcing of 1.66 ± 0.17 W m^{-2} (Forster et al. 2007). However, this does not imply LULCC has no climatic impact, as Pielke et al. (2002) and Davin et al. (2007) have argued. A globally integrated measure of the impact of a forcing is important where a forcing has a global signature. Even if most experiments seem to show that LULCC has a negligible global signature, intense LULCC—where it has transformed large regions of the earth's surface—is spatially organized into distinct regions (Fig. 1). These include (but are not restricted to) North America, Europe, India, China, Russia, Japan, and Indonesia (all account for about 64% of all arable land on about 50% of the total land—where 60% of the global population lives[1]). So, the appropriate question is not whether LULCC has a globally averaged significant impact, rather it is whether LULCC has an impact on regions that have undergone intensive LULCC that is worth accounting for when exploring the impact of other human forcings on regional climate.

To begin to systematically address this question, the project Land-Use and Climate, Identification of Robust Impacts (LUCID) was conceived under the auspices of the International Geosphere–Biosphere Programme (IGBP)–Integrated Land Ecosystem–Atmosphere Processes Study (iLEAPS) and the Global Energy and Water Cycle Experiment–Global Land Atmosphere System Study (GEWEX–GLASS). The goal of LUCID is to determine the scale of impact of historical LULCC at the regional and global scales. A key objective is to determine those impacts that are real and robust both above the level of natural variability in each model and common across the set of seven models used in the project (see section 2).

The preliminary global-scale results from LUCID were presented by Pitman et al. (2009), who mainly focused on the Northern Hemisphere summer season. The key result was a statistically significant impact of LULCC on the simulated latent heat flux and air temperature over the regions where LULCC was changed. However, the direction of summer temperature change was inconsistent

---

[1] Percentages include all land areas except Greenland and Antarctica.

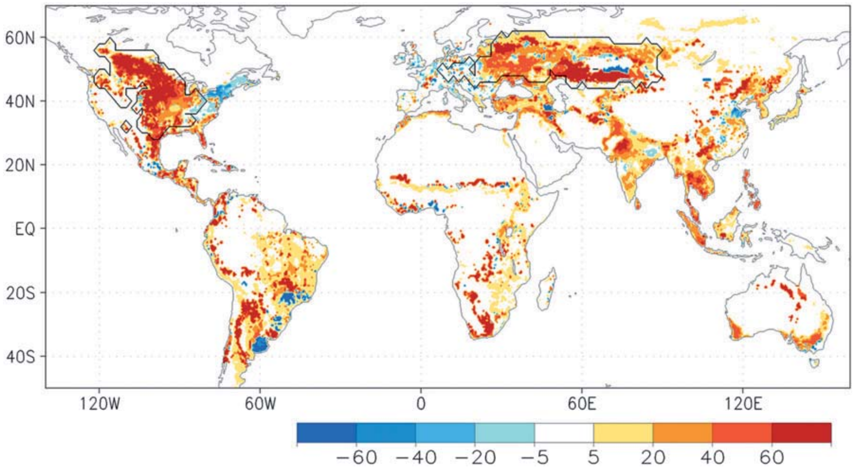

FIG. 1. Changes in the extent covered with crops and pasture between PD and PI times. Yellow and red are used when the extent of anthropogenic areas have increased since PI times, while blue refers to abandoned lands. The two contours that are drawn on the map highlight the regions that will further be used for specific analysis (North America and Eurasia).

among the models, which undermines our confidence in the robustness of this result. In the case of rainfall, Seneviratne et al. (2010) noted that results from LULCC were less convincing. Four of the coupled atmosphere–land models used in LUCID show a strongly significant impact on rainfall over regions of LULCC, while three models do not show impacts above the level expected by chance. Therefore, in terms of the results from LUCID, the model results do not simulate a consistent LULCC signal in terms of regional rainfall. Pitman et al. (2009) also failed to identify statistically significant impacts of LULCC *remote* from the actual LULCC for latent heat flux, temperature, or rainfall. Note that since LUCID did not use climate models with coupled oceans, this does not resolve the question of whether these teleconnections exist, as the coupled ocean can amplify or damp an initial regional perturbation (Davin and de Noblet-Ducoudré 2010).

A critical result from LUCID was the disagreement between the models in their response to LULCC in the simulation of summer temperature and latent heat flux change. Pitman et al. (2009) did not explore the reasons behind these differences. The goal of this paper is to provide a detailed examination of why the land surface models (LSMs) diverge in their response to LULCC and to provide advice on how to better approach realistic responses of climate models to such perturbations in the future. This paper highlights in detail where the models agree and where they disagree, and it explores the reasons for the disagreement.

Section 2 summarizes the main features of the atmosphere and land surface models used, describes the experimental protocol, the imposed vegetation changes, and the way they were implemented in individual LSMs. Section 3 compares the climatic impacts of LULCC to those resulting from the changes in sea surface temperatures, sea ice extent, and increased greenhouse gases. Section 4 discusses the resulting changes in land surface properties in each individual model, as well as their simulated impacts on fluxes and surface temperature. Section 5 focuses on the way the various models partition the available surface radiative energy into latent and sensible heat fluxes, and on how this partitioning is modified when the land cover distribution is changed. The results are discussed and summarized in section 6.

2. Models, experimental design, and resulting vegetation changes

a. Models description

Seven coupled atmosphere–LSMs have been used to carry out a common set of simulations using the same experimental design. The models and their references are listed in Table 1.

b. Experimental design

All seven models undertook two sets of two simulations (Table 2), spanning a matrix of present-day (PD) and preindustrial (PI) GHG concentrations–SSTs and present-day and preindustrial land cover. In these experiments the models are forced with two different vegetation distributions (representative of 1870 or 1992). Each model carried out at least five independent simulations for each experiment to increase the capacity to determine those changes that were robust from those that reflected internal model variability.

TABLE 1. List of climate (or atmosphere only) models and associated LSMs used in the first LUCID set of experiments.

Name of climate or atmospheric models (reference)	EC-EARTH (www.ecmwf.int/research/ifsdocs/CY31r1/)	SPEEDY (Strengers et al. 2010)	IPSL (Marti et al. 2010)	ARPEGE (Salas-Mélia et al. 2005)	CCAM (McGregor and Dix 2008)	CCSM (Collins et al. 2006)	ECHAM5 (Roeckner et al. 2006)
Name of land surface model (reference)	TESSEL (Van den Hurk et al. 2000)	LPJmL (Bondeau et al. 2007)	ORCHIDEE (Krinner et al. 2005)	ISBA (Voldoire 2006)	CABLE (Wang et al. 2007; Abramowitz et al. 2008)	CLM (Oleson et al. 2008)	JSBACH (Raddatz et al. 2007)

From these simulations we constructed responses to LULCC by averaging the results for land cover change experiments under both present-day and preindustrial GHG concentrations/SSTs [i.e., 0.5(PD − PDv + PIv − PI)]; values computed in this way are termed LULCC in the following. Similarly, the average response to GHG and SST changes is evaluated as 0.5(PD − PIv + PDv − PI) and labeled "CO2SST" (the combined CO2 and SST impacts) in the following. Results from all individual members of every participating model have been averaged in all the results presented below.

Both SSTs and sea ice extent were prescribed to vary interannually and seasonally using the Climate of the Twentieth Century Project specifications [see Met Office Hadley Centre Sea Ice and Sea Surface Temperature version 1.1 (HadISST1.1) at ftp://www.iges.org/pub/kinter/c20c/HadISST/]. For the vegetation distribution, each model was provided the same distribution of crop and pasture (Fig. 1), at a resolution of 0.5° × 0.5°. These were constructed by Ramankutty and Foley (1999) and combined with pasture area from Klein Goldewijk (2001). The fields are similar to the ones that are now being used for the Intergovernmental Panel on Climate Change (IPCC) Coupled Model Intercomparison Project phase 5 (CMIP5) historical simulations (Hurtt et al. 2011).

c. Resulting vegetation changes

The datasets provided to each modeling group did not specify the distribution of natural vegetation (land cover types that are neither crops nor pasture). The distribution of natural vegetation had to be obtained from the datasets currently used by each LSM from their "background" land cover map (BLCm) or from prognostic simulations of vegetation distribution. This was unavoidable, as climate models and their LSMs are commonly developed together with an assumed natural vegetation map. It is simply not feasible to require all modeling groups to use a common natural vegetation map, since it would require a restructuring of the LSM and a full-scale reevaluation of the coupled model.

As an implication, each LSM therefore integrated the crops and pasture distributions provided for both periods into its own land cover map. This has resulted in rather different land cover distributions (Fig. 2a) for

TABLE 2. Description of simulations performed by each coupled atmosphere–LSM.

Experiment name	Description of the experiment	CO_2 (ppm)	Aerosols	Year of vegetation map	SSTs
PI	PI simulation, with CO_2, GHGs, aerosols, land cover map and SSTs being prescribed at their preindustrial values	280	Preindustrial	1870	Prescribed 1870–1900
PD	PD simulation, with PD CO_2, land cover map, SSTs, and sea ice extent; other GHGs have been added to the CO_2 concentration as CO_2 equivalent,* while aerosols have been kept to their PI values.	375	Preindustrial*	1992	Prescribed 1972–2002
PIv	Preindustrial simulation with CO_2, GHGs, aerosols, and SSTs being prescribed at their PI value BUT with PD land cover map	280	Preindustrial	1992	Prescribed 1870–1900
PDv	PD simulation, with PD CO_2, SSTs, and sea ice extent; other GHGs have been added to the CO_2 concentration as CO_2 equivalent,* while aerosols have been kept to their PI values; but land cover map is PI.	375	Preindustrial*	1870	Prescribed 1972–2002

* Except in EC-EARTH, where those were changed proportionally to CO_2 changes.

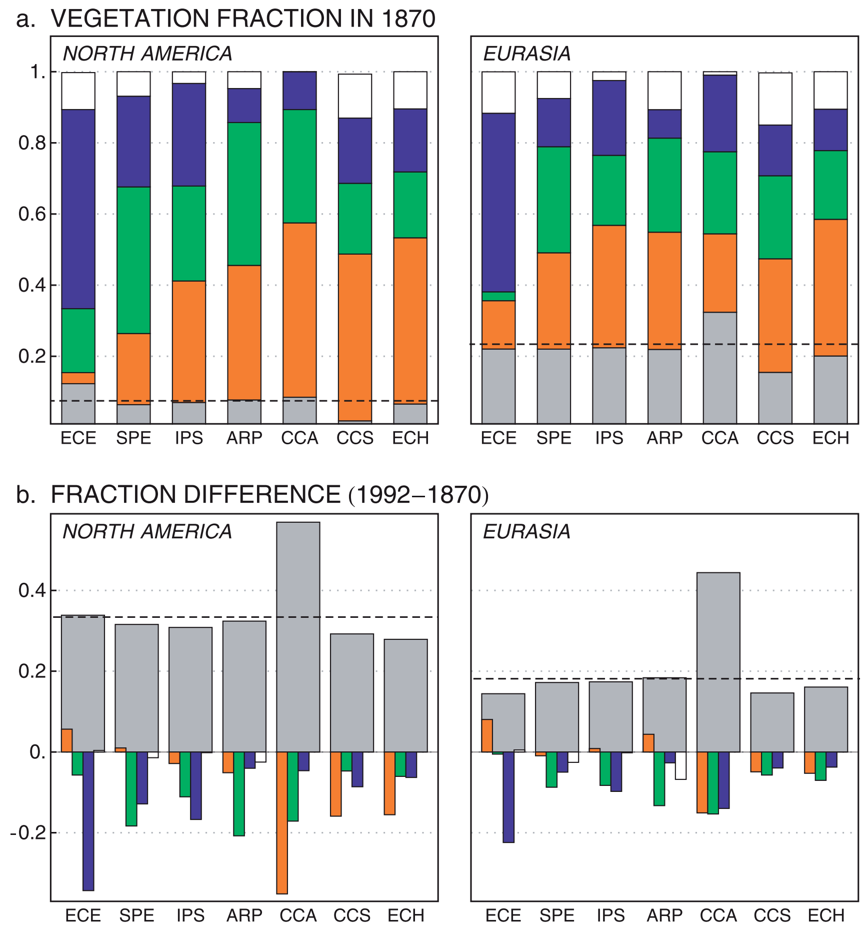

FIG. 2. (a) The 1870 extent (in fraction of total area) covered by crops (gray), grassland types (orange), evergreen trees (green), deciduous trees (blue), and desert (white) for all seven models and two different geographical locations (North America and Eurasia; located in Fig. 1). (b) Differences (in fraction of total area) in each of those vegetation types between PD and PI times. The dashed black line on both graphs shows the fractional coverage by crops that have been provided.

several reasons: 1) differences in the way land information is represented in different models; 2) different modeling groups use different sources of information to describe present-day and potential vegetation; and 3) various groups have developed different strategies to implement LULCC in their model (Table 3). Present-day crop fraction in North America, for example, varies from 35% in the Community Climate System Model (CCSM)–Community Land Model (CLM) to more than 60% in the Conformal–Cubic Atmospheric Model (CCAM), while the extent of deciduous forests varies from about 5% in both the Action de Recherche Petite Echelle Grande Echelle (ARPEGE)–Interactions between Soil, Biosphere, and Atmosphere (ISBA) and CCAM–Commonwealth Scientific and Industrial Research Organisation Atmosphere Biosphere Land Exchange (CABLE) to more than 30% in the earth system model based on European Centre for Medium-Range Weather Forecasts (ECMWF) modeling systems (EC-EARTH)–Tiled ECMWF Scheme of Surface Exchanges over Land (TESSEL). Moreover, although the areas covered with crops increase in all models from preindustrial times to the present (Fig. 2b), this increase varies from about 30% in CCSM–CLM, which is less than the 35% originally prescribed, to about 55% in CCAM–CABLE.

The models therefore all experience temperate deforestation but at varying degrees. For example, for North America, temperate deforestation ranges from 12% in ECHAM5–Jena Scheme for Biosphere–Atmosphere Coupling in Hamburg (JSBACH) to 40% in EC-EARTH–TESSEL (Table 4). In EC-EARTH–TESSEL, Simplified Parameterizations, Primitive-Equation Dynamics (SPEEDY)–Lund–Potsdam–Jena Model for managed land (LPJmL), ARPEGE–ISBA, and L'Institut

TABLE 3. Strategy used in the various models to implement the crops and pasture changes onto their background land cover map. CRU TS 2.0 = Climatic Research Unit Time Series version 2.0.

Climate/vegetation model	Number of vegetation types per grid cell	Are crops and pasture merged?	Background land cover map	LAI computed or prescribed?	Crop–pasture integration strategy
EC-EARTH–TESSEL	2	Yes	PD (Loveland et al. 2000)	Computed	Crop extent has been imposed from the given maps. Increases in crop/pasture were first taken from existing low natural vegetation, and subsequently from existing forest area.
SPEEDY–LPJmL	6	No	Potential, computed offline with LPJmL driven by observed climate (CRU TS 2.0)	Prescribed	Crop extent has been imposed from the given maps. Pasture is treated separately from cropland and natural grassland. It is harvested if productivity and phenology allow for that. Natural vegetation is then proportionally reduced. If it happens to be desert, this will be reduced if necessary, but crops may not develop if climatic conditions are unfavorable.
IPSL–ORCHIDEE	12	No	PD (Loveland et al. 2000)	Computed	Crop extent has been imposed from the given maps. Then PD natural vegetation (from BLCm) has been proportionally reduced/extended to occupy only the natural part of the grid cell that is imposed by the given maps. Desert extent is unchanged, except when change in the crop area is larger than the available extent of natural vegetation (deserts are then reduced). Pasture is finally summed up with natural grassland.
ARPEGE–ISBA	1 The associated parameter values are averaged from the values of the 12 cover types in the grid cell in ECOCLIMAP at higher resolution.	No	PD ECOCLIMAP (Masson et al. 2003)	Prescribed	Crop and pasture extent was kept from ECOCLIMAP for PD, with a redefinition of pasture to better match the LUCID database. The PI map was built by imposing the absolute change in crop and pasture area to ECOCLIMAP proportionally to each natural vegetation type.
CCAM–CABLE	1	Yes	Present-day	Prescribed	Crop and pasture extent were imposed from the given maps on the PD land cover. If the combined crop and pasture fraction was >51% in a grid cell, then the grid cell is assigned as crop. If the grid cell is crop in BLCm but not according to the crop and pasture map, then the grid cell is changed to the nearest natural vegetation. The aim is to preserve the differences in the crop and pasture extent in the PI and PD land cover maps.

TABLE 3. (*Continued*)

Climate/vegetation model	Number of vegetation types per grid cell	Are crops and pasture merged?	Background land cover map	LAI computed or prescribed?	Crop–pasture integration strategy
CCSM–CLM	4	No	Potential (Lawrence and Chase 2010)	Prescribed	Crop extent has been imposed from the given maps. Potential natural vegetation (from BLCm) has been proportionally reduced–extended to accommodate crops. Pasture is summed up with natural grassland.
ECHAM–JSBACH	6	No	Potential vegetation from Ramankutty and Foley (1999), reclassified as described in Pongratz et al. (2008).	Computed	Crops and pastures were first allocated on natural grasslands (proportional reduction of C3 and C4 grasses). Only if grassland area was not sufficient, was forest area reduced to accommodate crops and pastures (proportional reduction of the different forest plant functional types).

Pierre-Simon Laplace (IPSL)–Organizing Carbon and Hydrology in Dynamic Ecosystems (ORCHIDEE), crops have expanded predominantly at the expense of forests, while in CCAM–CABLE, CCSM–CLM, and ECHAM5–JSBACH, the reduction in herbaceous areas is as large or even larger than the reduction in forests.

For the LUCID experiments, five out of seven models have chosen to proportionally reduce/extend all natural vegetation types on the part of the grid cell that is not occupied by crops and/or pasture, while the remaining two have first reduced the grassland area and then forests. Other differences between the resulting maps come from 1) the number of vegetation types accounted for per grid cell and 2) the BLCm. Regarding the first point, CCAM–CABLE, for example, only considers the dominant vegetation type per grid cell. If one type exceeds 51%, then it is set to occupy the whole grid cell. This is why the increase in crop area is much larger in this model than in all others. CCAM–CABLE, moreover, groups both pasture and crops into a single vegetation type and both increase from preindustrial times to present day. The extent of herbaceous types decreases in most other models between the two periods, mainly because natural grassland and pasture are most often grouped within one vegetation type. Since natural grassland is severely reduced to allow for the growth of crops, the total grassland area is decreased. As with the choice of whether to grow crops at the expense of forests or herbaceous plants, there is no known ''right'' choice in the number of vegetation types per grid cell and therefore there is no right choice in how to implement LULCC in a climate model. However, our findings of large differences in the deforestation rate, for example, suggest that we should, collectively, focus on appropriate strategies to implement LULCC in our models. The remaining differences between the resulting maps come from the various configurations of the BLCm among the modeling groups. Various examples exist, including the following:

1) The LSM uses a potential vegetation map, that is, one that only includes natural vegetation types. The crop and pasture extent will therefore, for each individual year, replace some or all natural types (e.g., CCSM–CLM, ECHAM5–JSBACH).
2) The LSM uses an observed present-day land cover map that includes both natural and anthropogenic vegetation types. Reconstructing the historical land cover map means deciding which natural vegetation types, crops and pasture would be replaced or deciding what types existed prior to the current distribution of anthropogenic vegetation. Moreover, the distribution of crops and pasture in the BLCm may be different from the present-day distribution provided

TABLE 4. Forest extent (km^2; numbers in parenthesis represent the fractional area covered by forests) at both PI time and PD, together with changes in the forested areas (km^2 and %) between those two time slices. All models are shown for both geographical regions.

	Forest area—10^6 km^2 (% of covered area)					
	North America			Eurasia		
Climate/vegetation model	1870	1992	Change	1870	1992	Change
EC-EARTH–TESSEL	3.36 (74)	1.54 (34)	1.82 (40)	3.14 (31)	1.77 (30)	1.37 (23)
SPEEDY–LPJmL	3.04 (67)	1.62 (36)	1.42 (31)	2.58 (43)	1.77 (30)	0.82 (14)
IPSL–ORCHIDEE	2.53 (56)	1.26 (28)	1.27 (28)	2.42 (41)	1.35 (23)	1.07 (18)
ARPEGE–ISBA	2.26 (50)	1.13 (25)	1.13 (25)	2.05 (34)	1.1 (18)	0.95 (16)
CCAM–CABLE	1.93 (43)	0.94 (21)	0.99 (22)	2.66 (45)	0.91 (15)	1.75 (29)
CCSM–CLM	1.74 (38)	1.13 (25)	0.61 (13)	2.24 (38)	1.66 (28)	0.58 (10)
ECHAM5–JSBACH	1.65 (36)	1.09 (24)	0.56 (12)	1.84 (31)	1.2 (24)	0.64 (11)

(e.g., IPSL–ORCHIDEE, EC-EARTH–TESSEL, ARPEGE–ISBA, and CCAM–CABLE).

3) The natural distribution of vegetation is computed dynamically by a dynamic global vegetation model (DGVM) included in the climate model. The fraction of natural vegetation with internally computed vegetation composition is reduced in each grid cell to allow for simulating agricultural land (cropland and/or pastures) in the remainder of the grid cell (e.g., SPEEDY–LPJmL).

We emphasize that the way each modeling group has implemented LULCC is reasonable at this time because the land surface modeling community has not recognized before how many ways there are to implement LULCC, and the required research has not yet been done to establish a preferred methodology. However, while each approach is reasonable, they are different and those differences inevitably have an impact on how LULCC affects the near-surface climate.

3. How does the models' response to the LULCC signal compare to the response to other changes?

The four sets of simulations described in section 2b allow a comparison of the sensitivity of models to both LULCC and the combined changes in atmospheric greenhouse gases, and CO2SST. To do this, we use the framework of the surface energy balance equation that is implemented in all LSMs. In the absence of snow and on longer time scales, the basic form of this equation is

$$Q_S(1 - \alpha) + Q_{\mathrm{Ld}} - Q_{\mathrm{Lu}} = Q_H + Q_E + Q_G, \quad (1)$$

where all fluxes are in watts per square meter, Q_S is the shortwave radiation incident at the land surface, α is the surface albedo, Q_{Ld} is the downwelling infrared radiation, Q_{Lu} is upwelling infrared radiation, Q_H is the sensible heat flux, Q_E is the latent heat flux, and Q_G is the flux of heat being transmitted to deeper soil layers. The left-hand side of this equation is also known as net radiation. In our analysis we use available energy (Q_A; and not net radiation), defined as

$$Q_A = Q_S(1 - \alpha) + Q_{\mathrm{Ld}}. \quad (2)$$

Our choice for not including Q_{Lu} in the available energy (as is more traditionally done) is because we wish to separate Q_A into turbulent fluxes on the one hand and long-wave cooling on the other.

We also define the total amount of energy exchanged as a turbulent energy flux (Q_T) as

$$Q_T = Q_H + Q_E.$$

The responses of Q_A and ambient air temperature to both sets of changes are displayed in Fig. 3 for North America and Eurasia for all seasons, while the changes in the terrestrial water budget are displayed in Fig. 4.

a. Changes in energy budget and surface temperature

Changes in CO2SST lead to an increase in Q_A at the surface [typically 3–5 W m^{-2}, with larger values during summertime when incoming radiation is maximum (Figs. 3a,b)]. This increase is caused mainly by increased incoming infrared radiation (Q_{Ld}) associated with the higher atmospheric CO$_2$. This increased Q_A is associated with a surface warming of 0.61 ±0.2°C in North America and 0.63 ±0.27°C in Eurasia (Figs. 3c,d), over all seasons with slightly larger values during summertime. In contrast, LULCC, which reflects either deforestation or—at a minimum—shortening of the growing season (when crops replace grasses), results in decreased Q_A by a few watts per square meter over land. There is a small seasonal cycle in the reduction in Q_A, particularly over Eurasia, where larger reductions are simulated due to the combined effects of snow-increased albedo and larger incoming solar radiation in summer compared to winter. The response to increased surface albedo will be

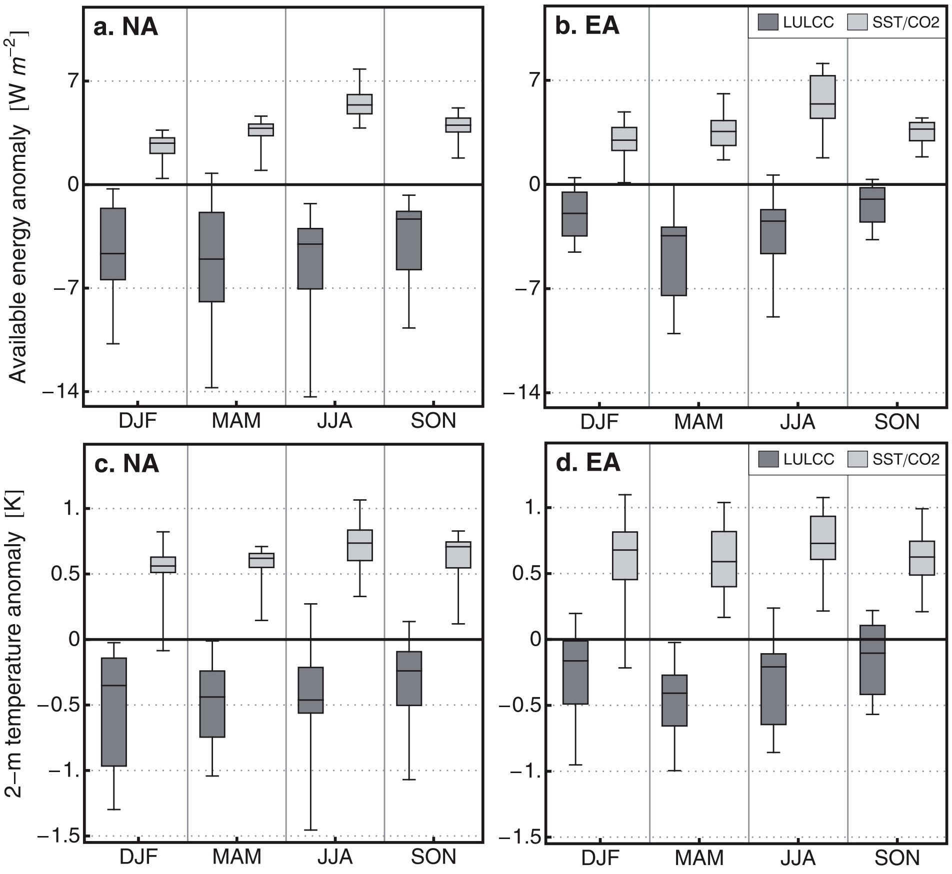

FIG. 3. Box-and-whisker plots of the simulated changes between the PI period and PD in (a),(b) available energy (W m^{-2}) and (c),(d) surface air temperature (°C) for all seasons and for (a),(c) North America and (b),(d) Eurasia. The mean ensemble values of each individual model and each set of experiment (i.e., PD − PIv and PDv − PI for the CO2SST impacts; PD − PDv and PIv − PI for the LULCC impacts) have been used to create this plot. The bottom and top of the box are the 25th and 75th percentiles, and the horizontal line within each box is the 50th percentile (the median). The whiskers (straight lines) indicate the ensemble maximum and minimum values.

discussed in section 5. The magnitude of the simulated changes is generally smaller over Eurasia than over North America due to smaller LULCC changes in the former region (see Table 4). The dominant impact of lowered Q_A is a quasi-systematic cooling of the land by about −0.44° ±0.4°C in North America and about −0.3 ±0.3°C in Eurasia in all seasons (Figs. 3c,d). The changes in temperature are larger in spring and summer, that is, during the growing season, but the uncertainty is large in December–February (DJF), particularly in North America.

There are two remarkable features that can to be highlighted from Fig. 3:

1) In the regions considered, the CO2SST-induced warming (and increase in Q_A) and LULCC-induced cooling (and decrease in Q_A) differ much less than their global mean values. This occurs despite that changes in CO2SST lead to significant mean global annual temperature change (an average over the seven models of 0.432°C globally and of 0.625°C over land only), while the response to LULCC is negligible at that scale (an average of −0.019°C over the globe and of −0.069°C over land; see Table 5). This emphasizes the global role of CO_2 (and resulting surface ocean changes) compared to the regional significance of biogeophysical effects of LULCC. It also points to the importance of not restricting the quantification of climate change to global averages (e.g., the change in mean global annual temperature), since this hides changes of similar importance over some specific (and densely populated) regions. This issue has been addressed thoroughly by Pielke et al. (2002) and Davin et al. (2007).
2) The spread among the models is larger when the models are forced with LULCC than when they are forced with CO2SST. This results from the absence

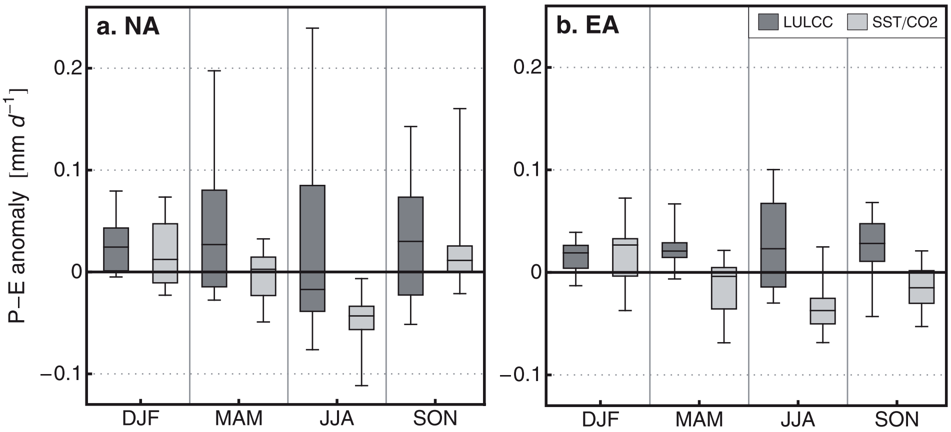

FIG. 4. As in Fig. 3, but for $P - E$ (mm day^{-1}).

of consistent change among the various models regarding the impact of land cover type on the partitioning of Q_A between Q_E and Q_H (section 6). When the models are forced with changes in CO2SST, it is the incoming total energy provided by the atmosphere to the LSMs that is perturbed and not necessarily the way this energy is subsequently partitioned. The increased incoming energy results in increased Q_A that leads to warming in all models, since more than 75% of it is used to warm up the land. When the models' external forcing is LULCC, it is not the total incoming energy that is perturbed (except potentially via resulting feedbacks), but the way it is partitioned into absorbed and reemitted energy. Not only is this absorbed energy (and thereby Q_A) systematically reduced in all models during all seasons due to increased surface albedo but the fraction of it that is used to warm up the land is also modified by LULCC (see section 6).

In the regions of maximum LULCC changes (i.e., North America and Eurasia), the CO2SST-induced warming is compensated for by the LULCC-induced cooling, resulting in almost no change between the periods. This has strong implications for the interpretation, detection, and attribution of the observed changes between preindustrial times and present day. If the model used to detect and attribute the observed changes to various causes does not include LULCC, then erroneous conclusions may be drawn from the analyzed simulations.

b. *Changes in the surface water balance*

The changes in the surface water balance, defined as the difference between rainfall (*P*) and total evapotranspiration (*E*) in each model, for each season and each region, shows a distinct seasonal cycle of the simulated anomalies in response to CO2SST. The response to LULCC shows no such cycle (Fig. 4). As a result of LULCC, $P - E$ increases slightly in the majority of models during winter, spring, and fall in response to a small reduction in *E* and no significant change in *P*. During summertime in North America, more than half of the models show decreased

TABLE 5. Changes in mean annual global 2-m air temperature, together with the mean annual values computed over land only, in all models and the average over the seven models. "LULCC" shows the impact of LULCC between PI times and PD, while "CO2SST" refers to the impact of the combined changes in atmospheric CO_2 (and equivalent GHGs) and SST and sea ice.

	Change in annual mean global 2-m air temperature (°C)		Change in annual mean 2-m air temperature over land only (°C) (excluding Antarctica)	
Climate/vegetation model	LULCC	CO2SST	LULCC	CO2SST
EC-EARTH–TESSEL	−0.042	0.511	−0.13	0.65
SPEEDY–LPJmL	−0.056	—*	−0.1	—
IPSL–ORCHIDEE	−0.005	0.48	−0.011	0.55
ARPEGE–ISBA	−0.041	0.451	−0.177	0.536
CCAM–CABLE	0.021	0.47	−0.013	0.67
CCSM–CLM	−0.007	0.496	−0.023	0.624
ECHAM5–JSBACH	−0.005	0.531	−0.032	0.718
Average	−0.019	0.432	−0.069	0.625

* SPEEDY–LPJmL did not carry out a CO2SST run.

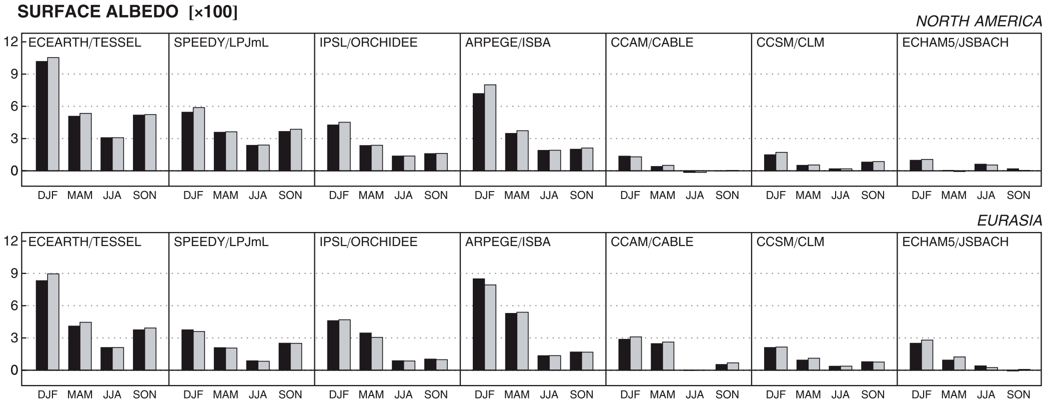

FIG. 5. Seasonal LULCC-induced changes in the simulated surface albedo (%) between PD and PI times by the models listed at the top of each panel. The shading refer to the differences calculated between the simulations that are forced with PD SSTs, CO_2, and GHG (black, simulation PD minus simulation PDv) and PI SSTs, CO_2, and GHG (gray, simulation PIv minus simulation PI). Presenting both dark and gray bars demonstrates the robustness of the impacts of LULCC changes, largely independent of the state of the background GHG and surface ocean's temperatures. (top) North America and (bottom) Eurasia. All seasons are plotted from (left) winter (DJF) to (right) fall [September–November (SON)].

$P - E$. However, Fig. 4 shows a very large level of spread between the models, much larger than the spread resulting from the CO2SST forcing. The reason for this increased dispersion (which was also referred to in the previous section) will be discussed in section 6.

When the models are forced with changes in CO2SST, a summer drying results from a combination of reduced rainfall and increased evapotranspiration. The latter is mainly a response to warmer temperatures (see, e.g., Wetherald and Manabe 2002; Gerten et al. 2007). For the summer season, for a number of models (less than half of them), the changes resulting from CO2SST are opposite of those resulting from LULCC. This again has consequences for detection and attribution efforts, since our results highlight the fundamentally different fingerprint LULCC has on the water availability in comparison to changes in CO_2.

4. Changes in surface properties, fluxes, and temperature

Changes in LULCC affect many land surface characteristics (e.g., albedo, roughness length, foliage density), some of which affect Q_A. Changes in these characteristics, and changes in Q_A, affect the total sum of Q_H and Q_E, and the partitioning of these two fluxes. These changes affect surface temperature, boundary layer profiles of water and heat, and potentially cloud, convection, rainfall, etc. (Betts et al. 1996; Pitman 2003).

a. Resulting changes in land surface characteristics

In all models, in all seasons, the mean land surface albedo is higher under modern land cover than in preindustrial times (Fig. 5), especially during winter, when snow cover affects some of the temperate regions that have experienced the largest LULCC. The magnitude of the albedo change varies from less than 1% in winter in some models (e.g., ECHAM5–JSBACH) to about 8% in others (e.g., SPEEDY–LPJmL, ARPEGE–ISBA, EC-EARTH–TESSEL). The spread is quite smaller during summer (from 0.05 to about 3% at most) and fall, when vegetation foliage is fully developed and snow is not a factor.

In summer (when snow plays no role), the spread in albedo among all but one model is nearly proportional to the scale of deforestation the various models have undergone (Fig. 6). CCAM-CABLE shows a small albedo change despite a significant deforestation. In this version of the model, the parameters used in calculating canopy albedo (Sellers et al. 1992) do not vary as a function of plant functional type, making the model albedo insensitive to changes in the vegetation structure (this has been revised in more recent versions of the model). For the other models, the JJA albedo changes are roughly proportional to the deforestation scale, with an average albedo increase of 7% for an almost complete forest clearance. This proportionality is quite interesting because it means that even though the LSMs have been developed independently, the albedo's response to deforestation is quite similar from one model to another. It also implies that, to first order, modelers can perform a presimulation test of their implementation of LULCC before running experiments. One could indeed require the change in forest area to be agreed upon between modeling groups, since this largely constrains the resulting change in albedo. In DJF the interactions between vegetation and snow significantly complicate the relationship between the change in forest fraction and albedo (Fig. 6, left panel).

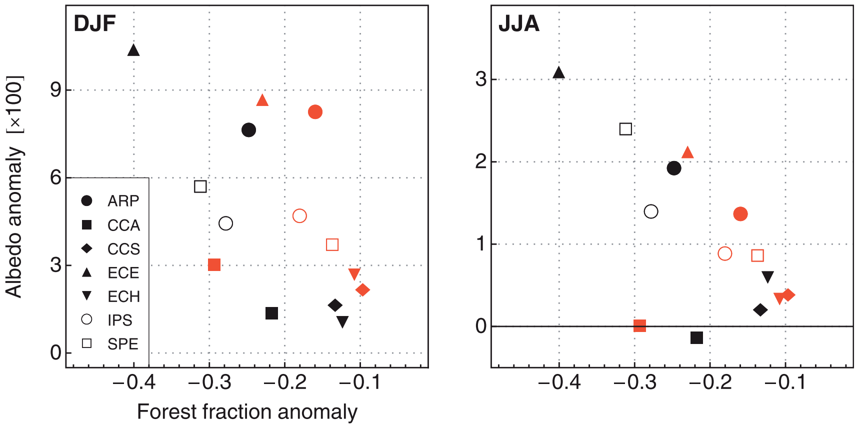

FIG. 6. LULCC-induced changes in the simulated surface albedo (%) plotted against the changes in forest fraction between PD and PI times. Symbols refer to the various models used (ARP: ARPEGE–ISBA; CCA: CCAM–CABLE; CCS: CSSM–CLM; ECE: EC-EARTH–TESSEL; ECH: ECHAM5–JSBACH; IPS: IPSL–ORCHIDEE; SPE: SPEEDY–LPJmL). Red symbols are for Eurasia, while black symbols are for North America. (left) Winter changes (DJF); (right) summer changes (JJA). Albedo values have been computed, for each model, as the mean over not only the various ensemble members but also the two sets of simulations (i.e., PD − PDv and PIv − PI).

The changes in leaf area index (LAI; Fig. 7) are not as homogeneous among the models as the changes in surface albedo. All models show decreased foliage development during wintertime in North America and Eurasia as expected, since forests and grasslands have commonly been replaced by crops, which have negligible foliage development at that time of the year. However, four out of the seven models show at least one season during which the LAI is increased once crops and pasture have replaced forests and grasses (ARPEGE–ISBA, CCAM–CABLE, ECHAM–JSBACH, IPSL–ORCHIDEE). The reasons for this increased LAI in spring (for IPSL–ORCHIDEE) or in summer (for ARPEGE–ISBA and ECHAM5–JSBACH) results either from a shift in the seasonal cycle (leaf phenology)—crop leaves in those models do not emerge at the same time as tree leaves, and the length of the growth season is quite shorter for crops than for most other plant types—or from a larger LAI for crops than for grasses (e.g., for ARPEGE–ISBA).

Regarding the relation between the scale of deforestation and the amplitude of albedo changes, there is no such clear link between the deforested fraction and changes in LAI (Fig. 8). Many variables determine the representation of LAI in most models. For example, in IPSL–ORCHIDEE, ECHAM–JSBACH, and SPEEDY–LPJmL, LAI is computed for each vegetation type and results from multiple simulated processes (photosynthesis, respiration, allocation) determined by parameters specific to individual plant function types. In all other models, LAI

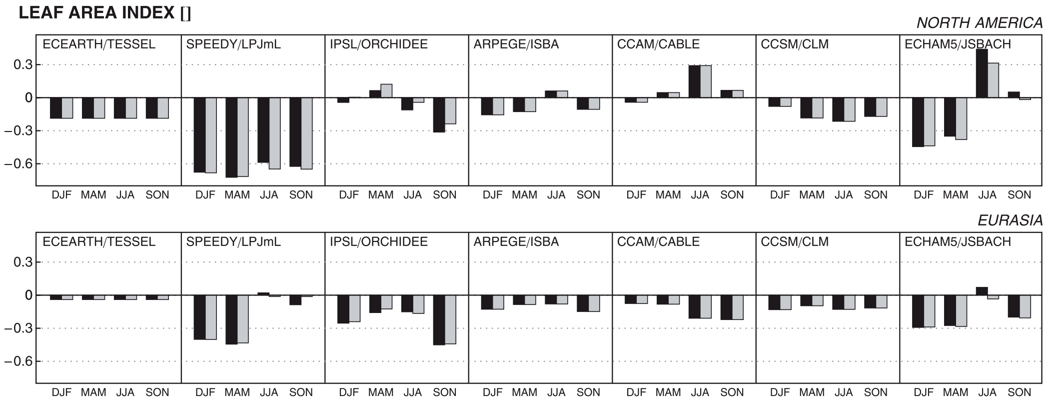

FIG. 7. As in Fig. 5, but for the simulated or imposed changes in LAI.

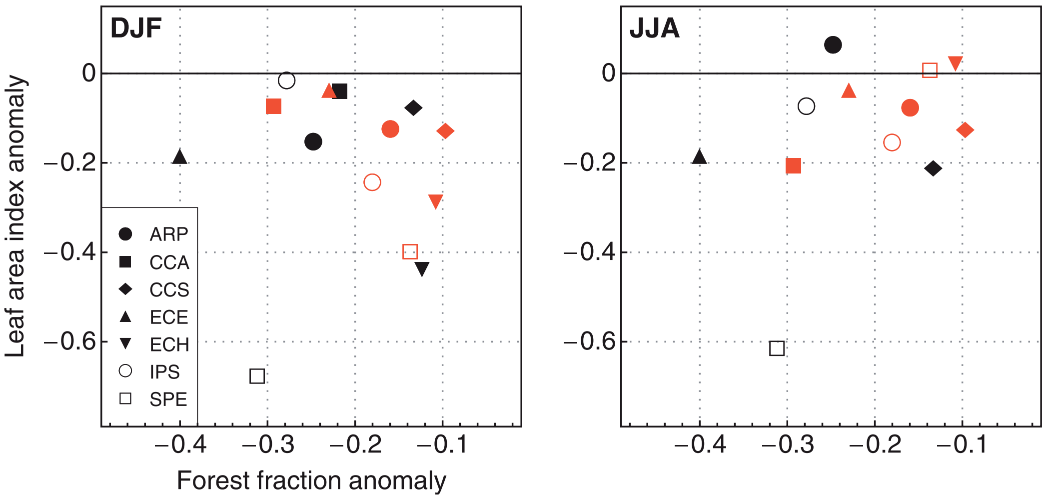

FIG. 8. As in Fig. 6, but for the simulated or imposed changes in LAI.

is prescribed per pixel and per vegetation type and is therefore independent of the potential surface climate change that the climate model may have undergone between preindustrial times and present day.

b. *Changes in available energy*

Following the changes in surface albedo, Q_A decreases in the temperate regions, for all seasons and all models (Fig. 9). This decrease in Q_A is proportional to the albedo change (not shown), and therefore approximately proportional to the scale of deforestation each model has undergone, except for CCAM–CABLE, as discussed in the previous section. In contrast to the albedo change, the changes in Q_A are at a maximum during spring and summer for all models when incident solar radiation is highest.

In addition, the LULCC simulations induce a reduced atmospheric longwave radiation emission. This (indirect) effect is led by the changes in the surface energy budget, which result in a reduced heat transferred back into the upper levels and in a lower equilibrium atmospheric temperature (Van der Molen et al. 2011).

Averaged over all models, the decrease in mean annual Q_A varies between 1 and more than 10 W m^{-2} (for EC-EARTH–TESSEL) in the northern temperate regions of North America and Eurasia, which represents a change of about 1%–10% compared to the preindustrial simulated values (Fig. 10).

c. *Changes in surface heat fluxes (turbulent and thermal radiative)*

The simulated decrease in Q_A discussed above is accompanied—for all models, in all seasons and locations—by a systematic decrease (Figs. 11a,c for summer changes)

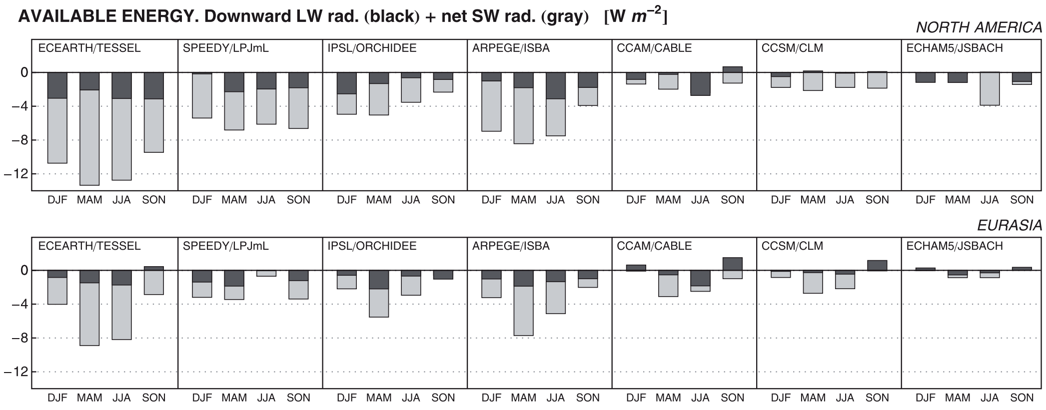

FIG. 9. As in Fig. 5, but for changes in Q_A (W m^{-2}), separately showing a response in net shortwave (SW) radiation (gray) and downward longwave (LW) radiation (black).

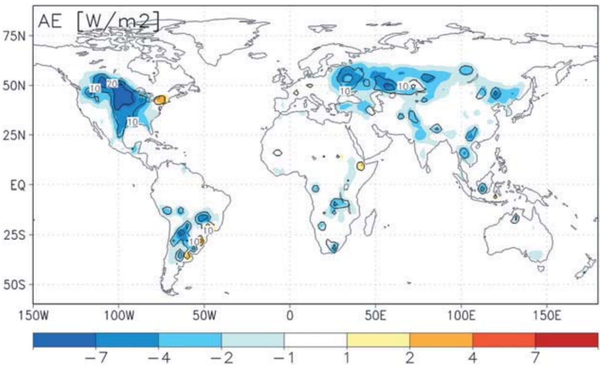

FIG. 10. Mean annual LULCC-induced change in available energy, averaged over all models and all experiments [0.5 (PD − PDv + PIv − PI)]. Shadings refer to the changes in W m^{-2}, while isolines represent the standard deviation between the models.

in Q_T. For most models the Northern Hemisphere summer change in turbulent fluxes is smaller than the change in Q_A. This suggests that the remaining energy decrease has been used to cool down the land, resulting in reduced emitted thermal radiation as illustrated by Figs. 11b,d. For the remaining models: IPSL–ORCHIDEE and CCAM–CABLE (as well as SPEEDY–LPJmL for Eurasia), ΔQ_A is larger than ΔQ_T. In IPSL–ORCHIDEE, this is compensated for by increased emitted thermal radiation, that is, surface warming, while in CCAM–CABLE (and SPEEDY–LPJmL for Eurasia) the smaller turbulent fluxes are compensated for by an increased heat flux into the ground (Q_G).

Even for the five (four in Eurasia) models that decrease Q_T less than Q_A, the relative change ($\Delta Q_T/\Delta Q_A$) varies from one model to the other. In Northern America it ranges from about 25% for ARPEGE–ISBA and ECHAM–JSBACH to more than 50% for EC-EARTH–TESSEL and CCSM–CLM and to about 100% for SPEEDY–LPJmL. Moreover, for two out of those five models (EC-EARTH–TESSEL, SPEEDY–LPJmL), the simulated change in Q_T is larger than what was expected, from the simple assumption that the fraction of energy used for turbulent fluxes is the same for all periods (gray shaded area in Figs. 11a,c). These results suggest that changing land cover and its associated characteristics have led to a change in the functioning of the soil–vegetation–atmosphere in a number of models. In most cases, crops and grasslands are less efficient than trees in transferring energy back to the atmosphere in the form of turbulent fluxes. This is further confirmed by Fig. 12, which shows a systematic decrease in the ratio: Q_T/Q_A for all seasons and for all models. Interestingly, all models at preindustrial times show rather comparable use of Q_A for turbulent fluxes for all seasons, with a maximum use during summertime (~25%), followed by spring (~20%) and fall (~12%), and with minimum use during wintertime (~5%). The largest changes in the use of this energy following the imposed LULCC are obtained for EC-EARTH–TESSEL, SPEEDY–LPJmL, and IPSL–ORCHIDEE, that is, the models that undergo the largest deforestation rates (−40%, −31%, −28% respectively), while the smallest changes are obtained for CCSM–CLM and ECHAM5–JSBACH, which experience the lowest deforestation rates (13% and 12%, respectively). Variations among the models can be found in the timing of the maximum change in the Q_T/Q_A ratio. For two models the maximum reduction of this ratio occurs in summer (IPSL–ORCHIDEE and CCAM–CABLE); for SPEEDY–LPJmL, ARPEGE–ISBA, and ECHAM5–JSBACH, the maximum changes occur in winter; while for EC-EARTH–TESSEL, it occurs in spring.

The decrease in the Q_T/Q_A ratio for all models at all seasons suggests that deforestation leads to an increased portion of Q_A that is used to warm up the land (reduced long-wave cooling), while the sum of the turbulent fluxes (Q_H and Q_E) decreases. This is a common feature shared by all models even though the season of maximum decrease varies from one model to the other. One possible cause is a decrease in the aerodynamic roughness length, which reduces the capacity of the land to exchange energy with the atmosphere via turbulence.

d. Changes in surface temperature

All models that undergo a change in their forest fraction that is larger than 15%[2] simulate cooler ambient air temperature in all seasons (Fig. 13). This results from the simulated decrease in both surface albedo and Q_A. One exception is IPSL–ORCHIDEE, which simulates a small warming during summer and fall in response to the large decrease in turbulent fluxes that exceeds the decrease in Q_A, as discussed earlier. CCSM–CLM, ECHAM5–JSBACH, and SPEEDY–LPJmL (for Eurasia only) experience the lowest deforestation rates (between 10 and 15%) and exhibit smaller changes in temperature. Those changes though still tend to be negative.

Our results then tend to point to a rather systematic (and therefore potentially robust) cooling associated with LULCC in the temperate regions, for six out of seven models. The IPSL–ORCHIDEE model shows warming instead of cooling during summer and fall due

---

[2] For example, ARPGE–ISBA, CCAM–CABLE, EC-EARTH–TESSEL, IPSL–ORCHIDEE, and SPEEDY–LPJmL in North America.

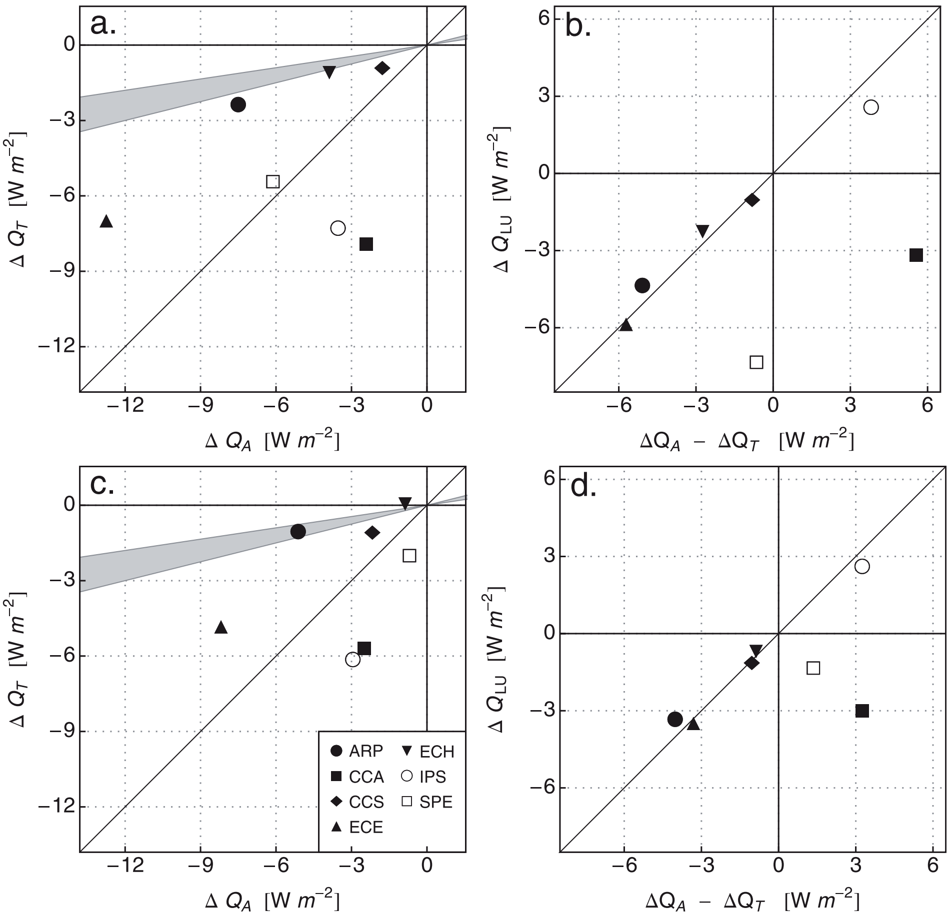

FIG. 11. Mean summer LULCC-induced changes (W m^{-2}) in (a),(c) Q_T plotted against the mean summer changes in Q_A; (b),(d) longwave radiation emitted by the surface (Q_{LU}) plotted against the changes in the difference between Q_A and Q_T. (a),(b) North America; (c),(d) Eurasia. Symbols refer to individual models. Plain line in all panels represents the 1:1 regression. Gray shaded area in (left) refers to the changes in Q_T that would have occurred if Q_T/Q_A ratios were the same at PD and PI periods (see section 4c for discussion).

to 1) the very strong subsequent partitioning of Q_A into Q_H rather than Q_E in all periods (see section 5) and 2) the strong sensitivity of Q_E to vegetation change through changes in surface parameters (notably, roughness length).

5. How do LULCC modify the partitioning of available energy in latent and sensible heat fluxes? Is there any consistency among the models?

The partitioning of turbulent fluxes into Q_E and Q_H (expressed by the Bowen ratio BR = Q_H/Q_E), and its changes since preindustrial times are shown in Fig. 14. *The spread among the models is large,* both in terms of its seasonal cycle and its response to deforestation. SPEEDY–LPJmL and IPSL–ORCHIDEE tend to maximize BR in all seasons except winter. From March to November, Q_H is 1.1–1.5 times larger than Q_E for those models, while for CCAM–CABLE, CCSM–CLM, EC-EARTH–TESSEL, and ARPEGE–ISBA, Q_H is always smaller than Q_E (from 0.39 to 0.71). However, this grouping of models does not imply they will similarly respond to deforestation. SPEEDY–LPJmL and IPSL–ORCHIDEE show a consistent decrease in BR in winter and increases in summer and fall, but they show opposite responses in spring. Both CCSM–CLM and EC-EARTH–TESSEL increase the return of energy in the atmosphere in terms of Q_E rather than Q_H, although their forest fraction has strongly diminished. For ARPEGE–ISBA, CCAM–CABLE, and ECHAM5–JSBACH, BR decreases marginally in summer, while changes in the other seasons show increases or decreases. *There is therefore no consistent pattern among the various models regarding how Q_E and Q_H change from one season to another.*

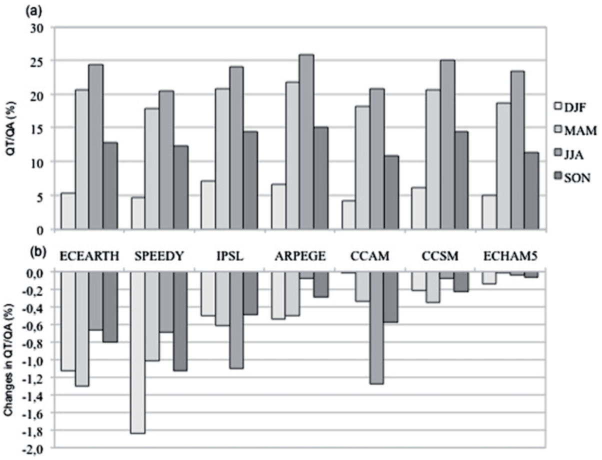

FIG. 12. Mean seasonal values of (a) the fraction of available energy used for turbulent fluxes (i.e., Q_T/Q_A; %) for each LSM for PI conditions. (b) The LULCC-induced changes in this fraction between PD and PI periods.

Some decrease both fluxes in response to the decrease in Q_T, others increase Q_H and decrease Q_E (or vice versa).

Moreover, the reasons why the models differ so considerably vary from model to model. We discuss the reasons for North America, from the results displayed in Fig. 14:

- The seasonal cycle of leaf area index in IPSL-ORCHIDEE is slightly shifted toward earlier dates (section 5a), which leads to larger values of LAI in spring and smaller values in all other seasons. ORCHIDEE is sensitive to changes in LAI, and Q_E is increased in spring (despite the decrease in Q_A) and decreased in all other seasons. The warming of the ambient air in summer and fall results from this significant reduction in Q_E that more than compensates the change in Q_H.
- In June–August (JJA), EC-EARTH mimics the effects of ORCHIDEE in spring: the reduction in Q_A gives rise to excessive reductions in Q_H and a compensating increase in Q_E, supported by lower evaporation and soil moisture depletion rates in DJF and March–May (MAM). Van der Molen et al. (2011) showed a positive temperature feedback of the surface energy balance in midlatitude deforestation areas, enhancing the albedo-induced cooling by an increased evaporation during boreal summer.
- The changes in CCAM–CABLE are very small. To a large degree, this is related to the small change in Q_A energy (Fig. 9), which relates to the use of parameters in the calculation of albedo that do not vary as a function of vegetation type. Thus, a change in vegetation type does not cause a change in albedo and by implication Q_A, and thus this element of the driver of the impact of LULCC is not captured.
- The increased Q_E in CCSM–CLM arises from the partitioning of Q_E into transpiration, evaporation of intercepted water, and soil evaporation. For example, summer transpiration generally decreases with the conversion of forest to crop, as does interception. Soil evaporation increases because the decrease in LAI allows more solar radiation to reach the ground. Soils in CCSM–CLM are wet, and the increased radiation produces increased evaporation. Increases in precipitation as a result of land cover change additionally increase Q_E, especially in regions of North America.
- In SPEEDY–LPJmL, crops have less access to soil water, as their roots are concentrated (80%) in the upper soil layer, while trees can have more roots (up to 40%) and thus access to water in the lower soil layer. Reductions in roughness length are responsible for more stable atmospheric conditions, which also reduces Q_E. During winter, the albedo increase is much larger than during summer for most models. The reduction in

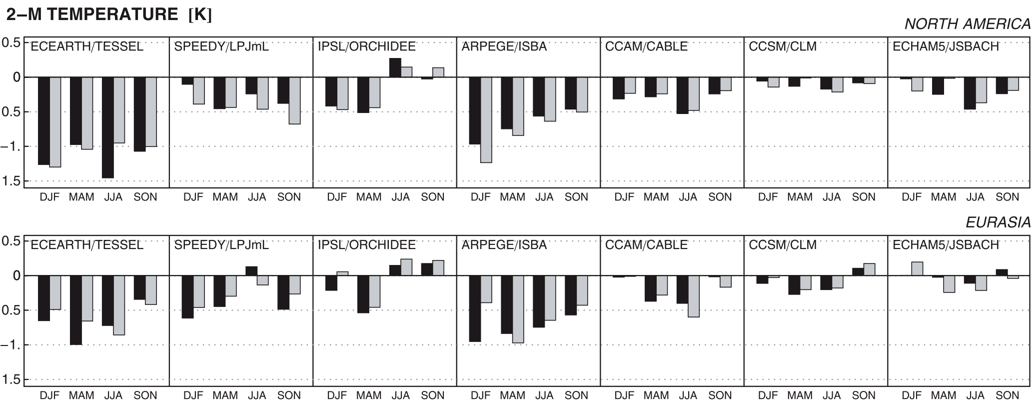

FIG. 13. As for Fig. 5, but for ambient air temperature (°C).

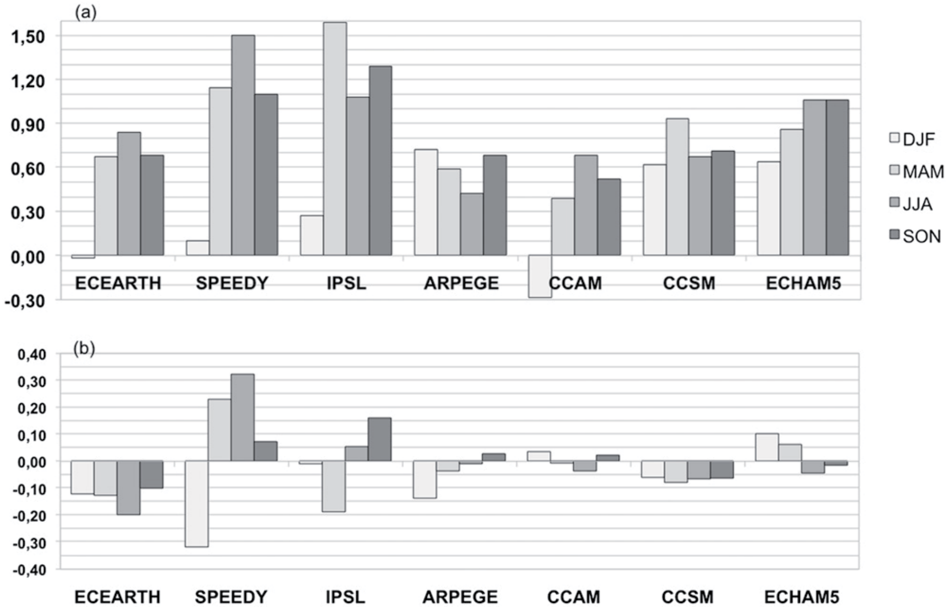

FIG. 14. Mean seasonal values of (a) the BR for each LSM for PI conditions. (b) The LULCC-induced changes in this fraction between PD and PI periods.

turbulent fluxes is more reflected on Q_H than on Q_E, which is always quite small in winter anyway.

- The largest signal with ARPEGE–ISBA comes from the increased snow cover over crops in winter and early spring, reducing the available energy. This reduction leads to a decrease in sensible heat flux because vegetation is mostly inactive. In summer and fall, the higher albedo of crops reduces the available energy and induces a decrease in sensible and latent heat fluxes. The reduction is larger for sensible heat flux in summer, while larger for latent heat flux in the fall. In ARPEGE–ISBA, crops have access to a smaller soil water reservoir than natural vegetation. This limitation is most obvious in the fall, when soil moisture is depleted.
- For ECHAM–JSBACH we see consistent signals in winter, spring, and summer: a decrease (increase) in LAI reduces (increase) the latent heat flux with the converse signal in the sensible heat flux. In fall the behavior is different: the almost unchanged LAI is consistent with almost no change in the latent heat flux but, surprisingly, goes along with a substantial reduction in sensible heat flux, so that maybe nonlocal effects play a role.

6. Discussion and conclusions

LUCID undertook a suite of climate model simulations, designed to diagnose and quantify the robust impacts of LULCC on climate between the preindustrial times and the present. Pitman et al. (2009) examined the spatial distribution of summer changes over the whole globe and concluded that there was a lack of consistency among the models. Various reasons for the discrepancies were suggested, without being able to attribute the changes to one or the other at that stage. This paper provides the detailed analysis of the LUCID results to identify the reasons for the discrepancies identified by Pitman et al. (2009).

The large spread of our model results both in terms of preindustrial and present-day values of latent and sensible heat fluxes, and their changes under deforestation confirm that the uncertainty in the Q_E response is a key uncertainty in the LULCC forcing at temperate latitudes (Bonan 2008). Our results show that it is not only the change in Q_E that matters but also (and probably *mainly*) how each individual model calculates the seasonally and surface-type-dependent Bowen ratio.

The model spread is quite surprising, given that many of the LSMs have undergone exhaustive validation of their fluxes via offline evaluation studies. However, there are a series of profound limitations in the ways LSMs are usually evaluated and intercompared. These include the following:

1) The evaluation of LSMs tends to be limited in scope, not always objective, relative to a previous version of a model (as distinct to the information content in the observed data), and rarely relative to a benchmark (Abramowitz 2005; Abramowitz et al. 2008).

2) Almost all LSM evaluation is uncoupled from an atmosphere (offline); this is necessary but insufficient to establish the utility of a model, because the forcing of the atmosphere is very strong and might overshadow some differences in the behavior of the models.
3) Almost all LSM evaluation has been focused on whether the mean state, or diurnal cycle, or seasonal cycle can be captured. Again, this is necessary but insufficient. Rarely is the land surface models' ability to simulate the impact, feedbacks, and associated responses to a *perturbation* (via elevated radiative forcing, LULCC, a severe rainfall anomaly, a drought, a heat wave, etc.) explored. However, LSMs must be able to simulate these kinds of phenomena to provide climate models the land surface influence required in climate modeling and climate projection.

Our finding therefore suggests that offline evaluation of LSMs is necessary but insufficient and should be complemented by the evaluation of the same models at least coupled to an atmospheric column. Further, an evaluation of a LSM's capacity to capture changes, as distinct from a mean state, has emerged as a priority.

The more in-depth analysis presented in this paper, compared to Pitman et al. (2009), suggests a number of robust common features shared by all models, including the following:

- LULCC leads to a systematic increase in surface albedo in all seasons. For most models, this increase is proportional to the amount of deforestation imposed on the individual models. This proportionality implies that while the LSMs have been developed independently, the models respond quite similarly to LULCC in terms of albedo (7% for a full transition from forest to crop/grassland).
- This larger surface albedo causes a decrease in Q_A (computed as the sum of absorbed solar energy and incident atmospheric infrared radiation); Q_A decreases everywhere in the temperate regions, in all seasons and for all models. The decrease in Q_A is proportional to the amount of deforestation imposed on a given model.
- The simulated decrease in Q_A is accompanied, for all models, in all seasons and locations, by a systematic decrease in the sum of Q_E and Q_H.
- All models show a similar seasonal cycle in the amount of Q_A being used for turbulent fluxes (i.e., similar Q_T/Q_A). This ratio is always decreased in response to LULCC in all seasons, but this decrease varies across the model ensemble. The mean annual decrease is proportional to the intensity of LULCC.
- In most cases, crops and grasslands are less efficient than trees in transferring energy to the atmosphere in the form of turbulent fluxes due to a lower aerodynamic roughness length.

These common features and their dependence on the amount of LULCC prescribed in each model suggest that, for an agreed amount of deforestation that occurred over specific periods, the dispersion among the models will be significantly smaller.

However, some persistent disparities remain. First, there is no consistency in how Q_T is partitioned between Q_E and Q_H throughout the annual cycle. Second, there is no consistency in the seasonal response of Q_H and Q_E to LULCC. In some LSMs, deforestation leads to a decrease in both fluxes in response to the decrease in Q_A and Q_T, while in others Q_H increases and Q_E decreases (or vice versa). This is dependent on how these processes are represented in each LSM. We are not able to attribute these differences to the many parameterization variations. However, our conclusions do point to an urgent need to revisit the way LSMs are evaluated if we are to resolve why they disagree on the impact of LULCC. One significant problem we are facing is that LSMs are generally evaluated offline, forced with prescribed atmospheric forcing. Our results suggest that this is necessary but insufficient. Evaluation of LSMs has to account for atmospheric feedbacks (e.g., Santanello et al. 2009). An evaluation framework should then be completed by series of analyses that determine how well LSMs capture the contrasting dynamic properties of various vegetation types, which are relevant for biosphere–atmosphere interactions (e.g., water use efficiency, dynamics of evaporative fraction, effective temperature sensitivity of carbon balance).

Increased concentration of greenhouse gases in the atmosphere, and the subsequent changes in sea surface temperatures and sea ice extent, are often used as the main drivers of climate change also over land. Our results suggest that such an assumption leads to erroneous conclusions regarding the land surface impacts of climate change in regions where LULCC has been significant. LULCC affects a number of variables to a similar magnitude, but of opposite sign, in increasing greenhouse gas concentrations. LULCC therefore has the potential to mask a regional warming signal, with the resulting risk that detection and attribution studies may miss a clear greenhouse signal or misattribute a greenhouse signal if LULCC is poorly accounted for. Detection and attribution is a complex process that is beyond the scope of this paper (see, e.g., Stott et al. 2010). However, our results suggest that including LULCC could improve the regional-scale detection of the impacts of specific forcings by ensuring that land cover's contribution to any regional changes is appropriately represented. LULCC will suppress the impacts of, for example, increasing

CO_2 in some regions that cool due to land cover change and amplify the impacts of increasing CO_2 in regions that warm due to land cover change. In the former case, there is a risk of missing the detection of a CO_2 signal, while in the latter there is a risk of a false-positive detection of a CO_2 signal. Aerosols, which typically cool, particularly strongly at regional scales, are an additional forcing that might be masked by the misrepresentation of LULCC.

Our findings argue for the inclusion of LULCC in climate projections, as now in process for the CMIP5 simulations (e.g., Arora et al. 2011). However, we have also shown that the differences among the seven models' response to LULCC is larger than the differences that results from the change in CO2SST. Since LULCC is implemented in most CMIP5 models, we expect a larger divergence among climate models in comparison to earlier efforts over regions of intense LULCC, coincident with dense human populations. This problem will only be resolved via a more systematic effort within the climate modeling and land surface modeling communities, starting with a coordinated evaluation of how to represent LULCC, how well models capture the impacts of LULCC in both offline and coupled simulations.

Acknowledgments. The authors gratefully acknowledge the inspiring discussions, input and collaboration among the participants of LULCC initiative, IGBP second synthesis topic on "Land-Use-induced Land-Cover Changes and the functioning of the Earth System."

REFERENCES

Abramowitz, G., 2005: Towards a benchmark for land surface models. *Geophys. Res. Lett.,* **32,** L22702, doi:10.1029/2005GL024419.

——, R. Leuning, M. Clark, and A. Pitman, 2008: Evaluating the performance of land surface models. *J. Climate,* **21,** 5468–5481.

Arneth, A., and Coauthors, 2010: Terrestrial biogeochemical feedbacks in the climate system. *Nat. Geosci.,* **3,** 525–532, doi:10.1038/ngeo905.

Arora, V. K., and Coauthors, 2011: Carbon emission limits required to satisfy future representative concentration pathways of greenhouse gases. *Geophys. Res. Lett.,* **38,** L05805, doi:10.1029/2010GL046270.

Betts, A. K., J. H. Ball, A. C. M. Beljaars, M. J. Miller, and P. A. Viterbo, 1996: The land surface-atmosphere interaction: A review based on observational and global modeling perspectives. *J. Geophys. Res.,* **101,** 7209–7225.

Bonan, G. B., 1997: Effects of land use on the climate of the United States. *Climatic Change,* **37,** 449–486.

——, 2008: Forests and climate change: Forcings, feedbacks, and the climate benefits of forests. *Science,* **320,** 1444–1449, doi:10.1126/science.1155121.

Bondeau, A., and Coauthors, 2007: Modelling the role of agriculture for the 20th century global terrestrial carbon balance. *Global Change Biol.,* **13,** 679–706.

Collins, W. D., and Coauthors, 2006: The Community Climate System Model Version 3 (CCSM3). *J. Climate,* **19,** 2122–2143.

Davin, E. L., and N. de Noblet-Ducoudré, 2010: Climatic impact of global-scale deforestation: Radiative versus nonradiative processes. *J. Climate,* **23,** 97–112.

——, ——, and P. Friedlingstein, 2007: Impact of land cover change on surface climate: Relevance of the radiative forcing concept. *Geophys. Res. Lett.,* **34,** L13702, doi:10.1029/2007GL029678.

DeFries, R. S., and Coauthors, 1995: Mapping the land surface for global atmosphere-biosphere models: Toward continuous distributions of vegetation's functional properties. *J. Geophys. Res.,* **100,** 20 867–20 882.

Denman, K. L., and Coauthors, 2007: Couplings between changes in the climate system and biogeochemistry. *Climate Change 2007: The Physical Science Basis,* S. D. Solomon et al., Eds., Cambridge University Press, 499–588.

Deo, R. C., J. I. Syktus, C. A. McAlpine, P. J. Lawrence, H. A. McGowan, and S. R. Phinn, 2009: Impact of historical land cover change on daily indices of climate extremes including droughts in eastern Australia. *Geophys. Res. Lett.,* **36,** L08705, doi:10.1029/2009GL037666.

Fall, S., D. Niyogi, A. Gluhovsky, R. A. Pielke Sr., E. Kalnay, and G. Rochon, 2010a: Impacts of land use land cover on temperature trends over the continental United States: Assessment using the North American Regional Reanalysis. *Int. J. Climatol.,* **30,** 1980–1993.

Findell, K. L., E. Shevliakova, P. C. D. Milly, and R. J. Stouffer, 2007: Modeled impact of anthropogenic land cover change on climate. *J. Climate,* **20,** 3621–3634.

——, A. J. Pitman, M. H. England, and P. Pegion, 2009: Regional and global impacts of land cover change and sea surface temperature anomalies. *J. Climate,* **22,** 3248–3269.

Forster, P. M., and Coauthors, 2007: Changes in atmospheric constituents and in radiative forcing. *Climate Change 2007: The Physical Science Basis,* S. Solomon et al., Eds., Cambridge University Press, 129–234.

Gallo, K. P., T. W. Owen, D. R. Easterling, and P. F. Jamason, 1999: Temperature trends of the U.S. Historical Climatology Network based on satellite designated land use/land cover. *J. Climate,* **12,** 1344–1348.

Gedney, N., and P. J. Valdes, 2000: The effect of Amazonian deforestation on the Northern Hemisphere circulation and climate. *Geophys. Res. Lett.,* **27,** 12 753–12 758.

Gerten, D., S. Schaphoff, and W. Lucht, 2007: Potential future changes in water limitations of the terrestrial biosphere. *Climatic Change,* **80,** 277–299, doi:10.1007/s10584-006-9104-8.

Hale, R. C., K. P. Gallo, T. W. Owen, and T. R. Loveland, 2006: Land use/land cover change effects on temperature trends at U.S. Climate Normals stations. *Geophys. Res. Lett.,* **33,** L11703, doi:10.1029/2006GL026358.

Henderson-Sellers, A., R. E. Dickinson, T. B. Durbidge, P. J. Kennedy, K. McGuffie, and A. J. Pitman, 1993: Tropical deforestation: Modeling local- to regional-scale climate change. *J. Geophys. Res.,* **98,** 7289–7315.

Hurtt, G. C., S. Frolking, M. G. Fearon, B. Moore III, E. Shevliakova, S. Malyshev, S. W. Pacala, and R. A. Houghton, 2006: The underpinnings of land-use history: Three centuries of global gridded land-use transitions, wood harvest activity, and resulting secondary lands. *Global Change Biol.,* **12,** 1208–1229.

——, and Coauthors, 2011: Harmonization of land-use scenarios for the period 1500–2100: 600 years of global gridded annual land-use transitions, wood harvest, and resulting secondary lands. *Climatic Change,* **109,** 117–161, doi:10.1007/s10584-011-0153-2.

Kaplan, J. O., K. M. Krumhardt, E. C. Ellis, W. F. Ruddiman, C. Lemmen, and K. Klein Goldewijk, 2011: Holocene carbon emissions as a result of anthropogenic land cover change. *Holocene,* **21,** 775–791, doi:10.1177/0959683610386983.

Klein Goldewijk, K., 2001: Estimating global land use change over the past 300 years: The HYDE database. *Global Biogeochem. Cycles,* **15,** 417–433.

——, A. Beusen, G. van Drecht, and M. de Vos, 2011: The HYDE 3.1 spatially explicit database of human-induced global land-use change over the past 12,000 years. *Global Ecol. Biogeogr.,* **20,** 73–86, doi:10.1111/j.1466-8238.2010.00587.x.

Krinner, G., and Coauthors, 2005: A dynamical global vegetation model for studies of the coupled atmosphere-biosphere system. *Global Biogeochem. Cycles,* **19,** GB1015, doi:10.1029/2003GB002199.

Lawrence, P. J., and T. N. Chase, 2010: Investigating the climate impacts of global land cover change in the Community Climate System Model. *Int. J. Climatol.,* **30,** 2066–2087.

Lobell, D. B., and C. Bonfils, 2008: The effect of irrigation on regional temperatures: A spatial and temporal analysis of trends in California, 1934–2002. *J. Climate,* **21,** 2064–2071.

Loveland, T. R., B. C. Reed, J. F. Brown, D. O. Ohlen, Z. Zhu, L. Yang, and J. W. Merchant, 2000: Development of a global land cover characteristics database and IGBP DISCover from 1 km AVHRR data. *Int. J. Remote Sens.,* **21,** 1303–1330.

Mahmood, R., K. G. Hubbard, R. D. Leeper, and S. A. Foster, 2008: Increase in near-surface atmospheric moisture content due to land use changes: Evidence from the observed dewpoint temperature data. *Mon. Wea. Rev.,* **136,** 1554–1561.

Marti, O., and Coauthors, 2010: Key features of the IPSL ocean atmosphere model and its sensitivity to atmospheric resolution. *Climate Dyn.,* **34,** 1–26, doi:10.1007/s00382-009-0640-6.

Masson, V., J.-L. Champeaux, F. Chauvin, C. Meriguet, and R. Lacaze, 2003: A global database of land surface parameters at 1-km resolution in meteorological and climate models. *J. Climate,* **16,** 1261–1282.

McCarthy, M. P., M. J. Best, and R. A. Betts, 2010: Climate change in cities due to global warming and urban effects. *Geophys. Res. Lett.,* **37,** L09705, doi:10.1029/2010GL042845.

McGregor, J. L., and M. R. Dix, 2008: An updated description of the Conformal-Cubic Atmospheric Model. *High Resolution Numerical Modelling of the Atmosphere and Ocean,* K. Hamilton and W. Ohfuchi, Eds., Springer, 51–76.

Oleson, K. W., G. B. Bonan, S. Levis, and M. Vertenstein, 2004: Effects of land use change on North American climate: Impact of surface datasets and model biogeophysics. *Climate Dyn.,* **23,** 117–132.

——, and Coauthors, 2008: Improvements to the Community Land Model and their impact on the hydrological cycle. *J. Geophys. Res.,* **113,** G01021, doi:10.1029/2007JG000563.

Pielke, R. A., Sr., G. Marland, R. A. Betts, T. N. Chase, J. L. Eastman, J. O. Niles, D. D. S. Niyogi, and S. W. Running, 2002: The influence of land-use change and landscape dynamics on the climate system: Relevance to climate-change policy beyond the radiative effect of greenhouse gases. *Philos. Trans. Roy. Soc. London,* **A360,** 1705–1719.

Pitman, A. J., 2003: The evolution of, and revolution in, land surface schemes designed for climate models. *Int. J. Climatol.,* **23,** 479–510.

——, and Coauthors, 2009: Uncertainties in climate responses to past land cover change: First results from the LUCID intercomparison study. *Geophys. Res. Lett.,* **36,** L14814, doi:10.1029/2009GL039076.

Pongratz, J., C. H. Reick, T. Raddatz, and M. Claussen, 2008: A reconstruction of global agricultural areas and land cover for the last millennium. *Global Biogeochem. Cycles,* **22,** GB3018, doi:10.1029/2007GB003153.

Raddatz, T. J., and Coauthors, 2007: Will the tropical land biosphere dominate the climate–carbon cycle feedback during the twenty-first century? *Climate Dyn.,* **29,** 565–574, doi:10.1007/s00382-007-0247-8.

Ramankutty, N., and J. A. Foley, 1999: Estimating historical changes in global land cover: Croplands from 1700 to 1992. *Global Biogeochem. Cycles,* **13,** 997–1027.

Roeckner, E., and Coauthors, 2006: Sensitivity of simulated climate to horizontal and vertical resolution in the ECHAM5 atmosphere model. *J. Climate,* **19,** 3771–3791.

Salas-Mélia, D., and Coauthors, cited 2005: Description and validation of the CNRM-CM3 global coupled climate model. [Available online at http://www.cnrm.meteo.fr/scenario2004/paper_cm3.pdf.]

Santanello, J. A., C. D. Peters-Lidard, S. V. Kumar, C. Alonge, and W.-K. Tao, 2009: A modeling and observational framework for diagnosing local land–atmosphere coupling on diurnal time scales. *J. Hydrometeor.,* **10,** 577–599.

Sellers, P. J., J. A. Berry, G. J. Collatz, C. B. Field, and F. G. Hall, 1992: Canopy reflectance, photosynthesis, and transpiration. III. A reanalysis using improved leaf models and a new canopy integration scheme. *Remote Sens. Environ.,* **42,** 187–216.

Seneviratne, S. I., T. Corti, E. L. Davin, M. Hirschi, E. B. Jaeger, I. Lehner, B. Orlowsky, and A. J. Teuling, 2010: Investigating soil moisture–climate interactions in a changing climate: A review. *Earth Sci. Rev.,* **99,** 125–161.

Stott, P. A., N. P. Gillett, G. C. Hegerl, D. J. Karoly, D. A. Stone, X. Zhang, and F. Zwiers, 2010: Detection and attribution of climate change: A regional perspective. *Wiley Interdiscip. Rev.: Climate Change,* **1,** 192–211, doi:10.1002/wcc.34.

Strengers, B. J., and Coauthors, 2010: Assessing 20th century climate–vegetation feedbacks of land-use change and natural vegetation dynamics in a fully coupled vegetation–climate model. *Int. J. Climatol.,* **30,** 2055–2065, doi:10.1002/joc.2132.

Teuling, A. J., and Coauthors, 2010: Contrasting response of European forest and grassland energy exchange to heatwaves. *Nat. Geosci.,* **3,** 722–727, doi:10.1038/ngeo950.

Van den Hurk, B. J. J. M., P. Viterbo, A. C. M. Beljaars, and A. K. Betts, 2000: Offline validation of the ERA40 surface scheme. ECMWF Tech. Memo. 295, 42 pp. [Available online at http://www.knmi.nl/publications/fulltexts/tm295.pdf.]

Van der Molen, M. K., B. J. J. M. van den Hurk, and W. Hazeleger, 2011: A dampened land use change climate response towards the tropics. *Climate Dyn.,* **37,** 2035–2043, doi:10.1007/s00382-011-1018-0.

Voldoire, A., 2006: Quantifying the impact of future land-use changes against increases in GHG concentrations. *Geophys. Res. Lett.,* **33,** L04701, doi:10.1029/2005GL024354.

Wang, Y. P., D. Baldocchi, R. Leuning, E. Falge, and T. Vesala, 2007: Estimating parameters in a land-surface model by applying nonlinear inversion to eddy covariance flux measurements from eight FLUXNET sites. *Global Change Biol.,* **13,** 652–670, doi:10.1111/j.1365-2486.2006.01225.x.

Werth, D., and R. Avissar, 2002: The local and global effects of Amazon deforestation. *J. Geophys. Res.,* **107,** 8087, doi:10.1029/2001JD000717.

Wetherald, R. T., and S. Manabe, 2002: Simulation of hydrologic changes associated with global warming. *J. Geophys. Res.,* **107,** 4379, doi:10.1029/2001JD001195.

Williams, M., 2003: *Deforesting the Earth: From Prehistory to Global Crisis*. University of Chicago Press, 689 pp.

Zhang, H., A. Henderson-Sellers, and K. McGuffie, 1996: Impacts of tropical deforestation. Part I: Process analysis of local climatic change. *J. Climate,* **9,** 1497–1517.

Zhao, M., and A. J. Pitman, 2002: The impact of land cover change and increasing carbon dioxide on the extreme and frequency of maximum temperature and convective precipitation. *Geophys. Res. Lett.,* **29,** 1078, doi:10.1029/2001GL013476.

Zhou, L., R. E. Dickinson, Y. Tian, J. Fang, Q. Li, R. K. Kaufman, C. J. Tucker, and R. B. Myneni, 2004: Evidence for a significant urbanization effect on climate in China. *Proc. Natl. Acad. Sci. USA,* **101,** 9540–9544.

2.4.5 Paper: Attributing the impacts of land-cover changes in temperate regions on surface temperature and heat fluxes to specific causes. Results from the first LUCID set of simulations

By J. P. Boisier, N. de Noblet-Ducoudré, A. Pitman, F. T. Cruz, C. Delire, B. J. J. M. van den Hurk, M. K. van der Molen, C. Müller, and A. Voldoire

Reference: Journal of Geophysical Research, Vol. 117, D12116, 16 PP., 2012. doi: 10.1029/2011JD017106

JOURNAL OF GEOPHYSICAL RESEARCH, VOL. 117, D12116, doi:10.1029/2011JD017106, 2012

Attributing the impacts of land-cover changes in temperate regions on surface temperature and heat fluxes to specific causes: Results from the first LUCID set of simulations

J. P. Boisier,[1] N. de Noblet-Ducoudré,[1] A. J. Pitman,[2] F. T. Cruz,[3,4] C. Delire,[5]
B. J. J. M. van den Hurk,[6] M. K. van der Molen,[6,7] C. Müller,[8] and A. Voldoire[5]

Received 9 November 2011; revised 28 March 2012; accepted 21 May 2012; published 30 June 2012.

[1] Surface cooling in temperate regions is a common biogeophysical response to historical Land-Use induced Land Cover Change (LULCC). The climate models involved in LUCID show, however, significant differences in the magnitude and the seasonal partitioning of the temperature change. The LULCC-induced cooling is directed by decreases in absorbed solar radiation, but its amplitude is 30 to 50% smaller than the one that would be expected from the sole radiative changes. This results from direct impacts on the total turbulent energy flux (related to changes in land-cover properties other than albedo, such as evapotranspiration efficiency or surface roughness) that decreases at all seasons, and thereby induces a relative warming in all models. The magnitude of those processes varies significantly from model to model, resulting on different climate responses to LULCC. To address this uncertainty, we analyzed the LULCC impacts on surface albedo, latent heat and total turbulent energy flux, using a multivariate statistical analysis to mimic the models' responses. The differences are explained by two major 'features' varying from one model to another: the land-cover distribution and the simulated sensitivity to LULCC. The latter explains more than half of the inter-model spread and resides in how the land-surface functioning is parameterized, in particular regarding the evapotranspiration partitioning within the different land-cover types, as well as the role of leaf area index in the flux calculations. This uncertainty has to be narrowed through a more rigorous evaluation of our land-surface models.

Citation: Boisier, J. P., N. de Noblet-Ducoudré, A. J. Pitman, F. T. Cruz, C. Delire, B. J. J. M. van den Hurk, M. K. van der Molen, C. Müller, and A. Voldoire (2012), Attributing the impacts of land-cover changes in temperate regions on surface temperature and heat fluxes to specific causes: Results from the first LUCID set of simulations, *J. Geophys. Res.*, *117*, D12116, doi:10.1029/2011JD017106.

1. Introduction

[2] Land-cover conversion has increased significantly over the last 300 years and, nowadays, more than half of the global land surface is perturbed by humans to some degree [*Ellis et al.*, 2010]. Since the preindustrial epoch, croplands and rangelands have expanded, mainly through the removal of natural forest and grasslands in the temperate regions of the Northern Hemisphere [*Ramankutty and Foley*, 1999; *Hurtt et al.*, 2006; *Ellis et al.*, 2010; *Klein Goldewijk et al.*, 2011].

[3] Land-Use induced Land-Cover Changes (LULCC) affect climate through many ways, some being changes in the continental energy and water surface budgets. Such biogeophysical impacts of LULCC have received special attention in the last two decades (e.g., *Betts et al.* [2007] and *Pitman et al.* [2009] at global scale and *Pielke et al.* [2011, and references therein] at regional scale), but still remain uncertain as they depend on many factors, such as for example the scale of perturbation and its geographical location (e.g., tropics, temperate or boreal lands).

[4] Studies using global climate models (GCMs) generally agree that historical LULCC has increased the surface albedo in regions where forests have been cleared, many of them showing this effect and the associated near surface

---

[1] Laboratoire des Sciences du Climat et de l'Environnement, Unité Mixte CEA-CNRS-UVSQ, Gif-sur-Yvette, France.

[2] ARC Centre of Excellence for Climate System Science, University of New South Wales, Sydney, New South Wales, Australia.

[3] Climate Change Research Centre, University of New South Wales, Sydney, New South Wales, Australia.

[4] Manila Observatory, Quezon City, Philippines.

[5] Groupe d'Étude de l'Atmosphère Météorologique, Unité Associée CNRS/Météo-France, Toulouse, France.

[6] Royal Netherlands Meteorological Institute, De Bilt, Netherlands.

[7] Meteorology and Air Quality Group, Wageningen University and Research Centre, Wageningen, Netherlands.

[8] Earth System Analysis, Potsdam Institute for Climate Impact Research, Potsdam, Germany.

Corresponding author: J. P. Boisier, Laboratoire des Sciences du Climat et de l'Environnement, Unité Mixte CEA-CNRS-UVSQ, Bat.712, Orme des Merisiers, Point Courrier 132, FR-91191 Gif-sur-Yvette CEDEX, France. (juan-pablo.boisier@lsce.ipsl.fr)

0148-0227/12/2011JD017106

cooling as the leading impact of LULCC [*Hansen et al.*, 1998; *Govindasamy et al.*, 2001; *Feddema et al.*, 2005b]. The global negative radiative forcing induced by surface albedo increases has therefore been estimated in several studies [*Betts*, 2001; *Matthews et al.*, 2003; *Myhre and Myhre*, 2003; *Betts et al.*, 2007; *Davin et al.*, 2007; among others] and has been commonly used to measure the historical impact of LULCC [*Forster et al.*, 2007]. However, a number of authors have alerted the community that non-radiative processes (i.e. alteration of surface fluxes) can also have large impacts on surface and air temperature, or precipitation [e.g., *National Research Council*, 2005; *Davin et al.*, 2007].

[5] The radiatively induced cooling at the surface may be enhanced or reduced by non-radiative processes including the partitioning of net radiation between latent and sensible heat [*Bonan*, 2008]. Temperate forest clearing may lead to evaporative cooling during spring and summer time because crops often have larger evaporation rates than forests if the water supply is sufficient [*Baldocchi et al.*, 1997; *Oleson et al.*, 2004; *Mahmood et al.*, 2006; *Puma and Cook*, 2010; *Teuling et al.*, 2010]. In contrast, strong decreases in latent heat flux resulting in net warming have been found at lower latitudes because the cropping systems in those regions are not as productive and efficient as in the developed temperate regions [*Bounoua et al.*, 2002; *Snyder et al.*, 2004; *Lawrence and Chase*, 2010], which echo the future projections of the LULCC-induced impacts in the tropics [*Feddema et al.*, 2005a]. While the two mechanisms mentioned above have a direct impact on the latent/sensible heat flux partitioning, LULCC in the form of deforestation could also reduce the magnitude of the ensemble of turbulent energy fluxes increasing surface temperatures through changes in surface roughness [*Davin and de Noblet-Ducoudré*, 2010].

[6] At smaller spatial scales (local to regional), there have been a number of observations [e.g., *Loarie et al.*, 2011; *Butt et al.*, 2011; *Lyons et al.*, 1993, 2008] and numerical simulations [e.g., *Marshall et al.*, 2004; *Gero et al.*, 2006; *Georgescu et al.*, 2011] that have highlighted the complexity of land-atmosphere interactions, the multiple ways through which LULCC may impact the atmospheric and surface states, the land-atmosphere exchanges and therefore the atmospheric circulation at those scales, as reported in more details in *Pielke et al.* [2011].

[7] Besides all these studies and some consistent regional climate signals, the net and robust effect of the different land-surface processes relevant to LULCC and the resulting impacts on surface temperatures and precipitation remain unclear at the large scale. Significant differences in land-use/land-cover representation and in the simulated biophysical processes are behind the uncertainties found by various modeling studies [*Matthews et al.*, 2003; *Myhre and Myhre*, 2003; *Oleson et al.*, 2004; *Feddema et al.*, 2005b; *Forster et al.*, 2007; *de Noblet-Ducoudré et al.*, 2012].

[8] Within the framework of the international IGBP/iLEAPS and GEWEX/GLASS project 'Land-Use and Climate, IDentification of robust impacts' (LUCID), an experimental design was conceived to assess the robust global biogeophysical impacts of LULCC on climate from the preindustrial period to present-day, using several GCMs forced with the same land-use datasets and using the same modeling protocol. *Pitman et al.* [2009] described the first results of LUCID at the global-scale for the Northern Hemisphere summer. They showed statistically significant impacts of LULCC on the simulated near-surface temperature and latent heat flux over the regions where the LULCC were imposed. Most models simulate cooling, but the strength of the changes varies considerably. The latent heat flux responses are even more heterogeneous, with different signs and amplitudes. *de Noblet-Ducoudré et al.* [2012] further explored those results and the reasons behind the variety of LULCC-induced responses in North America and Eurasia. One important finding of their analysis is that, although the dispersion among the models' response to LULCC is large, there are a number of robust common features shared by all models. Absence of consistency only regards how LULCC affects the partitioning of available energy between latent and sensible heat fluxes at a specific time in the various models. Quite importantly as well, they showed that, regionally, LULCC has an impact on the near surface temperatures and other variables of similar magnitude (opposite in sign) than the resulting from increased greenhouse gases and a warmer ocean that occurred during the same time period. This in itself reinforces the message brought forward by scientists working at the regional level, arguing that LULCC has the potential to significantly affect climate and should be accounted for in detection/attribution studies and projections of climate change at smaller scales.

[9] This paper builds on *de Noblet-Ducoudré et al.* [2012] to a) examine the mechanisms through which the models involved in LUCID respond to LULCC, and b) try to explain why some of their responses to LULCC diverge. We quantify the causes of the inter-model dispersion focusing on the relative role of two key components. First, variations in the land-cover distribution that may largely differ from one model to another. Second, the individual GCM's sensitivity to the imposed LULCC, which includes how land-surface processes are parameterized and how these represent, and respond to, a land-cover perturbation.

[10] Our analyses focus on changes in the surface energy balance and particularly on the boreal summer (JJA) and winter (DJF) changes of surface albedo, latent heat flux and total turbulent energy flux, since these are the key variables that explain the radiative and non-radiative impacts of LULCC. We used statistical models of these variables to estimate the responses of each GCM to a limited number of drivers, notably, to perturbations in the land cover partitioning. We used the statistically based models as benchmark to assess the various LUCID GCMs in a similar approach of that of *Koster and Milly* [1997] and *Abramowitz* [2005]. The LUCID experimental design and used methodology are presented in section 2. Section 3 describes the LULCC impacts on the different components of the surface energy budget and the resulting temperature changes. The attribution of the LULCC-induced changes on surface climate and a diagnosis of the inter-model dispersion are presented in section 4. Conclusions are provided in section 5.

2. Material and Methods

2.1. LUCID Simulations

[11] The LUCID simulations analyzed here are the same as those described in *Pitman et al.* [2009] and *de Noblet-Ducoudré et al.* [2012] (hereafter N2012). Four types of

Table 1. Simulations Carried out Within the LUCID Intercomparison Project[a]

Experiment Name	Land-Cover Year	SST/SIC Period	CO_2 (ppm)
PD	1992	1970–1999	375
PDv	1870	1970–1999	375
PI	1870	1870–1899	280
PIv	1992	1870–1899	280

[a] Prescribed land-cover maps years, sea-surface temperature/sea-ice concentrations (SST/SIC) period and atmospheric CO_2 concentrations.

simulations were conducted by seven global climate models (GCMs) to evaluate the impact of LULCC from the preindustrial period to present day. Each experiment includes an ensemble of 30-years simulations (five members), computed with prescribed sea surface temperatures (SSTs) and sea-ice concentration (SIC), atmospheric CO_2 concentrations ($[CO_2]$) and land-cover maps (Table 1). All the models used the same SST/SIC HadISST dataset of *Rayner et al.* [2003] and a combined crop/pasture data set of *Ramankutty and Foley* [1999] and *Klein Goldewijk* [2001]. The preindustrial (*PI*) and present-day (*PD*) experiments used the prescribed data of the corresponding period, with interannual variability being accounted for uniquely for SSTs and SIC. Another experiment (*PDv*) was also performed using the present-day SST, SIC and $[CO_2]$ (hereafter SST/CO2) and the preindustrial vegetation (set to 1870). Finally, experiment *PIv* used the preindustrial SST/CO2 with the current vegetation (1992). Thus, the isolated effect of LULCC between 1870 and 1992 is defined by both differences $PD - PDv$ and $PIv - PI$. All simulations have been run in an ensemble mode to include more robustness in the results reported herein.

[12] In this study we explore the main effect of land-use embedded in both SST/CO2–related climate states, and will refer to the LULCC-induced anomaly of a generic variable Y as

$$\Delta Y = \frac{1}{2}(Y_{PD} - Y_{PDv} + Y_{PIv} - Y_{PI}) \qquad (1)$$

where Y_E is the climatological value of Y in a given experiment E.

[13] The seven GCMs involved in LUCID and the land surface models (LSMs) embedded in each GCM (hereafter GCM/LSMs), are ARPEGE/ISBA [*Salas-Mélia et al.*, 2005; *Voldoire*, 2006], CCAM/CABLE [*McGregor and Dix*, 2008; *Abramowitz et al.*, 2008], CCSM/CLM [*Collins et al.*, 2006; *Oleson et al.*, 2008], ECEARTH/TESSEL [*van den Hurk et al.*, 2000], ECHAM5/JSBACH [*Roeckner et al.*, 2006; *Raddatz et al.*, 2007], IPSL/ORCHIDEE [*Marti et al.*, 2010; *Krinner et al.*, 2005] and SPEEDY/LPJmL [*Strengers et al.*, 2010; *Bondeau et al.*, 2007]. For further details on the experiment setup and model descriptions, see N2012.

2.2. Methodology

[14] Results from the LUCID simulations show clear impacts on the near-surface temperature and latent heat flux in regions where the land-cover is perturbed, and do not show statistically significant signals elsewhere [*Pitman et al.*, 2009]. Therefore, we focus our analysis on areas where the imposed LULCC is significant. Two regions in respectively North America and west Eurasia were defined where the absolute change in the fraction of the surface occupied by crops or pastures between 1870 and 1992 exceeds 5% (Figure 1). In this study we do not shows specific comparison between these two regions (while N2012 did), so the analyses are related to the combined overall North American and Eurasian region (hereafter NAEA). We focus on the temperate mid-latitudes because *Pitman et al.* [2009] and N2012 showed these regions to be particularly sensitive to historical LULCC.

[15] Our analysis is based on the components of the surface energy budget (SEB):

$$Q_{SN} + Q_{LD} = Q_T + Q_{LU} + Q_R \qquad (2)$$

$$Q_{SN} = (1 - \alpha)Q_{SD} \qquad (3)$$

where Q_{SN} and Q_{SD} are the net and downward shortwave radiation, Q_{LD} and Q_{LU} the downward and upward longwave radiation, Q_T the sum of the latent (Q_{LE}) and sensible (Q_H) heat fluxes, Q_R a residual term (all values are in Wm^{-2}), and α is the surface albedo. In order to have a closed SEB

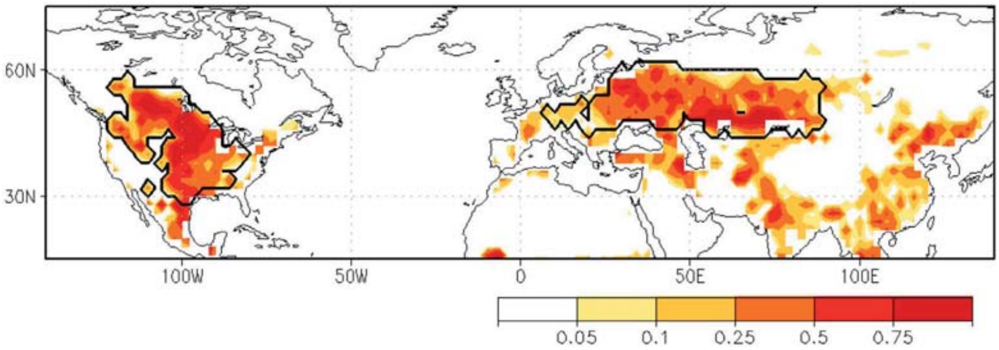

Figure 1. Absolute changes in crop and pasture fractions between 1870 and 1992. Solid contours indicate areas with changes larger than 5% in crop or pasture fractions confined to North America and west Eurasia (NAEA).

Table 2. Regressed (Predictands) and Explanatory (Predictors) Variables Used in Multivariate Statistical Analyses[a]

Predictand	Predictor
α	$\mathbf{F_v}$, *LAI*, *SWE*
Q_{LE}, Q_T	$\mathbf{F_v}$, *LAI*, Q_{SN}, R, R_{-}

[a] α: Surface albedo. Q_{LE}: Latent heat flux. Q_T: Total turbulent energy flux. $\mathbf{F_v}$: Land-cover fractions [evergreen trees (F_v), deciduous trees (F_d), crops (F_c), grasses (F_g), bare soil (F_s)]. *LAI*: Leaf area index. *SWE*: Snow water equivalent. Q_{SN}: Net shortwave radiation. R: Precipitation. R_{-}: 1-season lag precipitation.

relation, Q_R is derived explicitly from the other terms in equation (2), and accounts for the energy fluxes not considered here (the soil heat flux principally).

[16] The results described in section 4 are based on multivariate statistical analyses. Linear regressions of α, Q_{LE} and Q_T were computed for each GCM/LSM within the NAEA region from a set of predictors including surface and atmospheric variables. In order to account for the land-surface properties related to the different types of vegetation, the grid-fractions occupied by the various land-cover types were used as part of these predictors in all analyses. In most of the LSMs assessed here, the biogeography is represented through Plant Functional Types (PFTs). Depending on the model, the grid cell includes one (CABLE), two (TESSEL) or multiple PFTs (CLM, JSBACH, ORCHIDEE, LPJmL). In the case of ISBA, a set of parameters, averaged from those of the different PFTs co-existing within each grid-cell, describes the vegetation-related grid properties. Considering this, the regression models for the three analyzed variables were based on a mosaic approach of the sub-grid heterogeneity; that is, the grid mean value of a generic land-surface quantity Y_g is obtained as the linear combination of the components associated with the different land cover types present in the grid-cell, i.e.,

$$Y_g = \sum_v F_v Y_v \tag{4}$$

where F_v is the grid area fraction of the land-cover type v and F_v is the associated tile value of Y.

[17] To have consistent land-cover types across the models, the various PFTs used in the different LSMs were grouped in four main vegetation classes (evergreen trees, deciduous trees, grasses and crops), in addition to bare soil. These five land-cover types were then used in the regression analysis.

[18] Our objective here is to evaluate the sensitivity of each GCM/LSM to the same historical LULCC perturbation or change in another predictor. Our method therefore estimates seasonal anomalies rather than absolute values. This choice also helps to minimize the effect of non-linear relationships (e.g., soil water availability versus evapotranspiration), and avoid the spatial variability of some surface properties that do not change between the various experiments and that are not assessed here (e.g., soil color). For each GCM/LSM, the seasonal anomalies (Y'_g) represent departures from the climatological mean state of all four experiments ($\overline{Y_g}$). The statistical models we used take the first order terms of the expansion of equation (4) when applying perturbed forms of Y_g, Y_v and F_v. The functions regressed have then the form:

$$Y'_g(\mathbf{P}) = \sum_v \left[F'_v \overline{Y_v}(\mathbf{P}) + \overline{F_v}\, Y'_v(\mathbf{P})\right]. \tag{5}$$

[19] The first term on the right-hand side of equation (5) represents the direct effect of LULCC led by changes in the land-cover partitioning (F'_v) and accounts for grid-mean change in the surface properties resulting from the vegetation perturbation. The second term represents the indirect impact led by a perturbation in the tile values of Y'_g (Y'_v), which is driven by changes in the environmental variables (e.g., the contribution of snow-cover change to the surface albedo response).

[20] The array $\mathbf{P}$ represents the set of predictors used (Table 2) excluding the land-cover fractions F_v, which are explicitly taken in account in equation (5). The seasonal mean state $\overline{Y_v}$ and the corresponding anomaly Y'_v are modeled as polynomial expansions over the components of $\mathbf{P}$ (see Appendix A).

[21] For the Q_{LE} and Q_T analysis, the explanatory variables included in $\mathbf{P}$ were the seasonal means of leaf area index (*LAI*), net shortwave radiation (Q_{SN}) and precipitation (R), in addition of a 1-season lag precipitation value (R_{-}). The latter was included to take into account the effect of soil moisture memory [*Seneviratne et al.*, 2006]. The surface energy supply by radiation was considered using only Q_{SN}. Longwave radiation fluxes are explicitly isolated because they have the potential to mislead the interpretation of the regression results, as they are highly coupled with other drivers and predictands.

[22] The surface roughness (Z_0) is another important driver of Q_{LE} and Q_T, but it was not considered here because it is highly correlated with the forest fraction (Table 3) and, therefore, implicitly accounted for through F_v. On the same ground, depending on the model, the role that *LAI* plays in the three assessed predictands should be interpreted with caution, since it may also be significantly collinear with the forest fraction (Table 3). The results shown in section 4.2 were obtained from a second analysis carried out without using *LAI* as a predictor. This simpler choice allows us to evaluate the statistical models with different land-cover forcings without losing consistency with the *LAI* patterns.

Table 3. Spatial Correlation Between Forest Fraction and Leaf Area Index ($r_{F,L}$), and Between Forest Fraction and Roughness Length ($r_{F,Z}$) in JJA

GCM/LSM	$r_{F,L}$	$r_{F,Z}$
ECEARTH/TESSEL	0.51	0.92
CCAM/CABLE	0.71	0.90
IPSL/ORCHIDEE	0.54	0.99
SPEEDY/LPJmL	0.65	0.92
ARPEGE/ISBA	0.71	0.93
ECHAM5/JSBACH	0.45	0.57
CCSM/CLM	0.88	0.88

Table 4. Winter (DJF) and Summer (JJA) LULCC-Induced Surface Temperature Changes (K) in NAEA[a]

	DJF		JJA	
GCM/LSM	$\Delta_R T_S$	ΔT_S	$\Delta_R T_S$	ΔT_S
ECEARTH/TESSEL	−1.62	−0.91	−1.33	−0.78
CCAM/CABLE	−0.14	−0.14	−0.32	−0.54
IPSL/ORCHIDEE	−0.81	−0.26	−0.41	0.43
SPEEDY/LPJmL	−0.99	−0.25	−0.39	−0.66
ARPEGE/ISBA	−1.11	−0.76	−0.81	−0.67
ECHAM5/JSBACH	−0.09	0.02	−0.29	−0.24
CCSM/CLM	−0.29	−0.11	−0.25	−0.19
MEAN	−0.72	−0.34	−0.54	−0.38

[a] ΔT_S is the surface temperature changes simulated by each GCM/LSM, while $\Delta_R T_S$ are the ones expected from the sole changes in surface radiation. Values derived from changes in upward longwave radiation flux (following equations (6)–(8)).

[23] A more complete description of the statistical analysis, of the regression models used, and of the skills of the predicted responses, is provided in Appendix A.

3. How Strongly Do the Non-radiative Fluxes Contribute to the Temperature Changes?

[24] The simulated cooling in the NAEA region is a clear impact of LULCC on the surface climate in the ensemble of LUCID simulations, despite the inter-model spread (N2012). In both DJF and JJA the model-mean surface temperature anomalies (ΔT_S) averaged over NAEA are −0.34 K and −0.38 K respectively (Table 4). In DJF, the individual model responses range from −0.91 K (ECEARTH) to 0.02 K (ECHAM5). In JJA, the model spread is slightly greater, ranging from −0.78 K (ECEARTH) to +0.43 K (IPSL).

[25] Using equation (2) we can attribute the changes in surface temperature to changes in each of the SEB components. A perturbation in Q_{SN}, Q_{LD}, Q_T or Q_R can be expressed as an upward infrared radiation anomaly (ΔQ_{LU}), by fixing the non-perturbed terms. Then, ΔT_S is calculated by inverting the Stefan-Boltzmann law:

$$\Delta T_S = (\epsilon\sigma)^{-1/4}\left[\left(Q^*_{LU} + \Delta Q^*_{LU}\right)^{1/4} - Q^*_{LU}1/4\right] \qquad (6)$$

where Q^*_{LU} is derived from the unperturbed components of SEB. The surface emissivity (ϵ) is set to 1.0.

[26] Figure 2 shows the monthly near-surface temperature change induced by LULCC in NAEA averaged over all the models (solid line). Dots and shaded bars indicate the net ΔT_S and the contributions from changes in the different SEB components (derived from equation (6)). Since the surface energy balance must be maintained, the simulated model-mean temperature response matches closely the one derived from the various SEB fluxes.

[27] The ensemble of LUCID models shows a cooling throughout the year dominated by a consistent decrease in available energy at the surface (defined here as the sum of the net shortwave and the downward longwave radiation; $Q_A = Q_{SN} + Q_{LD}$). The Q_A decreases are mainly driven by the albedo-induced reductions in net solar radiation (Q_{SN}) but also by reductions in the incoming long-wave radiation (Q_{LD}). Q_{LD} changes represent an indirect impact of LULCC and, in all models, are approximately proportional to the changes in T_S (not shown). This underlines the existence of a positive feedback between T_S and incident long-wave radiation as discussed by *van der Molen et al.* [2011] and reported in N2012. The Q_{SN} decrease is stronger during the early spring (March), when the model-mean T_S anomaly reaches about −0.5 K. The radiative impact is larger during this season due to a maximized effect of the forest-induced snow-masking albedo change combined with the increasing solar radiation availability.

[28] The component of ΔT_S induced by Q_R (white bars in Figure 2) is directed by changes in CCAM/CABLE and SPEEDY/LPJmL principally. The LULCC-induced Q_R changes are near zero in most models except for these two cases, which show quite large positive values. This highlights an

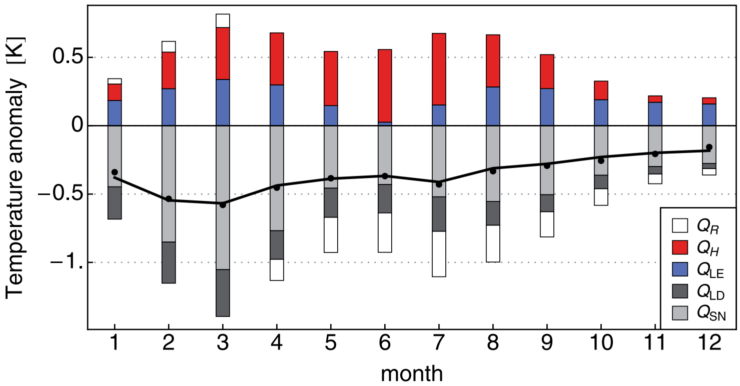

Figure 2. LULCC-induced monthly surface temperature anomalies derived from changes in the various components of the surface energy budget (inter-model average). Bars indicate the temperature anomaly induced by changes in latent heat flux (blue), in sensible heat flux (red), in net shortwave radiation (grey), in downward longwave radiation (dark grey) and in the residual term (white; see equation (2)). Dots indicate the computed net surface temperature anomalies (all components). Solid line indicates the model-mean of the simulated LULCC-induced monthly 2-m temperature anomalies.

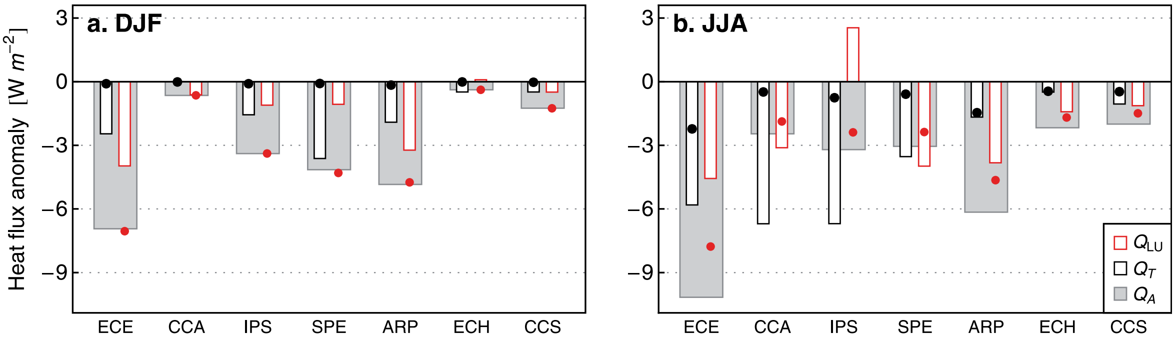

Figure 3. Seasonal LULCC-induced anomalies of available energy Q_A (gray bars), total turbulent energy flux Q_T (black edge bars) and upward longwave radiation Q_{LU} (red edge bars). Black and red dots indicate the anomalies of Q_T and Q_{LU} expected from the changes in Q_A (derived from equations (7) and (8)). ECE, CCA, IPS, SPE, ARP, ECH and CCS are the GCM/LSMs acronyms for respectively ECEARTH/TESSEL, CCAM/CABLE, IPSL/ORCHIDEE, SPEEDY/LPJmL, ARPEGE/ISBA, ECHAM5/JSBACH and CCSM/CLM.

issue in the surface energy closure of CABLE and LPJmL, showing a lack of consistency between the surface temperature responses and the changes in the SEB components.

[29] In contrast to the impacts on radiative fluxes, the model-mean changes of sensible (Q_H) and latent (Q_{LE}) heat fluxes lead to a systematic warming (red and blue bars in Figure 2). The radiatively induced drop in T_S is therefore dampened by the warming effect due to the decrease in the ensemble of turbulent heat fluxes (Q_T). The Q_T anomalies are almost as large as those of Q_A during the summer (JJA) and, as shown below and discussed in N2012, they are much larger than one would expect from the surface radiation perturbations. Figure 3 highlights these changes in the breakdown of Q_A between Q_T and Q_{LU} during the winter (DJF) and summer (JJA), for each individual model in NAEA.

[30] When land-cover is set to its preindustrial conditions (i.e., the mean between the experiments *PI* and *PDv*; see Table 1) the partitioning of Q_A into Q_T and Q_{LU}, averaged over NAEA, is about 0.25 (Q_T/Q_A) and 0.75 (Q_{LU}/Q_A) in JJA, and 0.05 (Q_T/Q_A) and 0.95 (Q_{LU}/Q_A) in DJF (these ratios are quite similar from one model to another). If one assumes that those ratios do not change when land-cover changes, then the radiatively induced responses of Q_T and Q_{LU} can be estimated by:

$$\Delta_R Q_T = \left(\frac{Q_T}{Q_A}\right)_{pi} \Delta Q_A \tag{7}$$

$$\Delta_R Q_{LU} = \left(\frac{Q_{LU}}{Q_A}\right)_{pi} \Delta Q_A. \tag{8}$$

[31] These estimates, calculated for each model from equations (7) and (8), are shown in Figure 3 as black and red dots respectively. Most models show larger absolute changes in Q_T than expected by the perturbation to Q_A. Since the SEB must be maintained, these ‘extra’ (non radiatively induced) Q_T reductions are associated with weaker Q_{LU} responses (relative surface warming) than those expected from the Q_A anomaly. This effect is particularly strong in the IPSL/ORCHIDEE case, model that therefore displays warming instead of cooling in JJA. Our conclusion does not hold for CCAM/CABLE and SPEEDY/LPJmL in JJA because their net changes (sum) of Q_T and Q_{LU} are larger than those of Q_A (i.e., large Q_R changes compared to the other models).

[32] Thus, the LULCC-induced reduction in Q_A plays a fundamental role explaining the surface cooling observed in most models and all seasons in NAEA. However, the large decrease in Q_T, which can partially be attributed to the LULCC-induced decrease in Z_0, dampens this cooling. Quantitatively, the net effect of Q_T changes (averaged over all GCM/LSMs) leads to T_S responses that are about 50% and 30% smaller (warmer), in DJF and JJA respectively, than the values that would be expected from reductions in Q_{SN} and Q_{LD} alone (Table 4). This means that if surface albedo changes were to be the only perturbation following LULCC, the ensemble of LUCID models would simulate stronger cooling in T_S (by -0.7 K and -0.5 K in DJF and JJA respectively; $\Delta_R T_S$ in Table 4). The temperature dampening is true for most models, but the magnitude of this effect varies, as do the changes in Q_T. We hypothesize, in the following, that the main cause of this dispersion resides in differences in the LSMs’ parameterizations of Q_{LE} and Q_H.

4. Attribution of the LULCC-Induced Changes to Specific Sources

[33] N2012 concluded that there are two main reasons why the various models have responses of different magnitude and even of different sign for some variables (such as latent heat flux for examples). One comes from the differences in the land-cover forcing itself. The GCM/LSMs indeed followed different rules to include the changes in crop and pasture, and thus, the nature and magnitude of imposed deforestation by the individual models between preindustrial times and present-day were quite different (Table 5). The other one comes from how LULCC affects the partitioning of Q_T between Q_{LE} and Q_H for a specific time period in the various models. N2012 however did not come to the point of quantitatively attributing the dispersion

Table 5. Forest Area Change in NAEA (10^6 km^2) Between 1870 and 1992

GCM/LSM	Evergreen	Deciduous	Total
ECEARTH/TESSEL	−0.3	−2.9	−3.2 (−30%)
CCAM/CABLE	−1.7	−1.0	−2.7 (−26%)
IPSL/ORCHIDEE	−1.0	−1.3	−2.3 (−22%)
SPEEDY/LPJmL	−1.4	−0.9	−2.3 (−21%)
ARPEGE/ISBA	−1.7	−0.3	−2.0 (−20%)
ECHAM5/JSBACH	−0.7	−0.5	−1.2 (−11%)
CCSM/CLM	−0.6	−0.6	−1.2 (−11%)

between the various models to one or the other source, which is what we do in the following.

4.1. How Sensitive Are the Various LSMs to LULCC?

[34] For four variables that are simulated within LSMs (α, Q_{SN}, Q_{LE}, Q_T), we have calculated their LULCC-induced changes relative to the net changes in areal fractions of the herbaceous vegetation ΔF_H (the resulting change in the fraction of crops and grasses; $\Delta F_C + \Delta F_G$) for each GCM/LSM. Figure 4 displays the resulting anomalies of each variable within each model in both DJF and JJA. Since LSMs did not include significant changes in bare soil areas, these normalized changes represent an estimate of the models responses to a hypothetical total deforestation over NAEA.

[35] Although consistent in sign, the sensitivity of α to LULCC varies in magnitude among the various models (Figure 4a), especially during the winter (DJF). In this season, the model differences roughly follow the LULCC-induced albedo changes when large snow-cover conditions prevail (obtained from grid-cells showing monthly *SWE* values larger than 50 mm; indicated by crosses in Figure 4a). The albedo responses under snow are estimates of the snow-masking albedo effect. This effect is of about 0.35 when averaged over the models, in agreement with previous observational studies that compared the snow-covered surface albedos of mixed forest and herbaceous [e.g., *Jin et al.*, 2002; see also *Bonan*, 2008]. However, the individual values range between 0.27 and 0.48, revealing quite different albedo sensitivities to LULCC in snowy conditions. In addition, the differences between the simulated net α responses in DJF are larger than those obtained with large snow coverage, thereby showing that snow extent and depth at specific time periods vary significantly from one model to another, increasing the uncertainty in the responses to LULCC.

[36] The LULCC-induced albedo changes in JJA are weak compared to the DJF ones, but are likely to result in larger changes in net solar radiation at the surface due to larger incoming values, as highlighted by the normalized changes in Q_{SN} (Figure 4b). The magnitudes of Q_{SN} anomalies are generally well correlated with those of α, in spite of a few exceptions. ECHAM5/JSBACH, for instance, undergoes an increase in incoming shortwave radiation, resulting from a decrease in cloud cover (not shown), which offsets the α effect in DJF. Such behavior has already been reported for ECEARTH/TESSEL in the tropics [*van der Molen et al.*, 2011].

[37] Figure 4d clearly shows that Q_T simulated for example by IPSL/ORCHIDEE is particularly sensitive to deforestation in JJA, while the same flux simulated by ECHAM5/JSBACH is insensitive to the removal of forests. Further, those models show opposite Q_{LE} responses during the same

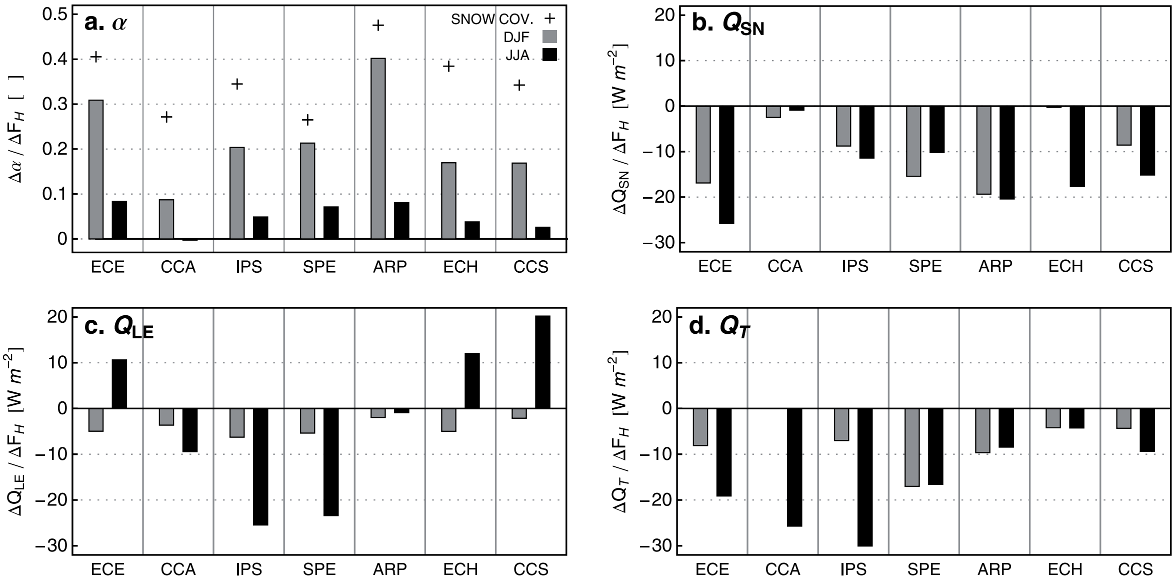

Figure 4. LULCC-induced changes in (a) surface albedo, (b) net shortwave radiation, (c) latent heat flux, and (d) total turbulent energy flux in NAEA. Anomalies normalized against the net changes in herbaceous fraction (crops + grasses/pasture, ΔF_H). Gray and black bars are for the Northern Hemisphere winter (DJF) and summer (JJA) respectively. Crosses in Figure 4a illustrate the normalized winter albedo anomalies calculated from grid-cells within NAEA showing large snow content (*SWE* > 50 mm). Model acronyms are the same as in Figure 3.

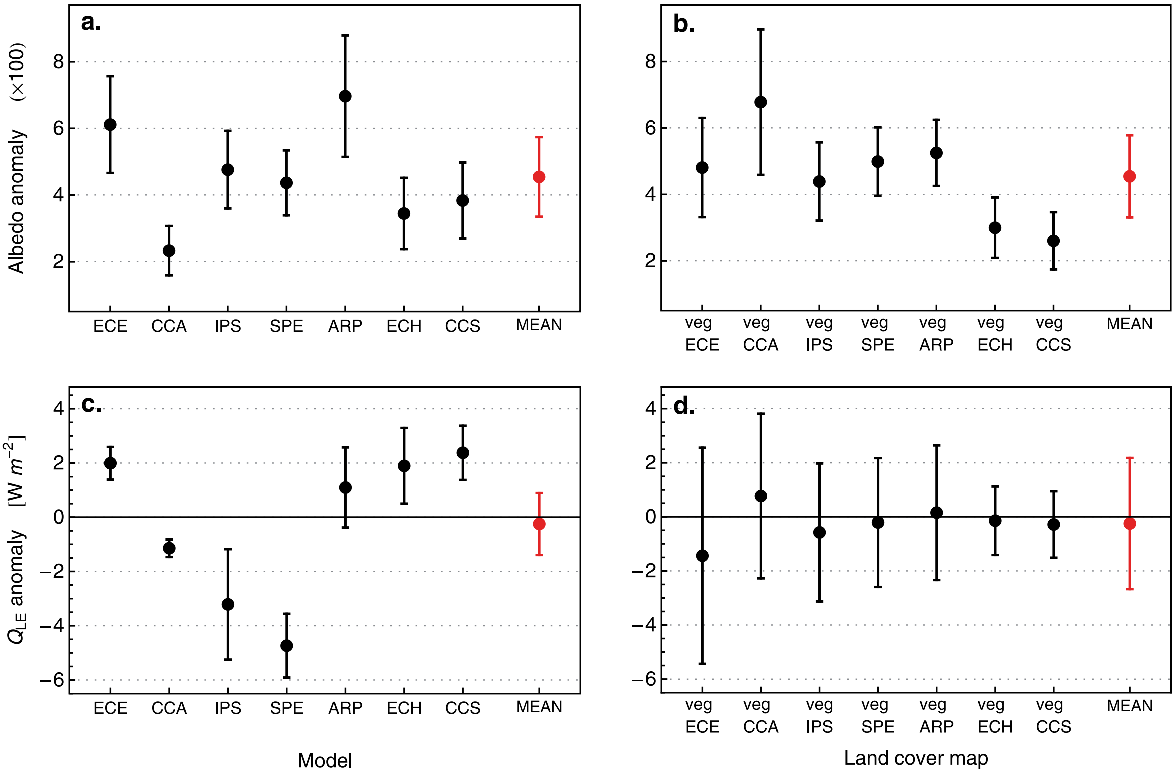

Figure 5. Reconstructed LULCC-induced changes in (a and b) surface albedo in DJF and (c and d) latent heat flux in JJA. Calculations are done for the seven LUCID GCM/LSMs and their specific land cover maps in NAEA. Figures 5a and 5c illustrate the mean response of each model and the ±1 mean deviation (MD) associated to various land-cover forcings. The length of each error bar therefore represents the sensitivity of each GCM/LSM to the various vegetation maps tested. Figures 5b and 5d show mean response associated to each land-cover map and the spread resulting from the choice of GCM/LSM. Veg'MOD' stands for the land-cover map of the specific model. Model acronyms are the same as Figure 3.

season (Figure 4c). It is also clear that one model may have a relatively (to other models) strong response in one variable (e.g., IPSL/ORCHIDEE for Q_{LE} or Q_T) and a relatively weak response in another one (same model for Q_{SN}). Quantifying the robust impacts of LULCC on climate from our simulations is therefore complicated by the wide range of sensitivities the LSMs display to LULCC. As noted by N2012, this highlights the need to evaluate LSMs by examining how they respond to a perturbation in addition to how they simulate an average state.

[38] Figure 4d therefore shows large differences between the models in ΔQ_T as a function of ΔF_H for individual seasons, while N2012 tended to conclude, from their Figure 12, that ΔQ_T was rather proportional to the magnitude of deforestation. This may be true at the annual timescale but is certainly wrong at the seasonal one. LSMs therefore also diverge in estimating how Q_T responds to LULCC, and not only in the way they partition Q_T and its changes between Q_{LE} and Q_H, as N2012 tended to conclude.

4.2. Relative Contributions of Land Cover Map and Model Sensitivity to the Inter-model Variability

[39] We used a multivariate regression analysis (section 2) to attribute the dispersion between the individual models' response to LULCC either to (a) the differences in land-cover changes since preindustrial times or to (b) the parameterizations included in the individual models that lead to different sensitivities to land cover perturbations. For the three variables assessed in this analysis (α, Q_{LE} and Q_T), the regression models allow an evaluation of parameterization differences between the various GCM/LSMs (represented by the regression coefficients) and of differences in land cover forcing. For each GCM/LSM we reconstructed the responses to LULCC in NAEA, and each model was forced with each of the seven alternative land-cover maps. The set of 7 (models) by 7 (land-cover patterns) reconstructions were evaluated with a common (model-mean) perturbation of the environmental drivers (snow content, precipitation and net shortwave radiation; see Table 2) to avoid including potential differences that would result from ranges in the climate forcing itself. In order to minimize the effect of outliers, we use the simple mean deviation (MD) statistic (i.e., the average of the absolute deviations of series elements from the series mean) as a spread measure instead of the more typical standard deviation.

[40] Figure 5 shows the reconstructed responses to LULCC for two sensitive cases: α in DJF and Q_{LE} in JJA. The LULCC-induced anomalies are illustrated in two ways (Figures 5a

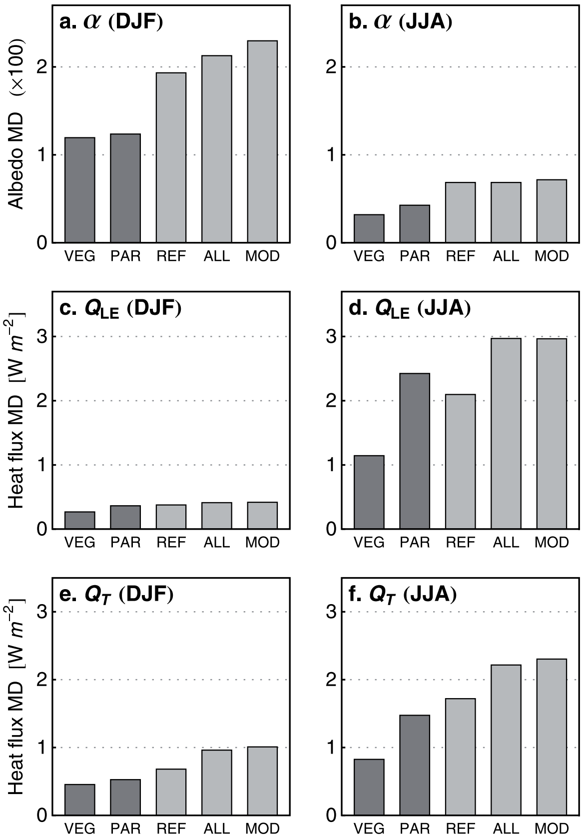

Figure 6. Inter-model mean deviation (MD) of the computed seasonal LULCC-induced anomalies (GCMs-based statistical reconstructions) of (a and b) surface albedo, (c and d) latent heat, and (e and f) total turbulent heat flux in NAEA. Bars VEG and PAR illustrate the estimated inter-model spread induced by respectively the different land-cover forcings and the different land-surface parameterizations (see Figure 5). REF indicates the MDs accounting simultaneously for VEG and PAR. Reconstructions VEG, PAR and REF are forced by common (model-mean) changes in the environmental predictors (see text). ALL indicates the MDs resulting from the fully reconstructed responses (accounts simultaneously for VEG and PAR and the individual model changes in environmental predictors). Differences between REF and ALL result therefore from the LULCC-induced environmental changes in each GCM/LSM. MOD illustrates the MDs between the responses simulated by the GCM/LSMs.

and 5c on one hand, and Figures 5b and 5d on the other). Figures 5a and 5c show the average responses of α and Q_{LE} reconstructed for each GCM/LSM and their associated variation (±1 MD) resulting from various land-cover forcing–derived responses. To construct these figures, each statistical model derived for a given GCM/LSM has been driven by the land-cover forcing of all individual GCM/LSMs. Thus, the error bar length (2 MD) is an estimate of how different the albedo (or the latent heat flux) anomaly would be had a given GCM/LSM used the land-cover forcing from another GCM/LSM.

[41] In turn, Figures 5b and 5d show the mean α and Q_{LE} responses reconstructed for each of the imposed LULCC maps and their resulting dispersion associated to the various model–derived results. The error bar length indicate in this case an estimate of how different the individual LSMs respond to the same land-cover forcing (e.g., vegECE refers to the reconstructed responses of all models to the land-cover forcing of ECEARTH/TESSEL). In all figures, the final value (labeled as MEAN) indicates the mean of the means (the resulting model-mean response of the concerned variable) and the corresponding error bar is the mean of the MDs (i.e., in Figures 5a and 5c, this represents the mean spread induced by the different land-cover maps). These averaged MDs have been re-plotted in Figure 6 and labeled as VEG to illustrate the multi-model spread component related to the various land-cover forcings (as those shown in Figures 5a and 5c), and labeled PAR to represent the mean spread resulting from the various LSMs parameterizations (as those shown in Figures 5b and 5d).

[42] The reconstructed anomalies of α and Q_{LE} highlight the different sensitivities to LULCC shown by the LUCID GCM/LSMs (Figures 5a and 5c) and agree with the results shown in Figure 4. Particularly, in the Q_{LE} case, the mean values reproduce the inherent responses to LULCC of each model (e.g., clearly negative in the case of IPSL/ORCHIDEE and SPEEDY/LPJmL, or positive in the case of ECEARTH/TESSEL and CCSM/CLM; dots in Figure 5c). Further, the MD values show that some models are fairly insensitive in their Q_{LE} responses to the differences between the imposed LULCC (ECEARTH/TESSEL, CCAM/CABLE and CCSM/CLM), while others show quite different amplitudes (IPSL/ORCHIDEE). For some models such as CCSM/CLM for example, the positive "mean" Q_{LE} response can be traced back to the way the CLM LSM calculates latent heat flux and more specifically the contribution, to total evapotranspiration, of soil evaporation, canopy interception and transpiration. *Lawrence and Chase* [2009] have qualified this evapotranspiration partitioning in this version of CLM as "inconsistent", and have concluded that changing this partitioning may have significant consequences on climate modeling experiments investigating the influence of LULCC.

[43] In Figures 5b and 5d, the land-cover forcing in the x-axis is sorted by decreasing amount of deforestation (from that prescribed in ECEARTH/TESSEL (vegECE) to that of CCSM/CLM (vegCCS); see Table 5). As expected, the mean responses and the associated spread are quite small when LULCC is small (i.e., all the models show weak responses when evaluated with the land cover of ECHAM5/JSBACH and CCSM/CLM), and increase with the magnitude of deforestation. One clear exception can be seen for α in DJF (Figure 5b): the larger response occurs when the models are forced with land cover maps of CCAM/CABLE (vegCCA) rather than those of ECEARTH/TESSEL (vegECE). This results from the type of forest that has been removed at the expense of crops and pasture. Deciduous forests are mainly decreased in TESSEL while in CABLE the largest decrease is in evergreen trees (Table 5), thereby inducing a larger change in snow-masking effect during the winter.

[44] The MD between the various model responses of α and averaged over the seven land cover patterns (MEAN error bar in Figure 5b) are almost identical to the averaged MD that

measures the spread between the various land-cover forcings (MEAN error bar in Figure 5a), showing that both the land cover forcing strength and the model sensitivity to LULCC play a similar role in explaining the final inter-model spread in the winter albedo responses. In contrast, for the summer Q_{LE} case, the mean spread related to the inherent responses of the models (MEAN error bar in Figure 5d) is clearly larger than the one related to the different LULCC forcing (Figure 5c), indicating a stronger role of the model's parameterizations in the resulting net inter-model spread.

[45] The averaged MDs illustrated in Figure 5 and those related to the other variables assessed (α, Q_{LE} and Q_T, in DJF and JJA) are summarized in Figure 6. As indicated above, VEG bars represent the contribution to the dispersion among the various models' responses to LULCC of the different magnitudes of LULCC, while PAR illustrates the contribution of the various model parameterizations. As a reference for these two quantities, the resulting MD between the individual model responses reconstructed with their corresponding land-cover forcings, but using a common perturbation in the environmental predictors (same as used in VEG and PAR reconstructions), is also illustrated in Figure 6 (labeled as REF). Further, values indicated as ALL and MOD in Figure 6 show the inter-model MDs of the fully reconstructed responses (including the individual environmental drivers) and of the simulated responses (from the GCM/LSMs), respectively.

[46] As already stated, for α in DJF or Q_{LE} in JJA, the LSM parameterizations play a role as important as the LULCC strength in explaining the differences between the model responses to LULCC. In general, the MD associated to the various land-surface forcings (VEG) is of the same order of magnitude, but often lower than PAR, particularly for the summer (JJA) responses of Q_{LE} and Q_T (Figure 6). While VEG and PAR are not identical, accounting for both simultaneously (REF bars) explains more than 75% of the MD resulting from the fully reconstructed responses (ALL) or the simulated responses (MOD). In the case of α and Q_T, both VEG and PAR generate less dispersion than REF in DJF and JJA, showing that those two sources of dispersion are additive, increasing the final spread. For the JJA Q_{LE} case, there is some compensatory effect and the spread induced by PAR is slightly greater than that obtained in REF. The differences between REF and ALL result from the LULCC-induced atmospheric changes in each GCM/LSM; i.e., atmospheric feedbacks amplify the Q_{LE} responses to LULCC, increasing the resulting inter-model spread (see section 4.3).

4.3. Attribution of LULCC Responses to Various Drivers

[47] Given that more than 50% of the inter-model dispersion in the responses of α, Q_{LE} and Q_T is explained by the different GCM/LSM sensitivities to LULCC, we have used our statistical models to evaluate the nature of the model responses and to estimate the contribution of the various drivers assessed. For each GCM/LSM and each variable (α, Q_{LE} and Q_T) we have therefore calculated the LULCC-induced variation components of their different predictors (Figure 7). To highlight the inherent model differences, the reconstructed responses to LULCC were normalized with the corresponding change in F_H, as was done for Figure 4.

[48] Since the regression model of α explicitly separates the snow-free and the snow-covered albedos (see Appendix A), the changes of this variable can be attributed to both quantities. In all models, the LULCC-induced winter (DJF) α anomalies are clearly led by the changes in its snow-covered component, which represents the change in canopy snow-masking effect (Figure 7a). The latter can be induced by changes in vegetation the partitioning (F_v; dark grey bars in Figure 7a) and/or by changes in the *LAI* for a given vegetation type (light grey bars). The type of response varies across the models: IPSL/ORCHIDEE and SPEEDY/LPJmL respond only to perturbations in F_v, while the rest also show a contribution of *LAI* changes. Changes in the snow content (*SWE*) represent an indirect impact of LULCC that could result from a positive feedback between temperature, snowpack and α (i.e., snow-albedo feedback). The sign of simulated *SWE* changes are consistent with this, but do not represent a significant contribution to the overall α responses (indicated with white bars in Figure 7a), and is only noticeable in some models (e.g., ECEARTH/TESSEL). The snow-free–related α changes also play a secondary role during the winter (green bars). Although different in amplitude, the α responses in DJF of the various models are quite similar in their form and are dominated by snow and foliage projected cover. This confirms the conclusions of N2012 that the main processes behind the changes in α are coherent between models.

[49] The summer (JJA) α responses to LULCC are driven by differences in the snow-free optical properties of the various land cover types (F_v), and by changes in LAI (the contributions of both drivers are displayed together in Figures 7 and 8). CCAM/CABLE shows a negligible α anomaly in JJA because this version of the model does not distinguish leaf/stem albedos between PFTs. The other models show an averaged snow-free α response of about 0.05, in agreement with observed snow-free albedo differences between herbaceous and forest [*Jin et al.*, 2002], but – as for the snow covered case– with significant differences between the individual results (ranging from 0.025 to 0.08).

[50] The results are clearly less uniform in the Q_{LE} case in JJA (Figure 7d). First, all drivers play a significant role explaining the LULCC-induced changes of this variable. Second, the scale of explanation varies greatly between models in both magnitude and sign. The anomalies induced by perturbations in the vegetation partitioning (F_v) and *LAI* are mainly responsible for the model differences in the overall Q_{LE} responses. Although different in sign, the precipitation-induced Q_{LE} anomalies (the contribution of both drivers R and R- are shown together; blue bars in Figure 7d) show a similar contribution between the models when compared to the precipitation changes themselves (see Figure 8b). In addition, the LULCC-induced precipitation anomalies in JJA are closely proportional to the Q_{LE} ones when compared between the models (not shown). These patterns show that the impacts of LULCC on Q_{LE} and precipitation are not independent and, on the contrary, suggest a coupling and positive feedback between these variables of similar intensity between the models. This agrees with previous studies that identify a positive soil moisture-evapotranspiration feedback in the Northern Hemisphere temperate regions [*Koster et al.*, 2004; *Seneviratne et al.*,

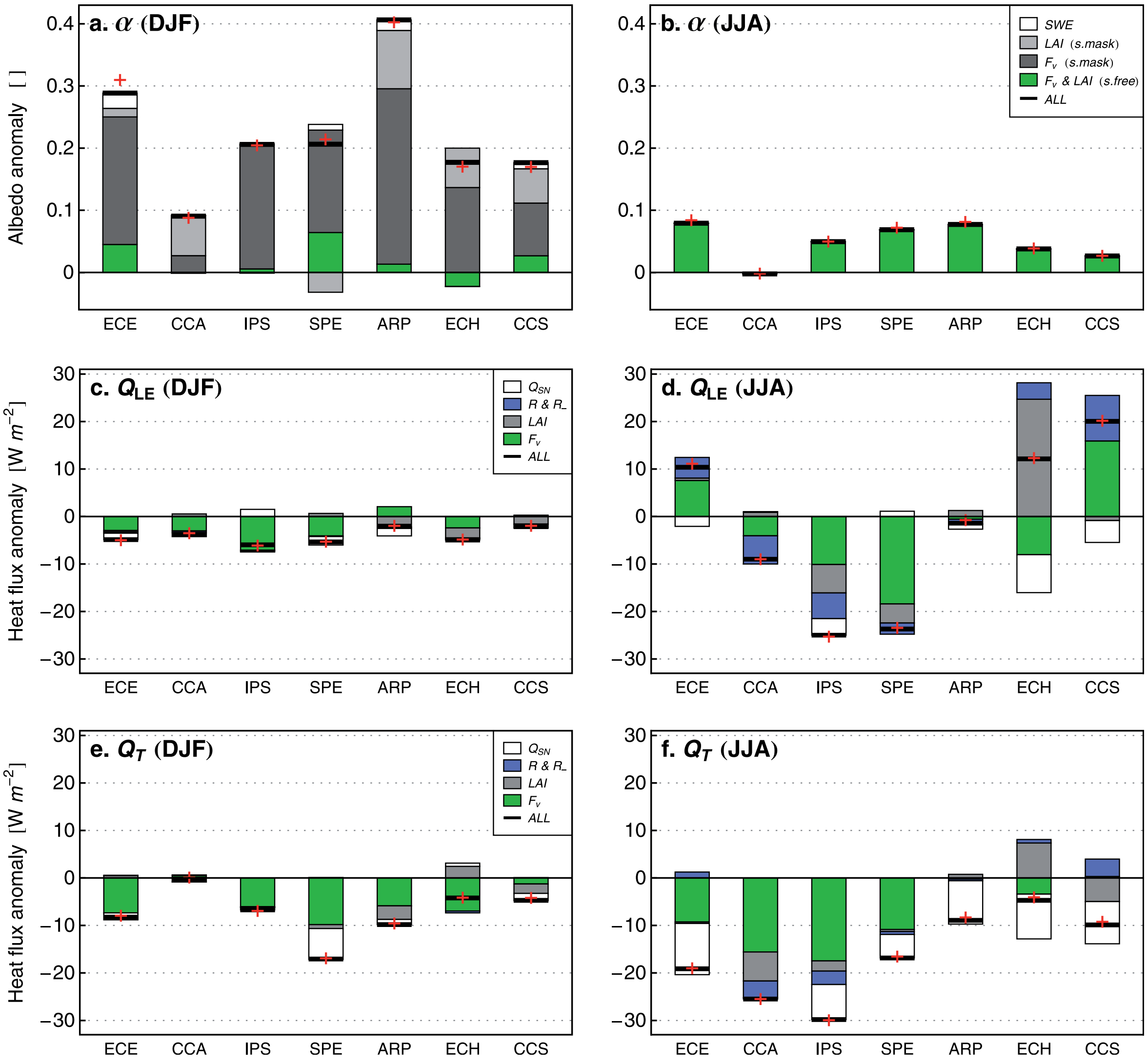

Figure 7. Reconstructed seasonal LULCC-induced anomalies of (a and b) surface albedo, (c and d) latent heat flux, and (e and f) total turbulent flux in NAEA. As for Figure 4, the anomalies are normalized with the corresponding change in herbaceous area (ΔF_H). Stacked bars illustrate the contribution from different drivers used in the corresponding multivariate analysis (Table 2). Red crosses indicate the LULCC-induced anomalies in the concerned variable simulated by the GCM/LSMs. Model acronyms are the same as Figure 3.

2010]. Except for SPEEDY/LPJmL, the Q_{LE} anomalies induced by shortwave radiation changes are also consistent between the models, with values approximately proportional to the Q_{SN} perturbations (white bars in Figure 7d).

[51] In the case of CCSM/CLM, the reconstructed Q_{LE} anomalies seem to underestimate the *LAI* effect against the contribution of F_v (this is not a surprise given the large spatial covariability between forest fraction and *LAI* in this model, Table 3). However, as already discussed in section 4.2, the contribution to total evapotranspiration of various soil-plant parts in this model is incorrect [*Lawrence and Chase*, 2009]. The JJA Q_{LE} response is largely explained by a significant increase of soil evaporation (resulting from both the decrease in canopy density and the increased amount of rainfall reaching the ground) largely counter-acting the drop in canopy interception and transpiration, and therefore reducing the sensitivity of Q_{LE} to LULCC. For other models such as ECHAM5/JSBACH, IPSL/ORCHIDEE and SPEEDY/LPJmL, *LAI* is an important driver in the Q_{LE} responses. As discussed in N2012, these three models are the only ones that do compute *LAI* on-line, as a function of biomass allocation. They show quite different seasonal *LAI* responses to LULCC resulting from their discrepancy in the way they parameterize the phenological cycle of crops compared to the other vegetation types. For example, the resulting LULCC-induced LAI anomaly in JJA is positive in

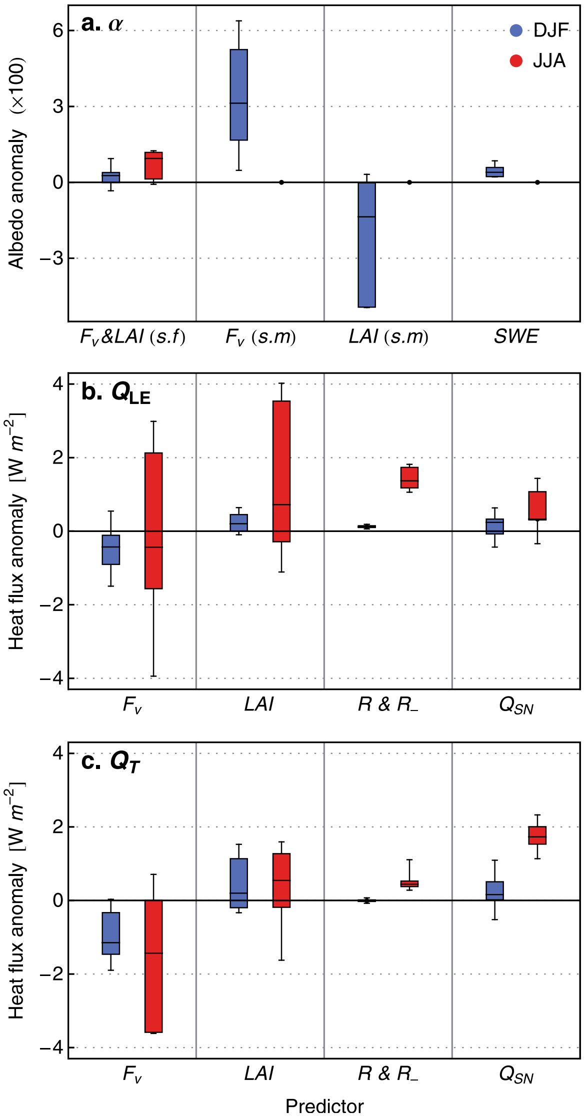

Figure 8. DJF (blue) and JJA (red) anomalies of (a) surface albedo, (b) latent heat flux, and (c) total turbulent flux in NAEA expected from changes in each of the corresponding predictors (see Table 2). The abbreviations s.f and s.m in Figure 8a indicate respectively the snow-free and the snow-covered components of the surface albedo calculations. All the LUCID GCMs-based statistical models were forced with a common set of perturbations (most of the used predictor's changes are positives; shown in Table 6). Box-whisker plots indicate the extremes, the inter-quartile and the median within the individual (GCMs-based) results.

the case of ECHAM5/JSBACH and negative in the cases of IPSL/ORCHIDEE and SPEEDY/LPJmL (not shown).

[52] The LULCC-induced Q_T anomalies are dominated by the changes in F_v and Q_{SN} for five out of seven models (Figures 7e and 7f). Exceptions are ECHAM/JSBACH and CCSM/CLM that are more sensitive to *LAI* changes than to F_v changes, especially during summer time. As for Q_{LE}, the JJA Q_T anomalies driven by Q_{SN} are proportional to the Q_{SN} perturbations themselves, and are coherent with the expected radiative impacts of LULCC in Q_T (Figure 3). The Q_T anomalies induced by precipitation in JJA, although quite small, show a similar pattern with those obtained in the Q_{LE} analysis, suggesting a positive impact of Q_{LE} on Q_T in all models (i.e., more/less rainfall leads to more/less Q_{LE} and thereby more/less Q_T). In most models, the non-radiative drivers (i.e. *LAI* and F_v) cause negative Q_T anomalies, confirming our discussion in section 3. Part of the negative contribution that changes the land-surface partitioning (F_v) exerts on the DJF and JJA Q_T responses can probably be attributed to decreases in surface roughness (Z_0), as discussed in *Davin and de Noblet-Ducoudré* [2010].

5. Discussion and Conclusions

[53] This paper extends the study of *Pitman et al.* [2009] and *de Noblet-Ducoudré et al.* [2012] that investigated the robust responses of the surface climate to the land-use induced land-cover change (LULCC) since pre-industrial times, using a coordinated set of experiments carried out by seven GCM/LSMs. Apart from reassessing some previous findings, we have quite thoroughly explained why the models show different responses to LULCC in the Northern Hemisphere temperate regions, and quantified the contribution of various drivers to the simulated inter-model spread.

[54] LUCID models simulate systematic decreases in net solar radiation in all seasons, mainly produced by an increase in the snow-free surface albedo and a reduction in the snow-masking albedo effect during winter. We show that the expected radiatively induced cooling is significantly dampened (and sometimes offset) by a decrease in the total turbulent energy flux, which is mainly driven by changes in land-cover properties other than canopy albedo (e.g., surface roughness). Although all the models show consistent signs for both radiative and non-radiative impacts on surface temperatures (respectively cooling and warming), their magnitude varies significantly, resulting in quite different net changes in surface temperature.

[55] One cause of discrepancy in the models' responses to LULCC results from the way individual LSMs have implemented land-use changes in their own land-cover map. For example, the resulting differences in biogeography explain about one third of the inter-model dispersion in the summer latent heat flux responses, and about one half in the winter albedo ones. This is quite significant compared to the contribution of the inherent model sensitivities to LULCC. Our quantification confirms the hypothesis set forward by *Pitman et al.* [2009] and *de Noblet-Ducoudré et al.* [2012]: they argue that reducing the inter-model spread in its responses to LULCC will imply that modelers do agree on common maps or, *a minima*, on methodologies to implement land-use changes. This could not be done before the coordinated set of CMIP5 experiments and, therefore, models may diverge in their regional response to LULCC due to discrepancies in their land-cover maps.

[56] One important conclusion of this study lies in the major role that the models' sensitivity to land-cover perturbations plays in the resulting climate impacts of LULCC. Within the LUCID models, the dispersion resulting from the different land-surface parameterizations is either comparable

Table 6. Predictors' Changes in DJF and JJA Used in the Statistical Models (Table 2) to Evaluate the GCMs Sensitivities (Illustrated in Figure 8)[a]

Season	ΔF_c	ΔF_g	ΔF_e	ΔF_d	ΔLAI	ΔSWE (mm)	ΔR (mm)	ΔR_- (mm)	ΔQ_{SN} (W m^{-2})
DJF	0.26	−0.06	−0.10	−0.10	0.30	1.54	3.4	4.8	2.6
JJA	0.26	−0.06	−0.10	−0.10	0.33	0.0	7.9	5.0	3.7

[a] The anomalies correspond to the mean (inter-model) of the absolute LULCC-induced changes in NAEA, except for those used for the land cover fractions F_v (F_c, F_g, F_e, F_d), which correspond to the simple means.

to (e.g., the surface albedo case) or quite larger than (e.g., in latent heat flux case) the one resulting from differences in the imposed land-cover (Figure 6). These different sensitivities that can be appreciated in Figures 4–7, are particularly explicit in Figure 8. This figure illustrates the surface albedo (α), latent heat flux (Q_{LE}) and total heat flux (Q_T) changes in NAEA, expected (reconstructed) in the various models, but induced by identical perturbations (most of them positives). Apart from the change in the land cover partitioning (F_v) that was set to the model-mean LULCC (i.e., deforestation), those perturbations are the model-mean of the absolute changes (in the corresponding drivers) induced by LULCC (see Table 6). Figure 8 therefore highlights the models' consistencies and divergences resulting from their different land-surface parameterizations and land-atmosphere coupling intensities. For instance, the LUCID models clearly agree in the magnitude of the summer Q_T and Q_{LE} increases, in responses to increases in respectively net solar radiation (Q_{SN}) and precipitation (R and R_-). Most models also show consistent signs in their α responses to LAI and F_v changes, or in their Q_T responses to F_v. In these cases, however, the models exhibit quite different amplitudes in their responses. It is also clear how different the model Q_{LE} responses to a common change in F_v and in LAI are during the summer, drivers that are therefore behind the uncertainties in the simulated LULCC-induced anomalies of this flux.

[57] As discussed by *de Noblet-Ducoudré et al.* [2012], the differences displayed by the LUCID models highlight the need to improve benchmarking tools for LSMs evaluation. These tools need to evaluate the capacity of the LSMs to simulate the mean climate, but also assess how LSMs respond, for example, to a land-cover perturbation. LSMs evaluation needs to be undertaken in uncoupled (off-line) simulations, but also needs to extend to the examination of processes in land-atmosphere coupled runs that capture the feedbacks between the land and atmosphere and account for differences in the coupling strength between these components [e.g., *Koster et al.*, 2004].

[58] Changes in the surface albedo, latent heat and total turbulent heat flux induced by LULCC were assessed through a multivariate statistical analysis. An important concern regarding the used method, as well as with all other techniques that measure covariability between data, is that these do not ensure causality between explanatory variables and predictands. Our assumption is that the selected predictors (land-cover types, leaf area index, snow content, precipitation and solar radiation) very likely explain the bulk of the spatial and temporal variability of the assessed variables, and are the main contributors to the LULCC-induced impacts on these variables. Taking into account this concern, the partial contribution of each predictor (as is shown in Figures 7 and 8) should be interpreted carefully, since it could be underestimated or overestimated depending on the co-linearity with another predictor (e.g., land-cover fractions and LAI) or with another important driver not considered here (e.g., wind speed). Nevertheless, the purpose of this analysis is to estimate and compare (model-by-model) the sensitiveness of the assessed predictands to perturbations in the corresponding drivers in a common framework, rather than to measure the exact contribution of each of these drivers (for which other ad-hoc simulations would be needed).

Appendix A: Multivariate Regression Analysis

A1. Regression Models

[59] As introduced in section 2 and presented in section 4, a multivariate statistical analysis was performed to mimic the LULCC-induced anomalies shown by the LUCID models in the NAEA in three variables: surface albedo (α), latent heat flux (Q_{LE}) and total turbulent energy flux (Q_T). Seasonal anomalies of these variables were regressed upon a selected number of drivers, including the land cover partitioning (represented by the surface area fraction of five land-cover types) within NAEA (Table 2). The regression models follow equation (5). The climatological means ($\overline{Y_v}$) and the anomalies (Y'_v) are estimated as first and second order polynomial expansions over the various predictors included in $\mathbf{P}$. That is,

$$\overline{Y_v}(\mathbf{P}) = a_v + \sum_{i=1}^{n} b_v^{(i)} \overline{P_i} \tag{A1}$$

$$Y'_v(\mathbf{P}) = \sum_{i=1}^{n} c_v^{(i)} P'_i + \sum_{i=1}^{n} \sum_{j=1}^{n} d_v^{(i,j)} \overline{P_i} P'_j \tag{A2}$$

where n is the $\mathbf{P}$ length. These two expressions define the sets of coefficients a_v, $b_v^{(i)}$ and $c_v^{(i)}$ and $d_v^{(i,j)}$ which are computed for each GCM/LSM using linear routines. The standard least squares method was used to minimize the difference between the expected predictands values and those simulated by the LUCID models. These parameters represent the partial derivatives of $\overline{Y_v}$ and Y'_v with respect to the various predictors. The mean states $\overline{P_i}$ were included as second-order predictors (the second term on the right-hand side of equation (A2)) to improve the effect of some non-linear dependencies of Y'_v.

[60] The analyses were performed for each season separately (only the winter and summer results are shown here) and, since most of the used drivers vary in time and space, the input data (predictors and predictands) were conformed by the multiannual seasonal values of all grid-cells within the NAEA region. In order to have a coherent domain and a good representation of the regional means, the GCM/LSM fields were previously interpolated to a common rectangular

Table A1. Coefficients of Determination (r^2) Between the Predicted and the Simulated Seasonal Anomalies of Surface Albedo (α), Latent Heat Flux (Q_{LE}) and Total Turbulent Heat Flux (Q_T)[a]

	α		Q_{LE}		Q_T	
GCM/LSM	DJF	JJA	DJF	JJA	DJF	JJA
ECEARTH/TESSEL	0.86 (0.99)	0.96 (1.00)	0.49 (0.77)	0.76 (0.90)	0.36 (0.54)	0.84 (0.94)
CCAM/CABLE	0.85 (0.91)	0.68 (0.98)	0.41 (0.65)	0.84 (0.90)	0.25 (0.17)	0.78 (0.92)
IPSL/ORCHIDEE	0.83 (0.96)	0.72 (0.99)	0.40 (0.57)	0.89 (0.94)	0.23 (0.45)	0.88 (0.98)
SPEEDY/LPJmL	0.78 (0.95)	0.87 (0.98)	0.50 (0.69)	0.80 (0.90)	0.73 (0.84)	0.84 (0.87)
ARPEGE/ISBA	0.88 (0.99)	0.92 (0.99)	0.39 (0.35)	0.71 (0.81)	0.22 (0.40)	0.83 (0.87)
ECHAM5/JSBACH	0.76 (0.92)	0.45 (0.97)	0.45 (0.51)	0.77 (0.85)	0.19 (0.33)	0.87 (0.88)
CCSM/CLM	0.86 (0.97)	0.68 (0.80)	0.37 (0.30)	0.78 (0.89)	0.18 (0.11)	0.87 (0.84)

[a] Values calculated with the entire data (i.e., r^2 measures the spatial and temporal covariability), and with the regional mean (averaged over NAEA) time series (in brackets).

2° × 2° latitude-longitude grid, and the regressions were computed using area-equivalent weighted values.

A2. Surface Albedo

[61] In the case of the surface albedo (α), the regression model was defined as a semi-empiric function in order to separate the albedo under snow (α_s) and the snow-free component (α_{sf}). The resulting net albedo of a grid-cell was therefore derived from the snow-covered area fraction of the cell, i.e.,

$$\alpha = (1 - f_s)\alpha_{sf} + f_s\alpha_s \tag{A3}$$

$$f_s = 1 - e^{-kSWE} \tag{A4}$$

The snow-cover fraction (f_s) was defined as an asymptotic function of the snow content (SWE). The convergence coefficient k is estimated for each model in a separated non-linear regression analysis.

[62] Keeping the first order terms when using perturbed forms of α_s, α_{sf} and f_s in equation (A3), we obtain the total albedo anomaly (α') used in the analysis:

$$\alpha' = \left(1 - \overline{f_s}\right)\alpha'_{sf} + \overline{f_s}\alpha'_s + f'_s\left(\overline{\alpha_s} - \overline{\alpha_{sf}}\right). \tag{A5}$$

[63] The first and second term in the right hand of equation (A5) represents the components of α' related to changes in the snow-free albedo and in the snow-covered albedo respectively, while the last term represents the contribution from a change in the snow-covered area. Equation (A5) was further generalized to each land-cover type and used to calculate the grid-mean values following equations (4) and (5). The land-cover type components of α_s and α_{sf} were therefore defined empirically as those of Q_{LE} and Q_T (equations (A1) and (A2)), using *LAI* as a single predictor.

A3. Regression Results

[64] We do not find significant autocorrelations within the interannual series of the variables assessed that could induce to misleading interpretation of the results. However, as pointed out in sections 2 and 5, the used explanatory variables are not statistically independent in some cases, mainly because the coherent spatial variability between them. One clear example of that occurs between the land cover fractions (F_V) and *LAI*. *LAI* was included in the analyses because the predictability of the statistical models is significantly enhanced, but for GCMs such CCSM (that show a strong correlation between forest fraction and *LAI*; Table 3), the particular contribution of this predictor to the expected responses is not reliable and must be taken in account together with the one of F_V.

[65] A synthesis of the regression analyses results is presented in Table A1 for DJF and JJA. The skill of the regression models are evaluated through the resulting coefficients of determination (r^2) between the predicted values of α', Q'_{LE} and Q'_T and the corresponding anomalies simulated by the GCM/LSMs. Two r^2 calculations are indicated in Table A1, computed respectively with the entire record of the concerned variable (i.e., accounting for the spatial and temporal covariability) and with the regional mean (NAEA) time series (shown in brackets).

[66] In the case of the surface albedo, the estimates fit comparatively well with the simulated values in both DJF and JJA, explaining about 80% of the α' variance. The reconstructed regional mean series of α' are better represented, with r^2 values greater than 0.9 in most cases and near 1.0 in several models. The predicted JJA series of Q'_{LE} and Q'_T also account for about 80% of the variance of the simulated values. In turn, the estimates of this two predictands are significantly worse in DJF, indicating that during the winter there are other significant drivers controlling the turbulent heat exchanges not considered in these analyses, notably wind speed.

[67] Besides the statistical model's skill to predict the analyzed variables, the utility of this method resides in the ability to represent the GCM/LSM responses to LULCC. The reconstructed seasonal responses of α, Q_{LE} and Q_T were calculated in NAEA from the predicted mean fields of each experiment (Table 1), and then evaluated using equation (1). As Figure 7 illustrates, the resulting anomalies in DJF and JJA fit closely those simulated by the GCM/LSMs in the three assessed variables, showing that the perturbations in the selected drivers explain the changes induced by LULCC.

[68] **Acknowledgments.** The authors are grateful to all LUCID participants for providing modeling data and supporting this research, as well as for to three anonymous reviewers for their constructive comments. We also acknowledge the inspiring discussions, input and collaboration between the participants of the LULCC initiative, IGBP 2nd Synthesis topic on 'Land-Use-induced Land-Cover Changes and the functioning of the Earth

System'. JPB thanks the grant support from the Chilean National Commission for Scientific and Technological Research (CONICYT). The computing time was provided by the Commissariat à l'Energie Atomique (CEA), France.

References

Abramowitz, G. (2005), Towards a benchmark for land surface models, *Geophys. Res. Lett.*, *32*, L22702, doi:10.1029/2005GL024419.

Abramowitz, G., R. Leuning, M. Clark, and A. Pitman (2008), Evaluating the performance of land surface models, *J. Clim.*, *21*, 5468–5481.

Baldocchi, D. D., C. A. Vogel, and B. Hall (1997), Seasonal variation of energy and water vapor exchange rates above and below a boreal jack pine forest canopy, *J. Geophys. Res.*, *102*(D24), 28,939–28,951.

Betts, R. A. (2001), Biogeophysical impacts of land use on present-day climate: Near surface temperature and radiative forcing, *Atmos. Sci. Lett.*, *1*, 39–51, doi:10.1006asle.2001.0023.

Betts, R. A., P. D. Falloon, K. Klein Goldewijk, and N. Ramankutty (2007), Biogeophysical effects of land use on climate: Model simulations of radiative forcing and large-scale temperature change, *Agric. For. Meteorol.*, *142*, 216–233.

Bonan, G. B. (2008), Forests and climate change: Forcings, feedbacks, and the climate benefits of forests, *Science*, *320*, 1444–1449, doi:10.1126/science.1155121.

Bondeau, A., et. al. (2007), Modelling the role of agriculture for the 20th century global terrestrial carbon balance, *Global Change Biol.*, *13*(3), 679–706.

Bounoua, L., R. DeFries, G. J. Collatz, P. Sellers, and H. Khan (2002), Effects of land cover conversion on surface climate, *Clim. Change*, *52*, 29–64.

Butt, N., P. A. de Oliveira, and M. H. Costa (2011), Evidence that deforestation affects the onset of the rainy season in Rondonia, Brazil, *J. Geophys. Res.*, *116*, D11120, doi:10.1029/2010JD015174.

Collins, W. D., et al. (2006), The Community Climate System Model Version 3 (CCSM3), *J. Clim.*, *19*, 2122–2143.

Davin, E. L., and N. de Noblet-Ducoudré (2010), Climatic impact of global-scale deforestation: Radiative versus non radiative processes, *J. Clim.*, *23*, 97–112.

Davin, E. L., N. de Noblet-Ducoudré, and P. Friedlingstein (2007), Impact of land cover change on surface climate: Relevance of the radiative forcing concept, *Geophys. Res. Lett.*, *34*, L13702, doi:10.1029/2007GL029678.

de Noblet-Ducoudré, N., et al. (2012), Determining robust impacts of Land-Use induced Land-Cover Changes on surface climate over North America and Eurasia: Results from the first of LUCID experiments, *J. Clim.*, *25*, 3261–3281.

Ellis, E. C., K. Klein Goldewijk, S. Siebert, D. Lightman, and N. Ramankutty (2010), Anthropogenic transformation of the biomes, 1700 to 2000, *Global Ecol. Biogeogr.*, *19*, 589–606, doi:10.1111/j.1466-8238.2010.00540.x.

Feddema, J., K. Oleson, G. Bonan, L. Mearns, L. E. Buja, G. A. Meehl, and W. M. Washington (2005a), The importance of land-cover change in simulating future climates, *Science*, *310*, 1674–1678.

Feddema, J., K. Oleson, G. Bonan, L. Mearns, W. Washington, G. Meehl, and D. Nychka (2005b), A comparison of a GCM response to historical anthropogenic land cover change and model sensitivity to uncertainty in present-day land cover representations,*Clim. Dyn.*, *25*, 581–609.

Forster, P., et al. (2007), Changes in atmospheric constituents and in radiative forcing, in *Climate Change 2007: The Physical Science Basis. Contribution of Working Group I to the Fourth Assessment Report of the Intergovernmental Panel on Climate Change*, edited by S. Solomon et al., pp. 129–234, Cambridge Univ. Press, Cambridge, U. K.

Georgescu, M., D. B. Lobell, and C. B. Field (2011), Direct climate effects of perennial bioenergy crops in the United States, *Proc. Natl. Acad. Sci. U. S. A.*, *108*, 4307–4312, doi:10.1073/pnas.1008779108.

Gero, A. F., A. J. Pitman, G. T. Narisma, C. Jacobson, and R. A. Pielke (2006), The impact of land cover change on storms in the Sydney Basin, *Global Planet. Change*, *54*, 57–78, doi:10.1016/j.gloplacha.2006.05.003.

Govindasamy, B., P. B. Duffy, and K. Caldeira (2001), Land use changes and Northern Hemisphere cooling, *Geophys. Res. Lett.*, *28*, 291–294.

Hansen, J. E., M. Sato, A. Lacis, R. Ruedy, I. Tegen, and E. Mathews (1998), Climate forcings in the Industrial era, *Proc. Natl. Acad. Sci. U. S. A.*, *95*, 12,753–12,758, doi:10.1073/pnas.95.22.12753.

Hurtt, G. C., S. Frolking, M. G. Fearon, B. Moore III, E. Shevliakova, S. Malyshev, S. W. Pacala, and R. A. Houghton (2006), The underpinnings of land-use history: Three centuries of global gridded land-use transitions, wood harvest activity, and resulting secondary lands, *Global Change Biol.*, *12*, 1208–1229.

Jin, Y., C. B. Schaaf, F. Gao, X. Li, A. H. Strahler, X. Zeng, and R. E. Dickinson (2002), How does snow impact the albedo of vegetated land surfaces as analyzed with MODIS data?, *Geophys. Res. Lett.*, *29*(10), 1374, doi:10.1029/2001GL014132.

Klein Goldewijk, K. (2001), Estimating global land use change over the past 300 years: The Hyde database, *Global Biogeochem. Cycles*, *15*(2), 417–433.

Klein Goldewijk, K., A. Beusen, G. van Drecht, and M. de Vos (2011), The HYDE 3.1 spatially explicit database of human-induced global land-use change over the past 12,000 years, *Global Ecol. Biogeogr.*, *20*, 73–86, doi:10.1111/j.1466-8238.2010.00587.x.

Koster, R. D., and P. C. D. Milly (1997), The interplay between transpiration and runoff formulations in land surface schemes used with atmospheric models, *J. Clim.*, *10*, 1578–1591, doi:10.1175/1520-0442(1997)010<1578:TIBTAR>2.0.CO;2.

Koster, R. D., et al. (2004), Regions of strong coupling between soil moisture and precipitation, *Science*, *305*, 1138–1140, doi:10.1126/science.1100217.

Krinner, G., N. Viovy, N. de Noblet-Ducoudré, J. Ogée, J. Polcher, P. Friedlingstein, P. Ciais, S. Sitch, and I. C. Prentice (2005), A dynamic global vegetation model for studies of the coupled atmosphere-biosphere system, *Global Biogeochem. Cycles*, *19*, GB1015, doi:10.1029/2003GB002199.

Lawrence, P. J., and T. N. Chase (2009), Climate impacts if making evapotranspiration in the Community Land Model (CLM3) consistent with the Simple Biosphere Model (SiB), *J. Hydrometeorol.*, *10*, 374–394.

Lawrence, P. J., and T. N. Chase (2010), Investigating the climate impacts of global land cover change in the community climate system model, *Int. J. Climatol.*, *30*, 2066–2087.

Loarie, S. R., D. B. Lobell, G. P. Asner, and C. B. Field (2011), Land-cover and surface water change drive large albedo increases in South America, *Earth Interact.*, *15*, Paper 7, doi:10.1175/2010EI342.1.

Lyons, T. J., P. Schwerdtfeger, J. M. Hacker, I. J. Foster, R. C. G. Smith, and X. M. Huang (1993), Land atmosphere interaction in a semiarid region—The bunny fence experiment, *Bull. Am. Meteorol. Soc.*, *74*, 1327–1334, doi:10.1175/1520-0477(1993)074<1327:LIIASR>2.0.CO;2.

Lyons, T. J., U. S. Nair, and I. J. Foster (2008), Clearing enhances dust devil formation, *J. Arid. Environ.*, *72*, 1918–1928, doi:10.1016/j.jaridenv.2008.05.009.

Mahmood, R., S. A. Foster, T. Keeling, K. G. Hubbard, C. Carlson, and R. Leeper (2006), Impacts of irrigation on 20th century temperature in the northern Great Plains, *Global Planet. Change*, *54*, 1–18.

Marshall, C. H., R. A. Pielke Sr., L. T. Steyaert, and D. A. Willard (2004), The impact of anthropogenic land-cover change on the Florida peninsula sea breezes and warm season sensible weather, *Mon. Weather Rev.*, *132*, 28–52, doi:10.1175/1520-0493(2004)132<0028:TIOALC>2.0.CO;2.

Marti, O., et al. (2010), Key features of the IPSL ocean atmosphere model and its sensitivity to atmospheric resolution, *Clim. Dyn.*, *34*, 1–26, doi:10.1007/s00382-009-0640-6.

Matthews, H. D., A. J. Weaver, M. Eby, and K. J. Meissner (2003), Radiative forcing of climate by historical land cover change, *Geophys. Res. Lett.*, *30*(2), 1055, doi:10.1029/2002GL016098.

McGregor, J. L., and M. R. Dix (2008), An updated description of the Conformal-Cubic Atmospheric Model, in *High Resolution Simulation of the Atmosphere and Ocean*, edited by K. Hamilton and W. Ohfuchi, pp. 51–76, Springer, New York.

Myhre, G., and A. Myhre (2003), Uncertainties in radiative forcing due to surface albedo changes caused by land-use changes, *J. Clim.*, *16*, 1511–1524.

National Research Council (2005), *Radiative Forcing of Climate Change: Expanding the Concept and Addressing Uncertainties*, 224 pp., Natl. Acad. Press, Washington, D. C.

Oleson, K. W., G. B. Bonan, S. Levis, and M. Vertenstein (2004), Effects of land use change on North American climate: Impact of surface datasets and model biogeophysics, *Clim. Dyn.*, *23*, 117–132, doi:10.1007/s00382-004-0426-9.

Oleson, K. W., et al. (2008), Improvements to the Community Land Model and their impact on the hydrological cycle, *J. Geophys. Res.*, *113*, G01021, doi:10.1029/2007JG000563.

Pielke, R. A., Sr., et al. (2011), Land use/land cover changes and climate: Modeling analysis and observational evidence, *WIREs Clim. Change*, *2*, 828–850, doi:10.1002/wcc.144.

Pitman, A. J., et al. (2009), Uncertainties in climate responses to past land cover change: First results from the LUCID intercomparison study, *Geophys. Res. Lett.*, *36*, L14814, doi:10.1029/2009GL039076.

Puma, M. J., and B. I. Cook (2010), Effects of irrigation on global climate during the 20th century, *J. Geophys. Res.*, *115*, D16120, doi:10.1029/2010JD014122.

Raddatz, T., C. H. Reick, W. Knorr, J. Kattge, E. Roeckner, R. Schnur, K.-G. Schnitzler, P. Wetzel, and J. Jungclaus (2007), Will the tropical land biosphere dominate the climate-carbon cycle feedback during the twenty-first century?, *Clim. Dyn.*, *29*, 565–574.

Ramankutty, N., and J. A. Foley (1999), Estimating historical changes in global land cover: Croplands from 1700 to 1992, *Global Biogeochem. Cycles*, *13*, 997–1027.

Rayner, N. A., D. E. Parker, E. B. Horton, C. K. Folland, L. V. Alexander, D. P. Rowell, E. C. Kent, and A. Kaplan (2003), Global analyses of sea surface temperature, sea ice, and night marine air temperature since the late nineteenth century, *J. Geophys. Res.*, *108*(D14), 4407, doi:10.1029/2002JD002670.

Roeckner, E., R. Brokopf, M. Esch, M. Giorgetta, S. Hagemann, L. Kornblueh, E. Manzini, U. Schlese, and U. Schulzweida (2006), Sensitivity of simulated climate to horizontal and vertical resolution in the ECHAM5 atmosphere model, *J. Clim.*, *19*, 3771–3791.

Salas-Mélia, D., F. Chauvin, M. Déqué, H. Douville, J. F. Guérémy, P. Marquet, S. Planton, J. F. Royer, and S. Tyteca (2005), Description and validation of the CNRM-CM3 global coupled climate model, *Note 103*, Cent. du Groupe de Météorol. de Grande Echelle et Clim., Toulouse, France. [Available at http://www.cnrm.meteo.fr/scenario2004/paper_cm3.pdf]

Seneviratne, S. I., R. D. Koster, Z. Guo, P. A. Dirmeyer, E. Kowalczyk, D. Lawrence, P. Liu, D. Mocko, K. W. Oleson, and D. Verseghy (2006), Soil moisture memory in AGCM simulations: Analysis of Global Land-Atmosphere Coupling Experiment (GLACE) data, *J. Hydrometeorol.*, *7*, 1090–1112.

Seneviratne, S. I., T. Corti, E. L. Davin, M. Hirschi, E. B. Jaeger, I. Lehner, B. Orlowsky, and A. J. Teuling (2010), Investigating soil moisture-climate interactions in a changing climate: A review, *Earth Sci. Rev.*, *99*(3–4), 125–161, doi:10.1016/j.earscirev.2010.02.004.

Snyder, P. K., C. Delire, and J. A. Foley (2004), Evaluating the influence of different vegetation biomes on the global climate, *Clim. Dyn.*, *23*(3–4), 279–302.

Strengers, B. J., C. Müller, M. Schaeffer, R. J. Haarsma, C. Severijns, D. Gerten, S. Schaphoff, R. van den Houdt, and R. Oostenrijk (2010), Assessing 20th century climate-vegetation feedbacks of land-use change and natural vegetation dynamics in a fully coupled vegetation-climate model, *Int. J. Climatol.*, *30*(13), 2055–2065, doi:10.1002/joc.2132.

Teuling, A. J., et al. (2010), Contrasting response of European forest and grassland energy exchange to heatwaves, *Nat. Geosci.*, *3*, 722–727, doi:10.1038/ngeo950.

van den Hurk, B. J. J. M., P. Viterbo, A. C. M. Beljaars, and A. K. Betts (2000), Offline validation of the ERA40 surface scheme, *Tech. Memo., 295*, Eur. Cent. for Med.-Range Weather Forecasts, Reading, U. K.

van der Molen M. K., B. J. J. M. van den Hurk, and W. Hazeleger (2011), A dampened land use change climate response towards the tropics, *Clim. Dyn.*, *37*, 2035–2043, doi:10.1007/s00382-011-1018-0.

Voldoire, A. (2006), Quantifying the impact of future land-use changes against increases in GHG concentrations, *Geophys. Res. Lett.*, *33*, L04701, doi:10.1029/2005GL024354.

2.5 Chapter summary and conclusions

This chapter describes the biogeophysical effect on the surface climate of land-use changes between the ends of the 19th and the 20th centuries, as a result of the multi-model set of global simulations carried within the LUCID project. Although a number of analyses are done globally, this study focuses on the climate responses to LULCC over areas of significant land cover changes in the temperate regions of the Northern Hemisphere.

The LUCID set of simulations show weak LULCC impacts at the global scale. Averaged over the region studied, including part of North America and Eurasia (~10.5 million km^2), the effects of LULCC are quite significant and, in most cases (model mean), dominated by negative near surface temperature anomalies along the year. This cooling is around −0.5 K, anomaly of the same order and opposite in sign than the one induced by changes in SST/SIC and [CO_2] (used as estimation of GHG-induced effects) between the same periods and in the same region. This result points out the necessity to take into account LULCC in climate change detection and attribution studies.

Direct impacts of LULCC

The analyses carried in this chapter try, on the one hand, to highlight those climate responses to LULCC that are shared by the different GCMs and, by the other, to understand the mechanisms that drive the model differences. With respect to the first point, the following robust signal of LULCC were found in the NH temperate regions:

1- All the LUCID GCM/LSMs simulate decreases in the available energy at the surface (Q_A), defined as the sum of net shortwave radiation (S_N) and downward longwave radiation (L_D). This radiative effect is present in all seasons and is principally directed by increases in surface albedo (α) and the associated reductions in S_N.

2- As a result of (1), almost all models exhibit significant near surface cooling during the NH winter.

3- All models simulate decreases in the total turbulent energy flux (Q_T) along the year. Q_T reductions are led by changes in the surface radiation budget and by direct perturbations in surface properties (e.g., decrease in surface roughness z_0).

4- In all models, the radiative-induced winter cooling is dampened by non-radiative effect. This dampening averages ~50% in winter and ~30% in summer.

Superimposed to these shared responses to LULCC, the models show significant difference between them. These differences are observed in the magnitude and, in some cases, in the sign of simulated LULCC-induced changes. The model dispersion of the summer change in latent heat flux (*LE*) reported by Pitman et al. (2009) is a key example of the latter. The model differences reside on two aspects:

1) the character of land-cover change prescribed in the various LSMs, and

2) the intrinsic model sensitivities to LULCC.

The role that these two factors play in the inter-model dispersion is quantified in Section 2.4.5 (Boisier et al., 2012) for changes in α, *LE* and Q_T. From these results, it should be noted that the model sensitivities explain about 75% of the inter-model dispersion in the summer *LE* responses to LULCC.

Coupling and feedbacks

Besides those expected impacts of LULCC directly induced by changes in land-surface properties (α, z_0, canopy conductance, root length, LAI, etc), a number of significant indirect effects resulting from the land-atmosphere coupling were also indentified.

Depending on the model and season, the changes in the incoming radiation (solar and infrared) could amplify or dampen the direct (α-induced) changes in Q_A. The following indirect radiative effects were found in NAEA:

1- During the northern winter (DJF), all the models show increases in the incoming (downward) shortwave radiation (S_D). As a result of this, the decrease in S_N are around 40% (model-mean) weaker in amplitude than that directly induced by changes in α. The LULCC-induced S_D anomalies are also significant in JJA, but not systematic among the models, amplifying or dampening the α effect in S_N. The mechanisms that could direct S_D changes were not explored in detail. No clear relation between ΔS_D and changes in cloud cover were found, although it was reported for one of the LUCID models (van der Molen et al., 2011).

2- Most models and seasons exhibit decrease in the incoming longwave radiation (L_D). In NAEA, the changes in L_D are responsible for 25% and 40% (model-mean) of the Q_A reductions in respectively DJF and JJA. These very likely represent the atmospheric feedback of the surface temperature changes.

Changes in precipitation represent another clear indirect impact of LULCC. In summer, precipitation anomalies explain a fraction of the simulated *LE* changes. In all the models, this fraction amplifies the LULCC signals of *LE* directly induced by surface perturbation. Further, precipitation anomalies follow the changes of *LE*, suggesting a positive feedback within these variables with similar amplitude between the models when averaged over the region studied (NAEA).

One of the main messages to be drawn from this chapter is that LSMs currently in use in GCMs need for a more thoroughly evaluation and intercomparison. If part of the differences in, e.g., their responses to LULCC, reflects the current uncertainties in the knowledge of land-surface processes, other part of the model dispersion could be narrowed through a more rigorous evaluation of LSMs.

A step forward could be a more systematic comparison of models outputs and observations at different spatial scales, from the site level to global-scale. The already long records of satellite-based observations could be used as benchmarks for large-scale comparisons. Large-scale data could also be used for models' assessments in the context of a specific subject, notably the impact of land-cover changes. This approach is explored in the chapter that follows for two key variables of the surface climate and the water cycle: the surface albedo and evapotranspiration.

Appendix 2.1: Individual model responses to LULCC

The following figures are included as a complementary material of this chapter. This includes maps of land-cover changes and seasonal (DJF and JJA only) responses to LULCC simulated by each LUCID GCM/LSM.

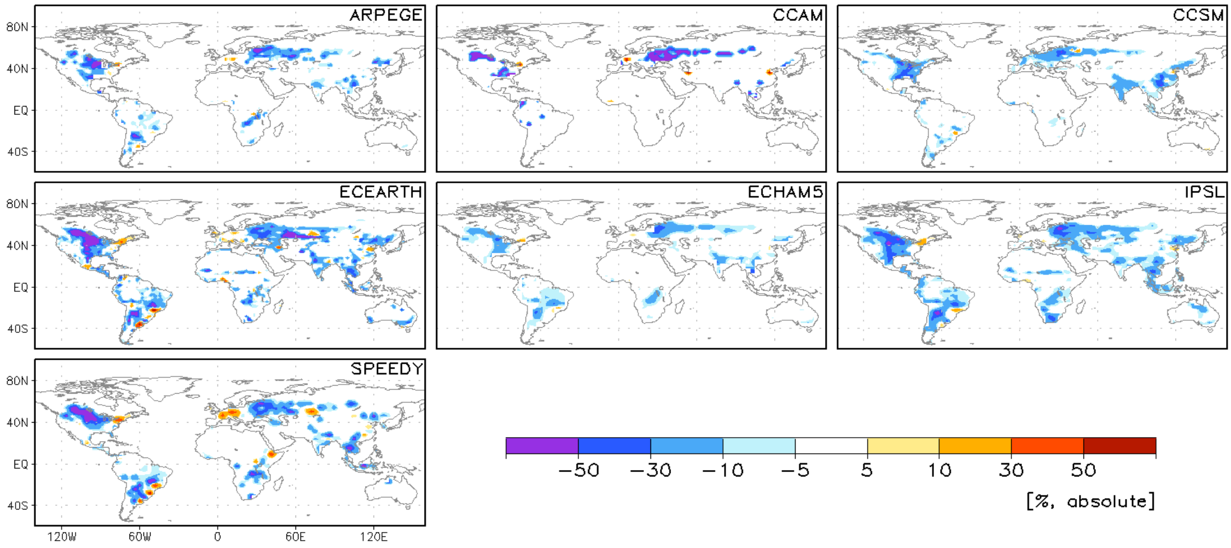

Figure A2.1
Difference in areal forest fraction prescribed in LUCID GCM/LSMs between 1870 and 1992.

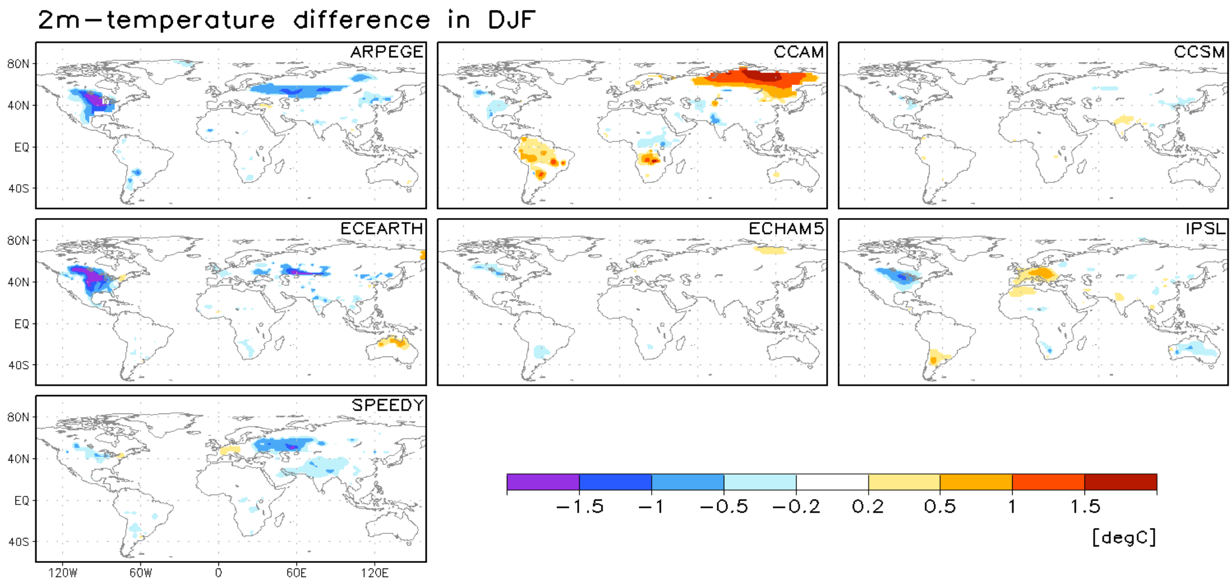

Figure A2.2
LULCC-induced 2-meter temperature anomalies in DJF. Only the changes significant different from zero are illustrated.

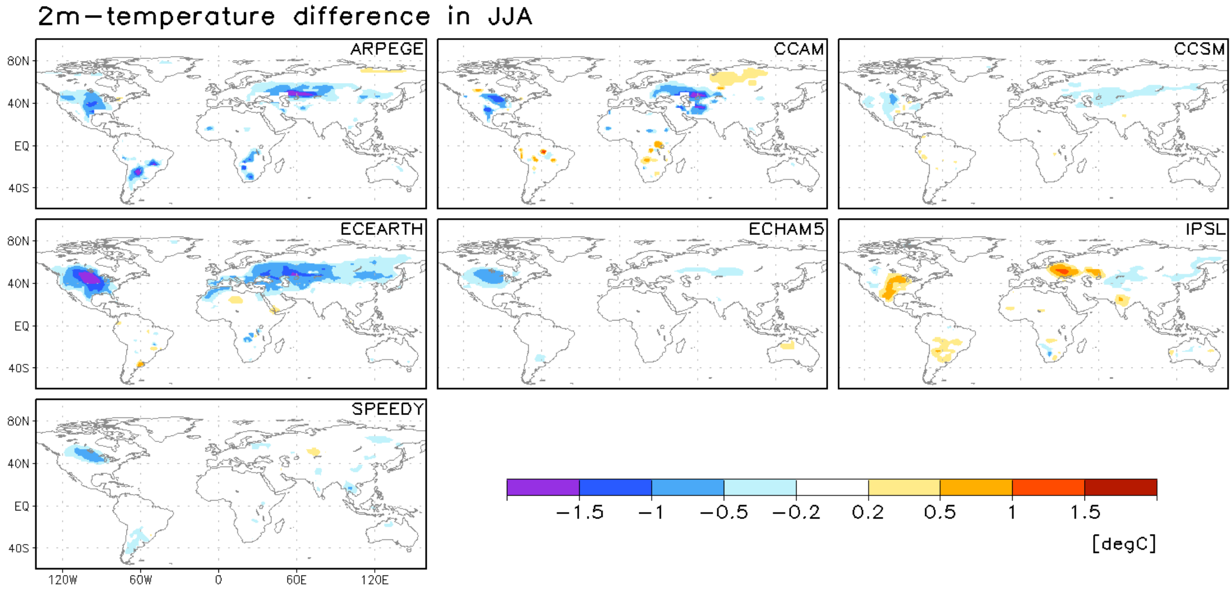

Figure A2.3
As in Figure A2.2, but for JJA.

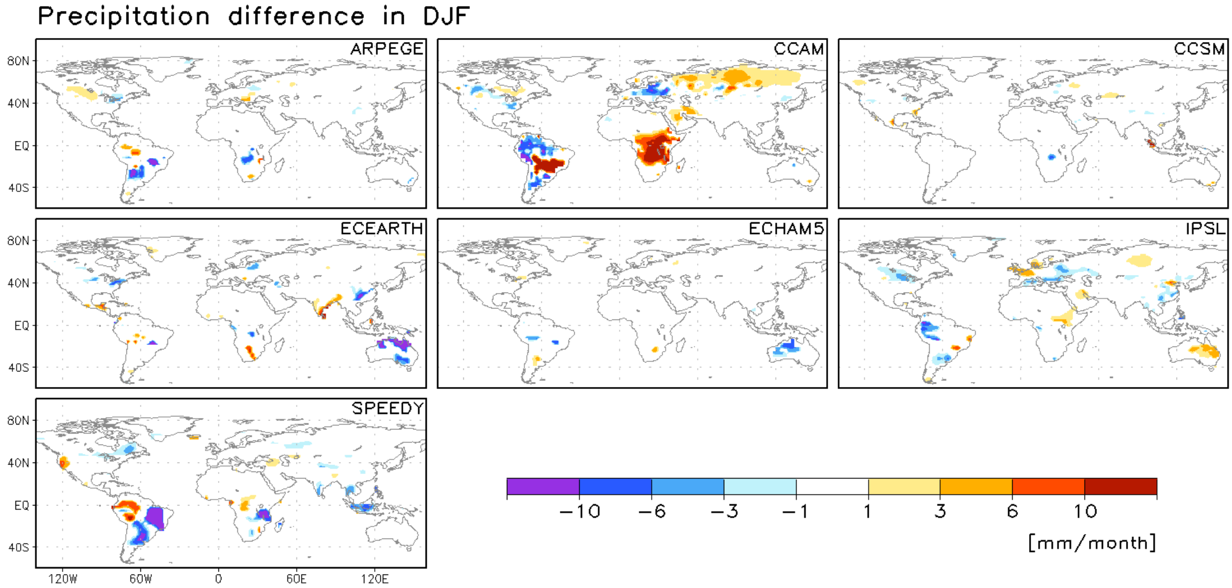

Figure A2.4
As in Figure A2.2, but for precipitation.

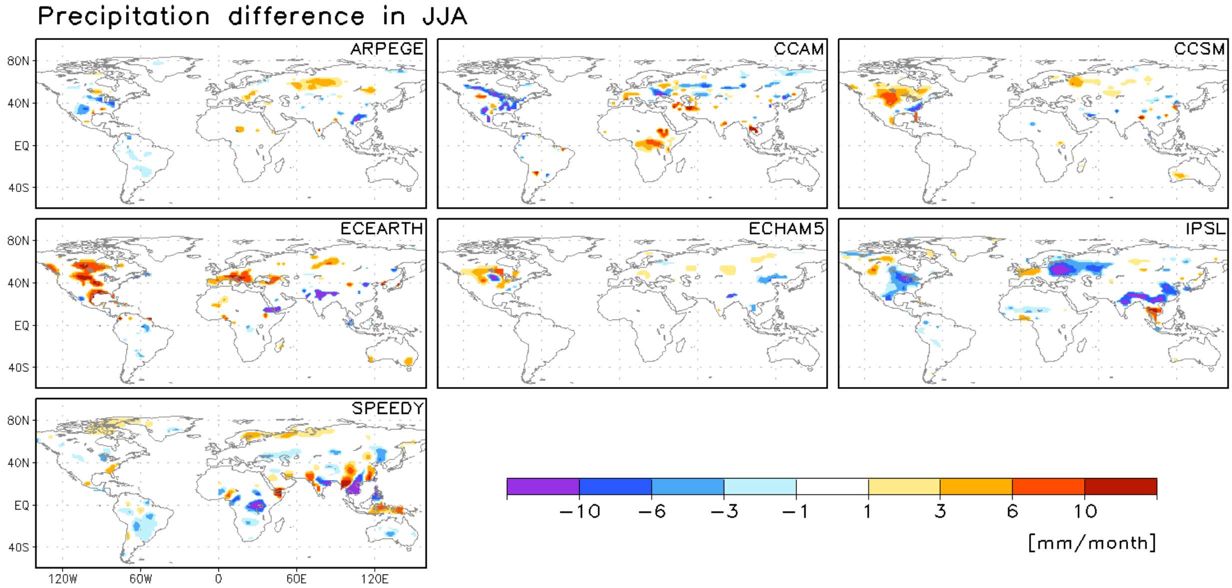

Figure A2.5
As in Figure A2.2, but for precipitation in JJA.

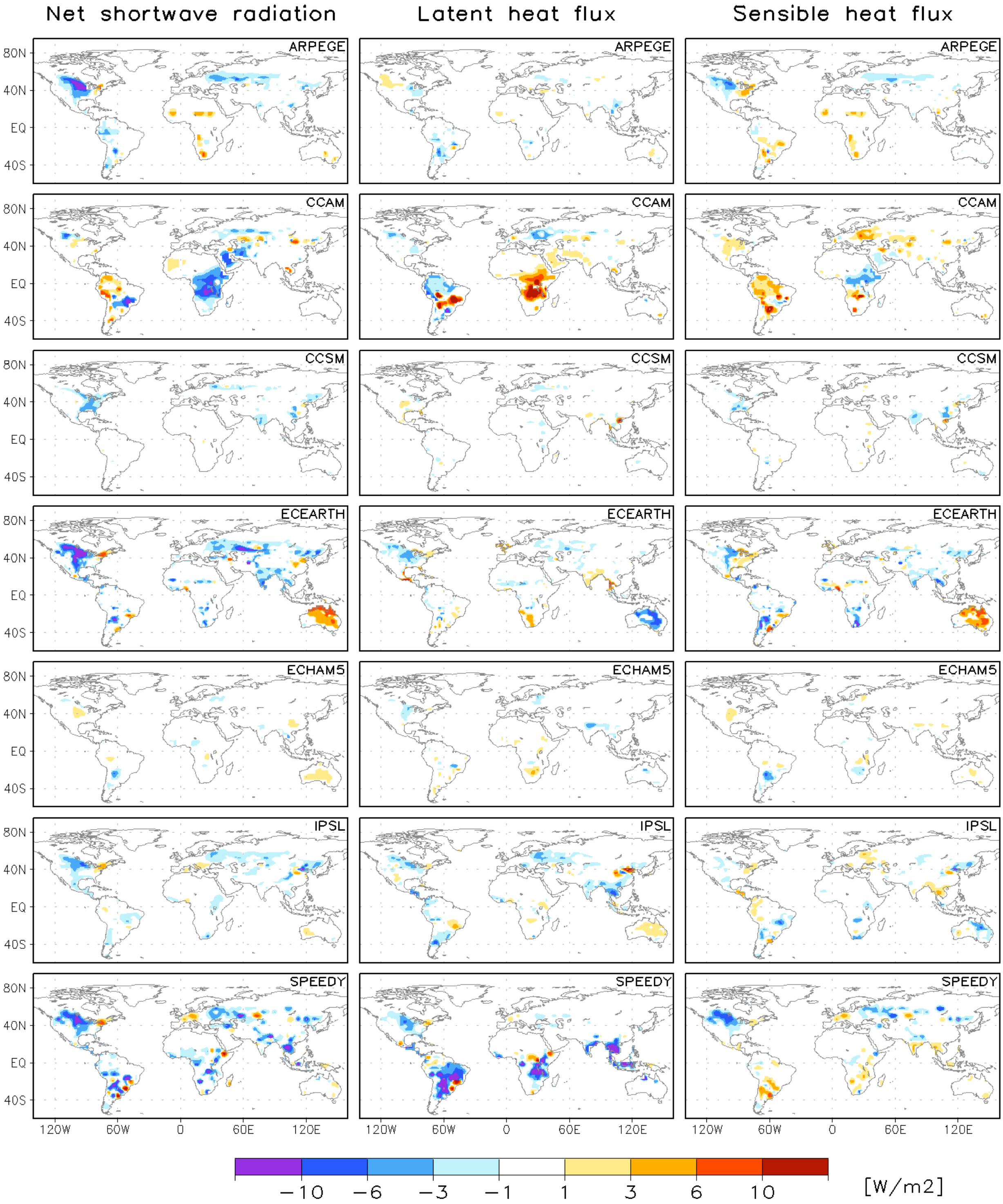

Figure A2.6
LULCC-induced changes in net shortwave radiation (left column), latent (center) and sensible (right) heat flux in DJF.

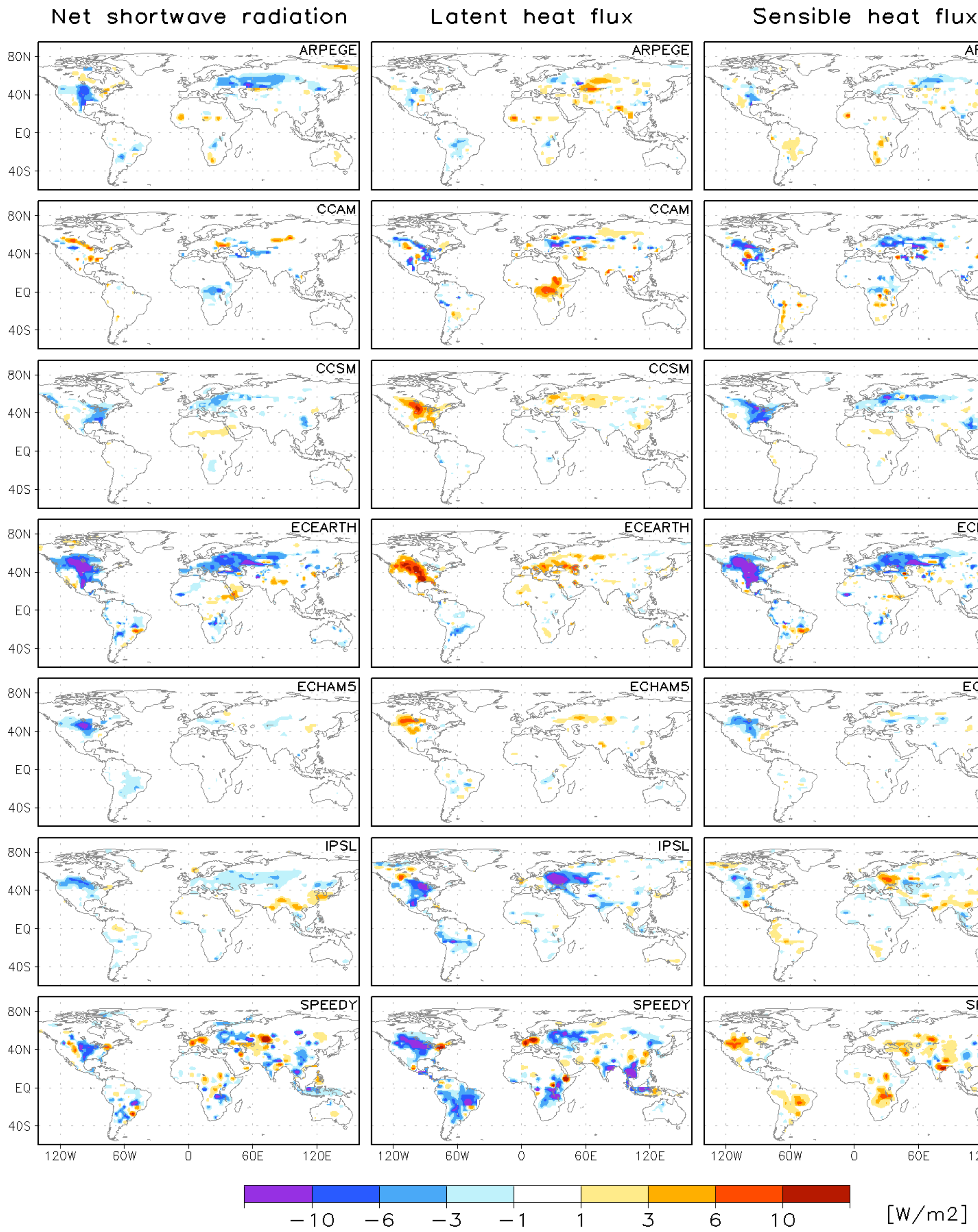

Figure A2.7
LULCC-induced changes in net shortwave radiation (left column), latent (center) and sensible (right) heat flux in JJA.

Chapter 3

Surface albedo and evapotranspiration changes due to past LULCC estimated from global observations

3.1 Chapter introduction

The biogeophysical impacts on climate of past changes in land-cover are assessed in Chapter 2 by means of global simulations in a model intercomparison framework. The results from LUCID show a number of common features within the model results but also show quite different responses to LULCC. These uncertainties have been attributed to both variations in the land-cover maps imposed in LSMs and intrinsic differences in GCM/LSMs (parameterization) that result in uneven sensitivities to land-cover conversions. Realistic estimates of the impacts of LULCC on climate, done independently from model simulations, stand as a major step forward to constrain these uncertainties.

Exploring the large-scale LULCC signatures on surface properties or in climate based on observations is not a simple task due to the lack of spatially coherent datasets of sufficiently long records. In addition, for variables such as near surface temperature or precipitation for which large datasets exist (e.g., those of the Climate Research Unit), it is not simple to distinguish the effects of the historical LULCC from those driven by other natural or anthropogenic climate forcings (e.g., the GHG-induced ones).

However, past LULCC-induced changes in surface variables should in part echo the observed present-day dependence of these variables to the spatial land-cover distribution. Hence, estimations of past changes in a given variable could be addressed combining large-scale observations, the current biogeography and historical scenarios of land-use changes. This is what the two studies presented in this chapter try to do.

In the first case, changes in surface albedo from 1870 to 1992 are estimated based on present-day satellite albedo retrievals (Section 3.2). As many studies (see Chapter 1) and LUCID simulations (Chapter 2) have shown, changes in this variable are of a major importance since they conduct the radiative impacts of LULCC. Looking at the goals of this chapter, surface albedo also appears as a logical variable to assess from observations since it is less dependent to environmental conditions than other quantities we are also interested in when assessing LULCC (e.g., temperatures, energy and water fluxes). Therefore, surface albedo can by forecasted (spatially or in time) in a simplest and robustly way based on limited land surface information compared to other surface quantities. In this case, the satellite-based albedo observations are projected to the past based only on land-cover and snow-cover data.

Section 3.3 presents a study that estimates the past LULCC-induce changes in evapotranspiration (ET). This variable is very important to the climate of the surface since it affects both the water cycle and the energy budget. Changes in ET also appear as one of the more uncertain impacts of LULCC based on modeling studies such as LUCID. In this case, estimations of ET changes are based on present-day global ET products constructed (statistically) with satellite data and surface observations. A multivariate statistical analysis was developed to extract the temporal and spatial ET variability in relation to land surface and environmental drivers; we use this information to reconstruct ET climatologies associated to a preindustrial land cover. Given that the ET products used as input data are estimation themselves, we assessed three of them following the same methodology for comparison and to give robustness to the results. We therefore evaluate the resulting ET sensitivity to land conversion that may be inferred from each of these products.

3.2 Inferring past land-use induced changes in surface albedo from satellite observations: A useful tool to evaluate model simulations

J. P. Boisier, N. de Noblet-Ducoudré and P. Ciais

(Paper in revision in *Biogeosciences*)

Abstract

Cooling resulting from increases in surface albedo has been identified in several studies as the main biogeophysical effect of past land-use induced land cover changes (LCC) on climate. However, the amplitude of this effect remains quite uncertain due to, among other factors, a) uncertainties in the magnitude of historical LCC and, b) differences in the way various models simulate surface albedo and more specifically its dependency on vegetation type and snow cover. We have derived monthly albedo climatologies for croplands and four other land-cover types from MODIS satellite observations. We have then estimated the changes in surface albedo since preindustrial times by combining these climatologies with the land-cover maps of 1870 and 1992 used by modelers in the context of the LUCID intercomparison project. These reconstructions show surface albedo increases larger than 10% (absolute) in winter and 2% in summer between 1870 and 1992 over areas that have experienced intense deforestation in the northern temperate regions. The MODIS-based reconstructions of historical changes in surface albedo were then compared to those simulated by the various models participating to LUCID. The inter-model mean albedo response to LCC shows a similar spatial and seasonal pattern to the one resulting from the reconstructions, that is larger increases in winter than in summer driven by the presence of snow. However, individual models show significant differences with the satellite-based reconstructions, despite the fact that land-cover change maps are the same. Our analyses suggest that the primary reason for those discrepancies is how land-surface models parameterize albedo. Another reason, of secondary importance, results from differences in the simulated snowpack. Our methodology is a useful tool not only to infer observations-based historical changes in land surface variables impacted by LCC, but also to point to major deficiencies within the models; we therefore suggest that it could be more widely developed and used in conjunction with other tools in order to evaluate global land-surface models.

3.2.1. Introduction

Human-induced land-cover change (LCC) has modified large portions of the natural landscape since pre-agricultural times, and deforestation has been particularly extensive in the Northern Hemisphere temperate regions (Hurtt et al., 2006). Surface albedo is a key element in LCC-related climate change studies as it controls the magnitude of energy absorbed by land-surfaces, which heats the land and drives turbulent fluxes. In temperate latitudes, non-forested lands reflect about 5% (absolute) and 30% more solar radiation than forests in respectively snow-free and snow-covered conditions (Jin et al., 2002; Gao et al., 2005).

As spatially coherent global observations of land-surface properties only exist for the satellite period, impacts of large-scale historical LCC have been principally assessed using global climate models (GCMs) instead of observations. Most of these numerical results show that past LCC has principally led to cooling in the northern extratropics through the increase in surface albedo. This albedo-induced cooling opposes the warming induced by non-radiatively processes that in contrast tend to predominate at lower latitudes (e.g., Gowindassamy et al., 2001; Bounoua et al., 2002; Feddema et al., 2005; Betts et al., 2007; Kvalevag et al., 2010; Davin and de Noblet-Ducoudré, 2010). Changes in surface albedo have usually been characterized and quantified by means of the radiative forcing concept, in order to compare LCC to other climate forcings (Hansen et al., 1998; Betts, 2001; Matthews et al., 2003; Myhre and Myhre, 2003; Betts et al., 2007; Davin et al., 2007; Forster et al., 2007).

Myhre et al. (2005) estimated the LCC-induced changes in surface albedo and the resulting radiative forcing based on present-day observations of albedo using the Moderate Resolution Imaging Spectroradiometer (MODIS) data. Their results show weaker albedo changes than other published numerical studies, in part because of the lower MODIS-derived crops albedo values.

In the context of the ‘Land-Use and Climate: Identification of robust Impacts’ (LUCID) project (Pitman et al, 2009), a coordinated set of simulations was realized using seven GCMs to evaluate the robust biogeophysical impacts of LCC since the preindustrial period. All simulations were forced with observed sea-surface temperatures and sea-ice, CO_2 concentrations, and two land cover distributions: one for preindustrial times (year 1870) and one for present-day (year 1992). One robust result is that LUCID models systematically simulate increases in surface albedo in response to LCC changes between preindustrial and present-day. Although in most models the near surface cools down throughout the year, some simulate seasonal warming due to a dominant impact of the non-radiative effects (de Noblet-Ducoudré et al., 2012). Although the simulated change in surface albedo shows a common direction, its magnitude varies significantly from one model to the other. Such variability has two main causes, as discussed in Boisier et al. (2012): differences in land-surface model (LSM) albedo sensitivities to LCC and differences in land-cover maps prescribed in each LSM. Although all models used the same crop and pasture extents for both years 1870 and 1992, modelers have implemented them using different procedures into their own standard vegetation maps. This has induced significant differences in the deforestation rates that each model deduced between the preindustrial times and present-day (ranging from ~ 4 to 10 million km^2) and, therefore, in the simulated responses to LCC in e.g. surface albedo.

It is rather difficult to disclose one of the LUCID vegetation' reconstructions as there are many uncertainties in identifying what has been the 'real' anthropogenic LCC. One results from the reconstruction of the historical record of cropland and pastureland, while another may come from current land cover characterization as discussed in Feddema et al. (2005) and de Noblet-Ducoudré et al. (2012). Moreover, we often know little about the specificities of land conversion to croplands (i.e., deforestation or conversion from previously grass-covered area) although some initiatives have started to address this issue (e.g., Hurtt el al., 2006). With respect to the surface albedo's sensitivity to LCC, variations between models result from the snow cover simulated and different land-surface parameterizations, notably, the one used for cropland albedo (Matthews et al., 2003; Myhre and Myhre, 2003). The realism of this sensitivity should be assessed using datasets. This is what we are trying to do in this paper.

In this study we develop a new tool (Sect. 3.2.2) to reconstruct changes in surface albedo since the preindustrial period using satellite data, and following a methodology somewhat close to that of Myhre et al. (2005). The MODIS global albedo dataset is used to assign seasonally and spatially varying albedo values to different land cover types under snow-covered and snow-free conditions. This information is then combined with land cover and snow cover maps to reconstruct albedo climatologies. After an evaluation of the methodology adopted (Sect. 3.2.3.1), we estimate the albedo response to the different scenarios of land conversion used within the LUCID project (Sect. 3.2.3.2). We then evaluate the LUCID model's albedo sensitivity to changes in vegetation in relation to their simulated snow cover (Sect. 3.2.3.3). We finally evaluate the impacts of LCC in the net solar radiation at the surface based on the simulated and reconstructed albedo changes (Sect. 3.2.3.4). Discussion and conclusion are presented in Sect. 3.2.4.

3.2.2 Material and methods

The datasets used in this study gather a number of satellite-based data and global simulations from the LUCID model intercomparison project (Table 1). The shortwave broadband directional hemispherical reflectance (black-sky albedo)/snow cover (MCD43C3; Schaaf et al., 2002) and land cover (MCD12C1) products from MODIS were used to derive snow-free and snow-covered albedos of different land cover types. The National Snow and Ice Data Center (NSIDC) snow cover data (Armstrong et al., 2007) was used, in combination with present-day and pre-industrial LUCID vegetation maps, to reconstruct the surface albedo climatology of both time periods.

The set of LUCID simulations assessed here are 30-year runs carried out in ensemble mode (5 members) by seven global climate models (GCMs), forced with monthly varying sea-surface temperature and sea ice concentration (from 1970 to 1999) and atmospheric CO_2 concentration (set to 375 ppm). Two types of simulations were computed to assess the impacts of LCC from the preindustrial (PI) period to present-day (PD), which only differ by the land cover maps prescribed in each model, representing the vegetation of 1870 in one case and that of 1992 in the other. For more details on the modeling experiment carried out within LUCID see de Noblet-Ducoudré et al. (2012). The list of GCMs, the associated land surface models (LSMs; hereafter GCM/LSMs) and their references are provided in Table 1.

Table 1: Dataset summary.

Sources	Variables[a]	Period
MODIS (LP DAAC)	α, SC, LC	2000-2011
AVHRR/ SMMR/ SSM/I (NSIDC)	SC, SWE	1979-2006
LUCID simulations (7 GCM/LSMs[b])	α, LC, SC, SWE, S_N, S_D, T_{2M}	30-year runs (5 ensemble members) with prescribed SST/SIC from 1970 to 1999. LC: 1870 (PI) and 1992 (PD)

[a] Surface albedo (α), snow cover fraction (*SC*), land cover (*LC*), snow water equivalent (*SWE*), net (S_N) and downward (S_D) shortwave radiation and 2-meter temperature (T_{2M}).

[b] GCM/LSMs: ARPEGE/ISBA [Salas-Mlia et al., 2005; Voldoire et al., 2006], CCAM/CABLE [McGregor and Dix, 2008; Abramowitz et al., 2008], CCSM/CLM [Collins et al., 2006; Oleson et al., 2008], ECEARTH/TESSEL [van den Hurk et al., 2000], ECHAM5/JSBACH [Roeckner et al., 2006; Raddatz et al., 2007], IPSL/ORCHIDEE [Marti et al., 2010; Krinner et al., 2005] and SPEEDY/LPJmL [Strengers et al., 2010; Bondeau et al., 2007].

Figure 1 summarizes our methodology for constructing the albedo climatologies. To start with, the black-sky albedo, snow cover and land cover data from MODIS were used to assign albedo values to four groups of vegetation (crops, grasses, evergreen trees and deciduous trees), in addition to bare soil. These five land cover groups (LCGs) were defined in order to have a comparable land cover partitioning between the MODIS data and the vegetation maps of the various LSMs assessed here. As the definition of vegetation varies from one model to another, this grouping ensures consistency when comparing the various reconstructions.

From the 5.6-km resolution MODIS dataset (0.05-degree latitude-longitude grid), climatological (2000-2011) monthly snow-covered and snow-free albedo maps for each of the five LCGs were derived by the means of global interpolation of grid-cells values showing a dominant fractional area of the selected LCG. Those grid-cells were defined as the ones showing LCG's fractions of 95% or larger in MODIS land cover. Croplands dominate over large regions in North America, Eurasia and India (Fig. 2a). Grasses also dominate over extensive areas such in the North American Great Plains, in central Eurasia or in the Sahelian band. Evergreen trees are the major LCG in tropical rainforest and in some areas of boreal forest. Deciduous trees dominate in some areas such as in northeastern Eurasia, in eastern North America or in central South America. Besides desert regions, grid-cells with a dominant fraction of barren soil are sparsely found in other regions of the globe.

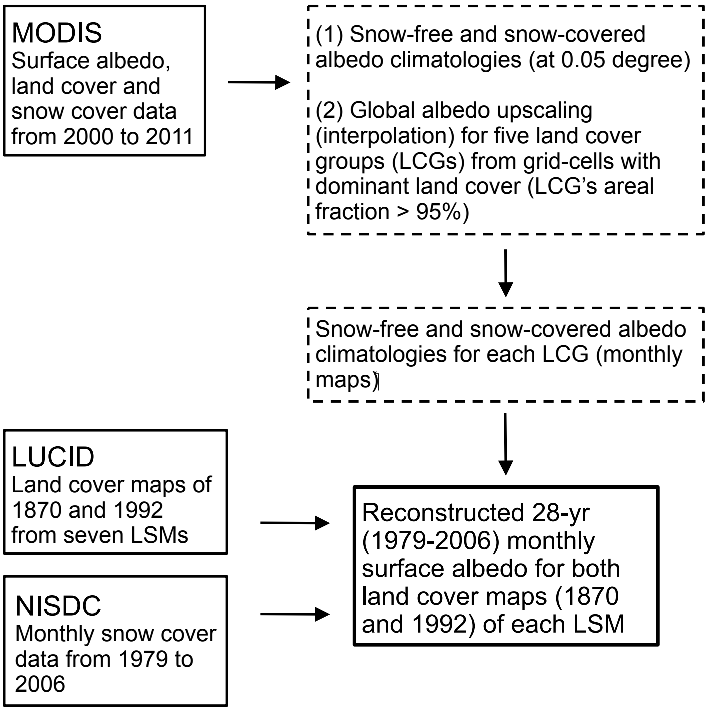

Figure 1: Flowchart of the methodology used to compute surface albedo climatologies for land cover maps of 1870 and 1992 based on satellite data.

The albedo values of the dominant LCG's grid-cells were globally mapped by simple interpolation, using the spatially nearest value method. The resulting monthly mean albedo maps were then degraded from the 0.05-degree grid to a 2.0-degree grid, the standard one used to combine and compare the ensemble LUCID simulations with satellite data. This method allows capturing the spatial and seasonal albedo variability of each LCG resulting, among other causes, from the plant life-form heterogeneity (e.g., broad-leaved vs. needle-leaved plants) or from the leaf area index (LAI) distribution within the concerned LCG.

In a second step, global maps of 'data-driven' albedo were reconstructed combining a) each LUCID GCM/LSM specific land cover map of 1870 and 1992, b) the LCGs' albedo data derived from MODIS observations and c) the monthly NISDC snow cover from 1979 to 2006. We used the NISDC snow cover data instead of the MODIS ones because of its larger period availability (large enough for a robust climatology), and time coherency with LUCID simulations that cover the 1970-1999 period (see Table 1). The net albedo of a grid-cell (at 2.0-degree resolution) is calculated as follows:

$$\alpha = \sum_{v} F_V[(1-f)\alpha_v^{sf} + f\alpha_v^{s}], \qquad (1)$$

where α_v^{sf} and α_v^{s} are respectively the MODIS-derived snow-free and snow covered albedos of the LCG v. F_v is the grid area fraction of LCG v, and f is the snow cover fraction of the corresponding grid-cell, assumed to be independent of LCG.

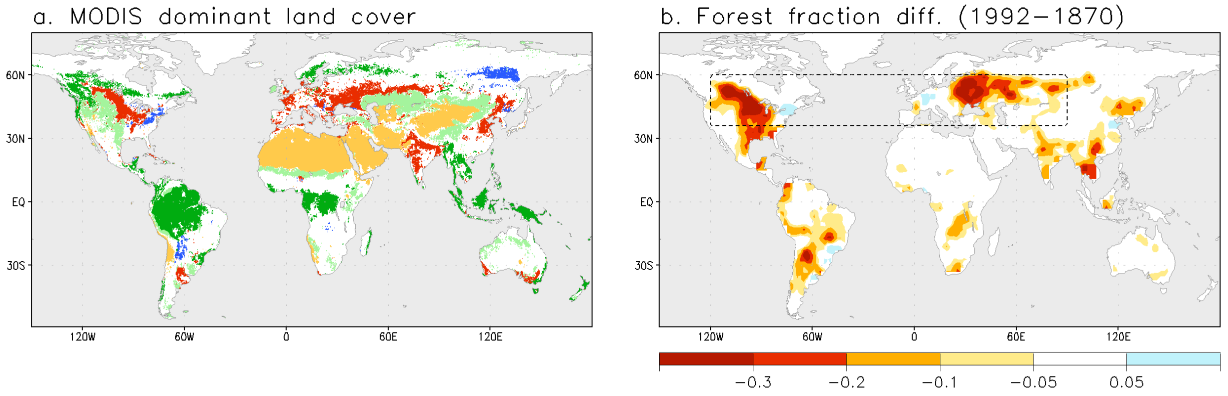

Figure 2: (a) Grid-cells in a MODIS-based vegetation map (at 0.05 degree latitude-longitude) showing a dominant land cover (fraction of 95% or larger) within the land cover groups used in this study: crops (red), grasses (lighter green), evergreen trees (darker green), deciduous trees (blue) and bare soil (orange). (b) Difference between the forest fraction of 1870 and 1992 from vegetation maps prescribed in the LUCID LSMs (model-mean). Box indicates the land areas of large deforestation further used for specific analyses.

Figure 2b illustrates the forest fraction difference between 1870 and 1992 imposed in the various LUCID GCM/LSMs (model mean). Deforestation dominates the historical LCC, notably in the northern temperate regions where the forest fraction decrease is larger than 30% (absolute) over extensive areas. Although the sign and the spatial pattern of the LCC agree within the various models, the strength of the resulting deforestation varies widely between them, because of the different strategies adopted by modelers to incorporate the prescribed historical crop and pasture data into the native land cover maps (de Noblet-Ducoudré et al., 2012).

In summary, 28-years monthly albedo maps (period determined by the availability of the NSIDC snow cover data) were computed for the preindustrial (1870) and present-day (1992) land cover maps of each of the seven LUCID GCM/LSMs. Both time periods are assumed here to have experienced the same snow-cover distribution (the present-day one from NISDC), so that the resulting albedo difference between them only takes into account the direct LCC-induced change (i.e., in contrast to the indirect LCC impacts in albedo through changes in, e.g., snow cover). Differences between the reconstructed (data-driven) albedos and those simulated by each GCM/LSM are used in the following to assess the models' parameterizations and its resulting albedo sensitivity to LCC.

In order to evaluate the skill of the method used (Sect. 3.2.3.1), another reconstructed albedo dataset was established in the same way described above, but using consistently the 12-year land cover and snow cover data from MODIS instead of the LUCID land cover maps and the NSIDC snow cover. Hence, since this reconstruction only uses information from MODIS, its difference with the MODIS albedo climatology measures the error of our methodology in scaling up the subset albedo data from grid-cells with dominant vegetation.

3.2.3 Results

3.2.3.1. Method evaluation: Reconstruction of the present-day MODIS-based albedo

The northern winter (DJF) and summer (JJA) mean albedo of the northern temperate (30-60°N) subset of the grid-cells used to derive the LCG's albedo maps are summarized in Table 2. For DJF both the snow-free and the snow-covered mean albedos are given. The mean albedo values of the four vegetation classes defined by the LCGs generally agree with previous results derived from MODIS (Jin et al., 2002; Gao et al., 2005; Myhre et al., 2005; Cescatti et al., 2012). In summer, the snow-free albedo of crops and grasses are similar to each other

(~0.15), and exceeds by near 0.06 and 0.03 those of evergreen and deciduous trees, respectively. As highlighted by Myhre et al. (2005), the mean snow-free albedo of croplands derived from MODIS (around 0.15 in this study) is lower than the standard values used in previous studies (e.g., Matthews et al. 2003). The recent MODIS albedo evaluation by Cescatti et al. (2012) have shown a good agreement between the satellite retrievals and in situ measurements, although a systematic underestimation in the MODIS-based albedo of herbaceous ecosystems with respect to the one observed in situ. They pointed out that these differences come from the landscape heterogeneity within these land-cover units (crops and grasses) and the resulting scale mismatch between the remote and in-situ observations.

The snow masking effect exerted by forest compared to that of herbaceous plants is noteworthy (Table 2). In the case of evergreen trees, the snow-covered winter albedo averages 0.22, almost three times lower than that resulting for grasses and crops (~0.6).

Table 2: MODIS seasonal mean shortwave broadband (0.3 – 5 μm) directional hemispherical reflectance (black-sky albedo) in the northern temperate regions (30-60°N) for the five land cover groups used in this study.

Land cover group	DJF (SC)	DJF (SF)	JJA (SF)
Crops	0.59 ± 0.07	0.15 ± 0.03	0.15 ± 0.02
Grasses	0.61 ± 0.07	0.19 ± 0.03	0.16 ± 0.02
Evergreen trees	0.22 ± 0.05	0.10 ± 0.02	0.09 ± 0.01
Deciduous trees	0.29 ± 0.04	0.12 ± 0.02	0.12 ± 0.02
Bare soil	0.59 ± 0.08	0.26 ± 0.07	0.26 ± 0.07

[a] The mean ± 1 standard deviation are indicated for snow-covered (SC) and snow-free (SF) surface albedo values of the ensemble of grid cells (at 0.05 degree resolution) with dominant land cover (areal fraction > 95%) within the 30-60°N latitude band.

In order to evaluate the skill of our global albedo reconstruction methodology, we have compared the reconstructed albedo fields based on the 2000-2011 MODIS land-cover and snow-cover data to the original MODIS albedo (Fig. 3). The global albedo patterns of January and July from MODIS (Fig. 3a and Fig. 3b) are generally well reproduced by the reconstructions (Fig. 3d and Fig. 3e). These patterns are characterized by relatively high albedo (larger than 0.3) over deserts and snow-covered areas, notably in the northern mid and high latitudes in January. By contrast, regions with closed forest show albedo values below 0.13, such as tropical rainforest or in boreal forest in July.

More specifically, the difference between the reconstructed and the observed mean albedo shows relatively small biases (< 0.01) in most land areas of the globe (Fig. 3c and Fig.

3f). Substantial differences are however observed in some regions such as in western and northern North America, in mid-Eurasia, in northern tropical Africa and in Australia. Most of these regions show rather large errors throughout the year (not shown) and correspond to areas for which, at the 5.6-km resolution MODIS land-cover data, very few grid-cells with more than 95% of one specific LCG were found (Fig. 2a). Therefore, in these regions of heterogeneous biogeography, the albedo values of each LCG were interpolated from values over remote regions, with potentially different species and soil colors.

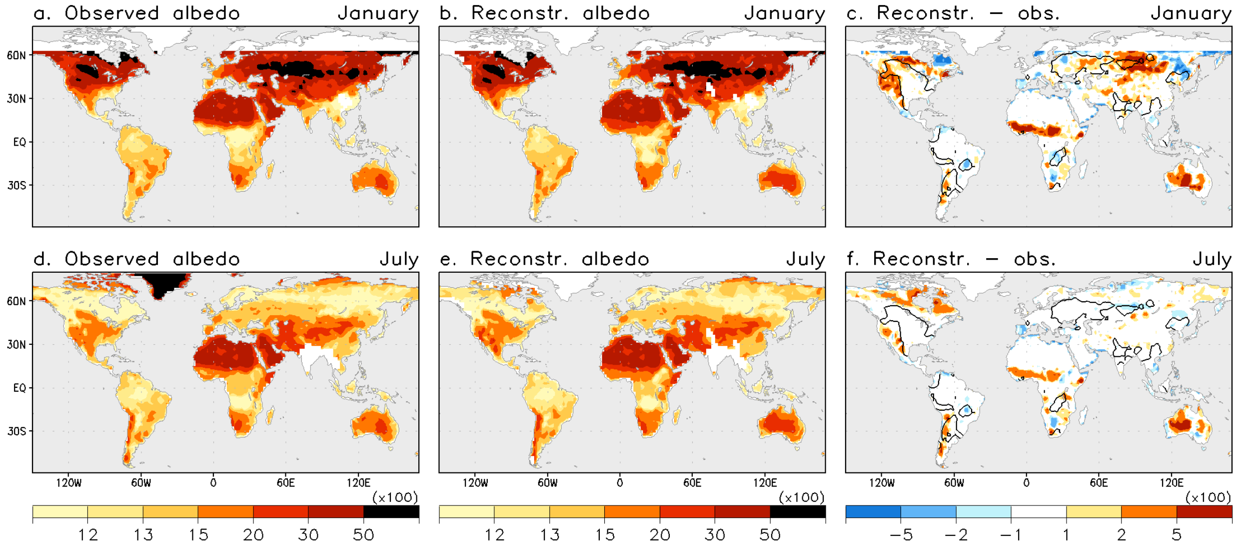

Figure 3: Mean surface albedo in January (top) and July (bottom) based on MODIS (2000-2011) observations (a, d) and reconstructions (b, e). Note the non-linear scale. Difference between the reconstructed and the observed albedo (c, f). Solid contours encompass regions with areal fraction deforested larger than 10% between 1870 and 1992.

The observed MODIS albedo is particularly overestimated by the reconstruction in Eurasia in January (~15%, relative), in central Africa in January (~30%) and in Australia in both January and July (~ 25%). The large positive bias of the reconstruction in Africa and Australia are particularly driven by their assigned barren soil albedos, which play a major role in these regions (i.e., they held open vegetation biomes), and were derived from extremely arid regions with high albedo located near them. These errors are important and could induce misleading estimates of LCC-induced albedo changes in regions where the latter are of the same order the corresponding bias. However, for the purpose of this study, the regions affected by the historical land use changes are principally located in the northern temperate regions, in areas with low bare soil fraction and small reconstruction errors (see solid contours in Fig. 3c denoting the regions in which the prescribed deforestation between 1870 and 1992 exceeds 10% of land fraction).

Figure 4 shows the mean seasonal cycle of the MODIS observed and reconstructed albedo averaged over the temperate regions that experienced significant vegetation changes between 1870 and 1992, including both North America and west Eurasia (land areas within the dashed box in Fig. 2b). The monthly mean reconstructed albedo shows a seasonal cycle that follows fairly well the original MODIS albedo data. The reconstructed albedo however slightly overestimates the observed values during most part of year, with a mean bias of about 0.002 (~1% of the observed mean albedo). This bias results from those regions showing systematically significant errors (Fig. 3), contributing to a mean absolute error (MAE) of around 5% in all seasons (the MAE, indicated by shaded areas in Fig. 4, is calculated from the ensemble of grid-cells within the selected region).

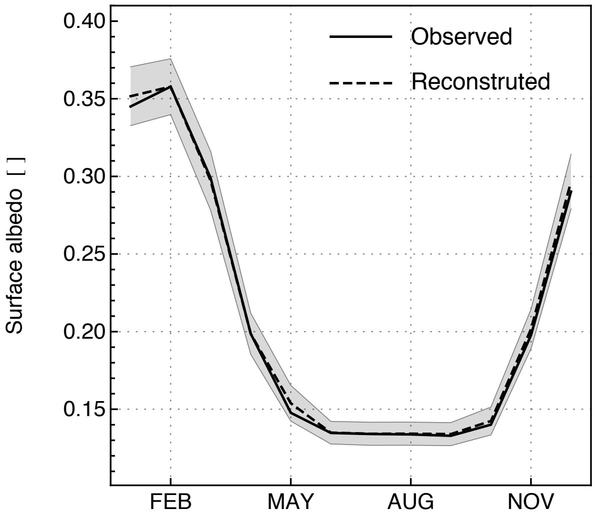

Figure 4: Monthly mean albedo for North America and Eurasia (land areas within the dashed box indicated Fig. 2b). Solid and dashed lines indicate the observed and the reconstructed values, respectively. Shading indicates the reconstruction ± mean absolute error (MAE) between the reconstruction and the observation, calculated from the ensemble of grid cells within the region studied.

3.2.3.2. Albedo changes between 1870 and 1992

As described in Sect. 3.2.2, seven pairs of MODIS-based albedo reconstructions were calculated for each of the seven LUCID LSM-specific present-day (1992) and preindustrial (1870) land-cover distributions. As with the simulated albedo, the MODIS-based estimated change in surface albedo was computed for each model as the difference between the present-day (PD) and preindustrial (PI) climatologies of the reconstructed dataset.

The simulated and reconstructed mean LCC-induced albedo differences (PD minus PI) in January and July are displayed in Fig. 5. In both the simulated and reconstructed cases, the multi-model mean albedo change is displayed. Both the LUCID average modeled albedo and the reconstructed albedo maps show clear albedo increases over areas that have experienced the most intense deforestation between 1870 and 1992 (Fig. 2b). In January, the albedo increases between PI and PD reach more than 10% (absolute) in some areas, around five times larger than those simulated in July. This difference results from the forest canopy snow-masking effect on albedo, which was larger in pre-industrial conditions when forests cover more area. The simulated mean albedo differences are very similar to the reconstructed one although slightly weaker in January and larger in July.

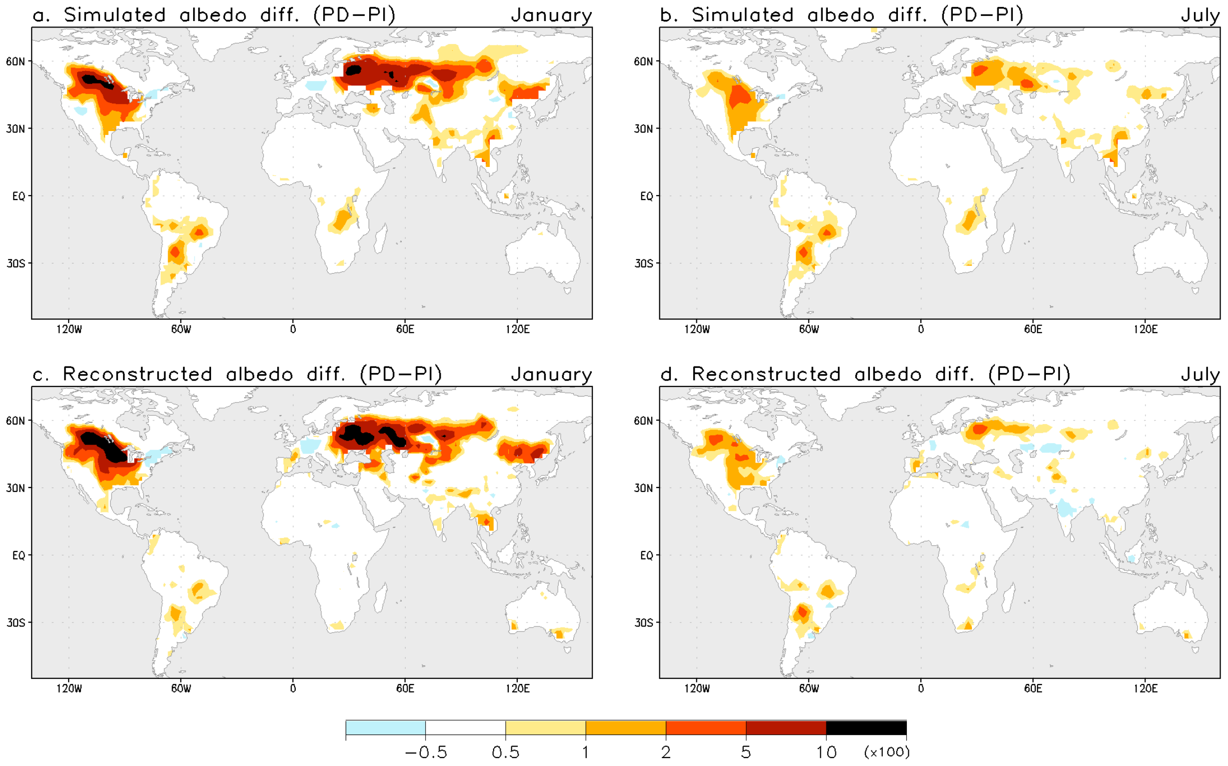

Figure 5: LCC-induced surface albedo change in January (a, c) and July (b, d). Model-mean change from LUCID simulations (a, b) and from reconstructions (c, d). Note the non-linear scale.

The consistency shown by the model-mean simulated and reconstructed albedo responses to LCC masks significant discrepancies when looking at each model individually. For each of the LUCID GCM/LSMs, Fig. 6 illustrates the simulated and reconstructed changes between PI and PD in seasonally varying albedo averaged over the region studied of maximum LCC (Fig. 2b). All models simulate a similar seasonal albedo change pattern characterized by marked maximum increases during the cold snowy season (black lines in Fig. 6). The amplitudes of the albedo anomalies between the winter and the summer are however quite at variance from one model to another. For example, CCAM/CABLE simulates null albedo changes between PI and PD in summer and near +2% (absolute) in winter, while the

ARPEGE/ISBA simulates albedo increases ranging from ~+1% in summer to more than +5% in winter. This is partly related to the different deforestation rates prescribed in each LUCID LSMs, as discussed in de Noblet-Ducoudré et al. (2012) and Boisier et al. (2012).

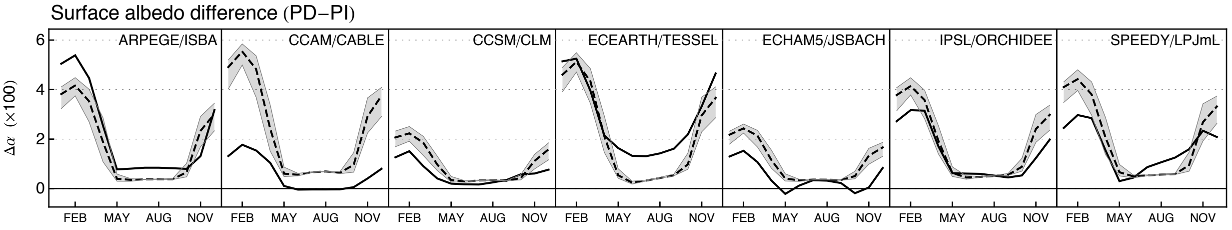

Figure 6: Monthly mean surface albedo change for each LUCID model in the region studied (North America and Eurasia). Solid and dashed lines illustrate the simulated and the reconstructed albedo changes, respectively. Shaded area indicates the range between the minimum and maximum anomalies within the reconstructed single years (i.e., with minimum and maximum snow cover).

Besides the differences between the model's albedo responses to LCC, strong discrepancies exist between the simulated and reconstructed albedo anomalies (the latter are illustrated as dashed lines in Fig. 6). The reconstructed winter albedo changes between PI and PD overestimate those simulated for five GCM/LSMs (CCAM/CABLE, CCSM/CLM, ECHAM5/JSBACH, IPSL/ORCHIDEE and SPEEDY/LPJmL) and underestimate them for two models (ARPEGE/ISBA, ECEARTH/TESSEL). Four models also show marked discrepancies between the reconstructed and simulated summer (snow-free) albedo changes (ARPEGE/ISBA, CCAM/CABLE, ECEARTH/TESSEL and SPEEDY/LPJmL).

Table 3 summarizes the annual mean albedo changes averaged over the global ice-free lands (i.e., excluding Antarctica and Greenland). The simulated model-mean albedo increases by 0.51% in response to increased (prescribed) crop and pasture areas between 1870 and 1992, globally. This simulated model-mean response to LCC includes all biogeophysical effects of LCC on climate. It hides quite different individual model responses ranging from 0.1% (CCAM/CABLE) to 0.97% (ECEARTH/TESSEL), i.e., an inter-model range (0.87%) larger than the model-mean albedo response. The model-mean albedo change derived from the 'data-driven' reconstructions is similar to the simulated change, but the associated inter-model range is more than halved (0.33%). As the reconstructed values isolate the sole contribution of the different land-cover maps to the model dispersion, this result suggests that the role of the land surface parameterizations, the simulated background climate (e.g., the snow cover during PI and PD periods) and atmospheric feedbacks play on the resulting albedo responses to LCC is of critical importance in explaining the differences in simulated albedo change between PI and PD in the LUCID models.

Given that the land cover prescribed in each single GCM/LSM is the same as the one used for the corresponding albedo reconstruction, each model's albedo sensitivity to LCC can be quantified by the difference between each simulated and reconstructed LCC-induced changes. This difference is principally explained by two causes. First, the distinct snow-cover extension simulated by each model with respect to that uniformly prescribed in the reconstructions (NSIDC). A related factor that also contributes to the simulated albedo responses to LCC, which is not taken into account in the reconstructions, is the change in the snow cover and content between the two periods simulated. Such change, which could result from, e.g., a positive snow-albedo feedback, was however not identified as a significant driver of the winter albedo responses to LCC within the LUCID simulations (Boisier et al., 2012). The second main cause behind the differences between the simulated albedo changes and the reconstructed ones is the inherent albedo sensitivity to land cover perturbations for a given snow cover condition, which directly depends on the LSMs parameterizations and may differ from the one derived from MODIS data. Land surface albedo parameterizations are responsible for the summer (snow-free) albedo responses to LCC, and should partially contribute for the winter ones. The relative role of these inherent LSM parameterization-related albedo sensitivities vs. the snow coverage in the simulated winter albedo sensitivities are examined in the following section.

Table 3: Global land annual mean LCC-induced change in surface albedo (×100).

	models							
	ARP.	CCA.	CCS.	ECE.	ECH.	IPS.	SPE.	mean (range)
Simulated	0.64	0.10	0.22	0.97	0.28	0.49	0.85	0.51 (0.87)
Reconstructed	0.48	0.55	0.30	0.63	0.36	0.63	0.55	0.50 (0.33)

3.2.3.3. Evaluating LUCID model's snow cover and the albedo sensitivity to LCC

In order to evaluate the snow cover and snowpack simulated by the various GCM/LSMs, we compared their modeled snow extent and the snow water equivalent (SWE) values in the region studied (North America and Eurasia; dashed box in Fig. 2b). Fig. 7a gives the simulated winter (DJF) area within this region covered by a snowpack with SWE equal or larger than the level indicated in x-axis. The snow coverage and content relation derived from the NSIDC data is also plotted as reference (dashed lines in Fig. 7a). In the models as well as in the NISDC dataset, most part of the region we are looking at (that totalizes nearly 25 million km^2) is covered with snow of at least 1 mm in DJF. The area decays asymptotically when increasing SWE and, e.g., no model shows an area larger than 7 million km^2 covered with a snowpack of 80 mm or deeper. More specifically, three GCM/LSMs, ECEARTH/TESSEL, ECHAM5/JSBACH and SPEEDY/LPJmL, clearly simulate too small snow extent at different given SWE levels with respect to what is diagnosed from the NISDC data, while ARPEGE/ISBA clearly overestimates it. CCAM/CABLE and CCSM/CLM simulate larger than observed snow covered areas with relatively high SWE values (SWE > 50 mm).

Comparing this analysis with what is depicted in Fig. 6, it is clear that discrepancies in snow cover simulated and that used as input to the reconstruction method are not the sole accountable for the differences between the simulated and reconstructed LCC-induced changes in albedo. For instance, IPSL/ORCHIDEE shows a quite good concordance in terms of snow content and extent with respect to reference dataset, buts its change in surface albedo between PI and PD nevertheless overestimate the reconstructed ones in winter.

To evaluate the albedo's sensitivity to LCC independently from the magnitude of the land-cover perturbation we use normalized anomalies. These are calculated as the net surface albedo change between 1870 and 1992 ($\Delta\alpha$) divided by the corresponding difference in the total fraction of herbaceous vegetation ΔF_H (i.e., $\Delta F_{CROPS} + \Delta F_{GRASS}$):

$$\Delta_N \alpha = \frac{\Delta\alpha}{\Delta F_H}. \qquad (2)$$

This coefficient therefore represents the expected albedo change induced by total deforestation when both the barren soil fraction and snowpack are kept constant (few grid-cells within the LUCID models show significant changes (> 5%) in bare soil fraction and are excluded in the analysis, as well as those pixels showing absolute SWE changes larger than 10 mm since pre-industrial times).

The $\Delta_N\alpha$ simulated by each GCM/LSM are plotted as a function of SWE in Fig. 7b. The results are illustrated as moving averages over SWE windows of 15 mm, along with the range of one standard deviation calculated over the same SWE windows (shaded area in Fig. 7b). The reconstructed $\Delta_N\alpha$ values are also plotted as a reference in Fig. 7b (dashed lines). This figure clearly shows how much the models differ in their albedo response per unit of area deforested, although the magnitude of $\Delta_N\alpha$ increases with SWE in all of them. ARPEGE/ISBA and ECEARTH/TESSEL show the strongest albedo sensitivity to deforestation when compared to all other models and to the reconstructed values. This is consistent with their large winter albedo responses to LCC described in the previous section (Fig. 6). This holds in the case of ECEARTH/TESSEL despite the lower snow coverage simulated by this model in the selected region (Fig. 7a). The simulated $\Delta_N\alpha$ in the other five models underestimate those reconstructed at different SWE levels. The weak albedo change simulated by CCAM/CABLE in winter (less than half of its associated reconstructed values) is consistent with the extremely low albedo sensitivity to LCC of this model.

a. Snow covered areas (DJF)

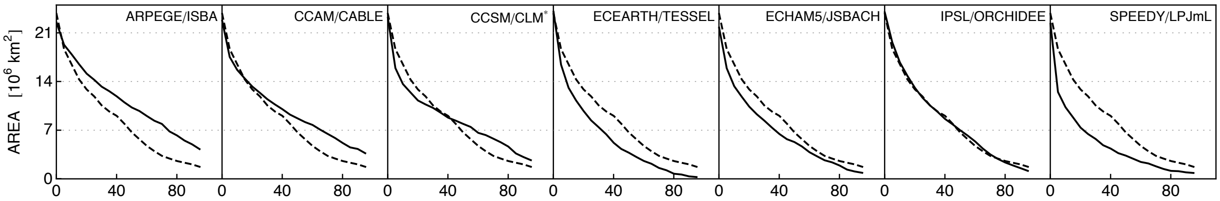

b. Normalized albedo change over snow−covered surfaces (DJF)

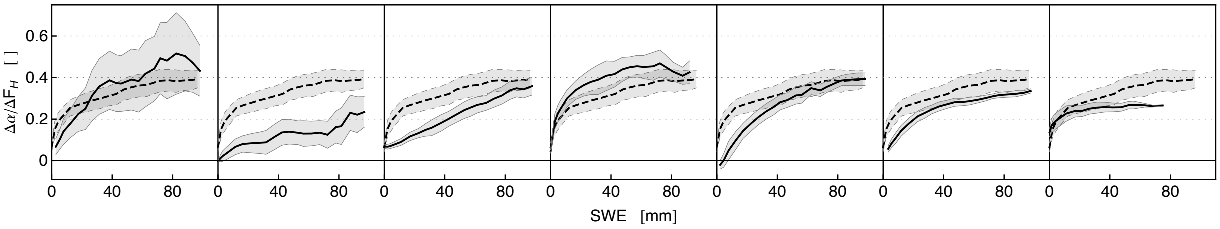

Figure 7: (a) Snow covered area within the region studied (North America and Eurasia) in winter (DJF) with minimum levels of snow content (snow water equivalent - SWE; indicated in the x-axis). Solid and dashed lines illustrate the results from LUCID models and from the NISDC data, respectively. (b) Normalized surface albedo changes ($\Delta\alpha/\Delta F_H$) averaged over SWE windows of 10 mm centered on the indicated values (see text). Simulated and reconstructed anomalies as solid and dashed lines, respectively. Shaded areas indicate the corresponding ±1 standard deviation at each SWE level.

The uneven winter albedo sensitivities to deforestation depicted in Fig. 7b reflect differences in land surface albedo parameterizations within the LUCID GCM/LSMs. As described above, these model sensitivities, independently from their simulated snow cover, are explaining an important fraction of the differences between the simulated and reconstructed winter LCC-induced albedo anomalies. To attribute these differences to either the albedo's sensitivity to deforestation or to the simulated snow cover/content, for each GCM/LSM we have plotted in Fig. 8a the relative error of the simulated winter (DJF) albedo response to LCC ($\Delta\alpha_{mod}$) with respect to that reconstructed ($\Delta\alpha_{rec}$) against the winter mean SWE. We use the relative error in $\Delta\alpha$ [defined by $(\Delta\alpha_{mod} - \Delta\alpha_{rec})/\Delta\alpha_{mod}$] in order to avoid the differences between the models due to their specific LCC strength. As well as Fig. 8a, Fig. 8b illustrates the relative errors of $\Delta\alpha$ but plotted against the normalized albedo anomaly ($\Delta_N\alpha$; see Eq. (2)) averaged at different SWE levels (i.e., this figure thus shows the 'intrinsic' albedo sensitivity of each model independently from snow cover). No clear relationship was found in the first case (Fig. 8a), implying that the simulated snow does not dominate the relative $\Delta\alpha$ errors. In contrast, an approximately linear relationship appears in the second case (Fig. 8b).

The reconstructed mean $\Delta_N\alpha$ of near 0.3 (dashed line in Fig. 8b) is consistent with the mean snow-covered albedo difference between forest and herbaceous vegetation found in this study (Table 2) and similar to the strength of the snow-masking effect reported earlier (e.g., Bonan, 2008). The two models that overestimate this value (ARPEGE/ISBA and ECEARTH/TESSEL) simulate a higher albedo response to LCC than that reconstructed, while the others models underestimate it. Hence, the intrinsic LSM albedo's sensitivities to deforestation and, therefore, related to the land surface parameterizations, appear as the major factor explaining their differences in winter mean albedo responses to LCC.

The effect of snow content may be distinguished as a secondary component in Fig. 8b. Based on the linear fit between $\Delta_N\alpha$ and the departures of the winter mean albedo responses (dashed line), those models that simulate more (ARPEGE/ISBA) and less (ECEARTH/TESSEL, ECHAM5/JSBACH, SPEEDY/LPJmL) snow than the reference data (NSIDC) respectively overestimate and underestimate their expected albedo responses based on their mean $\Delta_N\alpha$.

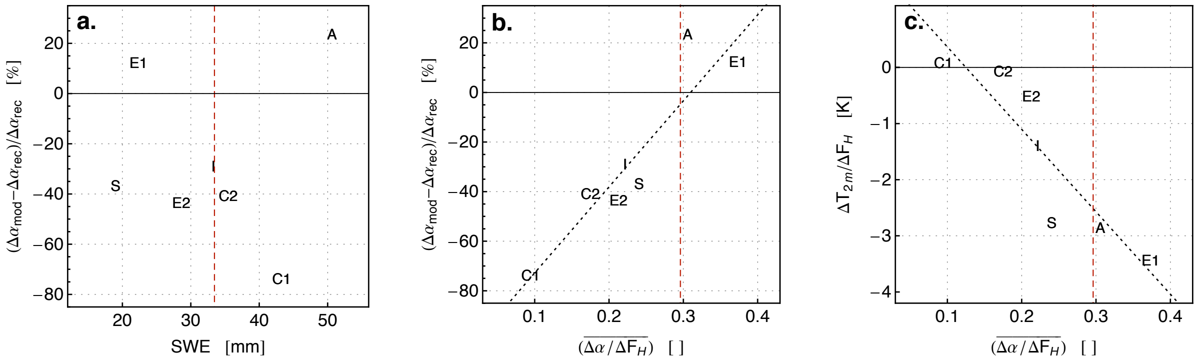

Figure 8: Differences (relative, %) between the winter mean (DJF) reconstructed and simulated albedo responses to LCC in North America and Eurasia, plotted against the simulated mean SWE (a), and plotted against the normalized albedo changes ($\Delta\alpha/\Delta F_H$) averaged at different snow cover contents (see text) (b). Winter mean normalized 2-m temperature changes ($\Delta T_{2m}/\Delta F_H$) versus the mean $\Delta\alpha/\Delta F_H$ (c). Dashed lines indicate the corresponding values obtained from the reference SWE dataset (NISDC) and the albedo reconstructions. Labels A, C1, C2, E1, E2, I and S indicate respectively ARPEGE, CCAM, CCSM, ECEARTH, ECHAM5, IPSL and SPEEDY.

Figure 8c illustrates the normalized 2-meter temperature ($\Delta T_{2m}/\Delta F_H$) responses to LCC simulated in DJF as function of the mean $\Delta_N\alpha$. In this season and region (North America and Eurasia) all the models simulate cooling of amplitude roughly proportional to the increase in surface albedo and, then, proportional to the mean $\Delta_N\alpha$. Hence, those models showing weak albedo sensitivities to deforestation (e.g., CCAM/CABLE) simulate almost null temperatures responses, while e.g. ECEARTH/TESSEL, with a mean $\Delta_N\alpha$ of ~0.37, shows a cooling exceeding 3 K. The MODIS-based mean $\Delta_N\alpha$ of ~0.3 projected on the linear fit between the simulated $\Delta T_{2m}/\Delta H_H$ and the mean $\Delta_N\alpha$ values (dashed lines in Fig. 8c), brings an estimated temperature response to total deforestation of around -2.5 K.

3.2.3.4. Impacts on the surface shortwave radiation budget

The importance of large-scale surface albedo changes on climate resides on their resulting impacts on the surface radiation budget and, then, on the energy balance. The LCC-induced changes in surface net shortwave radiation (S_N) not only depend on the surface albedo changes ($\Delta\alpha$), but also on indirect impacts of LCC and atmospheric feedbacks that, by means of perturbations in e.g. convection and cloud cover, might induce changes in the incoming solar radiation (S_D). In order to isolate the albedo-driven (α-driven) component in the LCC-induced change in S_N (ΔS_N) from the preindustrial period $S_N(PI)$ to present-day $S_N(PD)$, we use the following decomposition:

$$\Delta S_N = S_N(PD) - S_N(PI) = -\Delta\alpha\, S_D(PI) + [1-\alpha(PI)]\Delta S_D - \Delta\alpha\,\Delta S_D. \tag{3}$$

The first term in the right-hand side of Eq. (3) represents the α-driven S_N change, while the second term is the ‘indirect’ S_D-driven component briefly described above. The third term is an anomaly of second order (interactions between albedo and atmospheric feedback effects) that is negligible compared to the other terms when the perturbations are small compared to the net values (as in this case).

Figure 9 illustrates, for each of the LUCID models, the LCC-induced monthly S_N changes, averaged over the region studied in North America and Eurasia. The simulated S_N responses to LCC (indicated by solid lines in Fig. 9) are depicted along with the simulated (dotted lines) and reconstructed (dashed lines) α-driven ΔS_N. The latter are computed by evaluating the first term of Eq. (3) with the corresponding MODIS-based reconstructed $\Delta\alpha$ value, maintaining in each case the simulated $S_D(PI)$.

Most models simulate decreases in S_N that exceed 5 W m^{-2} in some cases (solid lines in Fig. 9). They also show very different seasonal patterns within their responses and, in most cases, quite different anomalies than those expected from the corresponding surface albedo changes (dotted lines). ARPEGE/ISBA is a clear exception regarding the latter. In this model, the simulated ΔS_N is led by the α-driven component, indicating comparatively weak changes in

S_D. Differences between the net ΔS_N and the α-driven component are not systematic among the different models but some patterns prevail. During the winter (DJF), most models simulated similar or weaker net ΔS_N than those expected from $\Delta\alpha$ alone. The opposite pattern, i.e., larger decreases in S_N than those induced by $\Delta\alpha$, is seen in most models in JJA with the clear exception of SPEEDY/LPJmL. The latter shows particularly large increases in S_D leading to net increases in S_N in May-June between PI and PD. These results suggest that the indirect impacts of LCC by means of changes in the S_D play quite an important role in the simulated S_N changes in response to LCC changes between PI and PD. Within the various LUCID models, this effect differs in amplitude and, in some cases in sign, amplifying or dampening the direct (α-driven) S_N perturbations.

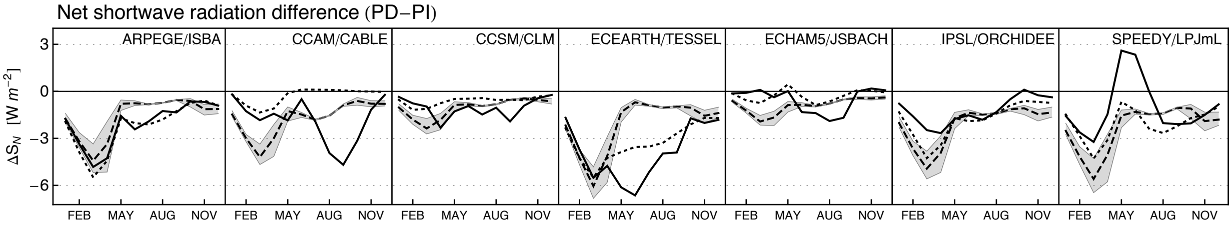

Figure 9: As in Fig. 6 but for net shortwave radiation (S_N). Simulated net and albedo-driven changes in S_N as solid and dotted lines, respectively. Dashed lines indicate the reconstructed albedo-driven S_N changes.

Except for ECHAM5/JSBACH all models show larger changes in α-driven S_D reduction during the winter and spring than in summer (dotted lines in Fig. 9), as we get in the reconstructions (dashed lines). The seasonal pattern of the simulated and reconstructed a-driven ΔS_D is however quite different for most models (except for IPSL/ORCHIDEE). For instance, in the case of ECEARTH/TESSEL, the difference between the simulated and reconstructed surface albedo change under snow-free conditions (Fig. 6) lead to a substantially overestimated α-driven decrease in S_N with respect to the MODIS-based reconstruction from May to October. A similar effect occurs with ARPEGE/ISBA and SPEEDY/LPJmL. In turn, the simulated α-driven S_N changes underestimate those reconstructed during most part of the year for CCSM/LSM, ECHAM5/JSBACH, IPSL/ORCHIDEE and CCAM/CABLE, in accordance to their differences between the reconstructed versus the simulated albedo changes (Fig. 6).

The global land annual mean LCC-induced changes in S_N are summarized in Table 4. As for the data shown in Fig. 9, the simulated net ΔS_N values and the α-driven components computed from both the simulated and the reconstructed $\Delta\alpha$, are indicated. The simulated model-mean ΔS_N between PI and PD is near -0.9 W m^{-2} with a large inter-model range of 1.21

W m^{-2}. The global land α-driven change in S_N is lower in amplitude than the total S_N changes when averaged across the models (−0.75 W m^{-2}). The models differ between each other in their individual total S_N responses compared to their α-driven ΔS_N, and the inter-model range of this component of 1.44 W m^{-2}, i.e., twice as large as the its model-mean response. Consistent with what is obtained for the surface albedo (Table 3), the inter-model range of the MODIS-based reconstructed α-driven ΔS_N is strongly reduced from that simulated (0.62 W m^{-2}), highlighting the major contribution of differences in land-surface parameterization in explaining the simulated albedo responses to LCC and the resulting spread between the models.

Averaged over the whole globe, the LUCID models show a annual mean S_N difference between PI and PD of −0.16 W m^{-2} (total simulated). Considering the α-driven component only, the model-mean S_N change is −0.14 W m^{-2} (simulated) and −0.12 W m^{-2} when using the reconstructed albedo change. These values are coherent with what Matthews et al. (2003) reported. They found a change in S_N larger in amplitude (−0.15 W m^{-2}) using a crop albedo of 0.17 (i.e., higher, in average, than the crop albedo used in this study; Table 2) for a LCC from the pre-agricultural times (1700) to present-day (1992). Their simulated ΔS_N is almost twice when crop albedo is prescribed to 0.20, highlighting the large sensitivity of the radiative impact of LCC to land-surface parameterization.

Table 4: Global land annual mean LCC-induced changes in surface net shortwave radiation (W m^{-2}).

	models							
	ARP.	CCA.	CCS.	ECE.	ECH.	IPS.	SPE.	mean (range)
Simulated	−0.68	−1.53	−0.32	−1.10	−0.35	−0.52	−1.03	−0.89 (1.21)
α-driven (sim.)	−0.81	−0.04	−0.29	−1.41	−0.42	−0.79	−1.47	−0.75 (1.44)
α-driven (rec.)	−0.53	−0.53	−0.40	−0.80	−0.44	−1.01	−0.72	−0.63 (0.62)

The global mean ΔS_N found in this study are also within the typical radiative forcing (RF) of −0.2 ± 0.2 W m^{-2} attributed to the past LCC due to surface albedo changes in previous modeling studies (Forster et al., 2007; Davin et al. 2007) and higher in amplitude than the RF of −0.09 W m^{-2} that was estimated by Myhre et al. (2005) from satellite observations. The change in S_N is however a quite rough estimation of the LCC-induced RF, which is usually computed at the top of the troposphere and, therefore, accounts for the net changes in shortwave radiation due to combined surface and cloud cover perturbations, in addition to changes in longwave radiation as indirectly perturbed by LCC via atmospheric feedbacks. The net impact of LCC in terms of RF could also be amplified by positive feedbacks due to changes in, e.g., the water vapor (Davin et al., 2007).

3.2.4. Discussion and conclusions

Results from the LUCID model intercomparison project have demonstrated that changes in surface albedo were one of the main drivers of the GCMs' responses to historical land-use induced land cover changes (LCC). This initiative has also showed that the simulated albedo change was quite different from one model to another. It then became important to evaluate the magnitude of this albedo response to historical LCC based on available observations.

In addition we have to recall that there is no current consensus on the intensity of past deforestation and, consequently, this aspect represents one of the main sources of uncertainty when comparing various studies addressing the impacts of LCC on climate (de Noblet-Ducoudré et al. 2012; Boisier et al., 2012).

We have used satellite-based surface albedo, land-cover and snow-cover data to derive snow-free and snow-covered monthly climatologies of albedo for five main land cover groups (LCGs). Those climatologies can be combined with any vegetation and snow cover distribution to reconstruct global albedo maps and then estimate LCC-induced albedo changes. We have used this methodology to assess changes in surface albedo since preindustrial times. Reconstructed albedos for both time periods used the land-cover maps provided by the seven GCM/LSMs that have been run in the context of the LUCID project. Preindustrial simulations and reconstructions only differ from present-day ones by the land-cover maps. The reconstructions were then compared to the albedo values simulated by each individual GCM/LSM to evaluate how realistic each model is with respect to the response of this specific variable to LCC.

It is important to note that the reconstructed preindustrial albedo maps use the present-day snow-cover data and LCG's monthly albedos. Thus, the resulting surface albedo change between 1992 and 1870 represents a first estimate of land-cover perturbation, i.e. prior to any climate feedback that could further modulate the albedo responses to LCC. However, our previous analyses of LUCID simulations show rather weak positive snow-albedo feedback (Boisier et al, 2012).

The LUCID models do not exhibit a systematic bias in their simulate albedo responses to LCC with respect to those reconstructed using the MODIS albedo and the NSIDC snow cover data. However, single model responses are significantly different from their respective reconstructions, notably when snow is present. We show that these differences reside principally on the land surface parameterizations of albedo which is summarized in the LSMs' albedo sensitivities to deforestation, while differences in snowpack simulated by the LUCID GCMs represent a secondary component of their winter albedo changes between pre-industrial and present. It should be noted that the winter temperature responses to LCC simulated by the LUCID models are mainly directed by surface albedo changes and, consequently, depend directly on the albedo sensitivity of LSMs (Fig. 8c).

The large dispersion in albedo responses to LCC shown by LUCID models echoes the reported uncertainty in the radiative forcing of past LCC (Forster et al., 2007). Our results show that the spread in the simulated albedo changes is in its major part associated to the LSMs' parameterizations, reinforcing previous conclusions from LUCID (Boisier et al., 2012). The remaining uncertainty is mainly related to the choice of land-cover maps. The indirect impacts of land-cover perturbations, inducing changes in the incoming solar radiation, are also quite model-dependent, adding additional uncertainty to the radiative effect of LCC.

Narrowing the large uncertainties in regional climate responses to LCC is a major challenge to move forward in the understanding of past climate trends and future projections, and will help other studies such as the climate change detection and attribution. Novel observation-based global products are a useful data source that could help to this purpose and notably be used as benchmark in climate modeling studies. Further, the methodology applied here may be used to estimated either past or future LCC-related changes in surface albedo, as well as in any other surface quantity that is available globally at relatively high resolution.

Acknowledgements

We thank the climate modeling groups participating in LUCID for providing model data and support. This research was partially funded by the Chilean National Commission for Scientific and Technological Research (CONICYT) and the EU-FP7 project AMAZALERT. The computing time was provided by the Commissariat à l'Energie Atomique (CEA), France. The MODIS MCD43C3 and MCD12C1 data were obtained through the online Data Pool at the NASA Land Processes Distributed Active Archive Center (LP DAAC), USGS/Earth Resources Observation and Science (EROS) Center, Sioux Falls, South Dakota (http://lpdaac.usgs.gov/get_data). The AVHRR/SMMR/SSM/I snow cover and snow water equivalent product (NSIDC-0271) were obtained from the National Snow and Ice Data Center (NISDC) Distributed Active Archive Center (DAAC).

References

Abramowitz, G., Leuning, R., Clark, M., and Pitman, A.: Evaluating the performance of land surface models, *J. Climate*., 21, 5468–5481, 2008.

Armstrong, R. L., M. J. Brodzik, K. Knowles, and M. Savoie: Global Monthly EASE-Grid Snow Water Equivalent Climatology. Boulder, Colorado USA: National Snow and Ice Data Center. Digital media. 2007.

Betts, R. A.: Biogeophysical impacts of land use on present-day climate: near-surface temperature and radiative forcing. *Atmos. Sci. Lett.*, 2: 39–51, DOI 10.1006/asle.2001.0023, 2001.

Betts, R. A., Falloon, P. D., Klein Goldewijk, K., and Ramankutty, N.: Biogeophysical Effects of Land Use on Climate: Model Simulations of Radiative Forcing and Large-Scale Temperature Change. *Agricultural and Forest Meteorology*,142, 216-233, 2007.

Boisier, J. P., de Noblet-Ducoudré, N., Pitman, A. J., Cruz, F. T., Delire, C., van den Hurk, B. J. J. M., van der Molen, M. K., Müller, C., and Voldoire, A.: Attributing the impacts of land-cover changes in temperate regions on surface temperature and heat fluxes to specific causes: Results from the first LUCID set of simulations, *J. Geophys. Res.*, 117, D12116, doi:10.1029/2011JD017106, 2012.

Bonan, G. B.: Forests and climate change: Forcings, feedbacks, and the climate benefits of forests, *Science*, 320, 1444–1449, 2008.

Bondeau, A., Smith, P. C., Zaehle, S., Schaphoff, S., Lucht, W., Cramer, W., Gerten, D., Lotze-Campen, H., Müller, C., Reichstein, M., Smith, B.: Modelling the role of agriculture for the 20th century global terrestrial carbon balance, *Global Change Biology,* 13 (3) 679-706, 2007.

Bounoua, L., DeFries, R., Collatz, G. J., Sellers, P., and Khan, H.: Effects of land cover conversion on surface climate, *Climatic Change*, 52, 2964, 2002.

Cescatti, A. and Coauthors: Intercomparison of MODIS albedo retrievals and in situ measurements across the global FLUXNET network, *Remote Sensing of Environment*, 121, 323-334, ISSN 0034-4257, 10.1016/j.rse.2012.02.019, 2012.

Collins, W. D. and Coauthors: The Community Climate System Model Version 3 (CCSM3). *J. Climate*, 19, 2122–2143. doi: http://dx.doi.org/10.1175/JCLI3761.1, 2006.

Davin, E. L., de Noblet-Ducoudré, N., and Friedlingstein, P.: Impact of land cover change on surface climate: Relevance of the radiative forcing concept, *Geophys. Res. Lett.*, 34, L13702, doi:10.1029/2007GL029678, 2007.

Davin, E. L. and de Noblet-Ducoudré, N.: Climatic Impact of Global-Scale Deforestation: Radiative versus Nonradiative Processes. *J. Climate*, 23, 97–112, 2010.

De Noblet-Ducoudré, N., Boisier, J. P., Pitman, A., Bonan, G., Brovkin, V., Cruz, F., Delire, C., Gayler, V., van den Hurk, B., Lawrence, P., van der Molen, M., Müller, C., Reick, C., Strengers, B., and Voldoire, A.: Determining robust impacts of land use induced land-cover changes on surface climate over North America and Eurasia; Results from the first set of LUCID experiments. *J. Climate*. doi:10.1175/JCLI-D-11-00338.1, 2012.

Feddema, J., Oleson, K., Bonan, G., Mearns, L., Washington, W., Meehl, G., and Nychka D.: A comparison of a GCM response to historical anthropogenic land cover change and model sensitivity to uncertainty in present-day land cover representations, *Climate Dyn.*, 25, 581609, 2005.

Forster, P. and Coauthors: Changes in Atmospheric Constituents and in Radiative Forcing. In: Climate Change 2007: The Physical Science Basis. Contribution of Working Group I to the Fourth Assessment Report of the Intergovernmental Panel on Climate Change [Solomon, S., D. Qin, M. Manning, Z. Chen, M. Marquis, K.B. Averyt, M.Tignor and H.L. Miller (eds.)]. Cambridge University Press, Cambridge, United Kingdom and New York, NY, USA, 2007.

Gao, F., Schaaf, C. B., Strahler, A. H., Roesch, A., Lucht, W., and Dickinson, R.: MODIS bidirectional reflectance distribution function and albedo Climate Modeling Grid products and the variability of albedo for major global vegetation types, *J. Geophys. Res.*, 110, D01104, doi:10.1029/2004JD005190, 2005.

Govindasamy, B., Duffy, P. B., and Caldeira, K.: Land use changes and Northern Hemisphere cooling, *Geophys. Res. Lett.*, 28, 291294, 2001.

Hansen, J. E., Sato, M., Lacis, A., Ruedy, R., Tegen, I., and Mathews, E.: Climate forcings in the Industrial era, *PNAS*, 95, 12,75312,758, doi: 10.1073/pnas.95.22.12753, 1998.

Jin, Y., Schaaf, C. B., Gao, F., Li, X., Strahler, A. H., Zeng, X., and Dickinson, R. E.: How does snow impact the albedo of vegetated land surfaces as analyzed with MODIS data?, *Geophys. Res. Lett.*, 29(10), 1374, doi:10.1029/2001GL014132, 2002.

Krinner, G., Viovy, N., de Noblet-Ducoudré, N., Ogée, J., Polcher, J., Friedlingstein, P., Ciais, P., Sitch, S., and Prentice, I. C.: A dynamic global vegetation model for studies of the coupled atmosphere-biosphere system, *Global Biogeochem. Cycles*, 19, GB1015, doi:10.1029/2003GB002199, 2005.

Kvalevåg, M. M., Myhre, G., Bonan, G., and Levis, S.: Anthropogenic land cover changes in a GCM with surface albedo changes based on MODIS data, *Int. J. Climatol.*, 30(13), 2105, 2010.

Marti, O. and Coauthors: Key features of the IPSL ocean atmosphere model and its sensitivity to atmospheric resolution, *Clim. Dyn.*, 34, 1–26, doi:10.1007/s00382-009-0640-6, 2010.

Matthews, H. D., Weaver, A. J., Eby, M., and Meissner, K. J.: Radiative forcing of climate by historical land cover change, *Geophys. Res. Lett.*, 30(2), 1055, doi:10.1029/2002GL016098, 2003.

McGregor, J. L. and Dix, M. R.: An updated description of the Conformal-Cubic Atmospheric Model, in High Resolution Simulation of the Atmosphere and Ocean, edited by K. Hamilton and W. Ohfuchi, pp. 51–76, Springer, New York, 2008.

Myhre, G. and Myhre, A.: Uncertainties in radiative forcing due to surface albedo changes caused by land-use changes. *Journal of Climate*, 16: 1511–1524, DOI: 10.1175/1520–0442, 2003.

Myhre, G., Kvalevåg, M. M., and Schaaf, C. B.: Radiative forcing due to anthropogenic vegetation change based on MODIS surface albedo data, *Geophys. Res. Lett.*, 32, L21410, doi:10.1029/2005GL024004, 2005.

Oleson, K. W. and Coauthors: Improvements to the Community Land Model and their impact on the hydrological cycle, *J. Geophys. Res.*, 113, G01021, doi:10.1029/2007JG000563, 2008.

Pitman, A. J. and Coauthors: Uncertainties in climate responses to past land cover change: First results from the LUCID intercomparison study, *Geophys. Res. Lett.*, 36, L14814, doi:10.1029/2009GL039076, 2009.

Raddatz, T., Reick, C. H., Knorr, W., Kattge, J., Roeckner, E., Schnur, R., Schnitzler, K. G., Wetzel, P., and Jungclaus, J.: Will the tropical land biosphere dominate the climate-carbon cycle feedback during the twenty-first century?, *Clim. Dyn.*, 29, 565–574, 2007.

Roeckner, E., Brokopf, R., Esch, M., Giorgetta, M., Hagemann, S., Kornblueh, L., Manzini, E., Schlese, U., and Schulzweida, U.: Sensitivity of simulated climate to horizontal and vertical resolution in the ECHAM5 atmosphere model, *J. Climate*, 19, 3771–3791, 2006.

Salas-Mélia, D., Chauvin, F., Déqué, M., Douville, H., Guérémy, J. F., Marquet, P., Planton, S., Royer, J. F., and Tyteca, S.: Description and validation of the CNRM-CM3 global coupled climate model, Note 103, Cent. du Groupe de Météorol. de Grande Echelle et Clim., Toulouse, France, 2005. [Available at http://www.cnrm.meteo.fr/scenario2004/paper_cm3.pdf]

Schaaf, C. B. and Coauthors: First operational BRDF, albedo nadir reflectance products from MODIS, *Remote Sens. Environ.*, 83, 135-148, 2002.

Strengers, B. J., Muller, C., Schaeffer, M., Haarsma, R. J., Severijns, C., Gerten, D., Schaphoff, S., van den Houdt, R., and Oostenrijk, R.: Assessing 20th century climate-vegetation feedbacks of land-use change and natural vegetation dynamics in a fully coupled vegetation-climate model, *Int. J. Climatol.*, 30(13), 2055–2065, doi:10.1002/joc.2132, 2010.

van den Hurk, B. J. J. M., Viterbo, P., Beljaars, A. C. M., and Betts, A. K.: Offline validation of the ERA40 surface scheme, Tech. Memo., 295, Eur. Cent. for Med.-Range Weather Forecasts, Reading, U. K, 2000.

Voldoire, A.: Quantifying the impact of future land-use changes against increases in GHG concentrations, *Geophys. Res. Lett.*, 33, L04701, doi:10.1029/2005GL024354, 2006.

3.3 Land-use induced global evapotranspiration changes since the preindustrial period estimated with current observations−based gridded products

J. P. Boisier, N. de Noblet-Ducoudré, P. Ciais

(Paper in preparation)

Abstract

Given that eddy-covariance evapotranspiration (ET) measurements are spatially sparse and have been performed systematically only during the last few years, the current large-scale ET distribution and its historical trends are uncertain. The regional changes in ET that occurred since the pre-agricultural times induced by land cover conversions are particularly difficult to estimate from measurements. Recent results from the LUCID model intercomparison project show that uncertainties in ET changes since pre-industrial period are also manifest in current global climate models (GCMs), mainly due to their different land-surface parameterizations. In this study, we used three different observations−based global ET products and constructed a statistical model to diagnose ET changes in response to land cover change between preindustrial and present-day. Two land-cover maps established for years 1870 and 1992 to force the IPSL GCM in the context of LUCID are adopted to derive preindustrial and present-day ET climatologies. The IPSL simulations carried out for LUCID are used to test the reliability of the statistical model to reconstruct ET changes from past land cover changes. By combining observations−based global ET maps for the current period, and our statistical model, we estimate a global ET decrease ranging from 1300 to 2000 km^3 per year between pre-industrial and present-day. While a decrease of annual ET from pre-industrial is inferred over most parts of the globe, some areas in temperate latitudes tend to show a significant ET increase, particularly during the summer and over those regions where crops have replaced natural grasslands.

3.3.1 Introduction

Human−induced changes in evapotranspiration (ET) due to land-use induced land cover changes (LULCC) or other land-use practices, such as irrigation, have received special attention in the recent decade because of their potentially large impacts on ecosystem services, on the hydrological cycle and on climate. Although most studies suggest that the LULCC between pre-industrial times and the present period has led to a decrease in global ET (Gordon et al., 2005) and an increase in runoff (Piao et al., 2006), the large-scale changes in ET remain quite uncertain, as well as its geographical and seasonal variations (Pitman et al., 2009; Pielke et al., 2011; Jackson et al. 2005).

Local cooling due to increases in surface albedo, and warming due to a reduced evaporative cooling are two biogeophysical effects of deforestation of opposite sign (Bonan et al., 2008). The latter effect may dominate in the tropical areas, as several modeling studies have shown (e.g., Nobre et al., 1991; Costa and Foley, 2000; Sampaio et al., 2007; Brovkin et al., 2009; Davin and de Noblet-Ducoudre, 2009) in accordance with observational evidence (Gash and Nobre, 1997; von Randow et al., 2004; da Rocha et al, 2009, Loarie et al., 2011). In contrast, because of the strong snow masking effect exerted by boreal forest, the radiative impact (albedo−induced) of forest clearing has likely led to surface cooling at high latitudes (e.g., Betts, 2001; Govindasamy et al., 2001; Bounoua et al., 2002; Brovkin et al., 2009).

In temperate regions, where historical land-use changes have been particularly extensive (Ramankutty and Foley, 1999), the impact of LULCC on the surface climate is particularly uncertain, in part, because of the unknown net effect of the above-mentioned radiative and non-radiative effect of deforestation. Further, the sign of ET change due to land-use practices is clearly not one-sided. For instance, irrigation leads to ET increases, subsequent surface cooling and other impacts on climate in, e.g., India (Douglas et al., 2006; Roy et al., 2007), in the Middle East and Asia (Lee et al., 2011), and in the North American Great Plains (Adegoke et al., 2003, 2007; Mahmood et al., 2004, 2006) or California (Lobell and Bonfils, 2008). Consistent with these studies, results from Puma and Cook (2010) have showed large-scale ET increases and cooling due to irrigation, effect that could have been as important in amplitude as the opposite footprint induced by deforestation (Gordon et al., 2005; Haddeland et al., 2007). Based on observations, Baldocchi et al. (1997) and Teulling et al. (2010) have also shown that well-watered croplands and grasslands can evaporate more water than temperate forest, in contrast with other findings (Baidya Roy et al. 2003; Twine et al., 2004; Jackson et al., 2005).

Recent results from the LUCID project ('Land Use and Climate: Identification of Robust Impacts'), aiming at comparing the results of different land surface models coupled to climate models for the climate effects of LULCC, have revealed large uncertainties on the simulated ET responses to LULCC (Pitman et al., 2009). During the first phase of LUCID, a coordinated set of simulations was carried out by seven climate models (GCMs) to assess the biophysical effects of LULCC between the preindustrial period and present-day. The simulated ET changes were found to vary in both magnitude and sign, across the various GCMs and from season to season, despite the fact that none of the GCMs included irrigation. This inter-model dispersion, in part explained by differences in the vegetation and land cover changes prescribed in each GCM, also resides on the different land surface parameterizations and the resulting model sensitivities to LULCC (Boisier et al., 2012).

The impact of historical LULCC on the continental water budget has been addressed principally through modeling studies, most of them showing negative ET trends either during the last century (Piao et al., 2006) or since the preindustrial period (Haddeland et al., 2007; Scanlon et al., 2007; Rost et al., 2008). Few studies have estimated the past ET trends at large scales based on observations. Gordon et al. (2005) calculated the global ET change induced by deforestation and irrigation separately. They estimated a total water vapor decrease due to deforestation of about −3000 km^3 per year, slightly stronger in amplitude than the opposite effect induced by irrigation (~+2600 km^3/year).

The scarcity of studies addressing the geographic distribution of changes in ET based on observations is partly due to the short period covered by ET measurements, and the limited number of sites. Nevertheless, a number of global ET gridded products have recently been developed, based upon already long records of satellite data and ET observations from eddy-covariance flux tower measurements (see Jimenez et al., 2010; Mueller et al., 2011; and references therein). Jung et al. (2010) present one of these ET products, and report a decrease in the global land ET during the recent years in relation to consistent decreases in soil moisture.

The aim of this study is to provide new estimations of the global-scale changes of ET due to past LULCC from observation-based datasets and compare them with model results. We also ambition to provide a seasonal and geographical distribution of those inferred changes. To address these questions, we use global (gridded) ET products as base information. The present-day spatial and temporal ET variability resulting in these products, combined with a number of environmental drivers and land-cover distribution are used to diagnose preindustrial ET climatologies. We assess three ET products; those of Jung et al. (2010), Zhang et al. (2010) and

Miralles et al. (2011), in order to quantify how sensible are our estimations of the past ET changes to the nature of the different ET datasets.

Our approach is empirical; we construct a multivariate statistical ET models for each of the three ET products assessed in combination with other global datasets used as ET drivers (Section 3.3.2). We then apply this model to reconstruct monthly ET climatologies for the vegetation distribution of 1870 and 1992 (Section 3.3.3). We also apply this method over output fields of the IPSL model simulations. The resulting diagnosed ET changes are compared to those simulated with the same model to evaluate the reliability of the statistical approach to reproduce the signals of the past LULCC from present-day gridded datasets.

3.3.2 Material and methods

3.3.2.1. Datasets

The set of data and model fields that we used is summarized in Table 1. Three observations−based global ET datasets were analyzed along with global fields of surface radiation, precipitation, snow and land cover used as predictor of a multivariate ET model. The three ET data products are those from Miralles et al., (2011; Global land surface evaporation: the Amsterdam methodology; thereafter GLEAM), from Zhang et al. (2010; Numerical Terradynamic Simulation Group; thereafter NTSG) and from Jung et al. (2010; Max Planck Institute for Biogeochemistry; thereafter MPI). GLEAM and NTSG explicitly calculate the total ET from the soil evaporation and the canopy ET components. These two products are based on semi-empirical evaporation models, which are mapped globally with remotely sensed data of land-cover distribution, surface properties, radiation and meteorology. In the NTSG case, meteorological input based on reanalysis and flux towers observations from the FLUXNET network were used to calibrate the ET model. The MPI global latent heat flux (LE) product was empirically derived from FLUXNET eddy-covariance measurements using a multiple regression tree ensemble technique. LE measured at flux tower sites was extrapolated in time and space using satellite land cover and FAPAR data, and gridded meteorological datasets. In this study, the MPI LE fields were converted to ET using a constant latent heat of vaporization (L) of 2.5×10^6 J kg^{-1}.

Global land-cover maps, surface downward (incoming) shortwave and longwave radiation, precipitation and snow water equivalent data are used here as predictors for an ET multivariate model (see section that follows). Global observations of these variables correspond to three satellite−based datasets: the Surface Radiation Budget project (SRB), the Moderate Resolution Imaging Spectroradiometer (MODIS) for land cover, and the National Snow and Ice data Center (NSIDC) snow water equivalent data; in addition to the Global Precipitation Climatology Centre (GPCC) observations−based gridded precipitation product (see Table 1).

Table 1. Global datasets used.

Source	Variables[a]	Used period	Description and references
MPI	LE	1983-2006	Global LE upscaling from eddy-covariance observations (FLUXNET). Use AVHRR NDVI and CRU/GPCC meteorology (Jung et al., 2006, 2010).
GLEAM	ET	1983-2006	Global ET product base on Priestley-Taylor model. Use remote sensed data from SRB (radiation), GPCP/CMORPH (meteo.), LPRM (soil moisture, temp, veget. optical depth), ISCCP (temp.) and NSIDC (SWE) (Miralles et al., 2011).
NTSG	ET	1983-2006	Global ET based on a Penman-Monteith and Priestley-Taylor (open water) approach. Use satellite data (AVHRR NDVI and SRB radiation), NCEP/NCAR reanalysis (meteo.) and FLUXNET observations (canopy conduct. calibration) (Zhang et al., 2010).
SRB	S_D, L_D	1983-2006	WCRP/GEWEX SRB project Release-3.0 remote sensed radiation data.
GPCC	P	1983-2006	Monthly gridded precipitation dataset calculated from in situ observations (Rudolf et al., 2010).
NISDC	SWE	1983-2006	Satellite-derived monthly EASE-Grid Snow Water Equivalent (Armstrong et al., 2007).
MODIS	LC (2001)	2001	Land-cover distribution based on IGBP classification (ref).
IPSL/ ORCHIDEE	LC (1870 and 1992), ET, S_D, L_D, P	1970-1999	LUCID experiments: 2 types of simulations were carried out with land cover of 1870 and 1992, respectively. In both cases, models performed 5 runs (ensembles) with prescribed SST/SICs from 1970 to 1999 and atmospheric CO_2 concentration set to 370 ppm. (Pitman et al., 2009; de Noblet-Ducoudré et al., 2012).
6 LUCID GCM/LSMs[b]	LC (1870 and 1992), LE		

[a] Excepting land-cover maps (LC), the used datasets are monthly mean fields of evapotranspiration (ET), latent heat flux (LE), downward shortwave (S_D) and longwave (L_D) radiation at the surface, snow water equivalent (SWE) and precipitation (P).

[b] In addition to IPSL/ORCHIDEE, the other GCM/LSMs that participated in the first LUCID set of simulations were ARPEGE/ISBA, CCAM/CABLE, CCSM/CLM, EC-Earth/TESSEL, ECHAM5/JSBACH and SPEEDY/LPJmL.

Global simulations carried out for the LUCID project (Pitman et al., 2009) with the coupled land-atmosphere configuration of the GCM/Land surface model (LSM) IPSL/ORCHIDEE (Marti et al., 2010; Krinner et al., 2005) were used in the analysis. These simulations (hereafter referred to as ORCH-ON) include two experiments that prescribed sea surface temperature and sea-ice coverage (SST/SIC) from 1970 to 1999, and atmospheric CO_2 concentrations (set to 375 ppm). The two experiments were done in an ensemble mode (with five realizations) and only differ in the land-cover prescribed in ORCHIDEE, representing respectively the vegetation distribution of 1870 and 1992. These land-cover maps were constructed from the observed vegetation distribution after Loveland et al. (2000) combined the historical crop and pasture distribution from the SAGE (Ramankutty and Foley, 1999) and HYDE (Klein Goldewijk, 2001) datasets, respectively. Another set of LUCID simulations, conducted 'offline' with ORCHIDEE (ORCH-OFF) and forced with atmospheric data obtained in ORCH-ON, is also evaluated for comparison in this study.

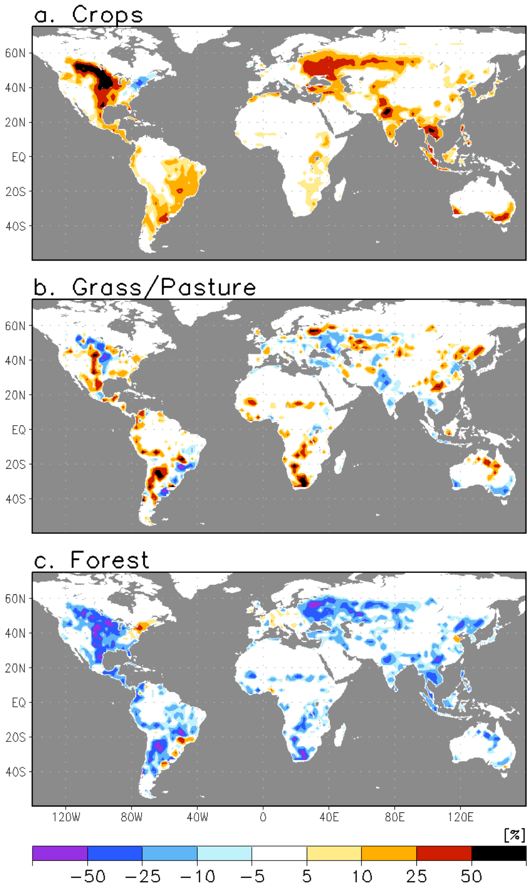

Figure 1: Differences in the fractional area (%) covered by crops (a), grass (b) and forest (c) between 1992 and 1870. These land-cover changes correspond to those prescribed in ORCHIDEE for the LUCID simulations and used in this study to diagnose the changes in evapotranspiration.

The land-cover maps prescribed in ORCHIDEE for LUCID simulations are adopted here to reconstruct global ET climatologies for 1870 and 1992 based on the three observation−based ET products. Any other land-cover map could have been used, and the same method is applicable in a broader context. Figure 1 illustrates the grid area fraction difference (1992 minus 1870) of crops, grass (including pasture) and forest resulting from the ORCHIDEE maps. In accordance with what is observed in the SAGE dataset (Ramankutty and Foley, 1999), increases in cropland area dominate LULCC between 1870 and 1992, notably in northern temperate and boreal regions. Cropland expands to the detriment of forest principally. Given that pastures are modeled as natural grass in ORCHIDEE, the resulting change in grass fraction shows uneven directions depending on whether it represents a (managed) pasture expansion/decline over natural ecosystems, or the conversion of natural grassland to croplands. The land-use rules defining how forest and natural grassland get reduced in area when crops and pasture expand is thus crucial regarding the final deforestation. Results from LUCID have shown that different rules to allocate new pasture and cropland into the various LSMs represent one of the major source of uncertainty in the simulated climate impacts of LULCC (de Noblet-Ducoudre et al., 2012; Boisier et al., 2012).

Some results shown in Section 3.3.3 contrast the diagnosed ET changes between 1870 and 1992 with our statistical model to those simulated by the ensemble of models that participated in the first LUCID set of simulations (including IPSL/ORCHIDEE and other six GCM/LSMs; see Table 1). For further details and references concerning the LUCID experiments and models see Pitman et al. (2009) and de Noblet-Ducoudre et al. (2012).

All the data was analyzed in a common rectangular 2.0-degree grid. Most of the LUCID GCM/LSMs were interpolated from grids of coarser resolution, while the ET products and the other observations−based dataset assessed were degraded from their corresponding finer projections.

3.3.2.2. Regional Multivariate Regression

We use a regional-weighted multivariate analysis (hereafter RMA) to derive empirical ET models as function of a few explanatory variables: the land-cover partitioning, the incoming radiation at the surface (short- and long-wave), precipitation and the snowpack. The biogeography was characterized by the grid areal fraction (F_v) of four groups of vegetation (crops, grass, deciduous trees and evergreen trees) in addition to that of bare soil. We use these five main land-cover types to simplify the analysis and have consistent vegetation partitioning within the different land-cover dataset used. These vegetation groups are used to capture the spatial ET variability induced by differences in those properties inherent to the type of vegetation, such as canopy conductance, root length, surface roughness, albedo (from canopy), foliage density and others.

The available energy at surface in the form of radiation is calculated from both the incoming shortwave (S_D) and longwave (L_D) components. As previously mentioned, the surface albedo is implicitly taken in account through F_v; we choose this option instead of explicitly including the albedo as predictor in order to include the radiative effect of LULCC in the diagnosed ET changes (i.e., the change in surface albedo remain constrained to a perturbation in land cover and not to a prescribed value). Snow water equivalent (SWE) fields are used as ET predictor to account for the radiative effect of the snowpack in the surface energy budget. Soil moisture as a controlling variable for ET is implicitly accounted for through the monthly mean precipitation (P) and 1-month lag value (P_{-}). P_{-} is included to consider water storage and lagged effects of soil moisture from P.

The statistical model is constructed so as to fit the mean present-day observation derived value of ET in grid-cell (E_g) as a linear combination of the ET components associated to various land-cover groups, i.e.,

$$E_g = \sum_v F_v\, E_v(\beta, X) \tag{1}$$

where E_v is the ET function associated to each land cover group (i.e., $v = 1, 5$). E_v is defined as a second order polynomial expansion of our chosen set of environmental predictors $\boldsymbol{X}$. This set includes both monthly climatological means of S_D, L_D, P, P_{-} and SWE, and the departures from those means. Using quadratic forms within the regression basis, and splitting the explanatory variables in their long-term means and its anomalies, allows to better capturing the non-linear character of ET, notably in regards to precipitation.

Equation 1 fitted to observation-based ET then defines a large set of parameters $\boldsymbol{\beta}$ that are further calculated trough the RMA. This technique consists of linear regressions over global data, but computed regionally in order to maximize the local information. The RMA use monthly mean values as inputs but, in order to better capture the seasonal ET patterns, the calculations are done for each month of the year separately (i.e., the temporal variability is only accounted interannualy). The temporal and spatially varying data is computed over each grid-cell separately with weighted least squares regressions. Before each calculation, a subset of the entire dataset is randomly selected in order to have a constant distribution in the input data vector's number in relation to the distance between the analyzed grid-cell and the remote ones. Weight values associated to the chosen data vectors, decreasing with the distance from the assessed grid-cell, are applied in the least squares fitting calculations. The used weight function has the following form:

$$w(x) = d/(d+x), \tag{2}$$

where x is the distance from the given grid cell and d a parameter that define the spatial scale of the RMA (indicating the distance in which a remote information is given a weight of half of the local one). The value of *d* was set to 1000 km in order to capture regional features and consider sufficient climate and vegetation heterogeneity, necessary to nurture the RMA. This technique allows to better capture the spatial ET variability within a single land-cover type, that might be explained by factors that are taken in account in the observation-based ET products but not included as predictor in the RMA (e.g., foliage density).

Table 2. List of reconstructed ET climatologies.

Acronym	Land cover	ET source	Environmental drivers
		Simulation outputs	
O1992	1992 (ORCH)	ORCH-ON	PD (all)
O1870	1870 (ORCH)	ORCH-ON	PD (all)
O1870p	1870 (ORCH)	ORCH-ON	PD (L_D, S_D, SWE), PI (P, P_-)
O1870rp	1870 (ORCH)	ORCH-ON	PD (SWE), PI (L_D, S_D, P, P_-)
		Datasets	
Gmodis	2001 (MODIS)	GLEAM	PD (all)
G1992	1992 (ORCH)	GLEAM	PD (all)
G1870	1870 (ORCH)	GLEAM	PD (all)
Mmodis	2001 (MODIS)	MPI	PD (all)
M1992	1992 (ORCH)	MPI	PD (all)
M1870	1870 (ORCH)	MPI	PD (all)
Nmodis	2001 (MODIS)	NTSG	PD (all)
N1992	1992 (ORCH)	NTSG	PD (all)
N1870	1870 (ORCH)	NTSG	PD (all)

The input data for the MPI, GLEAM and NTSG related analyses are the MODIS land-cover maps for F_v and the selected 24-year (1983-2006) monthly data of L_D, S_D (both from SRB), P, P_- (from GPCC) and SWE (from NSIDC) (see Table 1). Global ET climatologies were then reconstructed using Equation (1) for each observation-based ET product with the same monthly varying dataset. This step was done three times to reconstruct ET from different land-cover maps (Table 2). The first reconstruction is based on the MODIS land-cover, which was further used to evaluate the RMA skill against each observation-based ET product (see Table 3). The two other reconstructed ET fields are calculated with respectively the ORCHIDEE land-cover maps of 1870 and 1992. The difference between the ET climatologies of these two reconstructions is further used to diagnose the LULCC–induced ET changes.

A parallel RMA analysis, using the ORCH-ON outputs, was performed to evaluate the ability of the used methodology to reproduce the ET between the two assessed periods. In this case, the predictand (ET) and predictor fields corresponding to one ensemble's member within the present-day (PD) runs (i.e., a 30-year simulation with the prescribed land-cover of 1992) was used to compute the RMA. The statistically (RMA) diagnosed changes in ET between the two periods were then compared to the simulated ET changes.

The set of reconstructed ET climatologies using the ORCH-ON data are also listed in Table 2. In this case, four reconstructions were computed: one associated to the present-day land cover (O1992) and meteorological drivers, and three other calculated with the land-cover of 1870. One of the latter differs from O1992 by the choice of land-cover only (O1870). This reconstruction echoes the preindustrial (PI) reconstructions computed with the ET products, since it is evaluated with the present-day values of the environmental drivers. The other two PI reconstructions also account for the simulated changes in precipitation (O1870p), and for both changes in precipitation and surface downward radiation (O1870rp). These two reconstructions were included to evaluate the indirect contribution of the precipitation and radiation changes in the ET responses to LULCC, components that were forcibly not taken in account in the ET estimates based in the MPI, GLEAM and NTSG products. The changes in snow cover/content (SWE) were not assessed because these are very weak and have shown not have significant impact on the surface radiation budget (Boisier et al., 2012).

3.3.3 Results

3.3.3.1. Annual mean evapotranspiration change

A summary of the RMA skill to predict the observed (GLEAM, MPI and NTSG) and the simulated (ORCH-ON) annual mean ET is presented in Table 3. The RMA-diagnosed global mean ET is consistent with the corresponding observed (simulated) values, with biases not larger than 1.5%. Logically, the errors are higher at the grid-cell scale, with typical values (mean absolute error) ranging from 17 mm/yr (3.2%), in the case of ORCH-ON, to 30 mm/year (5.6%) in the case of NTSG. The spatial patterns are very well reproduced in all the four datasets with correlations of about 0.99. The year-to-year variability is however much less accurately reproduced than the spatial one. The correlations between the grid-cells' predicted and observed time-series average (globally) around 0.87, in the IPSL analysis, and drop to around 0.76, 0.73, 0.68 in MPI, GLEAM and NTSG cases, respectively. These mean values result from comparatively weak and high correlations in the tropical and temperate regions, respectively (not shown).

The distribution of the annual mean LULCC−induced ET changes (PD-PI) simulated in ORCH-ON, ORCH-OFF and reconstructed (RMA) from the ORCH-ON simulation are illustrated in Figure 2. The ET responses to LULCC simulated by the coupled model show significant changes in those regions that have been subject to intense changes in vegetation, particularly in North America and Eurasia (Figure 2a). Neither the ORCH-ON simulations nor those of any other GCM/LSM that participated in LUCID show significant latent heat flux changes beyond the regions with land-cover changes (Pitman et al., 2009). The annual mean ET changes are mostly negative over regions where LULCC has taken place, with some localized positive responses such as in Australia or in the northeast North America. The annual mean ET changes resulting from the ORCH-OFF simulations are quite weaker than those from ORCH-ON, showing significant ET decreases constrained in the mid-west Eurasia and around the Gulf of Mexico (Figure 2b). The weak annual ET anomalies simulated in ORCHIDEE hide significant positive and negative ET changes occurring at different seasons (section that follows).

Table 3. Comparison between observed (simulated in the case of ORCH-C) and diagnosed (RMA) global-land (excluding Antarctica) annual mean evapotranspiration.

Source (period)	mean ET [mm/yr]	mean error [mm/yr]	MAE[a] [mm/yr]	r (spatial)	r[b] (temporal)
ORCH-ON (1970-1999)	533	−0.4 (−0.1%)	17 (3.2%)	0.99	0.87
MPI (1983-2006)	578	+8.0 (+1.4%)	25 (4.4%)	0.99	0.76
GLEAM (1983-2006)	556	+4.8 (+0.9%)	27 (4.8%)	0.98	0.73
NTSG (1983-2006)	534	−6.9 (+1.3%)	30 (5.6%)	0.99	0.68

[a] Mean absolute error.

[b] Calculated over each grid-cell and then averaged.

The simulated (ORCH-ON) ET change induced by LULCC in the Northern Hemisphere (NH) extratropics is fairy well reproduced by the RMA-based reconstructions when both changes in surface radiation and precipitation are included (i.e., O1992-O1870rp; Figure 2c). In contrast, the amplitudes of the reconstructed ET anomalies clearly overestimate those simulated in the tropics and Southern Hemisphere. In particular, the ET decreases in the African savannas obtained from the reconstructions are not simulated in ORCH-ON. A similar spatial pattern, but with lower amplitudes, results from the diagnosed ET changes computed with the RMA evaluated without changes in any environmental driver (i.e., O1992-O1870; Figure 2d). This dampened change in ET is principally due to the use of a fixed precipitation in both periods. This result is consistent with what is observed in the ensemble of LUCID simulations, in which the precipitation' changes appear as a significant indirect contributor to the ET responses to LULCC (Boisier et al., 2012).

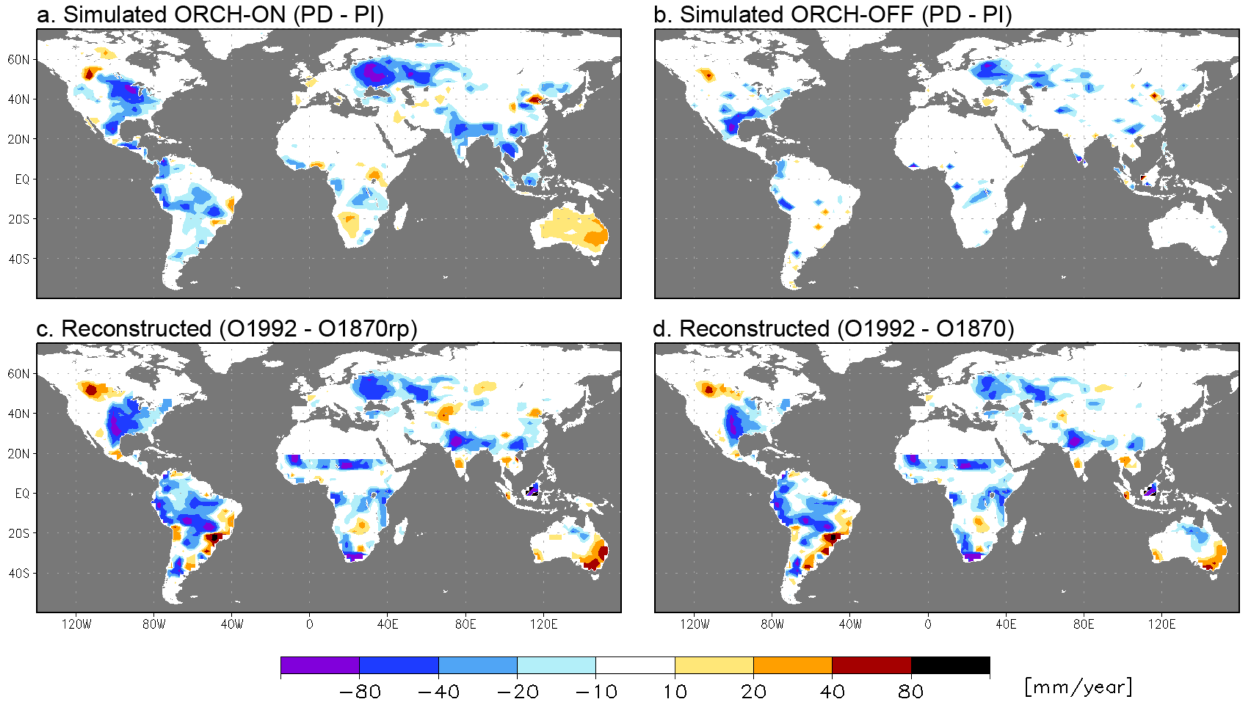

Figure 2: LULCC−induced annual evapotranspiration (ET) change (present-day – preindustrial) simulated by the coupled IPSL/ORCHIDEE model (a), simulated offline in ORCHIDEE (b) and statistically (RMA) reconstructed based on a present-day ORCH-ON simulation (c, d). In addition to the land-cover difference between 1870 and 1992, the reconstructed ET anomalies in plate (c) also accounts for changes in radiation and precipitation (see Table 2).

Figure 3 shows the RMA-diagnosed annual mean changes in ET (PD-PI) obtained from each of the three ET products assessed. Besides the ET changes diagnosed from NTSG, which shows ET increases over large areas in the northern extratropics, most part of the globe have associated decreases in ET. The three datasets show strong LULCC-induced impacts of LULCC on ET over North America, dominated by negative values (i.e., a loss of ET compared to 1870) in the central part of the continent. In general, a consistent decrease in ET is found in the three datasets over those regions where pasture has expanded between 1870 and 1992 in, e.g., southern South America, Africa, the north of Australia or around the Caspian Sea (see Figure 1). By contrast, the reconstructed ET changes are quite different upon GLEAM, NTSG and MPI over regions of cropland expansion, such as in the northeastern part of the North American Great Plains or in western Eurasia. In these regions, we infer a decrease of ET since 1870 with GLEAM and an increase with NTSG, while with MPI, there is a little decrease (Figure 3).

In terms of total water vapor, a global decrease between PI and PD of near 1800, 1340 and 2040 km^3 per year is estimated from the MPI, GLEAM and NTSG products, respectively (Table 4). These values are quite stronger than the global ET decrease simulated in ORCH-ON (−760 km^3/yr) and in ORCH-OFF (−471 km^3/yr), and than the inter-model mean LULCC signal of the seven LUCID GCM/LSMs of ~−650 km^3/yr (Table 4). The comparatively strong global

ET impact of LULCC diagnosed from the MPI and NTSG datasets is to a large extent explained by the tropical changes (with ET decreases larger than 1000 km^3/yr in both cases). These values could be overestimated, as the reconstructions based on ORCH-ON suggest (the reconstructed ET anomaly in the tropics overestimates by near 80% the simulated one; Table 4 and Figure 2).

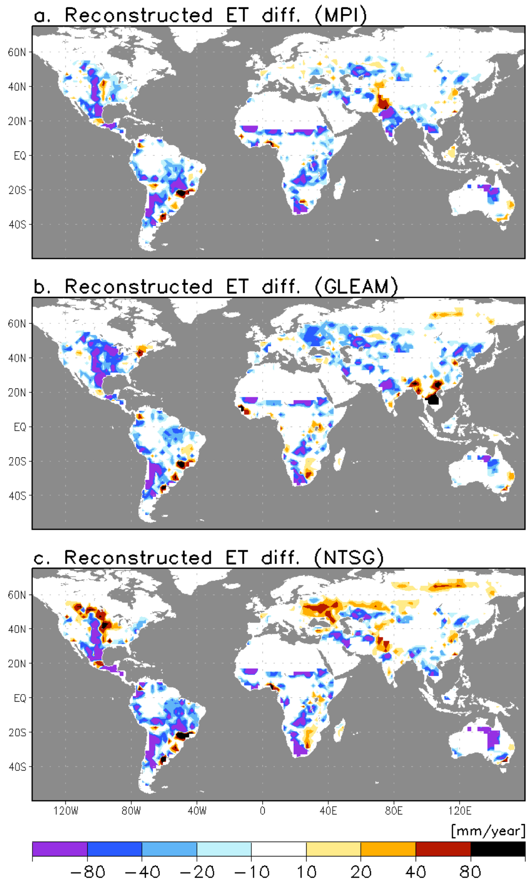

Figure 3: As for Figure 2, but for reconstructed ET changes based on the MPI (a), GLEAM (b) and NTSG (c) datasets.

Overall, the total ET difference between PI and PD estimated in the northern extratropical continents range from −295 km^3/yr (NTSG) to −823 km^3/yr (GLEAM). In this case, the diagnosed ET changes based on the ORCH-ON simulations are more accurately than in the tropics, showing a mean underestimation of ~10% compared to the values simulated (Table 4). As shown by Figure 3, the effect of LULCC on ET over northern temperate regions inferred from the NTSG dataset results into positive ET changes between 1870 and 1992, except for a region across the North American Great Plains, with a strong negative change. It is important to note, however, that the changes in global mean ET from 1870 to 1992 that we report in Table 4 do not only mask uneven spatial responses (as seen in Figure 3) but also different seasonal responses, which are examined in the following.

Table 4. Annual mean LULCC-induced evapotranspiration change [km^3/yr].

Source	Global	NH (> 25N)	Tropics	SH (< 25S)
Simulated				
ORCH-ON (PD−PI)	−760	−498	−275	+13
ORCH-OFF (PD−PI)	−471	−273	−198	+1
LUCID models (PD-PI)[a]	−652±800	−197±242	−395±573	−60±61
Reconstructed (RMA)				
ORCH-ON (O1992−O1870rp)[b]	−944 (−24%)	−443 (+11%)	−489 (−78%)	−11 (−184%)
IPSL (O1992−O1870p)	−1116	−539	−558	−20
IPSL (O1992−O1870)	−854	−361	−463	−30
MPI (M1992−M1870)	−1798	−461	−1124	−213
GLEAM (G1992−G1870)	−1340	−823	−289	−228
NTSG (N1992−N1870)	−2043	−295	−1275	−473

[a] The model mean ± the inter-model mean absolute deviation is given.
[b] In bracket values indicate the difference (in %) with regard to the simulated ET changes from ORCH-ON.

3.3.3.2. Seasonal ET changes in the northern extratropics

The LULCC−induced seasonal (monthly) changes in ET, averaged over the northern extratropical continents, are shown in Figure 4. The difference in ET between PI and PD simulated by the IPSL/ORCHIDEE model, both for the coupled and the offline simulations, show a marked seasonal cycle characterized by a positive difference in spring (March-April) and a negative one the rest of the year, with a noticeable minimum of near −150 km^3 in August (Figure 4a). This pattern is closely related to the way crop phenology is parameterized in ORCHIDEE, which is marked by an early start of the leaf onset and growing season compared to other LSMs (see de Noblet-Ducoudre et al., 2012). The resulting net leaf area index (LAI) increases as response to LULCC during the spring and early summer season over regions where cropland or pasture coverage has increased, and decreases during the late summer and fall (see Figure 5a).

The ET changes simulated in ORCH-OFF follow a similar seasonal pattern than the one obtained from the coupled simulations, but with a positive bias in May-June (red dotted line in Figure 4a). Hence, the increase in ET during the crops growing season appears to be nearly suppressed in the coupled simulations compared to that simulated offline. The resultant annual mean ET in the NH extratropics decreases PI to PD in both modeling experiences, but this decrease of ET is much smaller in ORCH-OFF in regard to ORCH-ON as seen in Figure 4 (and in Figure 2 for spatial patterns).

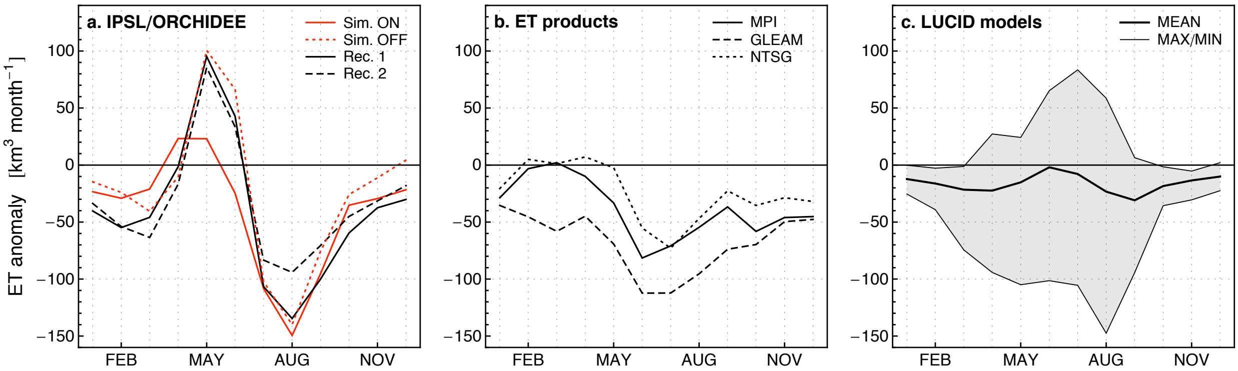

Figure 4: Monthly total ET change (PD-PI) averaged over the northern extratopical lands (beyond 25N). (a) Anomalies simulated in IPSL (solid red line), simulated in ORCHIDEE (dotted), and reconstructed with (solid black) and without (dashed) changes in radiation and precipitation. (b) Anomalies reconstructed from the MPI (solid line), GLEAM (dashed) and NTSG (dotted) datasets. (c) Anomalies simulated by seven GCMs in the context of the LUCID project. The inter-model mean, the minimum and the maximum anomalies of each month are indicated.

The seasonal pattern of the simulated LULCC−induced ET changes is well captured by the model−based ET reconstructions (black lines in Figure 4a). It is noteworthy that, although RMA is calibrated from the output of a coupled simulation, the diagnosed monthly ET changes follow more closely the changes obtained from the offline ORCHIDEE simulations, notably during spring when positive ET anomalies prevail (from April to June). The strong ET decreases simulated in ORCH-ON and ORCH-OFF during the late summer are well reproduced by the reconstructions when the changes (PD-PI) in the meteorological drivers are included (solid black line in Figure 4a). The change in ET reconstructed without accounting for changes in these drivers is also negative from July onward, but with a weaker amplitude (dashed line in Figure 4a). This difference is mainly the result of evaluating the RMA-based models with and without fixed precipitation (that decrease synchronously with ET this part of the year; not shown).

Although different in amplitude, the diagnosed changes in monthly ET obtained with the MPI, GLEAM and the NTSG datasets are similar in their seasonal variations (Figure 4b). All three reconstructions show total ET decreases between PI and PD for nearly the whole year, with a maximum difference centered on the summer. The GLEAM−based reconstruction shows the stronger summer ET decrease (of around 100 km^3/month) followed by that of MPI (~−70 km^3/month) and NTSG (~−60 km^3/month). Behind these differences, these results appear to be more consistent (i.e. less spread in the different reconstructions) than compared to the spread of ET changes in response to LULCC between pre-industrial and current land-cover, simulated by coupled models in the LUCID inter-comparison project (Figure 4c). The results of models run for the LUCID project did not show a robust (model-mean) ET change signal along the year due to different individual model responses to prescribed LULCC.

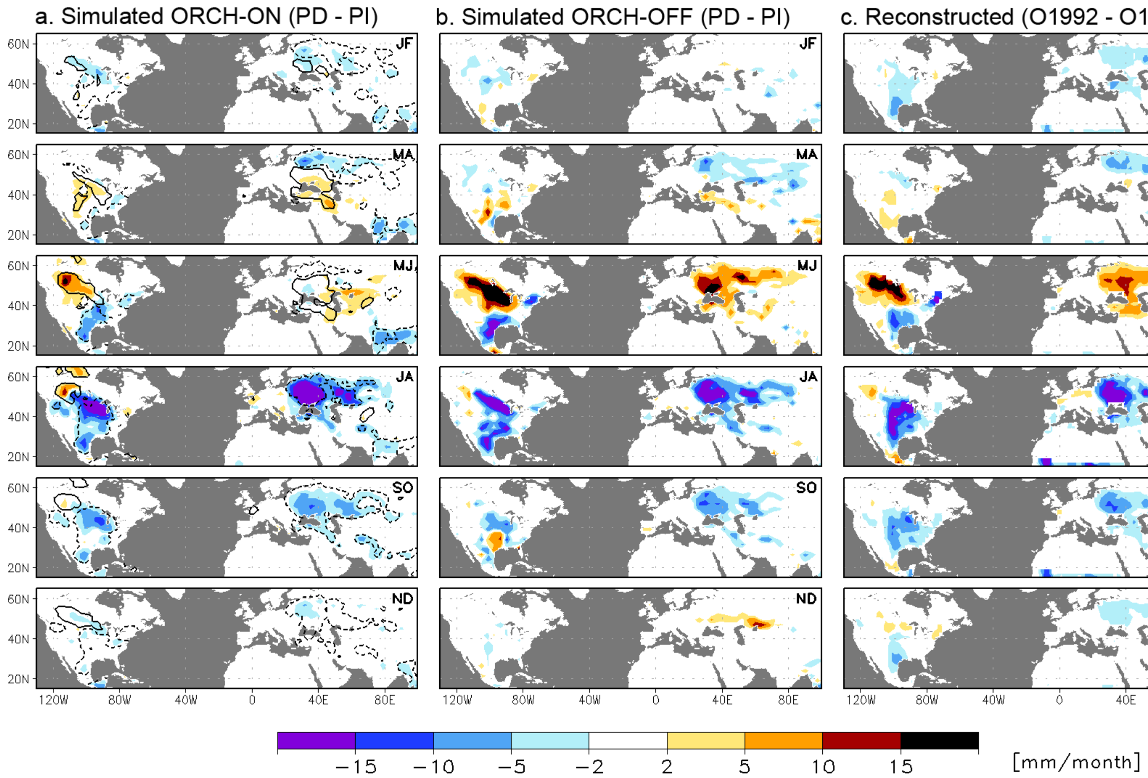

Figure 5: Seasonal mean (bi-monthly) LULCC-induced ET change (PD-PI) simulated by ORCHIDEE online (a), offline (b) and statistically (RMA) reconstructed based in ORCH-ON (c). Contour lines in (a) indicated the simulated (ORCH-ON) changes in LAI (solid and dotted isolines indicated LAI anomalies of +0.5 and -0.5).

The spatial distribution of the seasonal (bi-monthly) mean ET changes (PD-PI) are illustrated in Figure 5 for ORCHIDEE-based results, and in Figure 6 for those obtained from the GLEAM, MPI and NTSG products. These maps are restricted to North America and western Eurasia, where the strongest extratropical LULCC have occurred between the two assessed periods (Figure 1). As commented above, the simulated ET changes by ORCHIDEE (coupled and uncoupled) exhibit an abrupt shift from weaker or positive anomalies during the spring and early summer to negative anomalies during the late summer and fall, and this seasonal footprint in the ET difference clearly reflects changes in LAI (indicated by contour lines in Figure 5a). Although with a similar spatial and temporal pattern, the positive ET difference simulated in ORCH-OFF in May-June (Figure 5b) are stronger than the ones simulated in ORCH-ON during the same season (Figure 5a). The dampened response derived from the coupled model runs compared to that of the offline ones, also seen in Figure 4, is particularly pronounced over Eurasia in May-June, where no clear LULCC signals are found from ORCH-ON in contrast to the clear ET increases obtained in ORCH-OFF.

The main pattern of the simulated ET changes in the North America and Eurasia is well reproduced by the RMA-reconstructed ET changes based on the ORCH-ON output (Figure 5c). Yet, looking at regional details, some clear differences appear. For instance, the reconstructed ET difference underestimate and overestimate the July-August ET changes simulated in ORCH-ON in the northern and central North America, respectively.

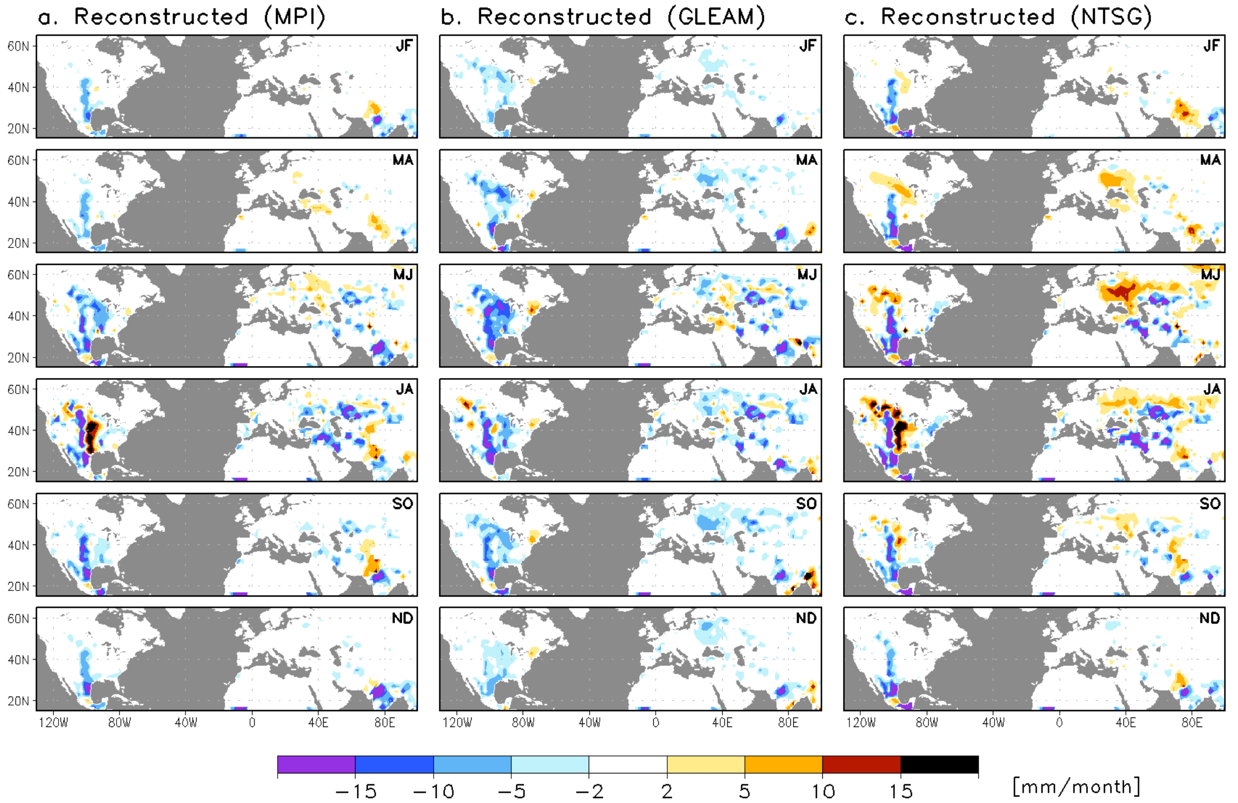

Figure 6: As for Figure 5, but for reconstructed ET changes based on the MPI (a), GLEAM (b) and NTSG (c) datasets.

The North American Great Plains region appears to be as a hotspot of strong ET changes between PI and PD in all the reconstructed datasets. The seasonal maps of ET difference reconstructed with GLEAM, MPI and NTSG datasets show a change in sign from negative values in the west part of the Great Plains to positive values in the east part of this region (Figure 6). In general, the ET differences derived from the three assessed ET products show a similar geographic and seasonal pattern in North America and Eurasia, characterized by anomalies in both directions with larger amplitudes during the late spring and summer. Superimposed to this shared spatial distribution, the three datasets show large-scale biases between them. The reconstructed ET response to LULCC based on GLEAM is more negative than with the other two products, showing therefore the stronger negative anomalies, notably from May to August, and the weaker positive ones. In turn, the ET difference reconstructed with the NTSG dataset shows a clear positive bias compared to the two other maps. The results obtained with this product show an area of positive ET difference over central-east US, which further extends northward and westward in the northern spring and summer. The maps of ET difference reconstructed with NTSG also show clear positive values in Eurasia, notably during the late spring, similar to that simulated in ORCHIDEE (Figure 5).

The spatial distribution of the reconstructed ET changes based on the observation-driven products also suggests different seasonal cycles from one region to another. This is more clearly appreciable in the NTSG–based estimates, showing maximum ET increases occurring earlier in Eurasia (May-June) compared to North America (July-August).

As commented in the precedent section, the patterns of reconstructed ET changes show a spatial coherency to the patterns of the imposed land-cover conversions (Figure 1). The regions that exhibit significant ET increases between preindustrial and present-day tend to match areas where crops expanded to the detriment of grasslands (Figure 6). Conversely, strong ET decreases between PI and PD are obtained in areas where forests have been cleared for pastures. Although this response of ET is qualitatively consistent between the reconstructions, the three assessed products show different ET sensitivities to each different type of LULCC. In order to evaluate these sensitivities to each specific land conversion type, we have defined a measure of the local ET change as a function of a perturbation in one land cover type with respect to another. This normalized ET response is defined in the following way:

$$\delta_{ET}(1 \rightarrow 2) = \frac{2\Delta ET}{\Delta F_2 - \Delta F_1} \tag{3}$$

where ΔET is the LULCC–induced ET change in a grid-cell and ΔF_i is the corresponding change in the surface area fraction of the land cover i. Thus, $\delta_{ET}(1 \rightarrow 2)$ estimates the expected ET change that should occur in a grid-cell when it is totally converted from one land cover type (1) to another (2).

Figure 7 illustrates the seasonal cycle of monthly δ_{ET} resulting from the ET reconstructions based on GLEAM, NTSG and MPI. The mean values of δ_{ET} were calculated for the North American and Eurasian regions separately, and for three kinds of land conversion: forest-to-grass (or pasture), grass-to-crop and forest-to-crop. To avoid misleading results, only those grid-cells that show a change in the fraction of the two land-cover groups considered (e.g., forest and grass/pasture in Figure 7a) at least four times larger than that of any other land cover type, have been included in the calculation of regional averages values of δ_{ET} show in Figure 7.

Reconstructions based on the three products show a quite similar ET response to land conversion from forest to pasture, with negatives δ_{ET} values (ET decreases) throughout the year but maximized in summer (Figure 7a). The data in Figure 7a also suggest a higher ET sensitivity to this type of land-cover change in North America than in Eurasia.

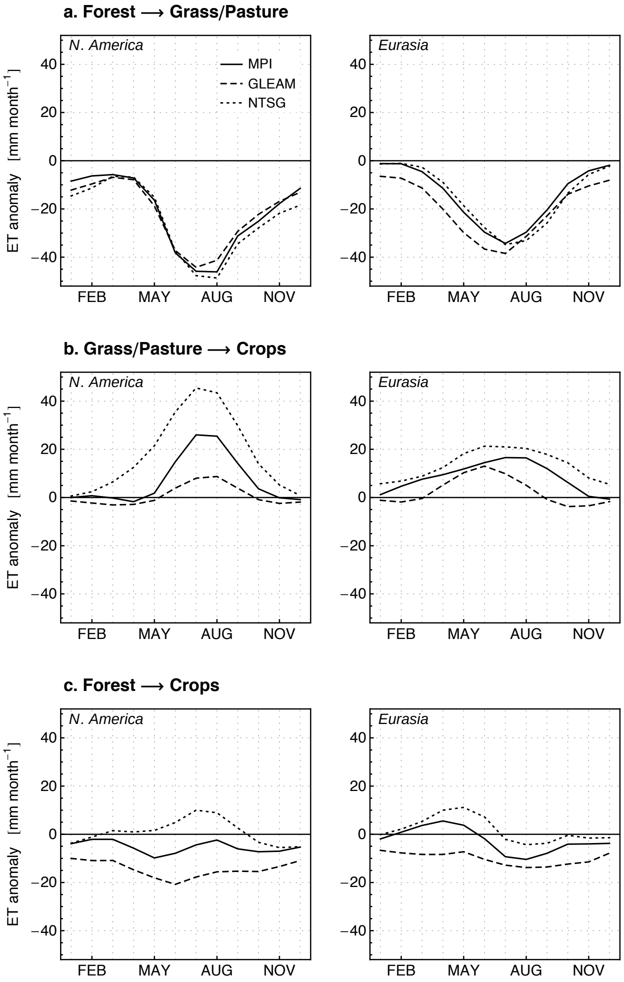

Figure 7: Monthly mean normalized LULCC-induced ET changes (δ_{ET}; see Equation 3) for land conversions from forest to grass (a), from grass to crops (b) and from forest to crops (c) based on GLEAM (dashed lines), MPI (solid) and NTSG (dotted) ET reconstructions. Averaged δ_{ET} over North America (right) and Eurasia (left).

The seasonal variation of δ_{ET} shows different sensitivities of ET changes due to LULCC between the products used for reconstructions, in the case of grassland or forest being replaced by crops. All three products coincide in that crops evaporate more than grasses in both North America and Eurasia (Figure 7b). Grassland to cropland conversion in North America leads to a summer ET increases of ~ 40 mm/month when calculated from the NTSG dataset, i.e., an impact of the same amplitude but in opposite direction compared to when forest is replaced by pasture (Figure 7a). Reconstructions from MPI and GLEAM results into a significantly lower

ET sensitivity to grass-to-crops changes than NTSG, with a summer ET anomaly of ~25 mm/month and ~10 mm/month, respectively. In the case of NTSG, the conversion of grass to crop leads to a much smaller ET response over Eurasia than over North America. In turn, GLEAM shows a slightly stronger response in Eurasia and a maximum impact shifted to the late spring.

The monthly values of δ_{ET} are less clearly defined in the case of a forest to cropland transition (Figure 7c). In North America, this type of land-cover change is estimated to produce a weak summer mean ET increase when calculated from NTSG, and a decrease rather constant throughout the year from GLEAM and MPI. In Eurasia, δ_{ET} calculated from NTSG and MPI show similar seasonal variations, with slightly positive and negatives anomalies during respectively the spring and late summer.

3.3.4 Discussion

We developed a multivariate statistical tool (RMA) to estimate the past LULCC-induced changes in ET, with a calibration of the RMA on three different observation-based global ET products. These products do not represent mapped ET observations during the assessed period (1983-2006), but are themselves statistical ET estimations using as input satellite and ground-based observations, and global-scale climatic variables and land surface properties for extrapolation to global gridded products. In this sense, the results here presented should be carefully interpreted since they are the result of two statistical analyses (the one used here in addition those used originally to derive those products).

The predictability skill of the RMA to reconstruct any ET field used for calibration is quite good given the limitations of the method (predictor number, time scale, simplicity of the empirical model, etc). When applied to 'cracking' the ET field generated by the complex coupled IPSL/ORCHIDEE model, the reconstructed annual ET distribution matches is particularly faithful, showing a typical grid error of ~3%, a spatial correlation of 0.99 and a grid mean interannual correlation of 0.87 (Table 3). When applied to reconstruct ET from the MPI, GLEAM and NTSG products, the agreement within reconstructed and original ET is lower than in the case of the IPSL model result, but remains quantitatively good. This is noteworthy given the independency between the ET datasets and the explanatory variables' data (in most cases different than those used originally to derive the ET products, Table 1). Withal, a typical error in ET reconstructed in a given grid-cell, around 25-30 mm/year (~5%), remains of the same order than the diagnosed LULCC-induced ET changes in regions of strong land cover perturbations

(Figure 3). Because of that, is of crucial importance that the reliability of the statistical model in reproducing the LULCC signals simulated in IPSL/ORCHIDEE. The estimated ET changes based on this model have shown quite a good reproduction of the main picture of the seasonal ET responses to LULCC simulated in the NH extratropics (Figure 5). In turn, the reconstructed ET changes significantly overestimated the tropical responses (Figure 2).

The diagnosed global mean ET changes between PI and PD range from near −1300 km^3/yr (GLEAM) to ~ −2000 km^3/yr (MPI). Given that the preindustrial reconstructions were evaluated using the present-day values for the environmental drivers (and, implicitly, present-day atmospheric CO_2 concentrations), the estimated ET changes do not consider any LULCC-related biogeophysical feedback. LUCID simulations have shown that precipitation tend to respond to LULCC synchronously with the changes in ET, amplifying the LULCC impact on ET when atmospheric feedbacks are accounted for (Boisier et al., 2012). However, the RMA-estimated global ET changes could be overestimated because the reconstructions lack a well characterized impacts in the tropics, as the analysis doing with the IPSL/ORCHIDEE outputs tend to show. Nevertheless, the obtained values are roughly consistent with the recent estimate by Sterling et al. (submitted; personal communication of Agnès Ducharne). Based on observations, they calculate a global ET decrease of near 3500 km^3/yr, i.e., larger than our estimates but associated to a LULCC from a potential (pre-agricultural) land-cover to the current one (i.e., a stronger perturbation than the one used here). The estimates of ET changes found in this study are clearly stronger than that reported by Gordon et al. (2005) between a pre-agricultural land-cover and a present-day one of ~−400 km^3/yr, including both the deforestation and irrigation effects.

Although irrigation is not explicitly taken account for in this study, it is implicitly included in the MPI and NTSG products thought their related Flux-Net data upscaling and calibration, respectively. It is noteworthy than the larger increase in ET as responses to the croplands expansion (from grass or forest) are obtained from these two datasets (Figure 7).

It is important to note that in this study we have chosen the specific set of land-cover maps of 1870 and 1992 used in ORCHIDEE to evaluate the changes in ET since the preindustrial period. Hence, the LULCC imposed results from the specific strategy used to incorporate historical agricultural data into the ORCHDEE vegetation maps. LUCID have shown that the rules adopted to create land cover maps could widely affect the character and amplitude of land conversion and the resulting impacts of LULCC in climate (de Noblet-Ducoudre et al., 2012). The uncertainties due to the imposed LULCC in the estimated ET changes following the methodology developed in this study were therefore not assessed here.

3.3.5 Conclusions

The present study estimates the global impact of the past land-use–induced land cover change (LULCC) on evapotranspiration (ET). The methodology used projects present-day global ET to the past, based on a land-cover distribution of 1870. This reconstruction lies on a multivariate analysis (RMA) of current spatially and time varying (1983-2006) ET data from three different state-of-the-art observation-based ET products. In order to evaluate RMA reliability to represent the past ET changes, the same technique was applied on a present-day global simulation carried out in the IPSL/ORCHIDEE global climate model. The resulting diagnosed changes in ET have then been compared to the ones simulated. The method has been shown to be able to reproduce the major ET signals of LULCC simulated, particularly those of the Northern Hemisphere lands.

A global ET decrease of 1300-2000 km^3/yr has been obtained in accordance with recent estimates based on observations (Sterling et al., submitted). The impact of LULCC is highly regionally and seasonally dependent, so the annual mean changes mask strong seasonal patterns. While few studies have estimated the global ET changes globally (Gordon, Sterling), none of them have brought estimations at the seasonal time scales.

While most of the globe shows strong ET decreases, especially where pasture expands in detriment of forest, our results also show extensive areas of ET increases in the Northern Hemisphere extratropics, notably during the corresponding spring and summer. Increases in ET occur in regions of intense crops expansion, highlighting the high ET efficiency of (well-watered) crops in two out of three of the assessed datasets (MPI, NTSG). The elevated ET of temperate crops is in accordance to observation, as e.g. Baldocchi et al. (1997) or Teuling et al (2010) have shown.

We show that the different estimated ET changes since the preindustrial period found with the different ET products assessed mainly depend on the rates of ET these products show for croplands. In the same ground, the changes in ET resulting from land conversions that do not include change in crop area (e.g. from forest to pastureland) are widely consistent within the three dataset-based estimates. Averaged on large regions, the diagnosed impacts of LULCC on ET (mainly ET reductions after deforestation) are more consistent within the different ET products assessed than the ET changes simulated between the same periods by the ensemble of models that participated in LUCID.

The increasing number of ground-based ET observations and satellite data, combined with statistical tools, are very helpful not only to estimate current large-scale ET, but also to constraint our uncertainties looking the past changes of the global hydrological cycle due to LULCC or other climate forcings, and compare with models simulations. The results presented here try to step forward in that direction.

References

Adegoke, J. O., R. A. Pielke Sr., J. Eastman, R. Mahmood, and K. G. Hubbard (2003), Impact of irrigation on midsummer surface fluxes and temperature under dry synoptic conditions: A regional atmospheric model study of the U.S. High Plains, Mon. Weather Rev., 131, 556–564, doi:10.1175/1520-0493(2003)131<0556:IOIOMS>2.0.CO;2.

Armstrong, R. L., M. J. Brodzik, K. Knowles, and M. Savoie. 2007. *Global Monthly EASE-Grid Snow Water Equivalent Climatology*. Boulder, Colorado USA: National Snow and Ice Data Center. Digital media.

Baidya Roy, S., G. C. Hurtt, C. P. Weaver, and S. W. Pacala (2003), Impact of historical land cover change on the July climate of the United States, *J. Geophys. Res.*, 108(D24), 4793, doi:10.1029/2003JD003565.

Baldocchi DD, Vogel CA, Hall B. Seasonal variation of energy and water vapor exchange rates above and below a boreal jackpine forest. J Geophys Res 1997;102:28939–52.

Betts, R.A. (2001) Biogeophysical impacts of land use on present-day climate: near-surface temperature and radiative forcing. Atmos Sci Lett 2: 39–51, DOI 10.1006/asle.2001.0023

Boisier, J. P., N. de Noblet-Ducoudré, A. J. Pitman, F. T. Cruz, C. Delire, B. J. J. M. van den Hurk, M. K. van der Molen, C. Muller, and A. Voldoire (2012), Attributing the impacts of land-cover changes in temperate regions on surface temperature and heat fluxes to specific causes: Results from the first LUCID set of simulations, J. Geophys. Res., 117, D12116, doi:10.1029/2011JD017106.

Bonan, G. B. (2008), Forests and climate change: Forcings, feedbacks, and the climate benefits of forests, Science, 320, 1444–1449.

Bounoua, L., R. DeFries, G. J. Collatz, P. Sellers, and H. Khan (2002), Effects of land cover conversion on surface climate, *Climatic Change*, *52*, 2964.

Brovkin, V., T. Raddatz, C. H. Reick,M. Claussen, and V. Gayler (2009), Global biogeophysical interactions between forest and climate, Geophys. Res. Lett., 36, L07405, doi:10.1029/2009GL037543.

Costa, M. H., and J. A. Foley (2000), Combined Effects of Deforestation and Doubled Atmospheric CO2 Concentrations on the Climate of Amazonia. *J. Climate*, **13**, 18–34.

da Rocha, H. R., et al. (2009), Patterns of water and heat flux across a biome gradient from tropical forest to savanna in Brazil, *J. Geophys. Res.*, 114, G00B12, doi:10.1029/2007JG000640.

de Noblet-Ducoudré, N., J. Boisier, A. Pitman, G. Bonan, V. Brovkin, F. Cruz, C. Delire, V. Gayler, B. van den Kurk, P. Lawrence, M. van der Molen, C. Müller, C. Reick, B. Strengers, and A. Voldoire (2012), Determining robust impacts of land use induced land-cover changes on surface climate over North America and Eurasia; Results from the first set of LUCID experiments. *J. Climate*. doi:10.1175/JCLI-D-11-00338.1, 2012.

Douglas, E. M., D. Niyogi, S. Frolking, J. B. Yeluripati, R. A. Pielke Sr., N. Niyogi, C. J. Vörösmarty, and U. C. Mohanty (2006), Changes in moisture and energy fluxes due to agricultural land use and irrigation in the Indian Monsoon Belt, *Geophys. Res. Lett.*, 33, L14403, doi:10.1029/2006GL026550.

Gordon, L. J., Steffen, W., Jonsson, B. F., Folke, C., Falkenmark, M., and Johannessen, A. (2005), Human modification of global water vapor flows from the land surface, Proc. Natl. Acad. Sci., 102, 7612–7617, doi:10.1073/pnas.0500208102

Govindasamy, B., P. B. Duffy, and K. Caldeira (2001), Land use changes and Northern Hemisphere cooling, *Geophys. Res. Lett.*., *28*, 291294.

Haddeland, I., Skaugen, T., and Lettenmaier, D. P.: Hydrologic effects of land and water management in North America and Asia: 1700–1992, Hydrol. Earth Syst. Sc., 11, 1035–1045, 2007.

Jimenez, C., et al. (2011), Global inter-comparison of selected 1993–1995 monthly averaged land surface heat fluxes, J. Geophys. Res., 116, D02102, doi:10.1029/2010JD014545.

Jung, M., et al. (2010), Recent decline in the global land evapotranspiration trend due to limited moisture supply, Nature, 467(7318), 951–954, doi:10.1038/nature09396.

Klein Goldewijk, K. (2001), Estimating global land use change over the past 300 years: The Hyde database, {\it Global Biogeochem. Cycles}, \textit{15}(2), 417–433.

Krinner, G., N. Viovy, N. de Noblet-Ducoudre, J. Ogée, J. Polcher, P. Friedlingstein, P. Ciais, S. Sitch, and I.C. Prentice (2005), A dynamic global vegetation model for studies of the coupled atmosphere-biosphere system, {\it Global Biogeochem. Cycles}, \textit{19}, GB1015. doi: 10.1029/2003GB002199.

Lee, E., W. J. Sacks, T. N. Chase, and J. A. Foley (2011), Simulated impacts of irrigation on the atmospheric circulation over Asia, J. Geophys. Res., 116, D08114, doi:10.1029/2010JD014740.

Lobell, D. B., G. Bala, and P. B. Duffy, 2006: Biogeophysical impacts of cropland management changes on climate. *Geophys. Res. Lett.,* **33,** L06708, doi:10.1029/2005GL025492.

Lobell, D. B., C. Bonfils, 2008: The Effect of Irrigation on Regional Temperatures: A Spatial and Temporal Analysis of Trends in California, 1934–2002. *J. Climate*, **21**, 2063–2071.

Loveland, T., B. Reed, J. Brown, D. Ohlen, Z. Zhu, L. Yang, and J. Merchant (2000), Development of a global land cover characteristics database and IGBP DISCover from 1 km AVHRR data, Int. J. Remote Sens., 21, 1303– 1330.

Mahmood, R., S. A. Foster, T. Keeling, K. G. Hubbard, C. Carlson, and R. Leeper (2006), Impacts of irrigation on 20th century temperature in the northern Great Plains, Global Planet. Change, 54, 1–18.

Marti, O., P. Braconnot, J. L. Dufresne, J. Bellier, R. Benshila, S. Bony, P. Brockmann, P. Cadule, A. Caubel, F. Codron, N. de Noblet-Ducoudre, S. Denvil, L. Fairhead, T. Fichefet, M. A. Foujols, P. Friedlingstein, H. Goosse, J. Y. Grandpeix, E. Guilyardi, F. Hourdin, G. Krinner, C. Lévy, G. Madec, J. Mignot, I. Musat, D. Swingedouw, and C. Talandier (2010), Key features of the IPSL ocean atmosphere model and its sensitivity to atmospheric resolution, *Clim. Dyn*., 34, 1–26, DOI 10.1007/s00382-009-0640-6.

Miralles, D. G., Holmes, T. R. H., De Jeu, R. A. M., Gash, J. H., Meesters, A. G. C. A., and Dolman, A. J.: Global land-surface evaporation estimated from satellite-based observations, Hydrol. Earth Syst. Sci., 15, 453-469, doi:10.5194/hess-15-453-2011, 2011.

Nobre, C. A., P. J. Sellers, and J. Shulka (1991), Amazonian deforestation and regional climate change, J. Clim., 4, 957–988.

Mueller, B., et al. (2011), Evaluation of global observations-based evapotranspiration datasets and IPCC AR4 simulations, Geophys. Res. Lett., 38, L06402, doi:10.1029/2010GL046230.

Piao, S., Friedlingstein, P., Ciais, P., de Noblet-Ducoudré, N., Labat, D., Zaehle, S., 2007. Changes in climate and land use have a larger direct impact than rising CO2 on global river runoff trends. Proc. Natl. Acad. Sci. 104, 15.242–15.247.

Pielke Sr., R.A., A. J. Pitman, D. Niyogi, R. Mahmood, C. McAlpine, F. Hossain, K. Goldewijk, U. Nair, R. Betts, S. Fall, M. Reichstein, P. Kabat, and N. de Noblet-Ducoudré (2011), Land use/land cover changes and climate: Modeling analysis and observational evidence, WIREs Clim. Change, doi: 10.1002/wcc.144

Pitman, A. J., N. de Noblet-Ducoudre F. T. Cruz, E. L. Davin, G. B. Bonan, V. Brovkin, M. Claussen, C. Delire, L. Ganzeveld, V. Gayler, B. J. J. M. van den Hurk, P. J. Lawrence, M. K. van der Molen, C. Mueller, C. H. Reick, S. I. Seneviratne, B. Strengers, and A. Voldoire (2009), Uncertainties in climate responses to past land cover change: First results from the LUCID intercomparison study, *Geophys. Res. Lett.*, 36, L14814, doi:10.1029/2009GL039076.

Puma, M. J., and B. I. Cook (2010), Effects of irrigation on global climate during the 20th century, J. Geophys. Res., 115, D16120, doi:10.1029/2010JD014122.

Ramankutty, N., and J. A. Foley (1999), Estimating historical changes in global land cover: Croplands from 1700 to 1992, Global Biogeochem. Cycles, 13, 997–1027.

Roy, S. S., R. Mahmood, D. Niyogi, M. Lei, S. A. Foster, K. G. Hubbard, E. Douglas, and R. Pielke Sr. (2007), Impacts of the agricultural Green Revolution–induced land use changes on air temperatures in India, J. Geophys. Res., 112, D21108, doi:10.1029/2007JD008834.

Rudolf, B., et al. (2010): GPCC Status Report December 2010.

Sampaio, G., C. Nobre, M. H. Costa, P. Satyamurty, B. S. Soares-Filho, and M. Cardoso (2007), Regional climate change over eastern Amazonia caused by pasture and soybean cropland expansion, Geophys. Res. Lett., 34, L17709, doi:10.1029/2007GL030612.

Scanlon, B. R., Jolly, I., Sophocleous, M., and Zhang, L.: Global impacts of conversions from natural to agricultural ecosystems on water resources: Quantity versus quality, Water Resour. Res.,43, W03437, doi:10.1029/2006WR005486, 2007.

Sterling, S.M., A.D. Ducharne, M. Mancip, J. Polcher, S. Rojstaczer, L. Bozec*. Impact of Land Cover Change on the Terrestrial Hydrologic Cycle: Implications for Human Induced Change in Evapotranspiration and Runoff. Nature Climate Change, in review NCLIM-12010012.

Teuling AJ, Seneviratne SI, Stockli R, Reichstein M, Moors E, Ciais P, Luyssaert S, van den Hurk B, Ammann C, Bernhofer C, et al. Contrasting response of European forest and grassland energy Exchange to heatwaves. *Nature Geosci* 2010, 3:722–727. doi:10.1038/NGEO950.

Zhang, K., J.S. Kimball, R.R. Nemani, and S.W. Running (2010), A continuous satellite-derived global record of land surface evapotranspiration from 1983 to 2006. Water Resources Research, 46, W09522, doi:10.1029/2009WR008800.

3.4 Chapter summary

Based on present-day observation-based datasets, this chapter presented two studies that estimate the changes in respectively the surface albedo and evapotranspiration induced by land-cover changes since the preindustrial period. The goal of these studies is twofold: bring realistic estimations of the LULCC-induced changes in these variables independently from climate simulations, and use them as benchmark for model results.

The MODIS-based estimates of surface albedo change is coherent with what LUCID models simulate altogether (model-mean signal), but reveal important model deficiencies when compared individually to reference dataset. The biases in the simulated albedo changes between the preindustrial and present-day with respect to what is expected following current observation explain the different impacts on the surface radiation budget and, therefore, an important fraction of the uncertainties in the simulated climate responses to LULCC. This result highlights the need of more in-depth evaluations and improvements of the land-surface albedo parameterizations in LSMs.

LULCC-induced changes in evapotranspiration (ET) between 1870 and 1992 were estimated from three present-day global ET products. The results show that decreases in ET have dominated in areas where past LULCC involved deforestation. The ET changes are however very seasonally and geographically dependent, and some regions with large cropland expansion may have produced large increases in ET. These results have an important degree of uncertainty, in part because of the nature in the used datasets themselves (statistically-based), and because of limitations in the methodology adopted to estimate the past ET changes. The results based on these three different datasets, which use different approaches to map their ET values, show however a good agreement within them if compared to the spread in the ET responses to LULCC simulated within LUCID. The results also suggest that the differences found in the diagnosed ET changes are principally led by the ET rates that the different products show over croplands.

Chapter 4

Land-use and climate changes from the preindustrial period to the end of the 21st century

4.1 Introduction

Continental landscapes are nowadays evolving and are expected to be under strong pressure during the 21st century due to human activities. Such pressure will be directly exerted by means of land-use activities related to food, energy and environmental requirements, and might be indirectly exerted through changes in the global carbon cycle and climate. The future evolution of tropical forest is a question of particular interest because of its major role in regulating the global water and carbon cycles and, consequently, the climate.

Production of biomass and its derived products for heating and electricity, such as ethanol or biodiesel, have dramatically increased in the last decade and should play a major role in the near future as a renewable source of energy (Coyle, 2007). Crop plantations for the production of biofuels, such as of corn in North America –the world largest ethanol producer– or those of sugarcane and soybean in Brazil, to respectively produce biodiesel and ethanol, have been established over secondary lands principally (i.e., previously managed areas). The extensive tropical forest clearing that occurred since the mid-20th century in, e.g., Central America or the Amazonia, has been motivated by cattle activities principally (Fearnside, 2005). However, there is an increasing opinion that oil price and the biofuels market are playing a major role as tropical deforestation drivers. The rising soy price that follows the increasing demand for biofuels and animal ration has put additional pressure on the Amazon due to direct deforestation to allocate cropland, or the use of pasture areas for soybean plantations that lead to more forest clearing elsewhere (Morton et al., 2006; Nepstad et al., 2008).

Besides the local impacts, future deforestation following the current rates could significantly contribute to the global climate trends by altering the global carbon budget. In the same sense, carbon sequestration by means of reforestation and afforestation has also been proposed as one of the leading mitigation strategies to climate change (Nabuurs et al., 2007). The environmental and energy requirements are subject to debate because of their confronting demand for land and water, and particularly because of their uncertain sustainability in time along with the increasing food necessities (e.g., Fischer and Schrattenholzer, 2001; Campbell et al., 2008). The future evolution of climate due to land-use changes is also uncertain because of its secondary effects. For instance, some studies have alerted the misleading view with regard to the climate responses of large-scale reforestation when the associated biogeophysical effects are ignored (e.g., Betts, 2000; Arora and Montenegro, 2011; Swann et al., 2011).

In contrast to the considerable research on the past large-scale LULCC and its impacts on climate (see Chapter 1), few studies have addressed future scenarios of land-use and the potential climate responses. Based on the IMAGE 2.2 land-use scenario, DeFries et al. (2002) showed that forest topical clearing and the resulting transpiration decrease could dry the local climate and increase surface temperature by 2 K. Sitch et al. (2005) investigated both the biogeochemical and biogeochemical effect in climate following different SRES LULCC scenarios. They show that the biochemical effect dominates within the LULCC signals in climate, amplifying the GHG-induced warming due to fossil fuel emissions. Regarding only the biogeophysical effects of LULCC, Feddema et al. (2005b) alert for the different temperature trends in some regions when land-use change is included in climate projections based in SRES A2 and B1 scenarios. Consistent with other studies, they found that tropical and extratropical deforestation leads to local warming and cooling, respectively. Based on global simulations with the SRES B2 scenario combined with a coherent land-use scenario, Voldoire (2006) also shows that LULCC could significantly affect the regional climate projections, with temperature responses that vary in up to 30% in comparison to those induced by changes in CO_2 concentrations.

Arora and Montenegro (2011) performed a series of modeling experiments to explore the net effect of global afforestation scenarios of 50% and 100% of the current croplands. They pointed out that although afforestation produces a net global cooling of up to half a degree, this effect is far from counteracting the global warming induced by fossil-fuel GHG emissions. They also show that the expected climate impact of such large-scale afforestation (cooling) is more effective in the tropics than in mid-latitudes regions due to biogeophysical effects.

Trends in global climate and in the biogeochemical cycle might also drive changes in terrestrial ecosystems functions (e.g., carbon allocation or water use efficiency) as well as in the land-cover distribution. A number of GCMs project to the end of the 21st century global climate trends with an *El Niño*-like pattern and, consistent with this, some of them simulate a drying tendency in northeastern South America (Christensen et al., 2007). The increasing frequency in drought and fire in the Amazon, and the potential forest dieback described by Cox et al. (2004) represent a crude scenario in response to shifts in the tropical circulation and in the surface climate. Although other studies have not found such extreme impact (e.g., Sitch et al., 2008), the vulnerability of the Amazon to both the large-scale climate forcing and LULCC remains an open question that relies on the possibility of multiple equilibrium states between the vegetation distribution and the local climate (e.g., Oyama and Nobre, 2003; Hirota et al., 2011; see also the review by Nepstad et al., 2008, and references therein). The potential risk of non-reversible impacts and, if exist, the tipping points from which human perturbations could catalyze a natural evolution to other Amazonian states (e.g., savannization) are key matters that are being addressed in the context of the international initiative AMAZALERT (EU-FP7 project; see http://www.eu-amazalert.org/).

Some authors have pointed out the necessity of considering future land-use changes in climate simulations in order to carry out more realistic projections (e.g., Feddema et al., 2005b; Betts et al., 2007; Hibbard et al., 2010). Given that the comprehensive representation of the biophysical and biochemical land-surface processes in climate models is very recent and is in ongoing development, land-use changes and key mechanisms whereby vegetation interacts with the climate system have not being taken in account in past climate modeling assessment. Few GCMs have actually included LULCC in future simulations within the large model ensemble used in the Fourth Assessment Report (AR4) of the Intergovernmental Panel on Climate Change (IPCC) (Meehl et al., 2007). In turn, in preparation for the IPCC's Fifth Assessment Report (AR5), the Coupled Model Intercomparison Project Phase 5 (CMIP5) experimental protocol includes land-use change in its core transient simulations (Taylor et al., 2012). Further, a harmonized land-use dataset was provided to the climate modeling community in the context of CMIP5 (Hurtt et al., 2011). Based on the results from LUCID (Pitman et al., 2009; de Noblet-Ducoudré et al., 2012; Boisier et al., 2012), the model intercomparison analyses for AR5 might likely show in both past climate and future projections higher dispersion within the models outputs than in previous initiatives due to land-use changes, at least at the regional scale. Efforts for isolating and better understanding the simulated LULCC signals in climate are then required.

This chapter presents results from the set of simulations carried out with the IPSL earth system model (ESM) in the context of CMIP5 and of a new LUCID stage, which together allows evaluating the effects of LULCC on the climate of the 21st century. This set of transient simulations, done in fully coupled configuration, is analyzed here along with others including the historical period. These results and the prospects presented at the end of the chapter, regarding the potential changes in the Amazon land cover and climate, are part of a work in progress done in the framework of AMAZALERT. With the motivation of complementing the results presented in previous chapters, the following questions are particularly addressed here:

- How do projected changes in land cover, particularly those at low latitudes, affect the climate due to biogeophysical processes?
- How do these impacts relate with those simulated during the historical period and, are the latter consistent with those simulated in the previous phase of LUCID?
- What relevant additional information may be drawn from transient simulations?
- How strong is the biogeochemical impact of LULCC in a pessimistic future scenario?

The CMIP5 and LUCID simulations are presented in section 4.2. The biogeophysical and biochemical effects of LULCC are described in sections 4.3 and 4.4, respectively. Section 4.5 brings a perspective regarding the potential LULCC and climate impacts in the Amazon. A summary of this chapter is presented at the end.

4.2 LUCID-CMIP5 set of simulations

4.2.1 Representative Concentration Pathways and land-use scenarios

In the context of the IPCC's AR5, four scenarios of human-induced climate drivers were prepared to force GCMs, particularly in those simulations following the CMIP5 protocol. These scenarios include emissions and atmospheric concentrations of GHGs and other reactive gases, in addition to land-use trajectories (Moss et al., 2010). In contrast to other sets of scenarios, as the ones used in the IPCC AR4 (SRES), the Representative Concentration Pathways (RCPs) explicitly account for climate mitigation policies. The four RCPs were selected among several different scenarios produced by interdisciplinary modeling frameworks (Integrated Assessment Models – IAMs). They represent the range of potential climate drivers and mitigations strategies, characterized by pathways of radiative forcing and equivalent atmospheric GHG concentrations, in addition to land-use scenarios (van Vuuren et al., 2011a). The former may either be used to force GCMs in uncoupled carbon-climate simulations (GHG concentrations are provided for each RCP, see Figure 4.1) or as a reference to assess mitigation policies with IAMs and GCMs (Moss et al., 2010). Gridded dataset of related fossil fuel-related GHG emissions are also provided for each RCP to be used in fully coupled simulations.

An overview of the RCPs is given in Table 4.1. RCP 2.6 is the pathway chosen within a number of mitigation scenarios, and leads to limit global warming to around 2 K. In this case, the global RF should not exceed 3 W m^{-2} and decline to ~2.6 W m^{-2} in the 2100 horizon. The associated change in land-use is the strongest in terms of cropland expansion due, in part, to an enhanced development of biofuel industry, allowing reducing fossil-fuel emissions. RCP 4.5 is a medium-to-low stabilization scenario that leads to limit RF to ~4.5 W m^{-2} in 2100. In this case, land-use changes include extensive reforestation as carbon mitigation strategy. Crop areas decline for which improvements in yield production and trade are taken in account to satisfy the increasing food demand. RCP 6.0 is the third stabilization scenario in which RF must be limited to around 6 W m^{-2} in 2100. Agriculture expands worldwide following the food and energy demand, but this occurs mainly in detriment of preexisting grasslands inducing moderate changes in forest cover. RCP 8.5 represents the non-climate policy (business as usual) scenarios. The selected scenario have associated a RF of ~8.5 W m^{-2} a rising trend by 2100. In this case, croplands and pasturelands continue to expand at current rates, notably in developing countries, resulting in the largest deforestation scenario within the RCPs.

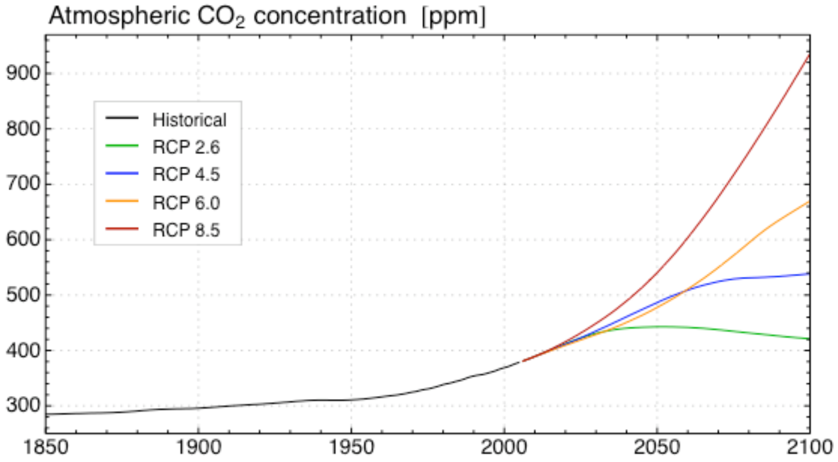

Figure 4.1
Annual mean atmospheric CO_2 concentration used in CMIP5 simulations for the historical period and future scenarios (RCPs).

4.2.2 Land-Use Harmonization (LUH) dataset and ORCHIDEE land-cover maps

In order to have consistent land-use data in time and space, ready to be used in climate models, the four RCPs land-use scenarios provided by each IAM were post-treated and integrated in a coherent way along with the historical agricultural information provided by HYDE 3.1 (Klein Goldewijk et al., 2011). The resulting dataset, referred to as Land-Use Harmonization (LUH; Hurtt et al., 2011), includes annual maps of agricultural (crops and grazed lands), urban, primary and secondary land data from 1500 to 2100, in addition to the underlying transition between these land-cover units, wood harvest and shifting cultivation.

Table 4.1. Representative Concentration Pathways (RCPs) summary.

Scenario	Radiative forcing pathway[a]	LULCC[b]	References
RCP 2.6 (IMAGE)	Peak in radiative forcing at ~3 W/m^2 (~490 ppm CO_2 equivalent) before 2100 and decline to 2.6 W/m^2 by 2100.	Mitigation scenario. High cropland expansion in part due to biofuels demand.	Van Vuuren et al. (2011b)
RCP 4.5 (GCAM)	Stabilization without overshoot pathway to 4.5 W/m2 (~650 ppm CO_2 equivalent) at stabilization after 2100.	Stabilization scenario include reforestation in NH. Food demand is basically achieved through yield improvements.	Wise et al. (2009)
RCP 6.0 (AIM)	Stabilization without overshoot pathway to 6 W/m2 (~850 ppm CO_2 equivalent) at stabilization after 2100.	Cropland expansion due to food and energy demand, mainly in detriment of grassland.	Fujino et al. (2006)
RCP 8.5 (MESSAGE)	Rising radiative forcing pathway leading to 8.5 W/m2 (~1370 ppm CO_2 equivalent) by 2100.	Strong increase and weak decrease in cropland areas in developing and developed countries, respectively.	Riahi et al. (2007).

[a] Adapted from Van Vuuren et al. (2011a)

[b] See Hurtt et al. (2011)

The LUH information was incorporated into the ORCHIDEE land-cover maps by applying a similar protocol than the one used in the first phase of LUCID (de Noblet-Ducoudré et al., 2012). The method basically consists in two steps, applied every year since 1700 to 2100 over the natural vegetation map currently in use in ORCHDEE (this is based on satellite data by Loveland et al., 2000). First, crop grid areal fraction from LUH dataset is prescribed as the two specific crop PFTs (C3 and C4 classes). At this stage, the natural vegetation –parametized through 10 PFTs (8 trees and 2 –C3 and C4– grass classes)– is proportionally reduced to allocate crops. Given that pastures are described as natural grasses in ORCHIDEE, the second step increases grass PFTs fractions at expense of those of forest and bare soil only if the grazed land fraction given by LUH is larger than the ORCHIDEE grass fraction resulting in the first step. Therefore, the resulting vegetation maps replicate cropland extension and evolution provided by LUH, while grass and forest areas could either increase or decrease depending on the crop area and grazed land evolution provided by LUH, and the background land-cover map used.

Figures 4.2 to 4.4 illustrate the resulting pathways of global cropland, forest and grassland areas respectively, prescribed in ORCHIDEE from 1850 to 2100, as well as the geographical distribution of their grid fraction differences between the ends of each corresponding period (i.e., 2005 minus 1850 and 2100 minus 2006 for the historical period and the projected one). According to the protocol used to incorporate the LUH agricultural data in ORCHIDEE, the global crop distribution and evolution is consistent to that of LUH. Hence, global croplands increase from ~5 to ~15 million km^2 from 1850 to 2005, consistent with what is reported from HYDE 3.1 (Klein Goldewijk et al., 2011), and continue to expand to the future in three scenarios: RCPs 2.6, 6.9 and 8.5 (Figure 4.2a). The largest crop increase takes place in the mitigation scenario (RCP 2.6), reaching ~20 million km^2 in 2100. In contrast, crop area decrease in the RCP 4.5 case, reaching 11 million km^2 in 2100.

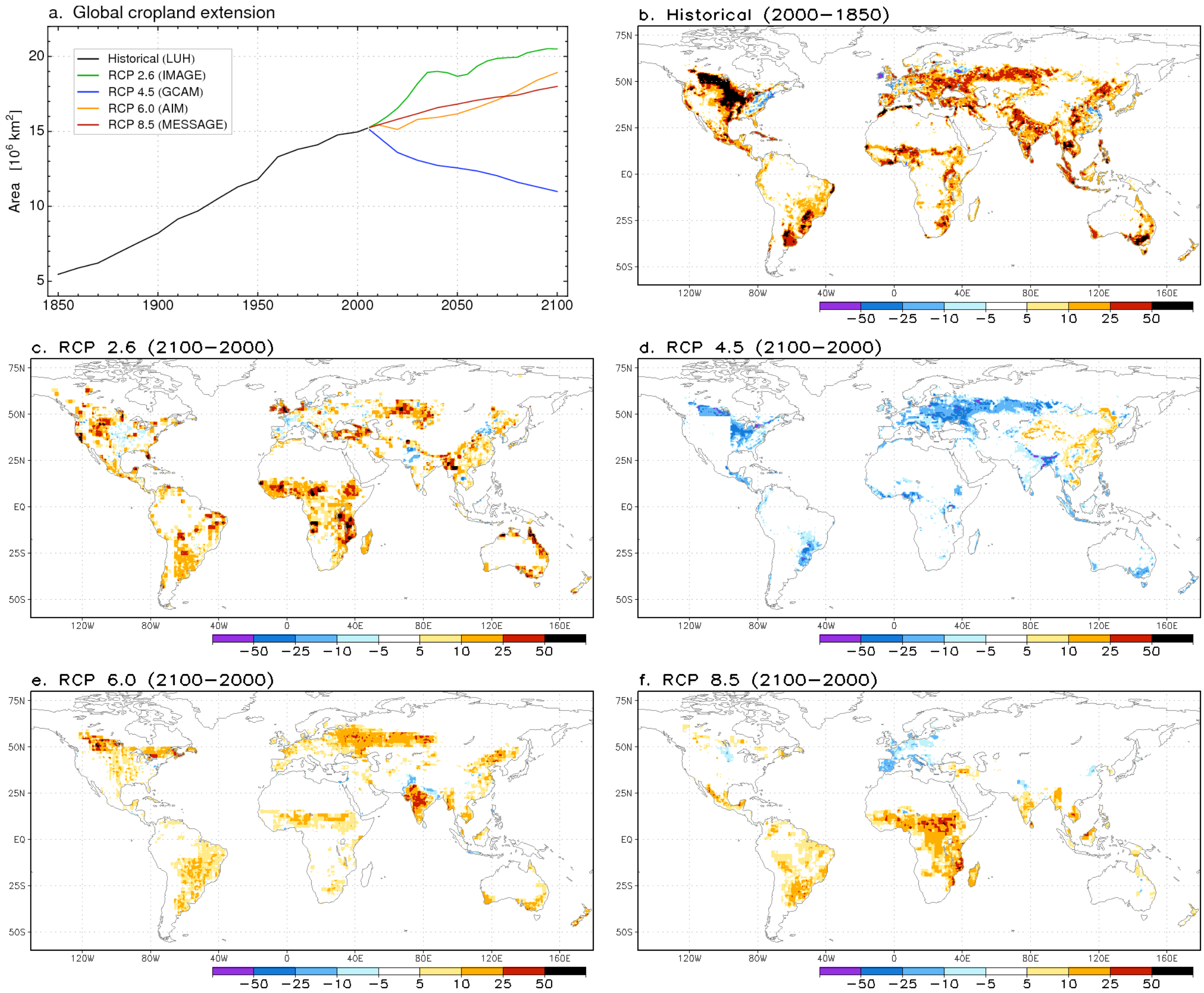

Figure 4.2
Global cropland area prescribed in ORCHIDEE between 1850 and 2100 based on the LUH dataset (a). Maps of crop fraction difference between the first and the last year of the historical period (2005–1850; b) and of the future scenario period (2100–2006) based on RCP2.6 (c), RCP4.5 (d), RCP6.0 (e) and RCP8.5 (f).

During the historical period, land conversion is particularly intensive in the northern mid-latitudes, notably in the North American Great Plains, with an extensive area showing changes in land-cover fractions larger than 50% (Figure 4.2b). In this region, croplands increase mainly at expense of grasslands, contrasting with the strong pasture increases in the southern part of North America (Figure 4.4b). As discussed in Chapter 2, it should be noted that the resulting changes in forest and grasslands following a land-use scenario might vary significantly following the used background (natural) vegetation map and the protocol chosen to incorporate the crop and pasture datasets.

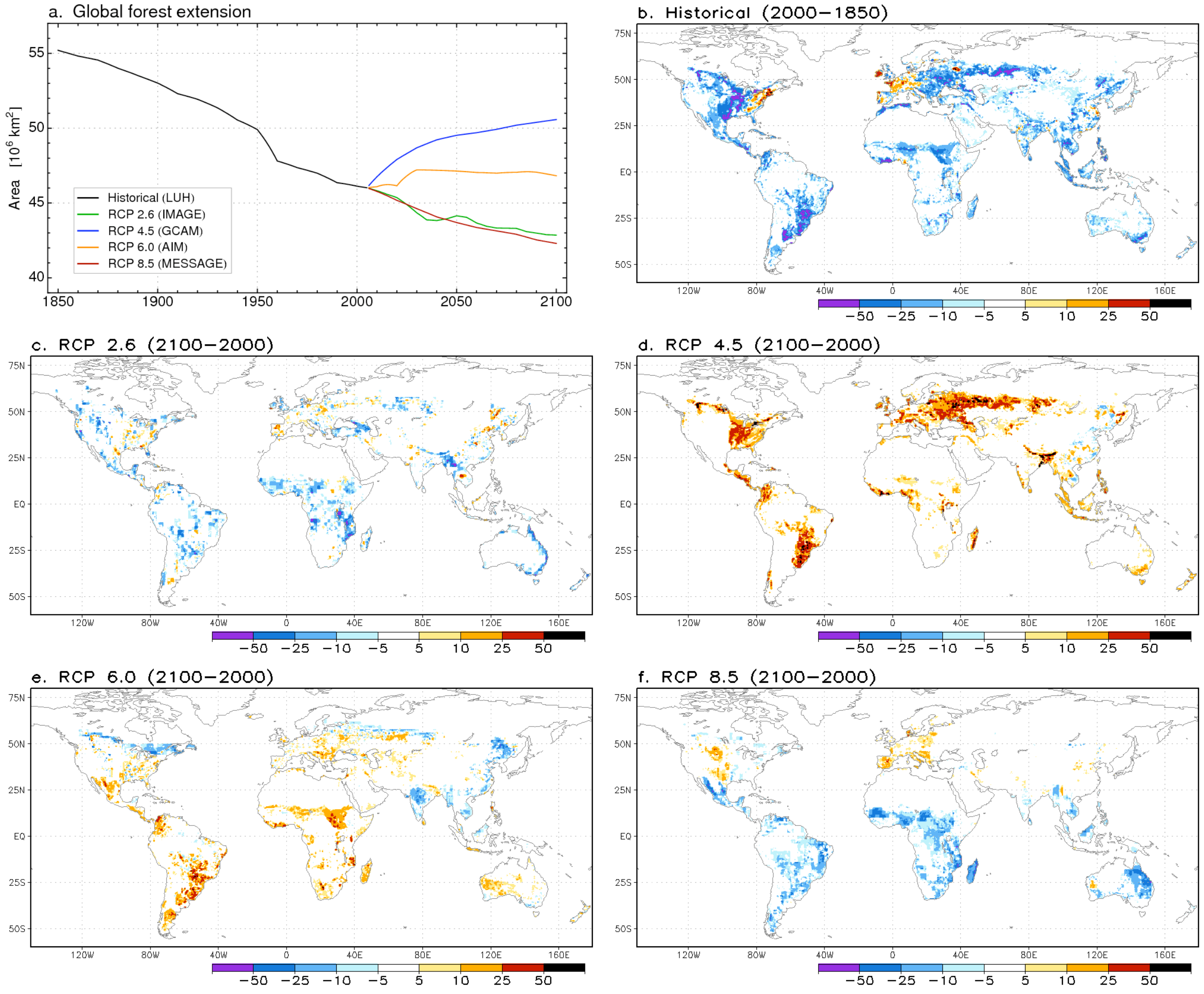

Figure 4.3
As in Figure 4.2 but for forest area.

Although comparable in the global totals, the future land-use scenarios do not show extensive regions with land conversion as large as those observed during the historical period; few and localized regions show fractional vegetation changes large than 25% between 2000 and 2100. For instance, RCPs 2.6 and 8.5 show the strongest disturbances at low latitudes. The resulting deforestation concerns areas of mixed vegetation (open forest and savannas), such as in sub-Sahel or in eastern tropical Africa, and do not affect rainforest particularly (Figure 4.3). This does not hold with either the observed forest clearing during the last decades and the regional-scale LULCC projections that foresee stronger pressure over tropical forest, notably in the Amazon (see the matter on this subject in Section 4.5).

Grazed land increases significantly in Australia in the RCP 8.5 case (treated as natural grass in ORCHIDEE; see Figure 4.4f). Land-use change towards 2100 in RCP 4.5 shows a general picture that roughly inverts the historical LULCC pattern, going back to the land-cover state of ~ the mid-20th century. In the case of RCP 6.0, cropland continues to expand in regions already modified during the historical period (Figure 4.2e), but mainly at the expense of grasslands (Figure 4.4e).

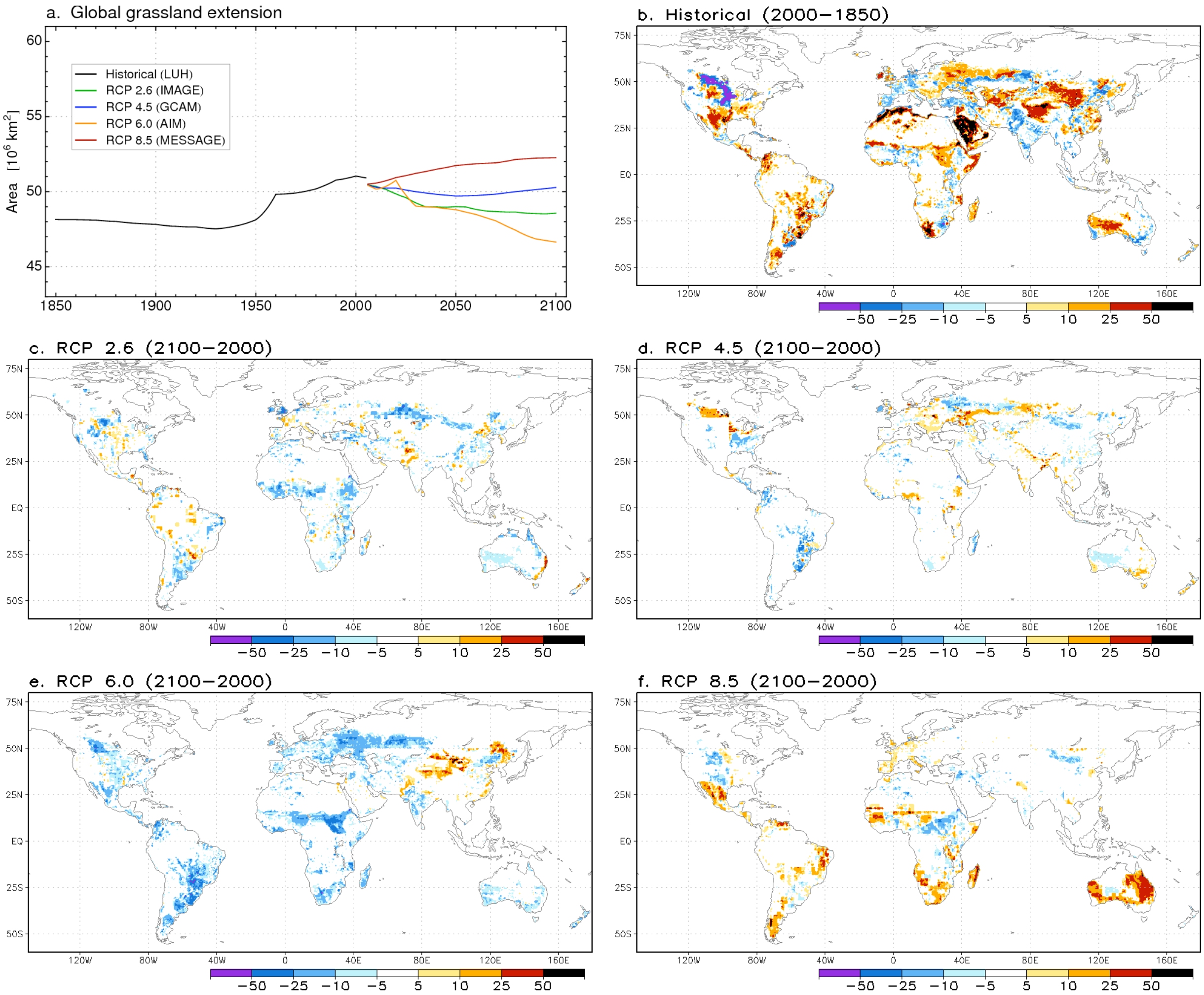

Figure 4.4
As in Figure 4.2 but for grassland area.

4.2.3 IPSL Earth System Model

The current version of the Institut Pierre Simon Laplace (IPSL) climate model, used to run CMIP5 simulations, corresponds to its fifth generation (IPSL-CM5; Dufresne et al., submitted). This version upgrade IPSL-CM4 used in CMIP3 and the first LUCID set of simulation. The model, in its fully coupled configuration (i.e., ESM), aggregates physically and chemically based schemes of the atmosphere, the land and the ocean. The base components of IPSL are LMDZ (Hourdin et al., 2012) and NEMO (Madec, 2008), the global circulation models of the atmosphere and the ocean, in addition to the land surface model ORCHIDEE (Krinner et al., 2005). The land and ocean biochemistry are respectively computed with the ORCHIDEE module STOMATE and the NEMO one PISCES (Aumont and Bopp, 2006). The tropospheric and stratospheric chemistry are treated in INCA and REPROBUS, both modules built in LMDZ.

Major model improvements from the version used in the CMIP3 concern the atmospheric chemistry and the carbon cycle. A new set of physical parameterizations for atmospheric processes was also developed (Hourdin et al, 2012), but is included in a parallel version of the model, which is not assessed here. The resolution was also enhanced from that used in CMIP3. The simulations here assessed were carried in a medium horizontal resolution configuration of 1.875° × 3.75° and 39 vertical levels. For an in-depth description of CMIP5 version of IPSL, see Dufresne et al. (submitted) and references therein.

4.2.3 Modeling experiment

Following the CMIP5 protocol, a number of transient simulations from the preindustrial period and until 2100 (2300 in some cases) should include land-cover changes within other anthropogenic and natural climate drivers. However, no specific future simulations were planned in CMIP5 permitting to isolate the effects of LULCC. To address this matter, a set of complementary simulations was designed in the context of the LUCID project (please see http://www.mpimet.mpg.de/en/science/the-land-in-the-earth-system/climate-biogeosphere-interaction/lucid-cmip5.html).

The results presented in this chapter concern an ensemble of CMIP5 and LUCID (CMIP5/LUCID) simulations carried out in IPSL. Those simulations and the set of diagnostics used to assess the effect of LULCC are listed in Table 4.2 and Table 4.3, respectively. The biogeochemical cycle computed in ESMs is forced in two ways within the CMIP5 transient simulation protocol. In one case, the net GHG emissions result from both prescribed fossil fuel emissions and those derived from land-use changes. Therefore, the atmospheric GHG concentration is simulated by the biosphere-climate system (emission-driven simulations). In the second case, the models prescribe time-varying atmospheric GHG concentrations (concentration-driven simulations). For the historical and the future scenarios (RCPs), pairs of forcing data are provided (emissions and concentrations). In this study we used four of those simulations (Table 4.2): a historical run forced with concentrations (HIST_LUc), two future runs forced with concentrations with respectively RCPs 2.6 and 8.5 (RCP26_LUc and RCP85_LUc), and another RCP 8.5 projection, but forced with emissions (RCP85_LUe).

Table 4.2. Set of simulations carried out with the IPSL ESM in the context of CMIP5-LUCID.

Simulation name	CMIP5 reference	LUCID reference	Period	Land-use	Atmospheric GHGs	#[a]
HIST_LUc	3.2 (core)	-	1850-2005	Historical (LUH)	Prescribed (historical)	7
RCP26_LUc	4.3 (tier1)	-	2006-2100[b]	IMAGE (rcp2.6)	Prescribed (RCP 2.6)	4
RCP85_LUc	4.2 (core)	-	2006-2100[b]	MESSAGE (rcp8.5)	Prescribed (RCP 8.5)	4
RCP85_LUe	5.3 (core)	-	2006-2100	MESSAGE (rcp8.5)	Diagnosed (emis. RCP 8.5)	1
HIST_NLUc	7.3 (tier2)	-	1850-2005	Fixed to 1850	Prescribed (historical)	1
RCP26_NLUc	-	L2A26	2006-2100	Fixed to 2005	Prescribed (RCP 2.6)	1
RCP85_NLUc	-	L2A85	2006-2100	Fixed to 2005	Prescribed (RCP 8.5)	1
RCP85_NLUce	-	L1A85	2006-2100	Fixed to 2005	Prescr. (RCP85_LUe)	1
RCP85_NLUe	-	L1B85	2006-2100	Fixed to 2005	Diagnosed (emis. RCP 8.5)	1

[a] Number of runs.
[b] Includes 1 realization until 2300.

In order to evaluate the effects of LULCC on climate, three kinds of simulations were run in the IPSL ESM in the context of LUCID, all of them without changes in land cover. The aim of this phase of LUCID is to evaluate the LULCC impacts in future scenarios with respect to present-day, so the land cover is fixed to 2005 in these runs. One group of simulations used the RCP-based prescribed atmospheric GHGs. Two simulations of this group were carried out with respectively RCP 2.6 and 8.5 (RCP26_NLUc and RCP85_NLUc in Table 4.2). These two simulations combined with their corresponding concentration-driven CMIP5 simulations (i.e., with changes in land-use) allow calculating the biogeophysical impacts of LULCC ($\Delta RCP26_{PHY}$ and $\Delta RCP85_{PHY\text{-}1}$ in Table 4.3).

Another kind of simulation provided in LUCID use prescribed GHG emissions. In this case, one simulation was run with the RCP 8.5 scenario (RCP85_NLUe), which allows assessing the net biogeochemical and biogeophysical effect of LULCC when compared with the corresponding emission-driven CMIP5 simulation ($\Delta RCP85_{ALL}$ in Table 4.3).

Another simulation use prescribed atmospheric GHG concentrations not from an RCP scenario, but those calculated in another simulation. In this case (RCP85_NLUce), the model used the ones obtained in RCP85_LUe. Given that GHG concentrations of these two simulations are identical, the difference between them brings another assessment of the biogeophysical effect of LULCC for the RCP 8.5 scenario ($\Delta RCP85_{PHY\text{-}2}$). The RCP85_NLUce simulation also allows assessing the sole biogeochemical effect of LULCC when compared to RCP85_NLUe, since both runs only differ in the atmospheric GHGs that result from land-use emissions ($\Delta RCP85_{CHE}$).

Finally, another simulation without land-use changes was carried out for the historical period in the context of CMIP5, using prescribed GHG concentrations. The latter along with the corresponding CMIP5 run including changes in land-use are used to evaluate the biogeophysical effects of LULCC from 1850 to 2005 ($\Delta HIST_{PHY}$).

Table 4.3. Diagnostics used to evaluate the effects of LULCC.

Name	Scenario	Effect	Diagnostic
$\Delta HIST_{PHY}$	Historical	Biogeophysical	HIST_LUc – HIST_NLUc
$\Delta RCP26_{PHY}$	RCP 2.6	Biogeophysical	RCP26_LUc – RCP26_NLUc
$\Delta RCP85_{PHY1}$	RCP 8.5	Biogeophysical	RCP85_LUc – RCP85_NLUc
$\Delta RCP85_{PHY2}$	RCP 8.5	Biogeophysical	RCP85_LUe – RCP85_NLUce
$\Delta RCP85_{ALL}$	RCP 8.5	All	RCP85_LUe – RCP85_NLUe
$\Delta RCP85_{CHE}$	RCP 8.5	Biogeochemical	RCP85_NLUce – RCP85_NLUe

4.3 Biogeophysical impacts of LULCC

4.3.1 Methods

Past and future scenarios of LULCC affect many different areas in the globe (figures 4.3 to 4.4). The northern temperate regions are particularly affected during the historical period. Parts of central Africa are also perturbed during this period as well as in the two scenarios assessed here (RCP 2.6 and RCP 8.5). Three regions were therefore defined in North America (NA; 120-80W, 30-55N), in Eurasia (EA; 0-90E, 40-60N) and in tropical Africa (AF; 20W-40E, 15S-15N) to perform regional-scale analyses. Given that the changes in land cover are mostly constrained to vegetated surfaces, the arid and semi-arid areas, defined as those grid-cells showing barren soil fractions larger than 25% in 1850, were excluded in each of the three domains selected (Figure 4.5).

Table 4.4 indicates the difference in forest area prescribed in ORCHIDEE between the first and last year of the historical period and the future ones over the regions assessed. Between 1850 and 2005, forest cover decreases by near 1 million km^2 in the three regions. RCPs 2.6 and 8.5 have associated relatively weak changes in the northern extratropics between 2006 and 2100, and forest decreases by near one million km^2 in tropical Africa. These changes represent reductions of little more than 5% of the total AF area (Figure 4.6b).

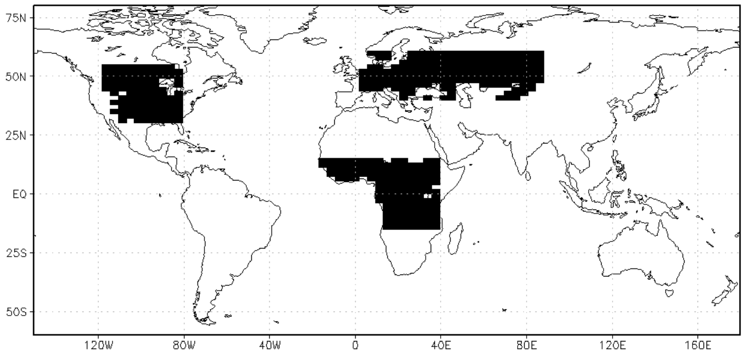

Figure 4.5
Regions used in analyses. North America (NA), Eurasia (EA) and tropical Africa (AF) regions comprise land areas covered with more than 75% with vegetation in 1850 within selected domains (see text).

Given the lack of multiple runs (ensembles) in the non-LULCC simulations (Table 4.2) that could increase robustness in climate signals induced by LULCC, for those analyses that do not evaluate the effect of LULCC along the whole period assessed (time-series), relatively large time slices of 50 years are used to compute climatologies and the diagnostics listed in Table 4.3. Given that LULCC evolve more or less monotonically over each period (Figures 4.2a, 4.3a and 4.4a), the last 50-year of each of them are used, i.e., 1956-2005 and 2051-2100, to capture the largest land-cover changes in the historical and future simulations, respectively. Figure 4.6 illustrates the resulting change in the area fraction occupied by forest, crops, and grass prescribed in simulation with LULCC with respect to those with fixed vegetation, for each LULCC scenario and the regions assessed (NA and EA are merged; thereafter NAEA). The net land-cover forcing when averaged over the 50-year periods is weaker in the future scenarios but not too different to that obtained between the ends of each period (indicated by dots in Figure 4.6). In turn, a weaker LULCC results in NAEA when averaged between 1956-2005, notably because deforestation stabilizes and reverses the pathway in the northern mid-latitudes (i.e., forest recovering) during the last 50 years (not shown).

Table 4.4. Forest area change in the studied regions (in millions km^2).

Region	Historical (2005-1850)	RCP 2.6 (2100-2006)	RCP 8.5 (2100-2006)
NA	−1.00	−0.15	+0.05
EA	−1.04	−0.22	+0.03
TR	−1.12	−0.87	−1.07

It is important to note that even if the regions selected show relatively large land-cover perturbations compared to the rest of the globe, the resulting regional mean LULCC is relatively weak, notably in tropical Africa, where the areal fraction changes are no larger than 12%. In this region, although the RCP 2.6 scenario has associated a larger crop increase than the RCP 8.5 one, the distinct changes in grass fraction result on deforestation of quite similar rates.

Student's hypothesis tests (t-tests) were applied in a number of analyses to evaluate the statistical significance of the mean difference between two time-series. T-tests do not consider equal variance in time-series. Given that simulations and, particularly, the time period assessed are not in equilibrium, each time-series was detrended before each evaluation in order to remove the long-term component in the variance calculations.

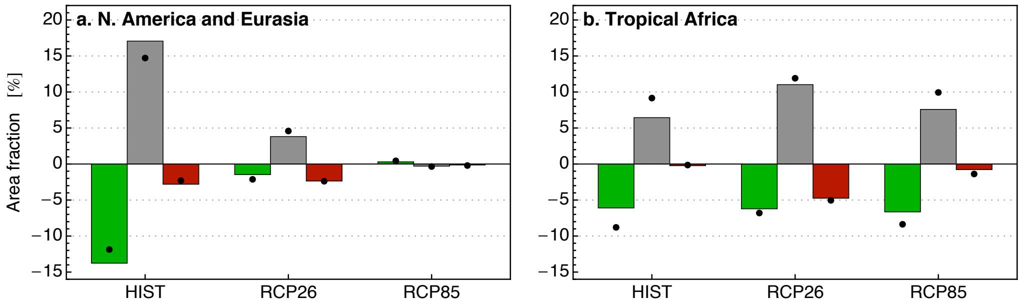

Figure 4.6
Change in forest (green), crops (gray) and grass (red) area fraction for the period 1956-2005 (average) relative to 1850 (HIST), and for the period 2051-2100 with respect to 2005 based on the RCP 2.6 (IMAGE) and RCP 8.5 (MESSAGE) land-use scenarios. Areal fraction changes are calculated over the regions defined in the NH extratropics (NAEA; a) and in Africa (AF; b). Dots indicate the corresponding area fraction change between the ends of each period (i.e., 2005 minus 1850 and 2100 minus 2005 for the historical and future scenarios, respectively).

4.3.2 Temperature responses to LULCC

Figure 4.7 illustrates the time series of the NH summer (JJA) mean surface temperature and in NAEA and AF, resulting from three couples of simulations computed with prescribed atmospheric GHG concentrations: the historical, the RCP 2.6 and the RCP 8.5. For each of them, both simulations including land-use and with fixed vegetation are shown (indicated with solid and dashed lines, respectively).

The simulated temperature trends are similar in both regions, with a clear warming of near 2 °C during the 20th century. This pattern responds to the global temperature evolution directed by atmospheric GHG increases, as is reported by Dufresne et al. (submitted). Surface temperature raises another ~6 °C between 2000 and 2100 in those simulations driven by the RCP 8.5 scenario. Following the RCP 2.6 one, the warming trends stabilize at ~+3 °C in the studied regions with respect to the corresponding preindustrial values. The GHG-induced temperature trends are weaker over the oceans, and the resulting global warming slightly exceeds the expected 2 °C warming in this scenario (Dufresne et al., submitted).

No clear land-use signals are recognized in Figure 4.7. The temperature differences between each couple of simulations (with and without LULCC) are non systematic in time and weak compared to both the long-term temperature evolution and the interannual variability.

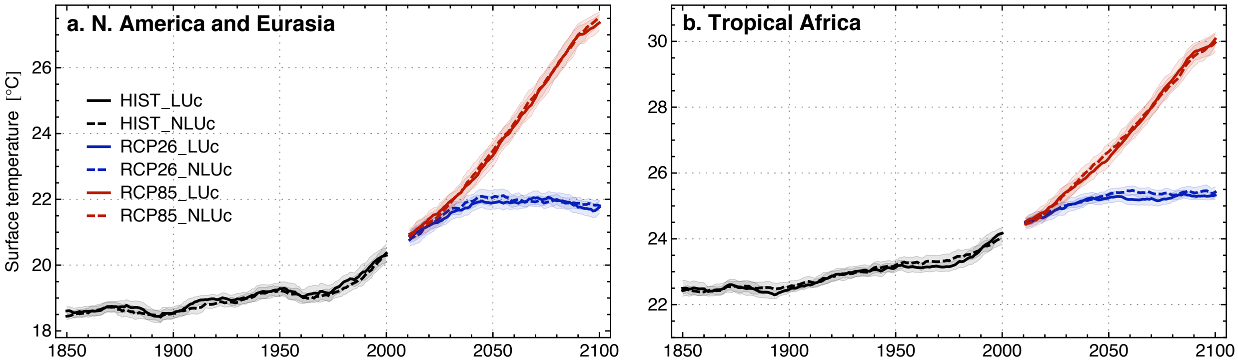

Figure 4.7
Annual mean surface temperature in NAEA (a) and AF (b) from 1850 to 2100. Time-series of the historical (black lines) and future (RCPs 2.6 and 8.5 in blue and red, respectively) simulations, including changes in land cover (solid) and with fixed vegetation (dashed). Lines and shaded areas indicate respectively the mean and 1 standard deviation of moving windows of 10-year.

Figure 4.8 illustrates seasonal surface temperature differences averaged over the global land surface and over the two regions assessed (NAEA and AF). All the four diagnostics assessing the biogeophysical effects of LULCC are shown (i.e., $\Delta HIST_{PHY}$, $\Delta RCP26_{PHY}$, $\Delta RCP85_{PHY1}$ and $\Delta RCP85_{PHY2}$), each of them computed over the last 50 years period of each simulation (see section 4.3.1). The regional mean temperature responses are generally weak (up to ~0.3 K) and not statistically significant in almost all cases. Such limited changes are somehow expected because of the strength of the imposed LULCC, weak when averaged regionally (Figure 4.6).

Given the amplitude of LULCC and the resulting small temperature differences, robust (i.e., statistically significant) signals of LULCC are not found in the selected regions. In other words, the record length used (50 years) is not as large as necessary in order to isolate these signals from the natural variability of the model. This highlights the need of multiple runs to well assess the changes in temperature due to LULCC, particularly in transient simulations. Given this, the resulting anomalies depicted in Figure 4.8 could be significantly biased by to non-deterministic differences between each couple of simulations analyzed. This is clearly appreciated in the RCP 8.5-based diagnostics in NAEA (ΔRCP85$_{PHY1}$ and ΔRCP85$_{PHY2}$). In this region, although the prescribed land-cover change following RCP 8.5 is roughly inexistent (Figure 4.6), both cases show comparable temperature anomalies to those resulting in the same region from the historical simulations (ΔHIST$_{PHY}$). The hypothesis of remote impacts of LULCC does not hold either in this case because both diagnostics ΔRCP85$_{PHY1}$ and ΔRCP85$_{PHY2}$ also show different results between them.

However, some temperature anomalies are consistent with those obtained in the previous LUCID stage. In NAEA, ΔHIST$_{PHY}$ show cooling and warming in respectively MAM and JJA, pattern expected due to maximized albedo effect (increase) in the first case, and due to decreases in LE in the second (the changes in the surface energy budget are addressed in the following section).

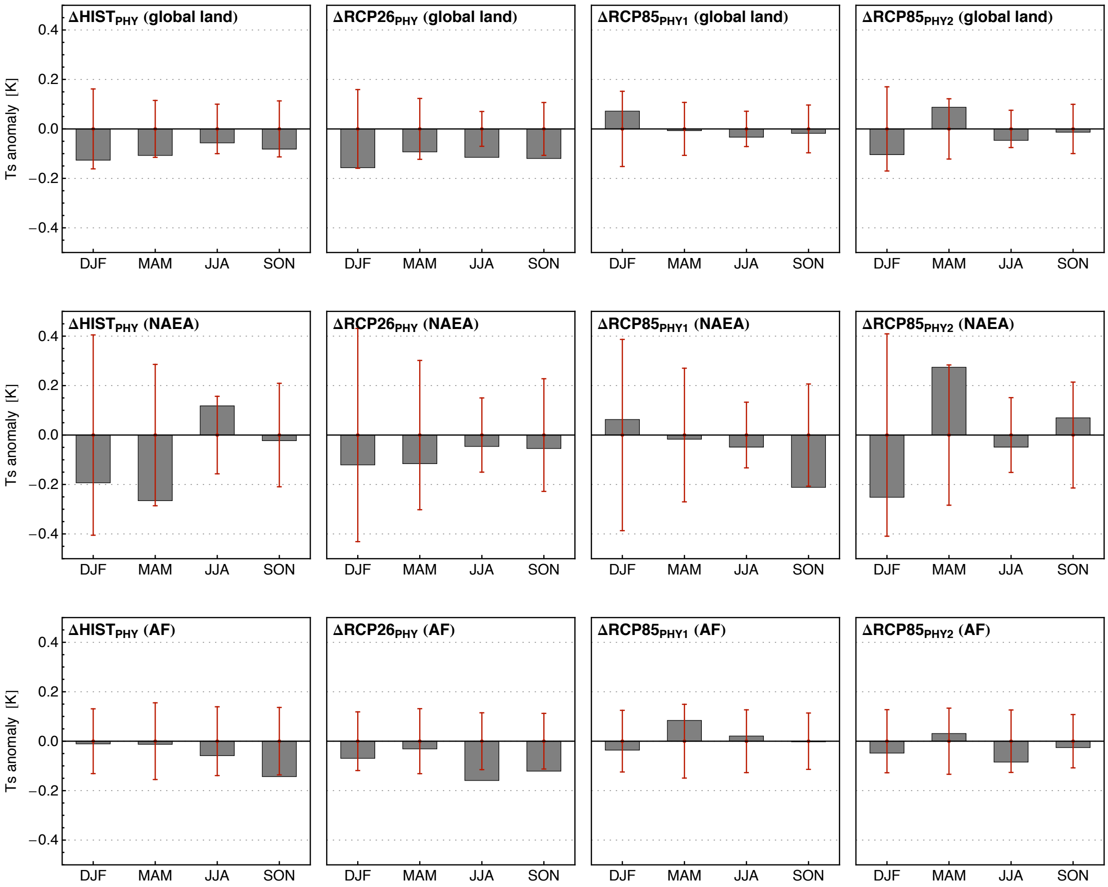

Figure 4.8
LULCC-induced seasonal surface temperature changes averaged over the global lands (excluding areas with permanent ice; upper panels), over NAEA (medium) and over AF (bottom). Changes computed from the historical (ΔHIST$_{PHY}$, left column) and the future (ΔRCP26$_{PHY}$, center-left; ΔRCP85$_{PHY1}$, center-right; and ΔRCP85$_{PHY2}$, right) simulations. Anomalies are calculated between 50-years climatologies (1956-2005 in the ΔHIST$_{PHY}$ case and 2051-2100 in the future ones). Error bars indicate the 95% confidence interval from which temperature departures are significantly different from zero.

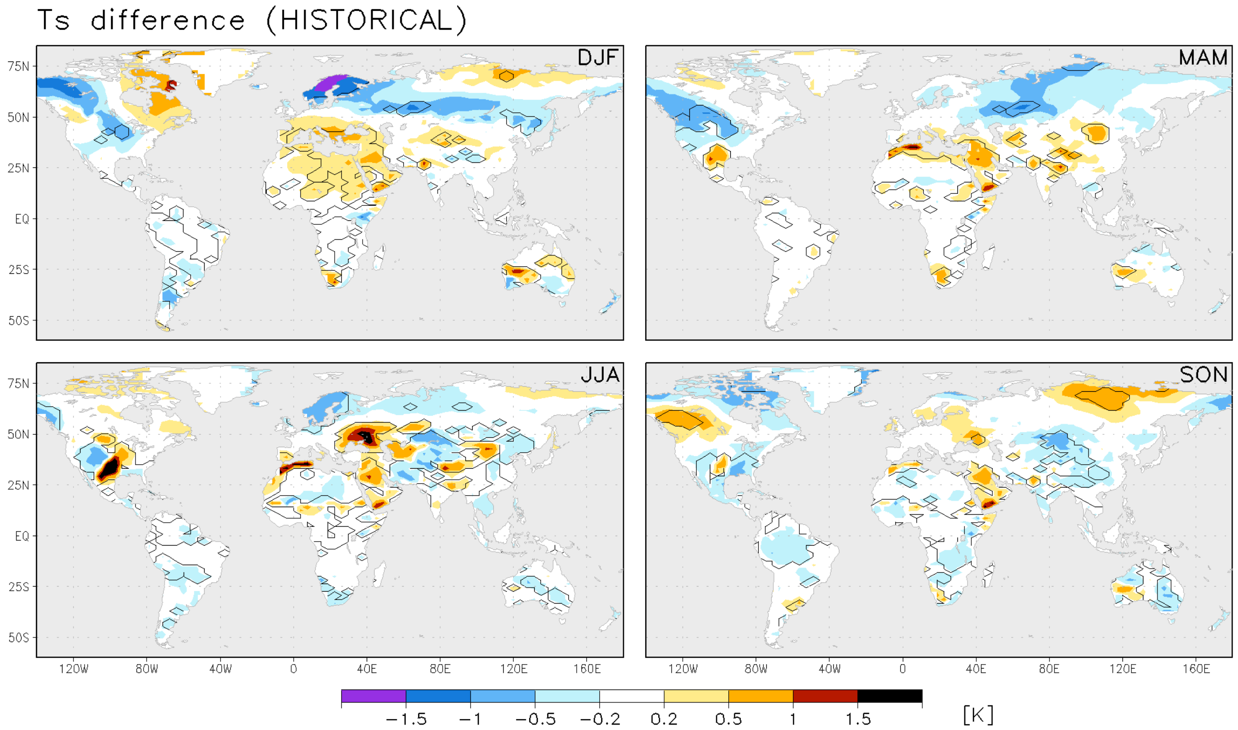

Figure 4.9
LULCC-induced seasonal surface temperature changes for the historical scenario ($\Delta HIST_{PHY}$). Differences computed from the 1956-2005 climatologies. Contour lines encompass areas with changes significantly different from zero at the 95% confidence level.

The global distribution of the seasonal temperature difference for two cases, $\Delta HIST_{PHY}$ and $\Delta RCP85_{PHY1}$, are depicted in Figures 4.9 and 4.10 (see Appendix 4.1 for the corresponding analyses of $\Delta RCP85_{PHY2}$ and $\Delta RCP26_{PHY}$). Even at the local scale, the temperature signals of LULCC are small and comparable with anomalies of the same order in areas far away from those perturbed. The latter are probably stochastic results due to the internal variability of the model. In the northern temperate regions, $\Delta HIST_{PHY}$ show statistically significant and geographically consistent temperature differences with those simulated by IPSL in the previous LUCID phase, such as the winter (resp. summer) cooling (resp. warming) in North America (see Appendix 2.1).

In the $\Delta RCP85_{PHY1}$ case there is significant warming in localized regions with land-cover changes, notably in subtropical lands of the Southern Hemisphere and in the Sub–Sahelian band (Figure 4.10). Such temperature responses are simulated throughout the year and are also present in $\Delta RCP85_{PHY2}$ (Figure A4.2). Comparing these two diagnostics ($\Delta RCP85_{PHY1}$ and $\Delta RCP85_{PHY2}$) it is very likely that temperature anomalies over regions distant from areas where LULCC is imposed, such as those observed in Eurasia in $\Delta RCP85_{PHY1}$ (Figure 4.10), are by-chance results of the internal variability of the model and not genuine remote impacts of LULCC. This reinforces the point that even using 50-year climatologies, single runs of coupled simulations are not enough to well characterize the impacts of LULCC when these are localized and of moderate strength.

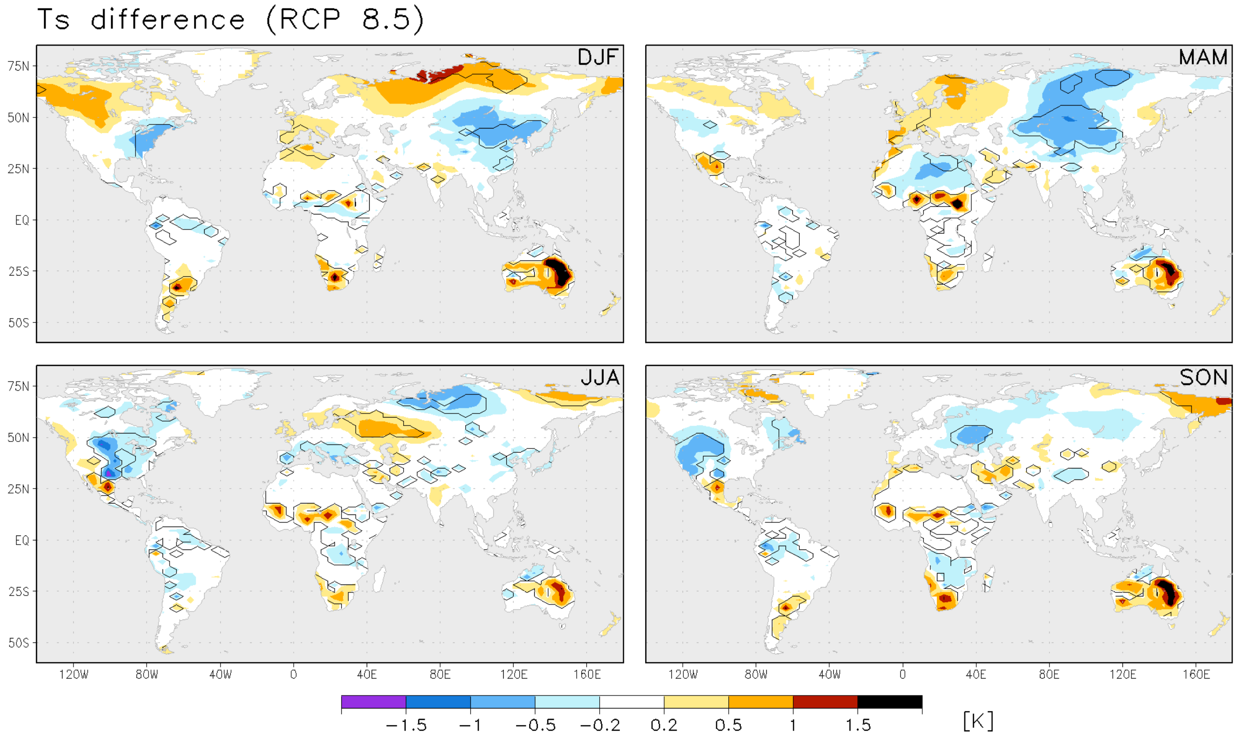

Figure 4.10
As in Figure 4.9 but for RCP 8.5 scenario (ΔRCP85$_{\mathrm{PHY1}}$). Differences computed from the 2051-2100 climatologies.

4.3.3 Changes in the surface energy fluxes

Unlike the simulated changes in surface temperature, the effects of LULCC are patent over the various components of the surface energy budget (SEB). Figures 4.11 and 4.13 illustrate the global distribution of the NH winter and summer differences in net shortwave radiation (S_N), latent heat flux (*LE*) and sensible heat flux (*H*) resulting from ΔHIST$_{\mathrm{PHY}}$ and ΔRCP85$_{\mathrm{PHY1}}$. The model responses to LULCC averaged over the studied regions are illustrated for the same two diagnostics in figures 4.12 and 4.14, respectively. In this figures, the various SEB components and the all the four seasons are shown. The corresponding analyses for ΔRCP26$_{\mathrm{PHY}}$ and ΔRCP85$_{\mathrm{PHY2}}$ are also provided in Appendix 4.1.

Significant decreases in S_N are simulated in regions with prescribed deforestation, notably directed by increases in surface albedo. In the ΔHIST$_{\mathrm{PHY}}$ case, areas with strong LULCC such as in North America or Eurasia show larger S_N anomalies in the corresponding summer (JJA) than in winter (Figure 4.11). This seasonal difference is not necessarily expected because, although solar radiation is lower during the winter, the change in S_N during this season might be as large as or greater than in summer because of the large snow-masking albedo effect exerted by forest, as the various GCMs showed in the first LUCID stage (see Figure 2.15 in Chapter 2).

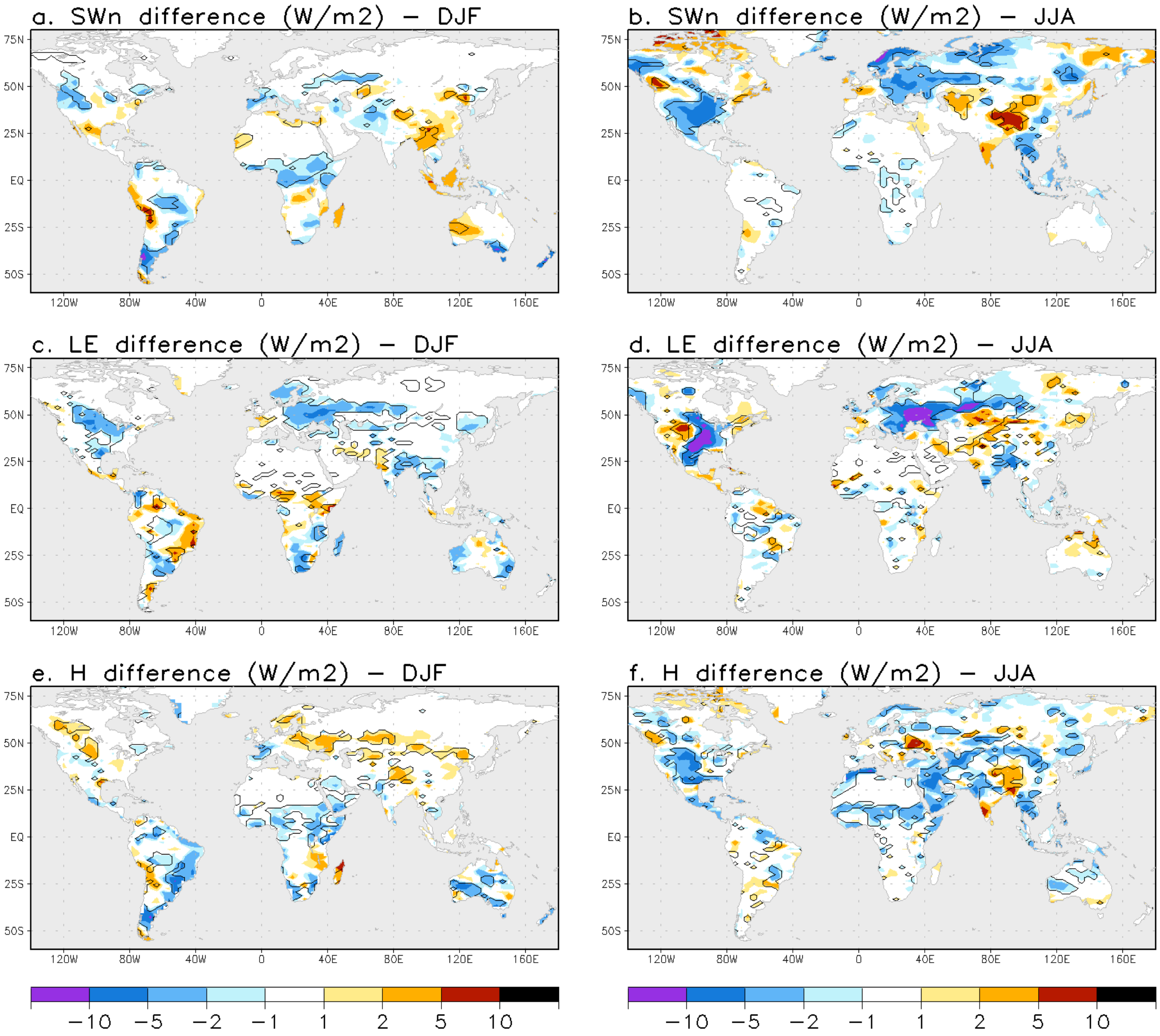

Figure 4.11
LULCC-induced net radiation (a, b), latent heat flux (c, d) and sensible heat flux (e, f) changes in DJF (a, c) and JJA (b, d) for the historical scenario (ΔHIST$_{PHY}$). Differences averaged over the 1956-2005 period. Contour lines encompass areas showing changes significantly different from zero at the 95% confidence level.

In Figures 4.12 and 4.14, the LULCC-induced anomalies of S_N are illustrated along with their components induced by changes in surface albedo (indicated by gray bars) and by changes in the incoming solar radiation (S_D; white bars) (these components are calculated following Equation 2.6, Chapter 2). It is noteworthy looking the historical case, that the lower radiative impact in summer in NAEA responds to a dampening albedo effect driven by S_D (Figure 4.12a).

The albedo-induced S_N decrease is almost completely offset by increases in S_D. This effect is also observed in previous LUCID results (see Figure 2.15, Chapter 2), but seems to be amplified in the simulations here assessed, leading to weak temperature responses in DJF (Figure 4.9a). More simulations (ensembles) are needed to assess the robustness of this effect, and to know if it is actually greater in fully coupled simulations compared to those carried out in the first LUCID phase (i.e., with prescribed SST/SIC), or if it is just a stochastic result.

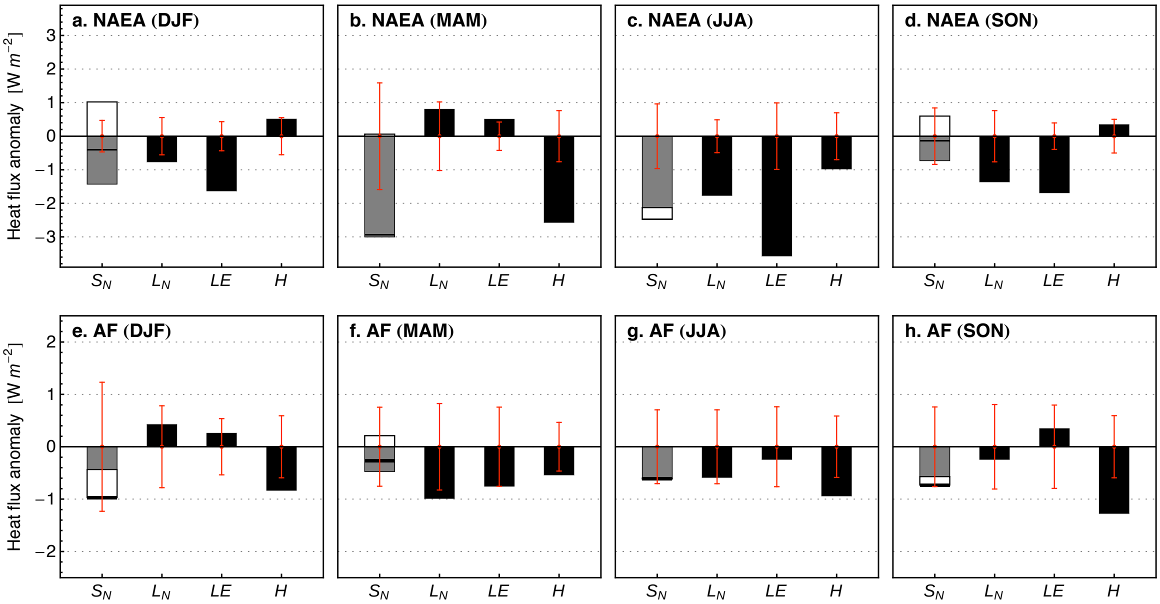

Figure 4.12
Seasonal changes in net shortwave (S_N) and longwave (L_N) radiation; latent (LE) and sensible (H) heat flux, simulated as response to the historical LULCC ($\Delta HIST_{PHY}$, differences averaged over the period 1956-2005) in North America/Eurasia (top) and in tropical Africa (bottom). S_N anomalies are separated between the component induced by surface albedo changes (gray) and that induced by changes in the incoming shortwave radiation (white). The horizontal black bars indicate the net (simulated) S_N change. Error bars indicate the limits from which anomalies are significantly different from zero at the 95% confidence level.

Looking the historical simulations, the *LE* and *H* changes due LULCC in NAEA are consistent with what the IPSL showed in previous LUCID simulations. Decreases in *LE* are simulated during most part of the year, except in spring (Figure 4.12[a-d]). As described in Chapter 2, this response to LULCC is closely related with the changes in LAI simulated in IPSL that, following the crop phenology, increase in spring and decrease during the late summer and fall.

In AF, an opposite pattern prevails. Decreases in net radiation (S_N + L_N) are in most seasons balanced with reductions in *H*, with little and either positive or negative changes in *LE* (Figure 4.12). In other words, the Bowen ratio (*H/LE*) decreases during most part of the year, and particularly in SON and DJF (Figure 4.12[e-h]). This pattern at low latitudes is also observed and is more pronounced in the future RCP 8.5-based simulations (Figure 4.14). In this case, the Bowen ratio clearly decreases during the four seasons with anomalies particularly large in DJF, JJA and SON. The same result is obtained with the other couple of simulations based on RCP 8.5 ($\Delta RCP85_{PHY2}$, Figure A4.4), showing the robustness of that LULCC signature.

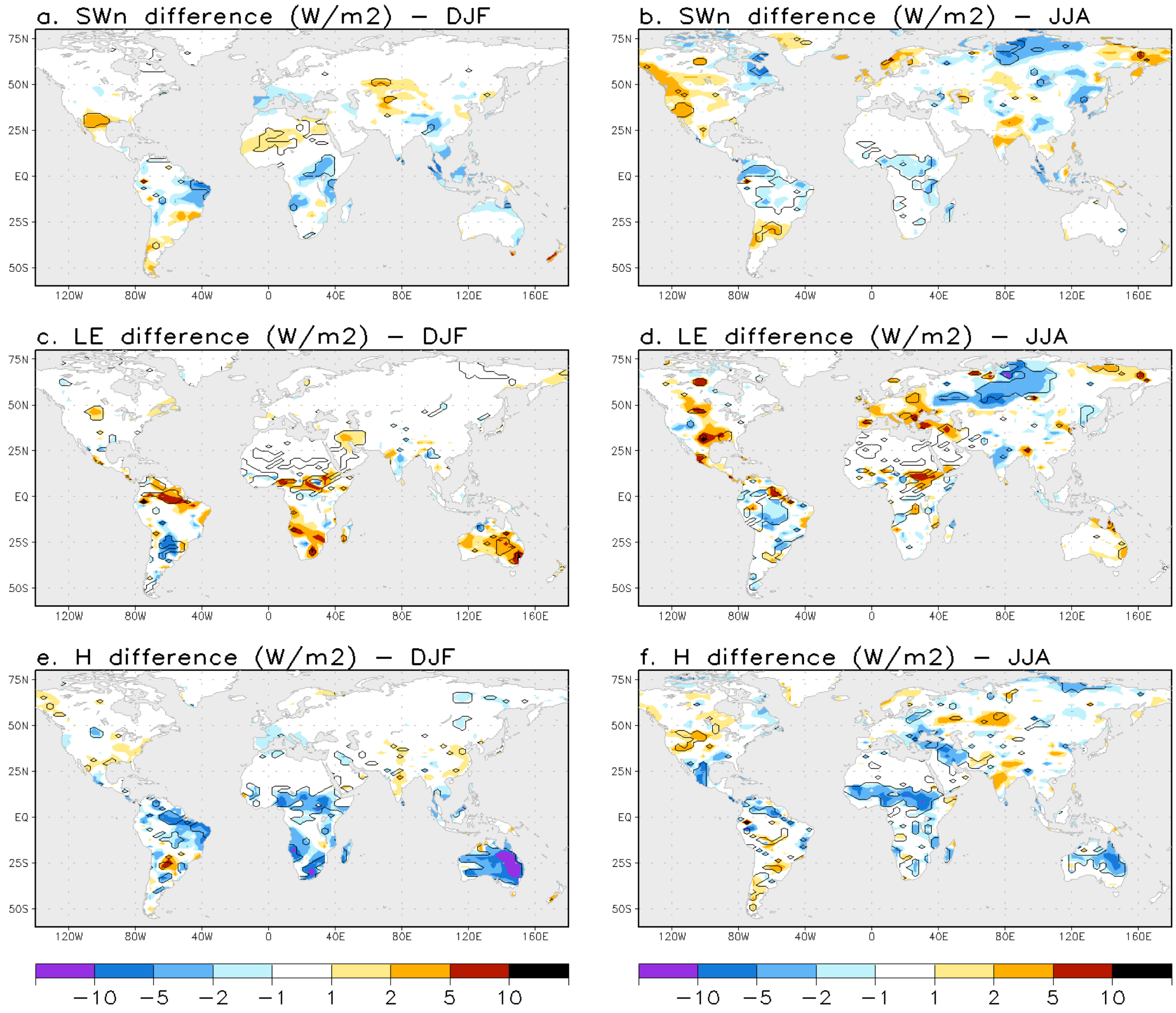

Figure 4.13
As in Figure 4.11 but for RCP 8.5 scenario ($\Delta RCP85_{PHY\text{-}1}$; mean difference for 2051-2100 period).

The LULCC-induced decrease in Bowen ratio simulated at low latitudes opposes the expanded view that deforestation should induce *LE* reductions in the tropics (Bonan et al., 2008b). However, it should be noted that neither in the historical scenario assessed here nor in the future ones, rainforest areas are particularly affected within the tropical band.

In addition to the change in the partitioning of *LE* and *H* induced by LULCC, it is notable in AF for RCP 8.5 case that the total turbulent energy flux Q_T ($LE + H$) generally decreases more than S_N (Figure 4.14). Since the SEB must be maintained, this condition leads to surface warming if any other flux is modified (notably the incoming longwave radiation, L_D). Although L_D actually changes, in part due to feedbacks with surface perturbations, the strong decreases in Q_T resulting in the RCP 8.5 simulations lead to warming in regions such as sub-Sahel or Australia (Figure 4.10). Strong Q_T decreases also explain the simulated historical warming in summer in the NH temperate regions (Figure 4.9). In these two examples, the negative Q_T anomalies have associated changes the LE and H of different sign, i.e., changes in Bowen ratio. This echoes the message pointed out by Davin and de Noblet-Ducoudré (2010) and the LUCID group (de Noblet-Ducoudré et al., 2012; Boisier et al., 2012) that in addition to the changes in surface radiation budget and in the turbulent heat partitioning, the temperature responses to LULCC strongly depends on other factors leading to changes in Q_T, notably the changes in surface roughness.

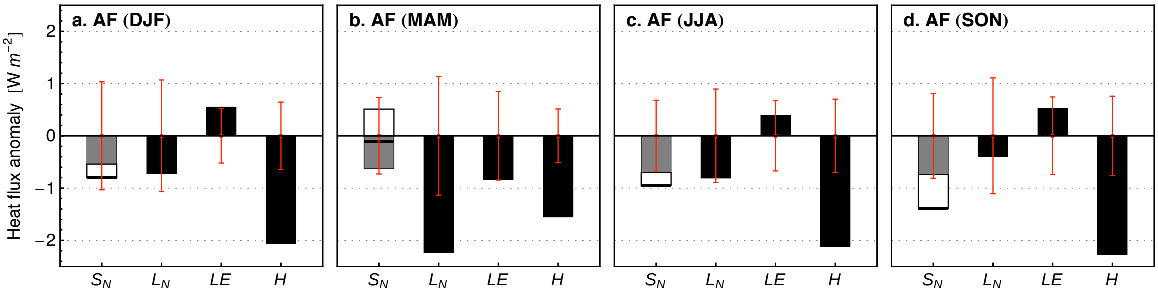

Figure 4.14
As in Figure 4.12 but for RCP 8.5 scenario ($\Delta RCP85_{PHY1}$) in AF. Differences averaged over the 2051-2100 period.

4.3.4 Changes in the hydrological cycle

The regional mean precipitation time-series for NAEA and EA, resulting from the historical, the RCP2.6 and the RCP 8.5 simulations are illustrated in Figure 4.15. Compared to the interannual variability, the long-term precipitation trends are less noticeable than those of temperature (Figure 4.7). A negative precipitation trend prevails in both regions during the whole period (1850 to 2100), but is particularly large in NAEA during the second half of the 21st century following the RCP 8.5 scenario. Curiously, when the model is forced with the mitigation scenario (RCP 2.6), the negative precipitation trend simulated in NAEA during the 20th century reverses during the 21st one.

During the second half of the 20th century, systematic lower precipitation rates are recognized in NAEA in the simulation including LULCC with respect to that with fixed land cover. No clear LULCC signals are observed in AF and in both regions in future simulations. Further, if evaluating the long-term (e.g., from 50 years climatologies) precipitation differences derived from LULCC is already difficult due to the lack of multiple runs, the large interannual and interdecadal variability in these regions make unfeasible assessing the impacts in precipitation along the simulated periods. Hence, no relevant information could be inferred from the transitory changes in LULCC unless these were evaluated in larger ensembles of simulations, at least regarding temperature and precipitation.

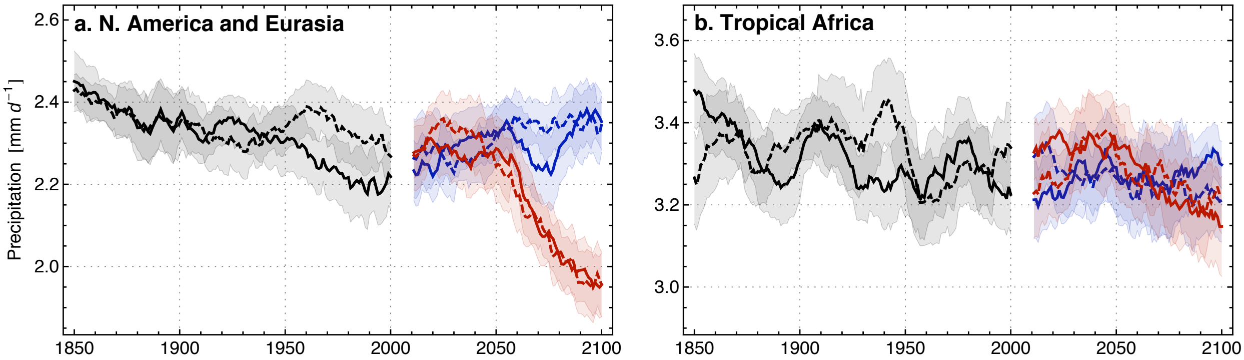

Figure 4.15
As in Figure 4.7, but for precipitation.

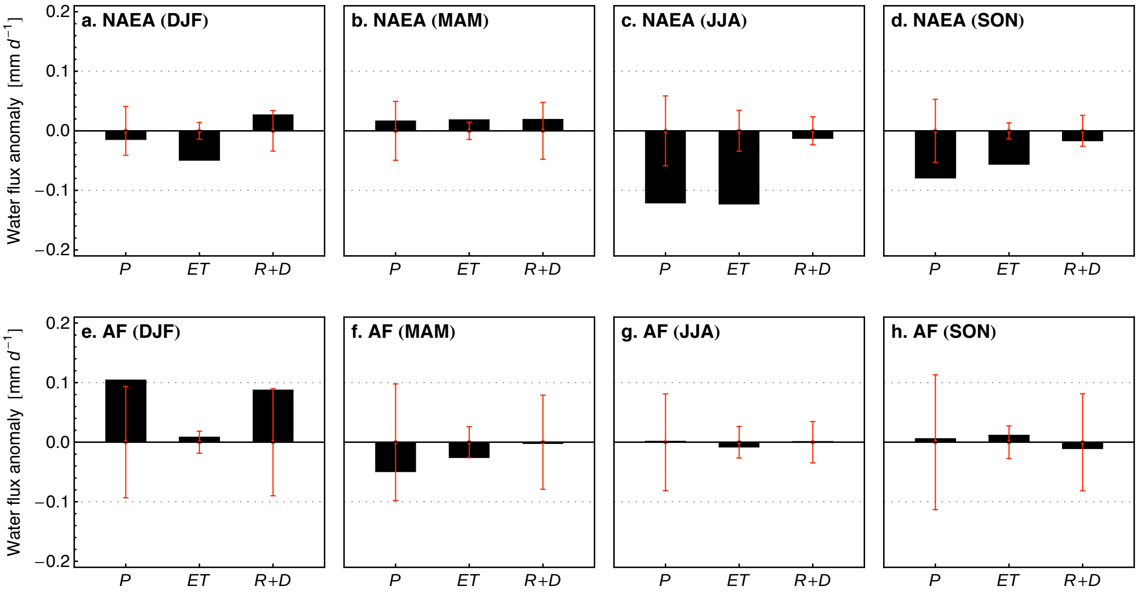

Figure 4.16
Historical LULCC-induced seasonal changes ($\Delta HIST_{PHY}$) in precipitation (P), evapotranspiration (ET) and runoff/drainage (R+D). Differences computed for the 1956-2005 period and averaged over NAEA (top) and AF (bottom). Error bars in red correspond to the limits from which anomalies are significantly different from zero at the 95% confidence level.

Figures 4.16 and 4.17 summarize for both cases $\Delta HIST_{PHY}$ and $\Delta RCP85_{PHY1}$ the seasonal LULCC-induced differences in the surface hydrology in NAEA and AF. As was described earlier for *LE*, evapotranspiration (*ET*) decreases in NAEA in response to the historical LULCC in most seasons except during the NH spring. Changes in precipitation follow a similar pattern than *LE*, further highlighting the positive coupling between these two variables. As is discussed in Chapter 2, the changes in precipitation in the NH temperate regions are likely a response to *LE* perturbations and not vice versa, although the initial LULCC-induced *LE* changes are probably amplified via a positive feedback along with precipitation.

Neither for the historical nor for the RCP 8.5 scenario of LULCC, the changes in precipitation (P), *ET* and in the net runoff plus drainage (*R*+*D*) are significant in the selected African region (Figure 4.16[e-h] and Figure 4.17). As discussed in the precedent section, the weak *ET* responses to LULCC in this region contrast with the significant decreases in *H*,

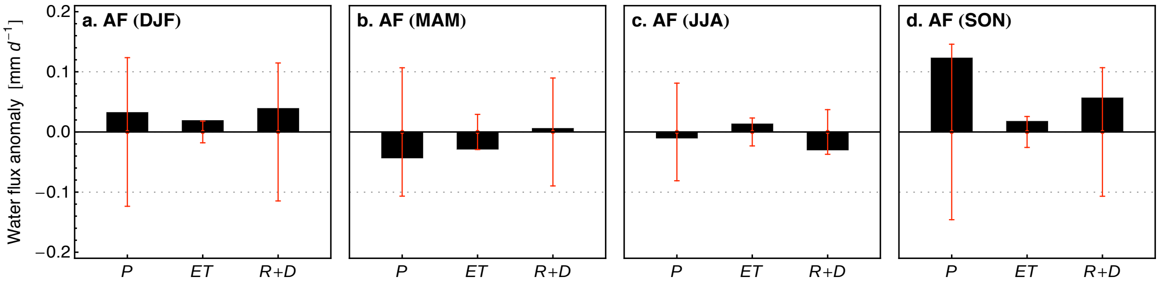

Figure 4.17
As in Figure 4.16 but for RCP 8.5 scenario ($\Delta \text{RCP85}_{\text{PHY-1}}$) in AF. Differences averaged over the 2051-2100 period.

To further understand the weak *ET* responses to LULCC at low latitudes, the hydrological components were more thoroughly analyzed in the northern part of AF (from the equator to 15°N). This sub-region of AF was chosen because it is particularly affected by deforestation in the RCP 8.5 scenario (Figure 4.3) and in order to well capture the phases of the African monsoonal regime.

Figure 4.18a illustrates the climatological monthly *ET* values (2051-2100 from the RCP85_NLUc simulation) from the grid-points within the selected region, plotted against precipitation (*P*). *ET* increases asymptotically with *P* and reaches ~4 mm day^{-1} for *P* values larger than ~6 mm day^{-1}. This value seems to be the maximum *ET* the region can sustain. A decomposition of *ET* for different *P* values into four different components is also depicted in Figure 4.18a. The mean grid soil evaporation (black line in Figure 4.18) and the canopy *ET* (interception loss plus transpiration) computed for three vegetation classes: trees (green line), grasses (red line) and crops (blue line) are shown (ORCHIDEE computed the water fluxes in each PFTs independently). This decomposed *ET* values are not pondered by the relative areal fraction of each of these land-cover groups, so they represent the model response if each of them were the unique land-cover unit within the region. Soil evaporation is clearly lower than vegetation *ET* until *P* values of ~6 mm day^{-1}. Grasses and crops maintain relatively high *ET* at low *P*, similar to that of trees, despite their lower root length. This may indicate soil moisture resilience during the dry season in this region.

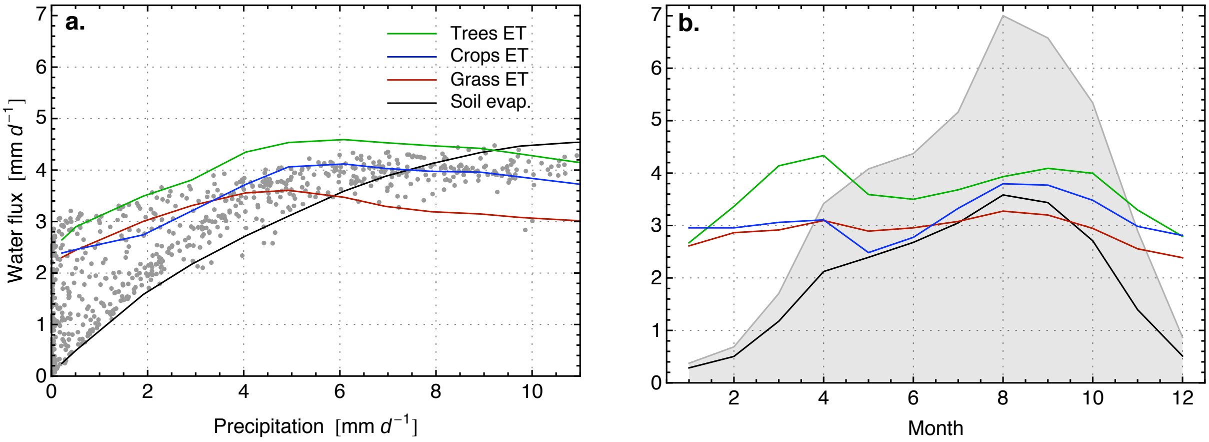

Figure 4.18
(a) Monthly mean (2051-2100) evapotranspiration (ET) simulated in RCP85_NLUc plotted against precipitation (P) for all of grid-points within the northern (0-15N) AF region (gray dots). Solid lines indicate the mean ET at different P levels calculated by ORCHIDEE for trees (green), grasses (red) and crops (blue) PFTs (include transpiration and interception loss), in addition to the soil evaporation (black) (see text).
(b) Monthly mean P (gray shaded area) and ET (solid lines) in northern AF. ET is decomposed in the same components shown in (a).

Figure 4.18b shows the annual cycle of *P* (shaded area) and *ET* for the same components illustrated in Figure 4.18a, averaged on the northern AF. Tree's *ET* is high than the other land-cover groups during most part the year but not too different than those of grasses and crops. This difference is marked from March to June, season that consistently shows *ET* decrease in AF as response to the RCP 8.5-based LULCC (Figure 4.17). In contrast, herbaceous *ET* is quite similar than that of trees during the NH summer (dry season). Given its larger canopy conductance, crops show larger *ET* rates than grasses during most part of the year, particularly from July onwards. Hence, in such areas where crops have in part been introduced in detriment of grasses, the negative *ET* expected from deforestation may be counteracted due to larger crops *ET* with respect to that of grasses. In addition to the limited land-cover change strength prescribed in the RCP 8.5 scenario, all these patterns are coherent with a weak *ET* response to LULCC simulated in this region.

The changes in *ET* due to LULCC can be actually estimated based on the different *ET* components depicted in Figure 4.18, by the simple evaluation of these components in both land cover maps (with and without LULCC). Such estimation represents then the expected change in *ET* due to LULCC in absence of any feedback within the atmosphere; that is, without changes neither in precipitation nor in radiation (the *ET* components are derived from a single simulation, RCP85_NLUc in this case). The result of this exercise, done over the northern AF region, is illustrated in Figure 4.19. In this figure, the estimated and simulated monthly changes in *ET* induced by the RCP 8.5 LULCC scenario ($\Delta \mathrm{RCP85}_{\mathrm{PHY1}}$) are shown along with the simulated change in precipitation in the northern AF. Both *ET* anomalies are very weak (the changes represent less than 3% of the net ET values) and match during the first months of the year, in which *ET* increases. From March onward the estimated changes in *ET* are negative. The model simulates a stronger *ET* decrease in April-May with respect to that estimated, corresponding with a relatively large *P* decrease; and *ET* increases the second half of the year, where positive *P* anomalies prevail.

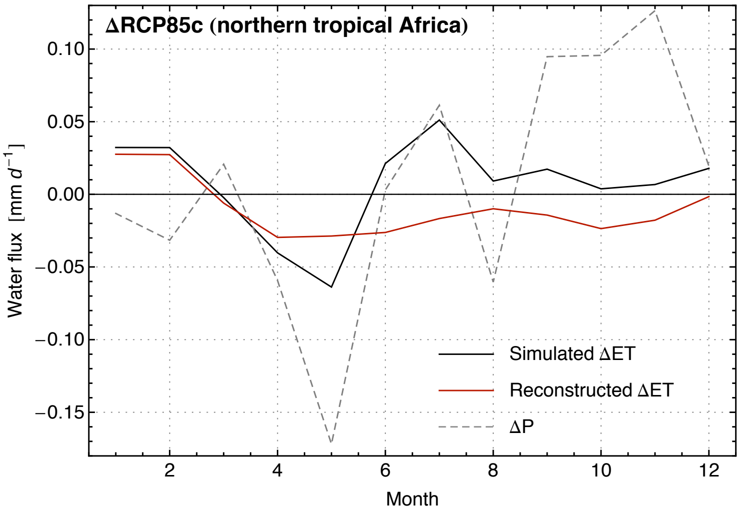

Figure 4.19
Monthly mean LULCC-induced evapotranspiration (solid line in black) and precipitation (dashed line) changes in the northern AF region (0-15N). Red line indicates the expected change in ET in absence of any feedback with the atmosphere (see text).

Figures 4.18 and 4.19 highlights that in addition to the strength of the imposed LULCC, IPSL has an intrinsic low sensitivity to land-use changes in the northern AF region (sub-Sahel) in terms of *ET*, because both trees and herbaceous vegetation maintain similar *ET* rates, even during the dry season. Further, given the weak inherent *ET* response in AF (characterized by the reconstructed *ET* changes show as red line in Figure 4.19), the simulated *ET* change is also controlled by non-deterministic changes in precipitation (i.e., the simulated *P* changes in this region, although large compared to the *ET* ones, are within the model variability; Figure 4.17).

4.3.5 Overview

The precedent sections describe the simulated biogeophysical impacts of large-scale LULCC for the historical and future scenarios based on LUH dataset. The IPSL model, in its fully coupled configuration, shows weak responses to LULCC in terms of surface temperature and precipitation, but clear perturbations in the surface radiation and turbulent heat fluxes over the regions affected by land cover changes.

The radiative effects of LULCC are, on one hand, directly driven by changes in the surface albedo that increases in areas with partial deforestation and, on the other, indirectly led by changes in the incoming shortwave (S_D) and longwave (L_D) radiation at the surface. Particularly, regarding the historical simulations, increases in $\mathrm{S_D}$ tend to counteract the albedo effect in the northern mid-latitude regions in DJF and SON (Figure 4.12), explaining in part the feeble temperature responses in those regions and seasons. However, the changes in atmospheric variables such as upper air moisture, cloud cover, and consequently, in S_D and L_D, are quite sensible to the model variability, whereby the indirect impacts of LULCC cannot be robustly quantified with single realizations.

To better quantify the inherent radiative response to LULCC of IPSL, zonal mean changes in the simulated S_N and in its associated component induced by the change in surface albedo (equation 2.15, Chapter 2) were calculated from the four diagnostics here assessed ($\Delta\mathrm{HIST_{PHY}}$, $\Delta\mathrm{RCP26_{PHY}}$, $\Delta\mathrm{RCP85_{PHY1}}$ and $\Delta\mathrm{RCP85_{PHY2}}$). This is illustrated in Figure 4.20. In order to avoid mixing different responses to different LULCC, the S_N differences at the grid-cell level were normalized against the corresponding changes the herbaceous fraction ($\Delta\mathrm{F_H}$), as well as done in previous analyses (e.g., section 3.2.3; Chapter 3). The resulting normalized changes are estimates of the model response to total deforestation.

Excepting high latitudes, the albedo-driven normalized S_N anomalies are around −10 W m^{-2} (indicated with dashed lines in Figure 4.20), which correspond to surface albedo increases of near 0.05. This value corresponds to the typical difference between the snow-free albedo of forest and that of herbaceous plants in ORCHIDEE. The simulated S_N changes (solid lines in Figure 4.20) are in most cases weaker (absolute) than those of the albedo-derived component, whereby illustrating the resulting net effect in S_N due to increases in S_D. Strictly, the difference between the simulated and the albedo-derived changes in S_N account for both the changes in S_D and a second order term (see equation 2.15), but the latter is negligible with respect to the former (not show). Hence, the expected responses in S_N due to surface albedo perturbations are clearly dampened by increases in S_D, effect that is particularly strong at high latitudes, but is also present at lower latitudes in DJF and MAM. During the northern winter (DJF), the increases in S_D almost completely offset the albedo induced S_N changes in areas north of 20°N.

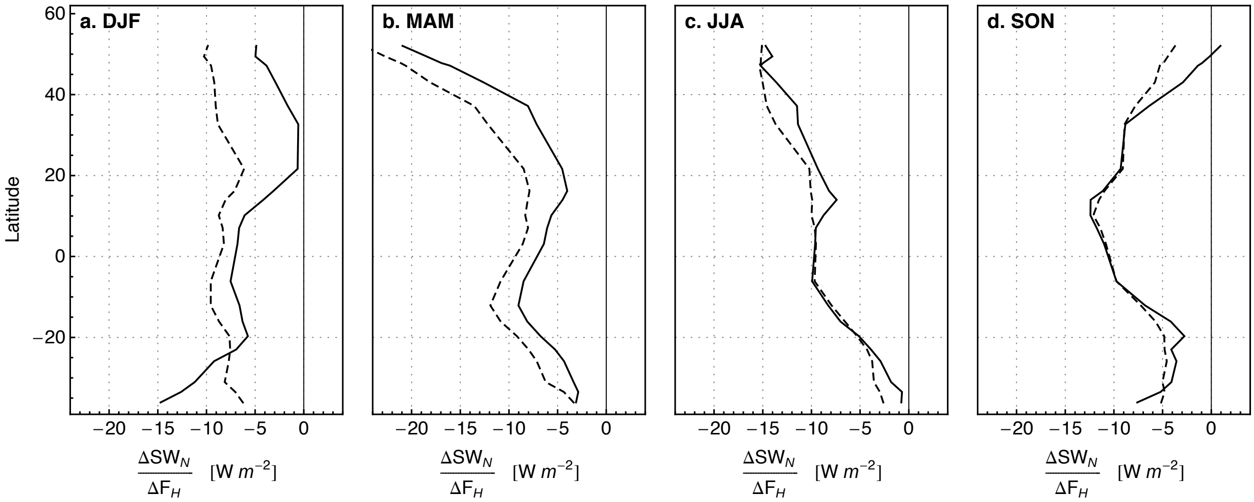

Figure 4.20
Zonal mean seasonal LULCC-induced changes in net shortwave radiation (S_N) normalized with the changes in the herbaceous fraction (ΔF_H) (solid lines). Dashed lines indicate the expected response in S_N due to changes in surface albedo alone (see text). Zonal means computed from the ensemble of grid-points within latitudinal bands of 10° showing absolute ΔF_H values larger than 0.1 in $\Delta HIST_{PHY}$, $\Delta RCP26_{PHY}$, $\Delta RCP85_{PHY1}$ and $\Delta RCP85_{PHY2}$.

The moderate temperature responses to LULCC simulated in IPSL are, in part, associated to the described dampened radiative impacts, but is more generally the result of counteracting effects induced by the relative changes of radiative fluxes with respect to the non-radiative ones. As Figure 4.21 illustrates, this is also an intrinsic response of the model. This figure shows the scatter plot between the changes in the total turbulent exchange ($\Delta Q_T = \Delta H + \Delta LE$) and the changes in available energy ($\Delta Q_A = \Delta S_N + \Delta L_D$), in a similar analysis than that used to compare the various model responses in the previous LUCID phase (see Figure 2.19, Chapter 2). Single seasonal values of individual grid-points with large changes in at least one land cover unit (greater than 25%) are illustrated four diagnostics here assessed ($\Delta HIST_{PHY}$, $\Delta RCP26_{PHY}$, $\Delta RCP85_{PHY1}$, and $\Delta RCP85_{PHY2}$). Most cases show decreases in these two variables after partial deforestation. Decreases in Q_A are mainly directed by decreases in S_N, while decreases in Q_T are led by different factors, including the increasing aerodynamic resistance, large LE decreases and the radiatively-induced drop in Q_T.

If the surface energy balance (SEB) is conserved and there are no significant changes in soil heat flux, the changes in surface temperature should respond to changes in Q_A and Q_T only, and then can be classified in the ΔQ_T versus ΔQ_A domain (this is qualitatively indicated in Figure 4.21 as $\Delta T << 0$, $\Delta T < 0$, $\Delta T > 0$ and $\Delta T >> 0$). Hence, large decreases of Q_A must produce large cooling if these are not accompanied with decreases in Q_T of the same order. This does not occur in the IPSL case since the simulated changes in Q_A and Q_T are of similar amplitude in most cases. Given that the model maintains SEB, the resulting surface temperature responses are moderate (the simulated temperature anomalies are indicated by colors in Figure 4.21). Conversely, the only cases showing relatively large temperature anomalies occur in regions or/and seasons with moderate radiative impacts (i.e., $\Delta Q_A \sim 0$) and strong decreases in Q_T, cases that consequently show strong warming.

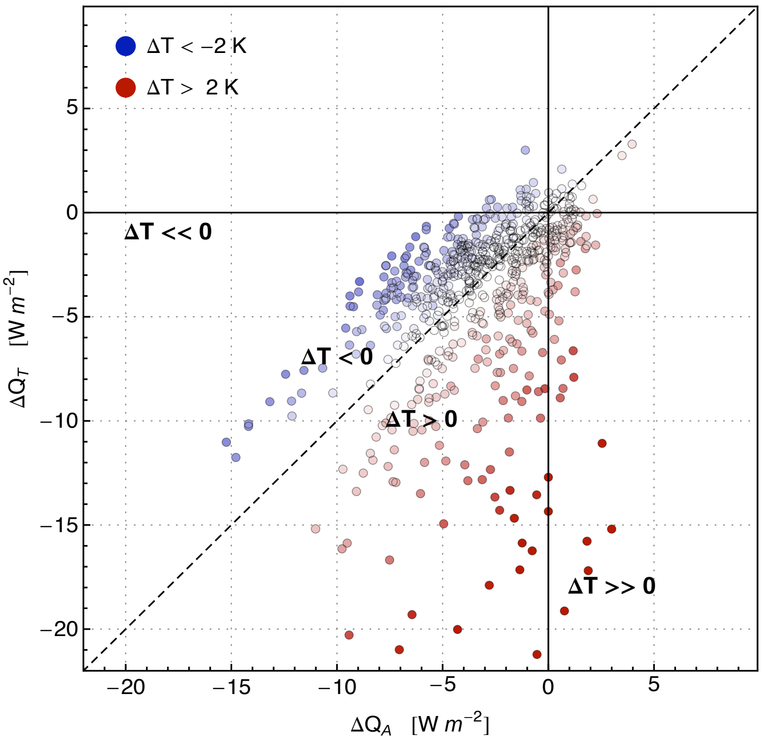

Figure 4.21
Seasonal LULCC-induced changes in total turbulent energy flux (Q_T) plotted against the changes in available energy at the surface ($Q_A = SW_N + LW_D$). Dots correspond to seasonal values in grid-points showing areal changes in forest fraction larger than 25%. The four diagnostics $\Delta HIST_{PHY}$, $\Delta RCP26_{PHY}$, $\Delta RCP85_{PHY1}$ and $\Delta RCP85_{PHY2}$ are included. If the surface energy balance is maintained and there is no perturbation on the soil heat flux, the surface temperature change should be negative/positive in those cases placed above/below the $Q_T = Q_A$ curve (dashed line). The simulated temperature responses are indicated with dot colors, from darker blue to darker red for large cooling to large warming, respectively.

The model also simulates significant and uneven perturbations in the breakdown of *H* and *LE* due to land-cover changes, which are highly dependant on the region, the LULCC character and the season. A general picture of these changes is illustrated in Figure 4.22, in which the seasonal paths of the evaporative fraction [$EF = LE/(H+LE)$] changes (ΔEF) are plotted. As well as for figure 4.20, the ΔEF values are normalized against the corresponding change of herbaceous fraction (ΔF_H) in order to represent the expected *EF* change given a total deforestation. Only those grid-points with absolute ΔF_H values larger than 10% from all four diagnostics assessed are illustrated.

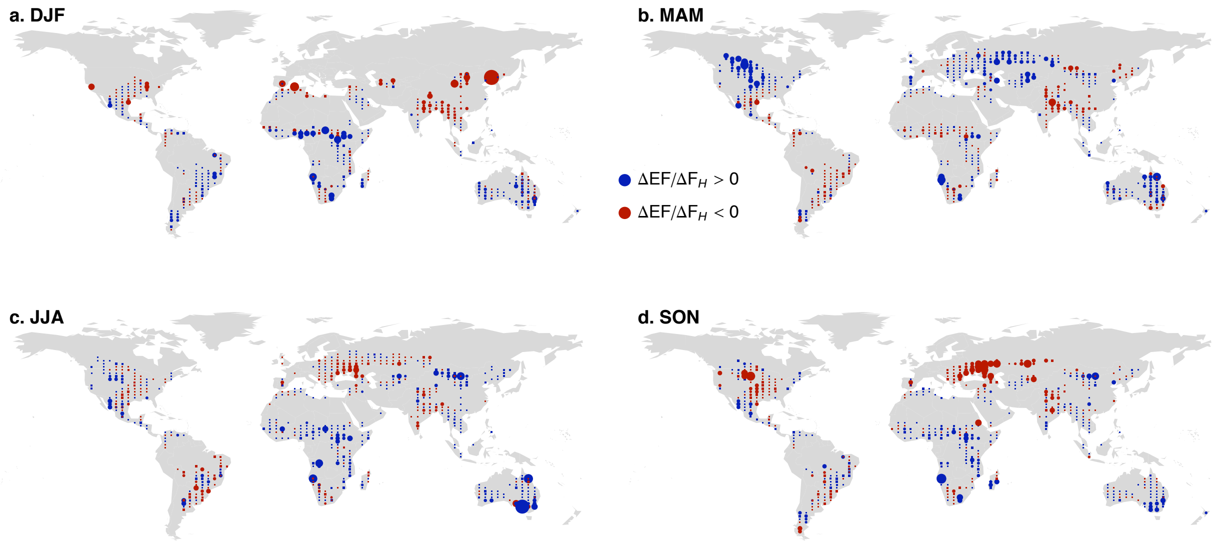

Figure 4.22
Seasonal LULCC-induced change in evaporative fraction [EF=LE/(LE+H)] normalized against the herbaceous fraction change (see text). Results from the $\Delta\text{HIST}_{\text{PHY}}$, $\Delta\text{RCP26}_{\text{PHY}}$, $\Delta\text{RCP85}_{\text{PHY-1}}$ and $\Delta\text{RCP85}_{\text{PHY-2}}$ are displayed together.

In North America and western Eurasia, the distinct seasonal pattern of ΔEF is recognized, with a clear shift from increasing *EF* during the NH spring (crop growing season) to decreasing *EF* in summer and fall. At low latitudes and in the Southern Hemisphere, positive changes in *EF* prevail in most areas and seasons. As has been described for Africa, these changes are mostly related to *H* decreases and weak *LE* changes. The LULCC-induced changes in *LE* cannot be robustly determined in these regions because the associated land cover perturbations are weak (few grid-cells show changes larger than 25% in e.g. forest fraction), and the resulting changes in *LE* are largely within the local *ET* variability. However, the results suggest that, for the northern tropical Africa, there is sufficient soil water availability during the year and notably during the dry season, from which small reductions and even increases in *LE* occur after partial deforestation.

4.4 Biogeochemical effects of LULCC

Two simulations performed within LUCID allow isolating the biogeochemical effects of LULCC in the context of the RCP 8.5 scenario: RCP85_NLUe and RCP85_NLUce (see tables 4.2 and 4.3). Both runs, with no changes in land cover, only differ by their evolution in the atmospheric carbon content computed by the model. One case accounts for fossil fuel emissions only (RCP85_NLUe) and, the other, for both the fossil fuel and the LULCC derived GHG emissions (RCP85_NLUce prescribes the atmospheric GHG concentration of calculated in RCP85_LUe).

Figure 4.23 illustrates the global land near-surface temperature and the global carbon budget from 2006 to 2100 simulated in RCP85_NLUe and RCP85_NLUce. The temperature evolution is very similar in both time series. More precisely, RCP85_NLUce shows a slightly higher temperature trend than RCP85_NLUe, but this difference is statistically insignificant.

The lack of a biogeochemical-induced temperature response to LULCC is consistent with the GHG concentrations resulting in both cases. Figure 4.23b show the atmospheric CO_2 concentration ([CO2]) computed in RCP85_NLUe and RCP85_NLUce. [CO2] computed in both simulations are actually similar to that prescribed in the RCP 8.5-driven runs (e.g., RCP85_LUc; indicated by a dotted line in Figure 4.23b). Along the 21st century, LULCC contributes little to the change in the atmospheric CO_2 compared to that induced by fossil fuel emissions. By the end of the 21st century, the atmospheric CO_2 computed in RCP85_LUe (and prescribed in RCP85_NLUce) exceeds by ~10 ppm that obtained in RCP85_NLUe (Figure 4.23c), which represents an increase ~2% higher that the one induced by the fossil-fuel emissions alone. The global land climate sensitivity of IPSL averages ~ 1°C per 100 ppm. Hence, the warming expected by an atmospheric CO_2 increase of 10 ppm might roughly be estimated to 0.1°C, value that is largely within the natural variability of model (the standard deviations of both of the detrended temperature time series depicted in Figure 4.23a are equal to 0.24 °C).

The limited impact of LULCC on the atmospheric [CO2] results from moderate carbon fluxes derived from LULCC as simulated in ORCHIDEE (Figure 4.23d). From 2006 to 2010 the direct carbon flux to the atmosphere derived from LULCC averages 0.34 PgC per year, rate that does not change too much until 2100 (deforestation rate is quite constant in time in the RCP 8.5 scenario; Figure 4.3), resulting in a cumulated LULCC-induced carbon emission of 29 PgC from 2006 to 2100. This value, however, does not represents the net carbon emissions derived from LULCC since it does not take into account a portion of biomass that is allocated in the litter carbon pool of ORCHIDEE, and its associated emission by decomposition (the model does not discriminate the natural litter fraction variability and that induced by LULCC).

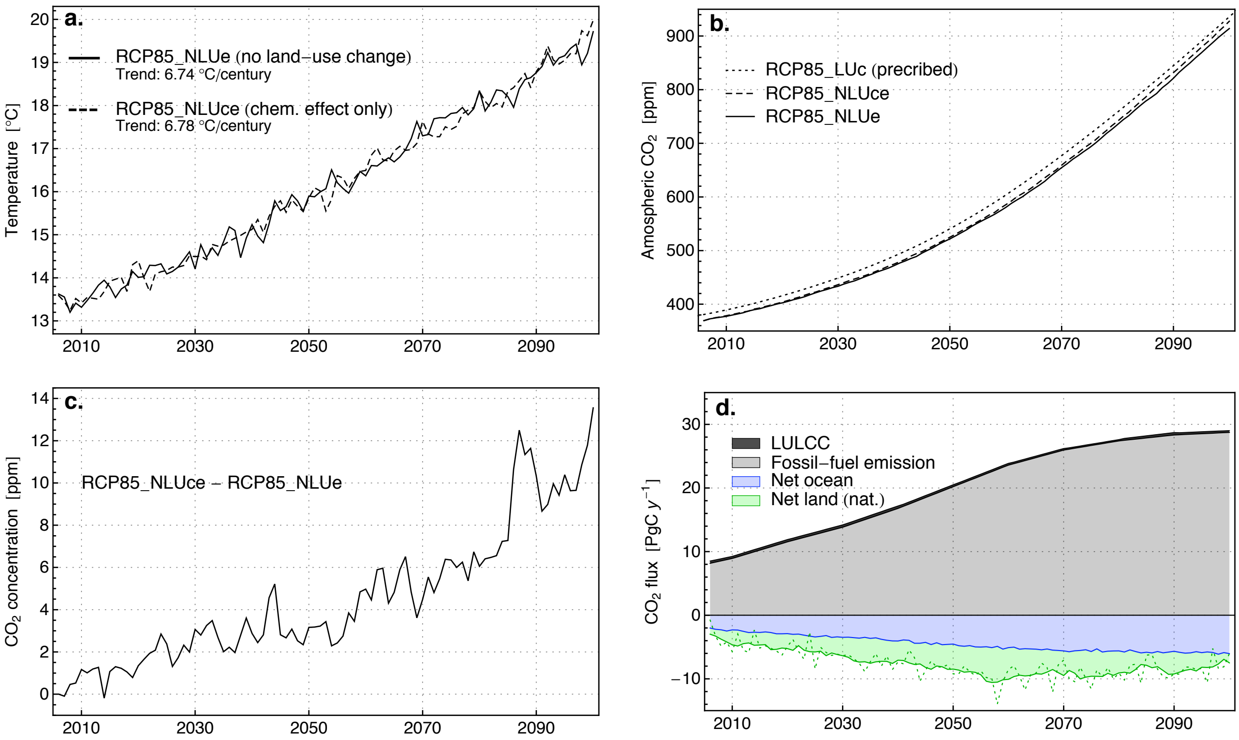

Figure 4.23
(a) Global-land annual surface air temperature projection following the RCP 8.5 scenario. Results from the RCP85_NLUe (solid line) and RCP85_NLUce (dashed) simulations. Differences within these two simulations account for the biogeochemical effect of LULCC.
(b) Atmospheric CO_2 concentration computed in RCP85_NLUe (solid line) and RCP85_NLUce (dashed). Dotted line indicates the RCP 8.5 CO_2 used in concentration-driven simulations.
(c) Atmospheric CO_2 concentration difference between RCP85_NLUe and RCP85_NLUce (LULCC effect).
(d) Atmospheric carbon sources and sinks simulated in RCP85_LUe. Fossil fuel and LULCC related direct CO_2 emissions in lighter and darker gray, respectively. Net natural annual CO_2 exchanges between the atmosphere and ocean (blue), and between the atmosphere and land biosphere (green; dotted and solid lines indicate the annual mean time-series and its 5-year moving average, respectively).

The net carbon emission derived from LULCC may be estimated from the net impact of LULCC in the biogeochemical budget. For the following calculation, the period 2006-2030 is used because the natural carbon sinks evolve approximately linearly with respect to the emissions (Figure 4.23d). During this period, the mean net ecosystem exchange (NEE) in both simulations RCP85_NLUe and RCP85_NLUce are near 6 PgC per year, with a difference within them of 0.46 PgC per year. This difference (ΔNEE_{LULCC}) represents the net impact of LULCC. For its part, based on the fossil-fuel only simulation (RCP85_NLUe), the fraction of the carbon released that is absorbed by the ocean-land system averages 0.47 from 2006 to 2030. Supposing that the same fraction of carbon will be absorbed following LULCC emission (E_{LULCC}), the latter might be estimated as follows:

$$\Delta NEE_{LULCC} = 0.46 = E_{LULCC} - S_{LULCC} = (1 - 0.47)\, E_{LULCC} \qquad [\ PgC\ y^{-1}\ ]$$

$$\Rightarrow E_{LULCC} = 0.87\ \ PgC\ y^{-1}$$

where S_{LULCC} is the amount of carbon within the LULCC-derived emissions that is reabsorbed by the land biosphere and the ocean.

Given that, from 2006 to 2030, the mean global deforestation prescribed in ORCHIDEE based on the RCP 8.5 scenario is 5.3 million ha per year, the net carbon emission from LULCC simulated in IPSL of 0.87 PgC per year results within the lower rates of the recent estimates based on biosphere carbon stock observations (Table 4.5).

Table 4.5. Estimations of global carbon emissions from LULCC.

	Period used	Global deforestation $[10^6\ ha\ y^{-1}]$	Mean flux of carbon $[PgC\ y^{-1}]$
Canadell et al. (2007)	2000-2005	7.3[a]	1.5
Friedlingstein et al. (2010)	2000-2009	5.2[b]	1.1 ± 0.7
Pan et al. (2011)	1990-2007	-	1.3 ± 0.7[c]
Baccini et al. (2012)	2000-2010	-	1.0[c]
Harris et al. (2012)	2000-2005	6.7[c]	0.81 ± 0.3[c]
Simulated (RCP 8.5)	2006-2030	5.3	0.87

[a] From FAO-FRA (2005); [b] From FAO-FRA (2010)
[c] Tropical forest only

4.5 Prospective: Projected land-use and climate changes in the Amazon

As briefly introduced in Section 4.1, through land-use changes humans have significantly disturbed the Amazon forest during the last decades. The current deforestation rates in the Amazon will likely continue in the near future driven, within other factors, by the biofuel demand. There is also a risk that large-scale human-induced climate trends will affect this ecosystem due to, e.g., modifications in the regional precipitation regime. Projected LULCC during the 21st century within the Amazon basin based on the LUH dataset is almost negligible, so the simulated LULCC-induced impacts in Amazon climate in the context of CMIP5-LUCID have not been assessed here. The reliability of such LULCC projections is discussed and compared with other regional-scale scenarios and the ongoing estimates of forest cover loss

(Section 4.5.1). This section also brings a shallow assessment of the simulated climate impacts in the Amazon basin resulting from the projected large-scale (GHG-induced) climate changes following the RCP 8.5 scenario (Section 4.5.2).

4.5.1 Current and projected land-cover changes in the Amazon

Brazil's National Space Research Institute (INPE) through the project PRODES estimates a total forest cover loss of around 35 million ha between 1990 and 2010 in the Brazilian Amazon Legal region. This recent trend is coherent with other estimates, such that of the UN-FAO Forest Resources Assessments (FRA2010) that reports a total deforestation from 1990 to 2010 of 55 and 70 million ha for the Brazilian Amazon and the whole Amazon basin, respectively. During the same period, the prescribed deforestation in ORCHIDEE based on LUH dataset reaches 16 million km^2 for the whole basin and taking the strongest scenario in terms of deforestation (RCP 2.6) for the 2006-2010 time-slice, i.e., more than four times lower than FAO estimates.

An overview of different historical and future scenarios of Amazonian deforestation is illustrated in Figure 4.24. The weak values resulting from LUH is manifest during the historical period (since 1950) when compared to the observation-based data. It is also clear that the resulting forest cover loss projected to the future based on the RCP scenarios are also extremely optimistic if compared with both the mitigation and non-policy scenarios proposed within the SimAmazonia framework (see figures 4.24 and 4.25). SimAmazonia takes into account recent observation-based forest clearing statistics (from PRODES), local socio-economical factors, governance conservation strategies and biophysical parameterizations to derive scenarios of land-use and forest cover (Soares-Filho et al., 2006).

The discrepancy between the LUH-based changes in land cover and the observation-based estimates during the historical period could in part result from the method adopted to include the agricultural data into the ORCHIDEE vegetation maps, notably due to the assumption that expansion of grazed areas does not affect forest lands as long as there is enough grasslands to allocate grazed lands. However, the strength of such differences also denotes that the historical agricultural information provided by HYDE (the one used in LUH), although probably the most up-to-date and adequate dataset to be used in global-scale and long-term LULCC studies, lacks of consistency at the regional scale. This is somehow logical given the number of local factors behind the land-use evolution other than the changes in population density, principal driver used in the HYDE dataset (Klein Goldewijk et al., 2011). Further, the

LULCC trajectories proposed in the CMIP5 framework (RCPs) do not appear either as realistic scenarios for regional-scale studies since they do not take into account recent observed LULCC and do not well represent local (country) complexities in the land-use dynamic and its responses to global requirements.

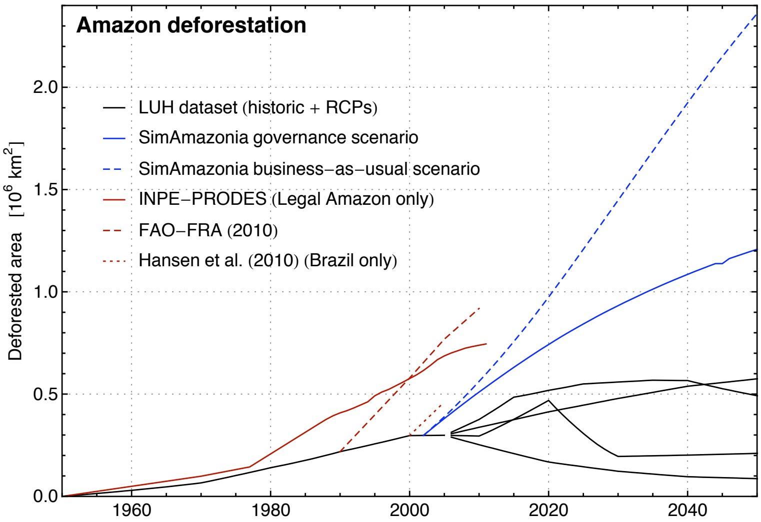

Figure 4.24
Total area deforested within the Amazonian basin (see Figure 4.23) prescribed in ORCHIDEE based on LUH (black lines indicate the historical data and the four RCP scenarios) and based on SimAmazonia (blue; solid and dashed line indicate the governance and non-policy scenarios). Solid, dashed and dotted red lines indicate estimations of forest cover loss from different sources: PRODES (concern the Brazilian Legal Amazon region only), FAO Global Forest Resources Assessment (2010) and Hansen et al. (2008; concern Brazil only). For clear displaying, the SimAmazonia and the observation-based deforestation time-series are shifted so that the first year of each of them matches the LUH curve.

In the context of the AMAZALERT project, a number of modeling experiments will be carried out with the IPSL model to assess the climate impact of LULCC based on regional scenarios, those provided by SimAmazonia among others. The SimAmazionia dataset prescribes gridded land-cover fraction of three units within the Amazon basin: forest, deforested and non-forest lands. The data was initially computed from 2002 to 2050, but have been recently updated to 2100. These land-use scenarios were, in a first stage, incorporated to ORCHIDEE following a simple protocol, which uses the CMIP5 land-cover of 2002 as background map (i.e., a vegetation map that already includes agricultural information from LUH). The forest fraction provided by SimAmazonia was first replicated in ORCHIDEE, maintaining the tree's PFT proportion preexisting in the background land cover. In the same manner, the deforested SimAmazonia unit was filled up by herbaceous PFTs, maintaining the background land cover proportion between the two (C3 and C4) grass and crop classes. Given that the remaining non-forest area prescribed in SimAmazonia may represent savannas, grassland or croplands, it was incorporated to the ORCHIDEE map maintaining the background land cover as long as the total tree fraction of the latter won't exceed 50%. Otherwise, tree and non-tree classes were proportionally adjusted to get a fifty-fifty proportion.

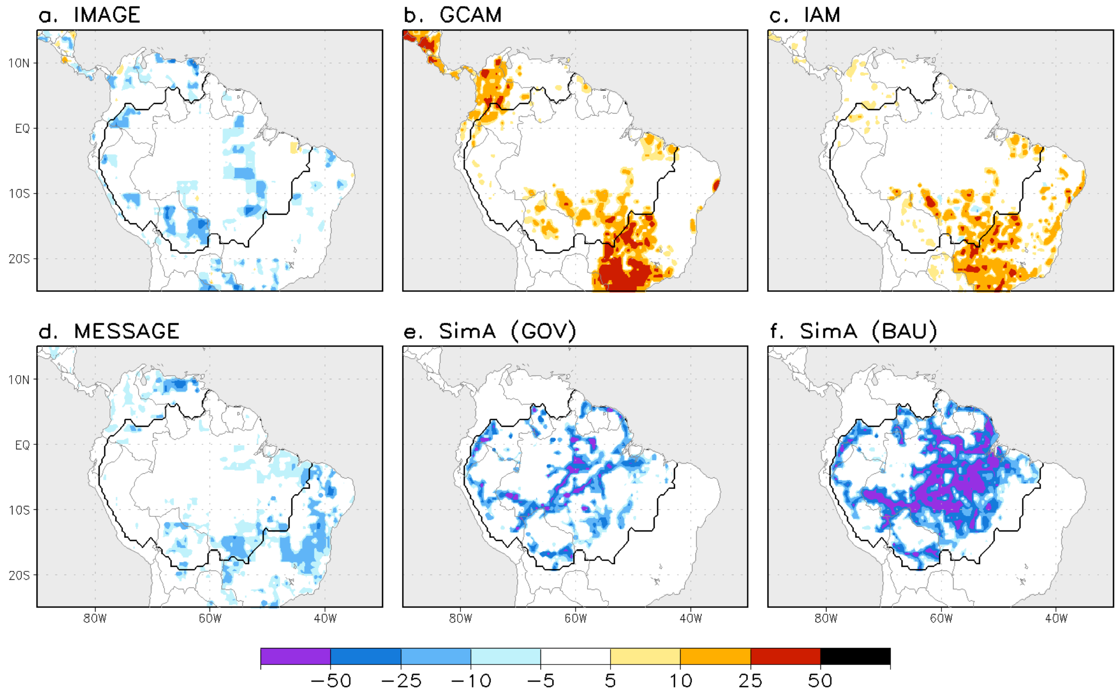

Figure 4.25
Change in the grid areal fraction covered by trees (%) between 2005 and 2050 prescribed in ORCHIDEE. Differences based on the RCP (a-d), SimAmazonia governance (e) and SimAmazonia business-as-usual (f) scenarios.

Figure 4.25 illustrates the forest fraction difference between the SimAmazonia-based maps of 2002 and 2050. The resulting changes in forest fraction from both SimAmazonia scenarios (governance and business-as-usual) are shown along with those prescribed by the RCP scenarios. It is clear from figures 4.24 and 4.25 that the SimAmazonia scenarios project a noticeably stronger pressure over the Amazon than the RCP ones. While the BAU scenario foresees extensive areas with 50% or larger reduction in forest cover, notably in the east side of the Amazon basin, RCP 2.6 –the pessimistic LULCC scenario within RCPs– shows few localized regions with forest reductions larger than 10%.

Simulations based on the SimAmazonia dataset will likely produce significant changes in climate due to LULCC, at least at the regional (Amazon) scale. In order to put forward the potential impacts on the hydrologic cycle, estimated changes in ET between 2002 and 2050 were calculated based on the water fluxes simulated in the HIST_LUc runs combined with the SimAmazonia BAU-derived land-cover maps. This was done following the same procedure used to reconstruct the LULCC-induced ET changes in the tropical Africa (Figure 4.19). The ET simulated for each PFT in HIST-LUc from 1970 to 2005 were used to derive monthly ET fields.

Then, net ET fields were reconstructed by evaluating these components in both the 2002 and 2050 SimAmazonia BAU-based land-cover maps. Since both reconstructions are based on the same run, i.e., with equal radiation, precipitation, soil moisture, etc (those simulated in HIST-LUc), the estimated ET change only accounts for a different vegetation partitioning within each grid-cell and does not take in account for any feedback with the atmosphere.

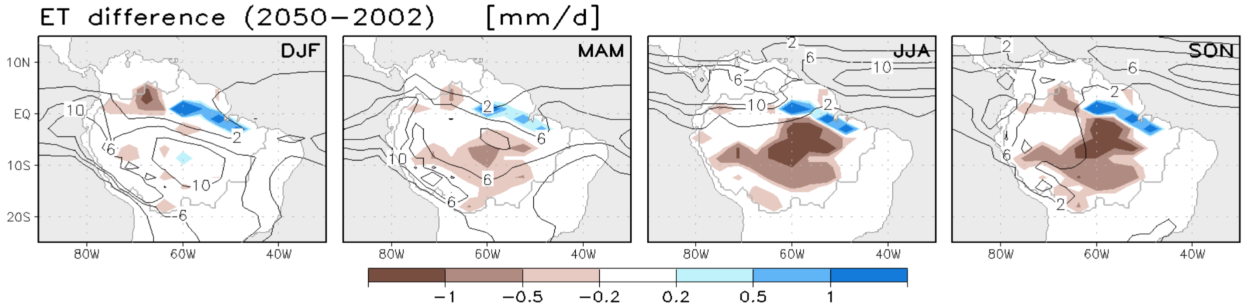

Figure 4.26
Estimated seasonal LULCC-induced evapotranspiration differences (filled contours; in mm day^{-1}) between 2002 and 2050 based on SimAmazonia BAU scenario in absence of any feedback with the atmosphere. Differences computed from single PFT ET components simulated from 1970 to 2006 (HIST_LUc) in combination with both SimAmazonia land-cover maps of 2002 and 2050 (see text). Contour lines indicate the simulated seasonal mean (1970-2005) precipitation (in mm day^{-1}).

The seasonal mean ET differences between both reconstructions (2050 minus 2002) are illustrated in Figure 4.26. This scenario of LULCC affects significantly ET in the monsoonal Amazon region (southern part of the Basin) during its corresponding dry season (southern winter and spring; the mean precipitation from 1970-2005 simulated in HIST_LUc is indicated with contour lines in Figure 4.26). This region shows an extensive domain with decreases in ET larger than 0.5 mm in JJA and SON; an impact quite considerable, larger than 25% of the net ET rates in many areas. Given that water recycling plays an important role in the precipitation regime of the Amazon, such direct LULCC impact in ET will likely be amplified in a coupled simulation due to feedbacks with precipitation.

4.5.2 GHG-induced changes in the regional climate and hydrological cycle

The following analyses show the climate impacts in the Amazon of large-scale disturbances (GHG-induced) following the RCP 8.5 scenario. We focus on this scenario to assess the Amazonian climate sensitivity simulated by IPSL to changes in GHGs' concentration. The impacts in the surface climate are calculated comparing the last 50-year of simulation in RCP85_NLUc (no LULCC) and HIST_LUc (Table 4.2). It is important to note that this diagnostic also accounts for land-use changes, corresponding to the difference between the vegetation prescribed in 2005 (the one used in RCP85_NLUc) with respect to the mean vegetation of the 1956-2005 period (from HIST_LUc). Given the limited strength of the prescribed (LUH) global and local (Amazon) LULCC during the last 50 years of the 20th century, LULCC should induce little impact on the climate of the Amazon compared to the one resulting from large-scale changes (GHGs).

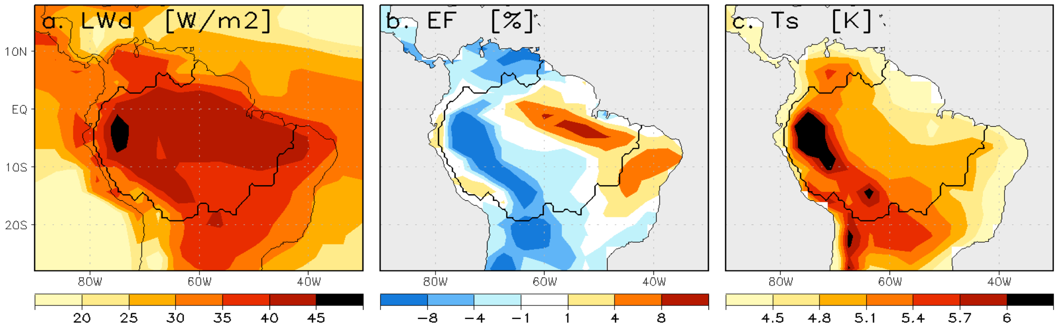

Figure 4.27
Projected annual mean changes in surface downward longwave radiation (a), evaporative fraction (absolute %; b) and temperature (c) following the RCP 8.5 scenario (2051-2100 minus 1956-2005). Thick contour indicates the Amazon basin limits further used in specific analyses.

Figures 4.27 show the annual mean surface change (2051-2100 minus 1956-2005) in the incoming longwave radiation (L_D), in the evaporative fraction EF [$LE/(LE+H)$] and in surface temperature. Most areas within the Amazon basin show increases in L_D larger than 35 W m^{-2} and associated temperature increases exceeding 4.5°C. Temperature responses show quite larger anomalies (> ~5.5°C) in the western side of the Amazon, along the Andes range and in El Gran Chaco region (south Bolivia and Paraguay). This marked pattern matches the annual changes in EF, which show large (>5%) negative and positive values in respectively the west and east sides of the continent, suggesting a major role of the hydrological changes in the resulting geographical variations of temperature anomalies.

Figures 4.28 illustrate the seasonal changes in precipitation (P), ET and runoff+drainage ($R+D$). The annual change in EF holds with the ET one that also decreases and increases near the Andes and in the eastern Amazon. The ET anomalies show a fairly steady pattern along the year compared to the changes in P, which show a markedly and a geographically coherent signal, but mainly constrained to the warm (wet) monsoonal seasons (DJF and MAM; the 1956-2005 seasonal mean P is indicated by contour lines in Figure 4.28a). The moderate ET changes and its low seasonal variation compared to the P ones highlight the role of forest and soil moisture inertia in regulating in water exchanges.

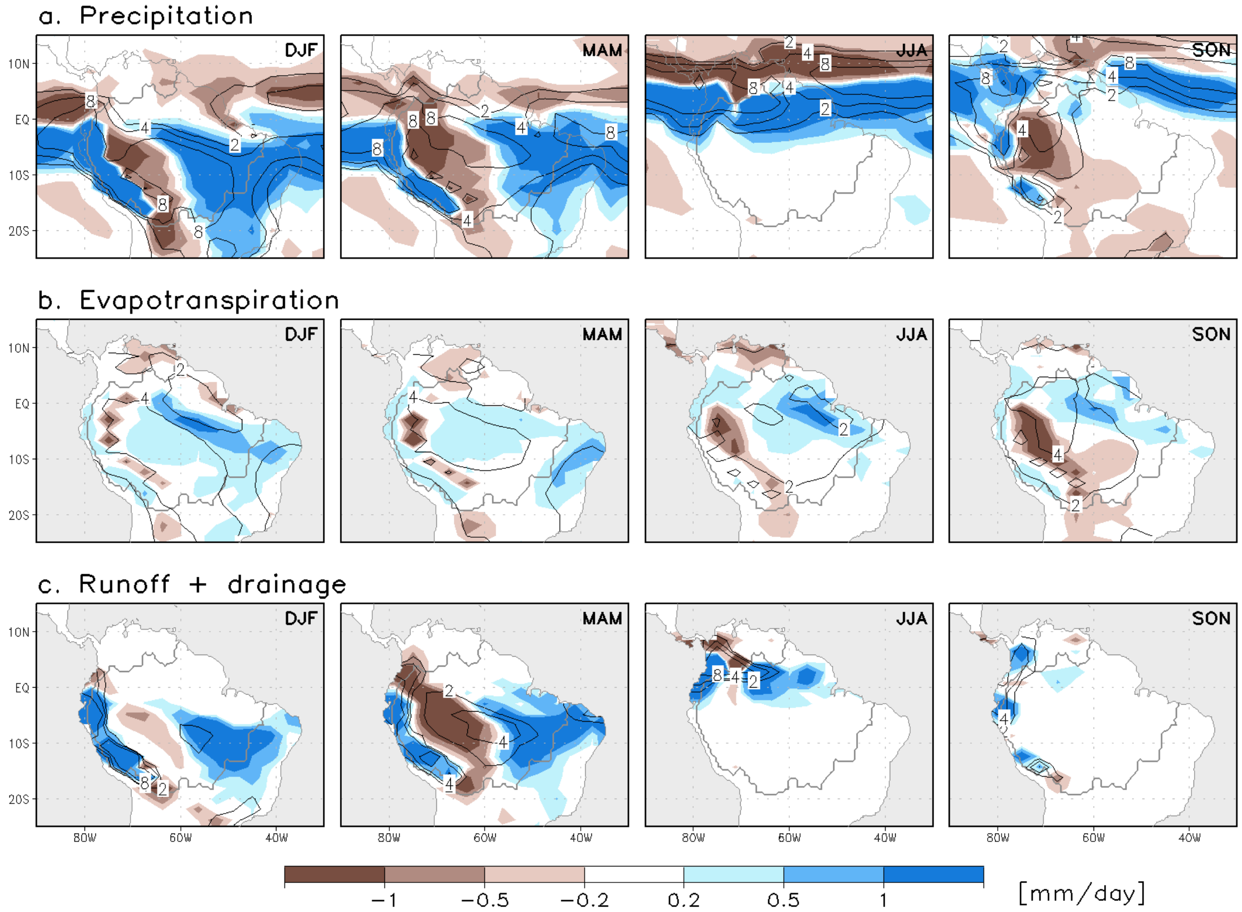

Figure 4.28
Seasonal mean difference (2051-2100 minus 1956-2005) in precipitation (a), evapotranspiration (b) and runoff plus drainage (c). Contour lines indicate the climatological (1956-2005) water flux of the corresponding variable (isolines of 2, 4 and 8 mm day^{-1} are drawn).

It is noteworthy that the negative anomalies in *P*, ET, and *R*+*D*, just at the east side of the Andes range, correspond to the region of maximum north-to-south moisture advection, known as South American Low Level Jet (SALLJ; e.g., Marengo et al., 2004). Further analyses of the simulated circulation are needed to assess the changes in SALLJ and in the associated water transport.

As the changes in ET remain roughly constant from season to season, the seasonality of the *P* changes strongly modulates the *R*+*D* responses, showing large changes (higher than 50% in many areas with respect to the net values) during the wet season (Figure 4.28c). This relation between *P*, ET and *R*+*D* is clearly illustrated in Figure 4.29, which shows the basin wide climatological values of these variables (1951-2005) and its projected changes. The soil evaporation, transpiration and interception loss components of ET are also indicated in Figure 4.29. Although *P* varies strongly following the monsoonal regime from ~6 to less than 2 mm per day from December-May to June-November, the simulated ET shows quite steady values of around 3 mm day^{-1} throughout the year. *R+D* is around half of ET during the wet season, and near zero during the dry one. ET is maintained during the latter mainly through plant transpiration which unaltered rates with respect to wet season, whereby showing a very low regional mean water stress.

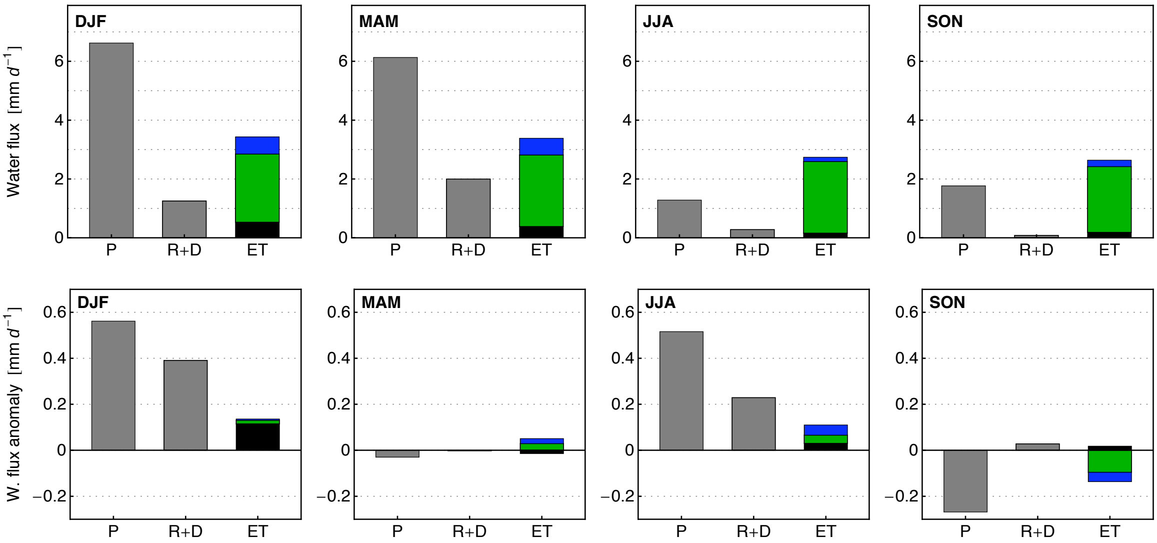

Figure 4.29
Seasonal mean (1956-2005) precipitation (P), runoff and drainage (R+D) and evapotranspiration (ET) in the Amazon Basin (top). Projected changes in the same variables following the RCP 8.5 scenario (2051-2100 minus 1956-2005). Stacked bars indicate the soil evaporation (black), canopy transpiration (green) and interception loss (blue) components of ET.

In DJF, the mean basin-wide *P* increases by ~8% from 1956-2005 to 2051-2100 (Figure 4.29). This change is almost completely balanced at the surface with large increases in *R+D* (~+35%) and soil evaporation (~+25%). The roughly unchanged soil water content (i.e., the residual term in the balance of *P*, ET and *R+D*) and transpiration reflect the saturated soil moisture condition during this season. In contrast, the large precipitation increases simulated in JJA (~+40%) is only partially balanced with changes in *R+D* and ET. Even in JJA (dry season), the canopy transpiration is only slightly modified when a significant large increase in *P* takes place. However, a significant decrease in transpiration is simulated in SON for a moderate change (drop) in precipitation compared to JJA, which could indicate a higher ET sensitivity at the end of the dry season.

The *P* change in the Amazon domain is principally driven by the large-scale perturbation in this variable (not shown; see Dufresne et al., submitted), although regional feedbacks are likely playing an important role, notably through changes in turbulent flux exchanges and, then, in convection. Further, the simulated Amazonian ET response to the increasing GHG appears closely related to the change in the precipitation regime. Other factors, such as changes in available energy or in physiological effects of CO_2 (changes in the stomata conductance) are not clearly affecting ET. This can be appreciated in Figure 4.31.

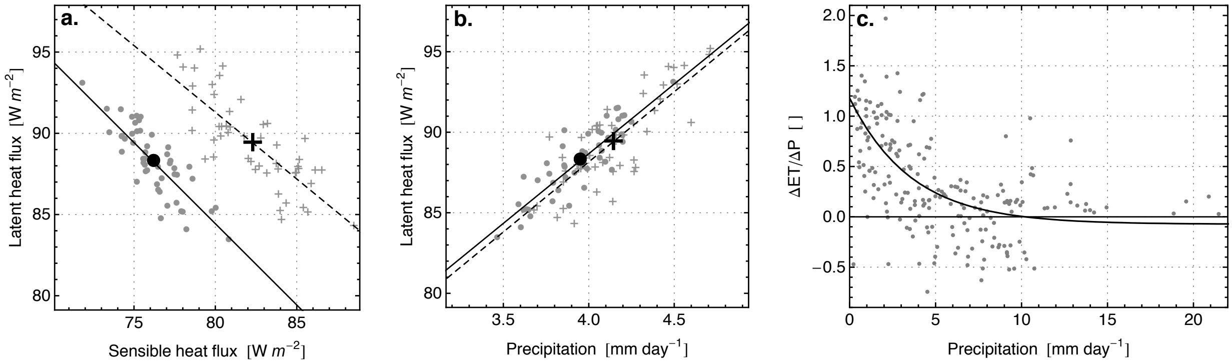

Figure 4.30
Annual mean latent heat flux in the Amazon basin plotted against sensible heat flux (a) and against precipitation (b). Gray dots and crosses indicate the multi-year values from HIST_LUc (1956-2005) and RCP85_NLUc (2051-2100), respectively. Black dot (cross) and solid (dashed) line indicate mean values and linear fits for HIST_LUc (RCP85_NLUc). Ratio between the changes (RCP85_NLUc – HIST_LUc) in evapotranspiration (ET) and P plotted against the mean P simulated in HIST_LUc (c). Dots and solid curve correspond to mean seasonal values from individual grid-cells within the Amazon basin, and an asymptotical (exponential) fit of them.

The scatter plot depicted in Figure 4.31a shows the annual and regional mean (Amazon basin) *LE* versus *H* of the individual years of both simulation HIST_LUc (1956-2005; dots) and RCP85_NLUc (2051-2100; crosses). Both fluxes are clearly anticorrelated at the interannual time-scale, with a similar relation in both simulations. The linear fit between both fluxes from the 21st century simulation shows a clear bias of around +7 W m^{-2} with respect to that of the 20th century. This difference, which stands for the GHG-induced net radiation change between both simulations, is almost completely taken over by *H*, while *LE* increases by 1.2 W m^{-2} only. Hence, there is a increase in the Bowen ratio or, equivalently, a decrease in EF, although ET increases. Further, the LE change of 1.2 W m^{-2} is more clearly related with the mean change in *P* than with the change in radiation or any other driver. *LE* and *P* show a strong interannual co-variability, quite similar in both simulations (Figure 4.29b). The linear fit of *LE* as function of *P* resulting from each simulation almost superposes each other; so that the mean annual increases in these variables (from 1956-2005 to 2051-2100) appear as a shift within their interannual relation. This pattern reveals either a minor role of any other ET driver, or that the effects from such drivers counteract each other.

The regional mean coupling between ET and *P* and the mean change of these variables depicted in Figure 4.31b hides quite a different coupling strength within the Amazon basin. As it is also suggested in Figure 4.30, ET is less sensible to *P* changes in regions or seasons with large water availability. This is more clearly illustrated in Figure 4.31c, showing the ratio between the changes in ET and *P* (ΔET/ΔP) plotted against the mean *P*. Such areas or seasons with relatively low precipitation show higher values of ΔET/ΔP, converging to ~1 when *P* reaches zero (i.e., a water limited regime). The mean ΔET/ΔP decays rapidly with increasing *P*. Grid-cells with seasonal *P* values larger than 5 mm day^{-1} show both positive and negative ΔET/ΔP, suggesting a secondary role of *P* regarding the changes in ET over saturated soils.

4.6 Chapter conclusions

Results from a set of fully coupled and transient simulations done with the IPSL ESM in the context of CMIP5 and LUCID are presented here. The analyses focus on the simulated global-scale changes in the surface climate due to land-cover changes from 1850 to 2100. The results describe the simulations outputs principally, with the aim of complementing the more in-depth analysis of the past LULCC effects done in the context of the first LUCID stage (Chapter 2). Hence the mechanism from which LULCC affect a number of surface variables in CMIP5-LUCID simulations are not particularly addressed here.

Regarding the four points proposed in the introduction, the following key results are highlighted:

Biogeophysical effects of LULCC

Four couples of simulations were analyzed to assess the biogeophysical impacts on the surface climate due the historical and future LULCC. The analyses focus on the historical period and the RCP 8.5 scenario because the associated simulations prescribe the larger deforestation rates in respectively the northern mid-latitudes and tropical regions. It should be note, however, that none of them neither the other three RCPs prescribe large perturbations over tropical rainforest. An overall view of the model response to LULCC is described in Section 4.3.5.

No statistically significant surface temperature differences, when averaged over global lands or over smaller regions affected by LULCC, were found in any of the four couples of simulation assessed. Few and very localized areas show significant changes in temperature. This feature reflects two aspects: (1) the temperature response of the model to the imposed LULCC is inherently weak and (2) single runs or time periods of up to 50 years are not enough to well characterize the effects on climate from realistic (moderate) scenarios of LULCC (in contrast to sensitive –total deforestation like– experiments).

The first point is discussed in Section 4.3.5 and illustrated in Figure 4.21. The IPSL model simulates relatively small temperature changes compared to the expected responses that should be induced by the simulated changes in radiation alone. Independently from the changes in the turbulent heat fluxes partitioning (e.g., in the evaporative fraction), the model systematically simulated decreases in the total turbulent exchange after partial deforestation, offsetting the cooling induced by reductions in the absorbed solar radiation. This effect was also observed in temperate regions in a number of GCMs assessed in the first LUCID phase (Chapter 2). In addition to the counteracting temperature responses due radiative and non-radiative effects, IPSL also simulates increases in incoming shortwave irradiance when deforestation takes place, counteracting the radiative impact that is primarily driven by increases in surface albedo.

With respect to the second point, given that the range of LULCC-induced temperature changes are generally of the similar amplitude than the interannual temperature standard deviation, the lack of ensemble of simulations does not allow to well quantify robust impacts of LULCC in the modeling experiments here analyzed. On the same ground, it is not possible to assess specific trajectories of such impacts along the period assessed.

Regarding the changes in the surface radiation budget and in turbulent exchanges in the northern temperate regions, the results from the historical CMIP5-LUCID set of simulation generally agree with those obtained in the previous LUCID phase. These are characterized by a yearlong reduction in the absorbed solar radiation due to increases in surface albedo and seasonally dependent changes in latent heat flux. The combined radiative and non-radiative effect led to significant regionally mean shift from cooling in MAM to warming in JJA.

Simulations of the 21st century based on the RCP 2.6 and RCP 8.5 scenarios, have associated moderate land-cover changes that concern lower latitudes principally, but no significant LULCC is prescribed in humid tropical forest. The temperature responses are moderate in the region with significant LULCC and, in most cases, positives due to dominating non-radiative effects upon the radiative ones. Significant decreases in total turbulent heat flux after partial deforestation are more related to aerodynamic factors (decreases in surface roughness) than change in evapotranspiration. Actually, latent heat flux remains unperturbed in many and even increases in others.

Biogeochemical effects of LULCC

Simulations do not show significant changes in surface temperature as biogeochemical response to LULCC following RCP 8.5. This scenario of LULCC produces an increment in the atmospheric CO_2 concentration of near 10 ppm to the end the 21st century, change that following the climate sensitivity of IPSL-CM5 should produce a net global warming of around 0.1 °C. This effect is negligible compared to one induced by the fossil fuel emissions of the same scenario. The carbon fluxes derived from deforestation as simulated in IPSL are of the same order but in lower part of recent estimates.

Simulated changes in the Amazon basin hydrology due to large-scale (GHG-induced) climate trends following the RCP 8.5 scenario were presented as prospective results. The model shows large changes in precipitation with a characteristic seasonal and spatial pattern within Amazon. Changes in precipitation produce strong impacts in runoff and moderate changes evapotranspiration, indicating a quite large soil moisture resilience during the dry season.

The general picture of the South American precipitation changes does not hold with the pattern shared by a number of CMIP3 climate models that project precipitation decreases in most parts of the Amazon during dry (local winter) season (Vera et al., 2006; Christensen et al., 2007; Seth et al., 2010). Such impact has usually interpreted as a local manifestation of large-scale El Nino-like climate trend. However, a large inter-model dispersion exists in the regional precipitation responses to the global climate trends, notably in the Amazon. Actually, in the particular case of IPSL, the new parameterization package for convection and cloud formation included a parallel version of the model, lead to a completely different precipitation response in the Amazon to increasing atmospheric GHG concentration (Hourdin et al., 2012).

Appendix 4.1

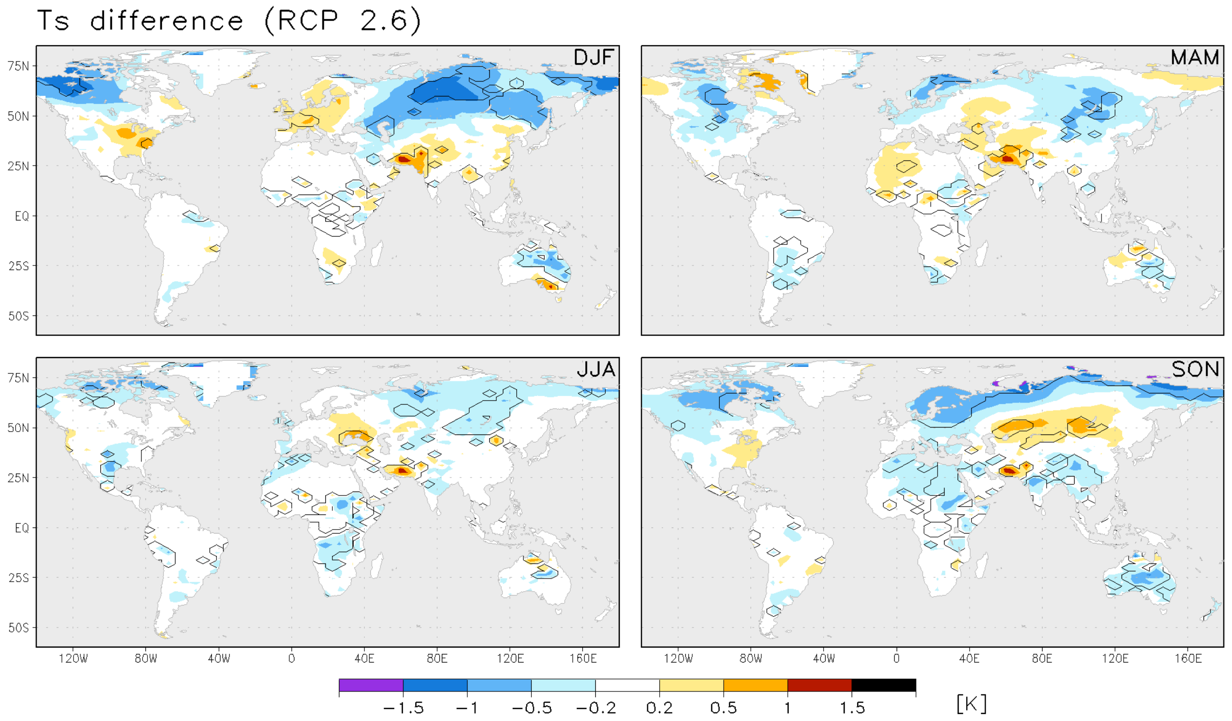

Figure A4.1
LULCC-induced seasonal surface temperature changes for the RCP 2.6 scenario ($\Delta RCP26_{PHY}$). Differences computed from the 2051-2100 climatologies. Contour lines encompass areas with changes significantly different from zero at the 95% confidence level.

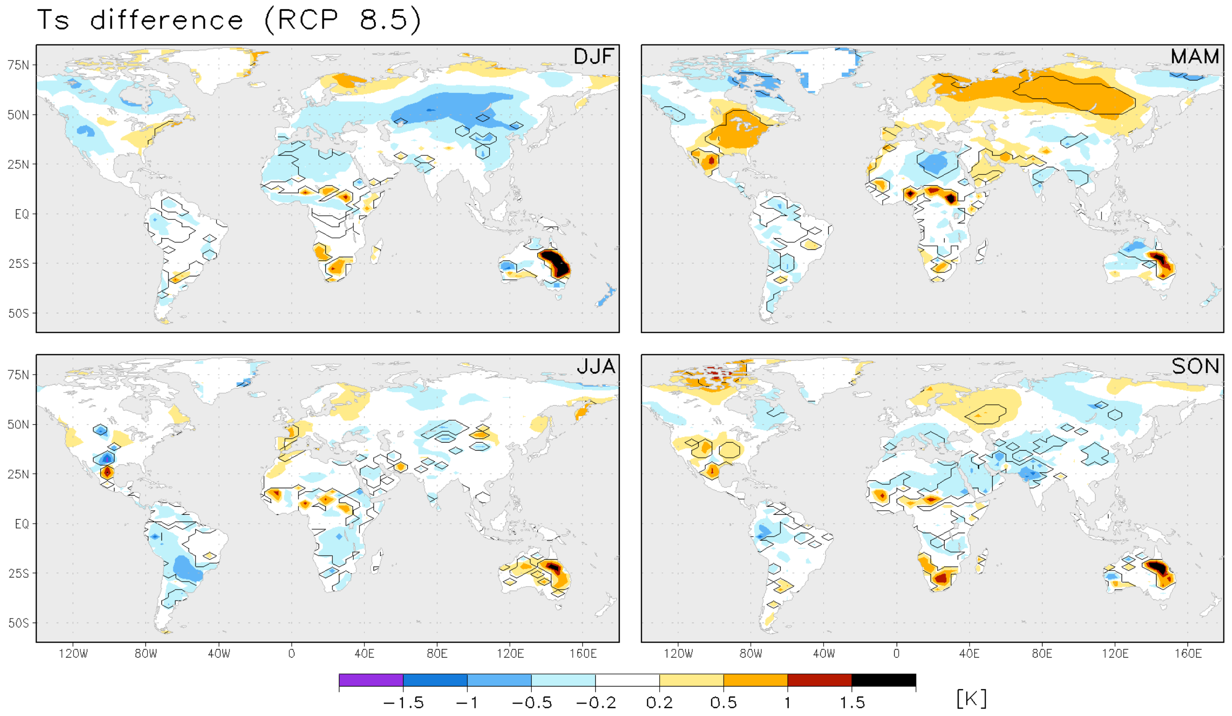

Figure A4.2
As for Figure A4.2 but for the RCP 8.5 scenario ($\Delta RCP85_{PHY2}$).

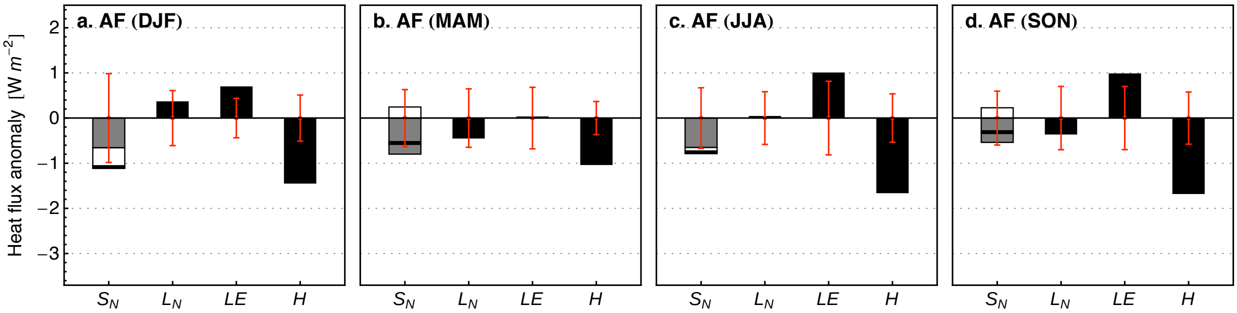

Figure A4.3
Seasonal changes in net shortwave (S_N) and longwave (L_N) radiation; latent (LE) and sensible (H) heat flux, simulated as response to the future LULCC ($\Delta RCP26_{PHY}$, differences averaged over the period 1956-2005) in North America/Eurasia (top) and in tropical Africa (bottom). S_N anomalies are separated between the component induced by surface albedo changes (gray) and that induced by changes in the incoming shortwave radiation (white). The horizontal black bars indicate the net (simulated) S_N change. Error bars indicate the limits from which anomalies are significantly different from zero at the 95% confidence level.

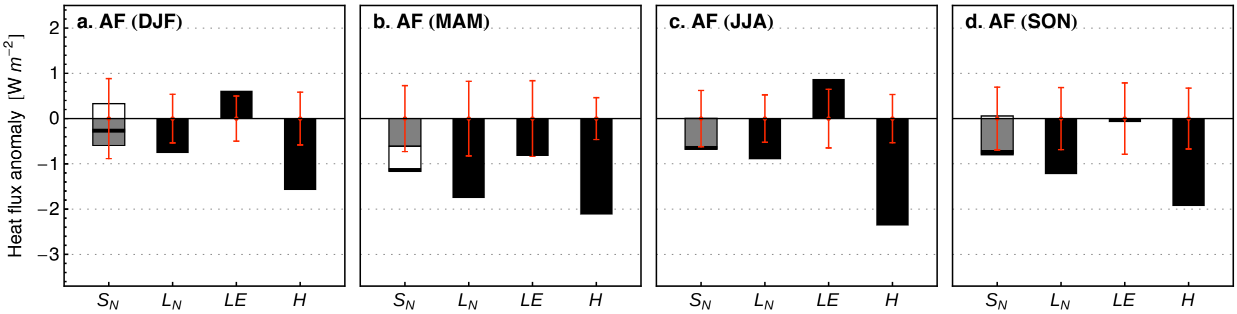

Figure A4.4
As for Figure A4.3 but for the RCP 8.5 scenario ($\Delta RCP85_{PHY2}$).

General conclusions

Changes in land cover affect a number of physical properties of the surface that lead to changes in the local climate of the affected regions. The climatic response to LULCC is triggered by direct perturbations in the surface radiation budget and in the exchange of momentum and turbulent energy between the surface and the atmosphere. Changes in surface albedo, in surface roughness and in other properties of the soil-vegetation system that affect the local hydrology (such as root length), are behind the biogeophysical effects of land-cover changes. In addition to these direct impacts, the surface is further affected by means of atmospheric feedbacks, which lead to changes in, e.g., precipitation or radiation. Remote areas from those with LULCC could also be affected through indirect effects or teleconnections.

This thesis explores the large-scale (i.e., at the spatial scale of global climate models) biogeophysical impacts on climate of LULCC. The first aim of this study is to detect the robust climate signals of LULCC. Corollary objectives are to quantify the uncertainties of such signals and identify the sources of these uncertainties. These objectives were addressed following two approaches:

1) The model intercomparison. Analyses of global simulations carried out by seven GCMs were done in the context of the LUCID project (Chapter 2).

2) Estimations of impacts of LULCC from observations-based datasets. Present-day satellite surface albedo data and global evapotranspiratrion products were used to reconstruct past LULCC-induced changes in these two key variables of the surface climate and hydrology (Chapter 3).

Both approaches were used to assess the impacts of LULCC between the preindustrial period and present-day. The analyses, in these cases, focused on the northern temperate regions, where the historical LULCC has been particularly intensive. Based on these results, the table that follows summarizes the main impacts of the past LULCC found in different variables at the surface, as well as their associated uncertainties.

Table 5.1. Main impacts of LULCC since the preindustrial period on different surface variables.

Robust signals	Uncertainties
LULCC	
Croplands and pasturelands have expanded dramatically since the preindustrial period, notably affecting the northern temperate latitudes.	If global crop and pasture datasets exist, the pre-agricultural (natural) vegetation and the historical transitions to agricultural land-cover units are more uncertain. Hence, the way the agricultural datasets are implemented in models lead to, e.g., very different past changes in global forest cover. The global deforestation from 1870 to 1992 prescribed in LUCID LSMs range from ~4 to ~10 million km^2. * These differences represent a primary source of uncertainty in the simulated impacts of LULCC, explaining 25 to 50% of the inter-model dispersion depending on the variable assessed.
Surface albedo	
Surface albedo has increased since the preindustrial period in regions with partial deforestation. The changes average near +0.1% (absolute) globally, ~+0.5% over the global ice-free lands, and exceed +10% in regions particularly affected by LULCC (with more than a third of the surface deforested) and under snowy conditions. These values represent the best estimates based on simulations and observations.	In addition to (*), large differences result from the models' land-surface parameterization, leading to a large dispersion in the amplitude of the simulated albedo responses to LULCC since the preindustrial period. The snow cover simulated by GCMs represents a secondary reason driving these differences.
Surface shortwave radiation	
Net shortwave radiation (S_N) has very likely decreased over areas partially deforested, mainly due to surface albedo increases. In the northern temperate regions, these changes are simulated throughout the year but are particularly strong in the late winter and early spring due to the large snow coverage and solar radiation availability. Models show systematic increases in downward solar radiation in temperate latitudes during the winter,	In addition to (*), the simulated changes in S_N vary significantly from one model to another mainly due to: (1) different albedo parameterizations and (2) the way the atmosphere feedbacks the surface perturbations, and the resulting changes in the incoming solar radiation. The direction and amplitude of the latter is particularly model-

dampening the direct LULCC impacts (albedo-driven) in S_N.	dependant during the warm season.
Turbulent heat fluxes	
All the LUCID models simulate decreases in the total turbulent flux in all seasons as response to partial deforestation. These changes, in part responding to perturbations in the surface radiation budget, are principally driven by direct alterations in the physical properties of the surface other than albedo, notably decreases in surface roughness. Land conversions in temperate regions have likely led to decreases in evapotranspiration (ET) where pastures replaced forest, and to increases where croplands replaced natural grasslands.	The simulated past LULCC-induced changes in total turbulent energy, although systematic in sign, vary significantly from model-to-model because of (*) and due to model-specific sensitivities to LULCC in this variable. The simulated changes in ET are particularly uneven within LUCID models, with differences in amplitude and sign. Data-driven estimations suggest that past LULCC has likely led to decreases in ET in most regions. However, large uncertainties remain in this subject, notably related to the ET values that are inferred for croplands.

The surface temperature responses to LULCC between the preindustrial period and present-day vary within LUCID models following their relative radiative impacts compared to the non-radiative ones, since in almost all cases both effects produce changes in temperature of opposite sign. Decreases in net shortwave radiation due to increases in surface albedo dominate in most cases in temperate latitudes. This is systematic within LUCID models during the northern winter and spring because of the presence of snow, when all LUCID models simulate cooling. In summer and fall, models show larger non-radiative effects and some of them simulate surface warming as responses to LULCC. It is important to note that besides the amplitude and sign in the simulated changes in latent heat flux, the models show systematic decreases in the total turbulent energy flux after deforestation (sum of latent and sensible heat flux), highlighting the major role that changes in aerodynamics properties of the surface (changes in surface roughness) play within the impacts of LULCC.

In general, the simulated temperature responses to past LULCC are weak when averaged globally, mainly because these are constrained to the regions where LULCC is prescribed (LUCID models' responses average –0.09 K over lands only), but important regionally. In regions where LULCC was particularly intense, such as over extensive areas (a few million km^2) in North America and Eurasia, the surface temperature changes simulated between 1870 and 1992 (mostly cooling) are comparable in amplitude to the GHG-related warming induced during the same period. This result emphasizes that without taking LULCC into account, studies such as climate change detection and attribution could produce misleading results at the regional scale.

One important conclusion from LUCID analyses is that specific model sensitivities in their climate responses to LULCC account for a half or a greater part of the inter-model spread found in the simulated changes of several variables. The other part of the model dispersion is explained by the differences in the land-surface forcing (e.g., amount of deforestation) prescribed in the various LSMs. Hence, the uncertainties related to the latter could be reduced with more constrained rules to incorporate agricultural data in land-cover maps. Meanwhile, the large differences that are intrinsic to the models (parameterization) and the resulting uneven climate sensitivities to LULCC, highlight the need for a more thoroughly validation of LSMs.

Land-use and climate studies based on observations are in most cases constrained to the local and regional scale, and to short time periods. Satellite-driven or other global datasets derived from present-day observations of the climate system have shown to be useful to infer past changes due to large-scale LULCC. Reconstructed surface albedo changes based on satellite data represent a realistic estimation of past LULCC effects on this variable, and on the associated surface shortwave radiation budget. These reconstructions also reveal deficiencies in current LSMs' parameterization, leading to large under/overestimation (depending on the model) in the surface albedo changes and, therefore, in the simulated climate impacts of LULCC.

Reconstructed past evapotranspiration climatologies based on current global data-driven products show significant changes in this variable due to LULCC. The amplitude and sign of such changes are seasonally and spatially dependent, notably following the type of land conversion (see Table 5.1). Although the evapotranspiration change estimations are subject to uncertainties that are in part inherent to the different dataset analyzed, they show a number of consistent signals that give robustness to the results, and point out major shortcomings in model simulations.

Techniques such as the ones developed in Chapter 3 represent a powerful tool that, in combination to global climate simulations, may permit reducing a number of uncertainties regarding the past and future climate impacts of LULCC.

Chapter 4 describes a number of climate projections to the end of 21st century carried out with the IPSL Earth System model in the context of LUCID and CMIP5. These simulations include land-cover changes following Integrated Assessment Models RCP-related scenarios.

Complementary simulations without land-use changes allow evaluating the effect of LULCC. Weak surface temperature changes were detected as response to future LULCC following RCP 8.5. These become statistically significant in very localized regions with LULCC and, then, are much smaller in amplitude than the temperature responses to increases in atmospheric greenhouse gases of the corresponding scenario (RCP 8.5). This scenario, as does the RCP 2.6 one, leads to major deforestation between 2005 and 2100 compared to the two other scenarios assessed in the CMIP5 context, notably in emerging countries in the tropics. These changes are however comparatively smaller than the ones occurred during the last 150 years, and few localized regions show changes in their forest area larger than 25%. In addition to the moderate land-surface forcing, the IPSL model exhibits inherent weak temperature responses to future LULCC because of the opposing impacts driven by the radiative effect of land conversions and of the non-radiative ones. These simulations do not show significant biogeochemical impacts of future LULCC. The results from IPSL echo those of other models that also performed LUCID-CMIP5 simulations (Brovkin et al., in revision).

Limitations and prospects

The simulations analyzed in this study from the first LUCID phase (Chapter 2) were carried out with prescribed sea surface temperature and sea ice concentration, as well as with fixed atmospheric CO_2 concentrations. The climate simulated is then constrained at the large-scale, with suppressed feedbacks to land-surface perturbations involving the ocean. This condition could limit both remote and local impacts of LULCC (Davin and de Noblet-Ducoudré, 2010). The importance of LULCC concerns the impacts on the local climate in first order, but potential amplification or dampening effects due to feedbacks within the whole climate system, as well as the possible teleconnections, are interesting questions to explore in a multi-model framework such as LUCID, however not addressed here.

The question of the future impacts of LULCC was not addressed in depth in this study, in part because of a lack of a sufficiently large ensemble of simulations that could bring robustness to the results, one of the principal goals of this thesis. However, based on one of the strongest scenario used in CMIP5, the simulations assessed in Chapter 4 suggest fairly small climate impacts of LULCC to the end of 21st century compared to the historical impacts. As commented before, this response is consistent with the imposed future land conversions, weaker in magnitude than the historical one. Intense deforestation however is nowadays occurring in tropical regions, notably in the Amazon, and will likely continue in the near future following the societal requirements (Nepstad et al., 2008). A simple comparison of the recent evolution of land-use in Amazonia and its projection to the near term reveals that the projected LULCC based on the RCP scenarios are extremely sanguine, at least in this region.

Although most techniques used in this study were developed to assess the large-scale LULCC, many of them could be used at the regional scale. This will be carried out in the context of the EU-FP7 AMAZALERT project. The question of the regional and global climatic responses to realistic scenarios of deforestation in the Amazon, the role that feedbacks from the climate system play in simulated climate changes, and the forest resilience to this forcing are the key questions that are being addressed in this project.

Estimations of past changes in surface albedo and evapotranspiration with observation-based datasets, carried out with statistical tools, are useful methods to assess the effect of LULCC independently from model simulations. These techniques may be adapted for other variables or surface properties, as well as applied for exploring different types of land conversion, being these historical or future scenarios of LULCC, or ad-hoc land-cover changes (e.g., extreme deforestation) for sensitivity analyses.

References

The following list includes all the references cited within the manuscript excepting those of sections 2.4.4, 2.4.5, 3.2 and 3.3 (papers), which are self contained.

Abramowitz, G. (2005), Towards a benchmark for land surface models, Geophys. Res. Lett., 32, L22702, doi:10.1029/2005GL024419.

Abramowitz, G., R. Leuning, M. Clark, and A. Pitman (2008), Evaluating the performance of land surface models, J. Climate, 21, 5468-5481.

Adegoke, J. O., R. A. Pielke Sr., and A. M. Carleton (2007), Observational and modeling studies of the impacts of agriculture-related land use change on climate in the central U.S. Agric. Forest Meteor. 142, 203–215.

Arora, V. K., and A. Montenegro (2011), Small temperature benefits provided by realistic afforestation efforts, Nature Geoscience (2011) doi:10.1038/ngeo1182.

Aumont O., and L. Bopp (2006), Globalizing results from ocean in situ iron fertilization, *Global Biogeochemical Cycles*, 20 (2).

Baccini, A. et al. (2012), Estimated carbon dioxide emissions from tropical deforestation improved by carbon-density maps. Nature Climate Change doi:10.1038/nclimate1354.

Baida Roy, S., and R. Avissar (2002) Impact of land use/ land cover on regional hydrometeorology in the Amazon. J. Geophys. Res. 107 8037, doi:10.1029/2000JD000266.

Baidya Roy, S., G. C. Hurtt, C. P. Weaver, and S. W. Pacala (2003), Impact of historical land cover change on the July climate of the United States, J. Geophys. Res., 108(D24), 4793, doi:10.1029/2003JD003565.

Baldocchi, D. D., C. A. Vogel, and B. Hall (1997), Seasonal variation of energy and water vapor exchange rates above and below a boreal jack pine forest canopy, J. Geophys. Res., 102(D24), 28, 939–28, 951.

Bala, G., K. Caldeira, M. Wickett, T. J. Phillips, D. Lobell, C. Delire, and A. Mirin (2007), Combined climate and carbon cycle effects of global deforestation, Proceedings of the National Academy of Sciences, 104(16), 6550-6555.

Ball, J., T. Woodrow, and J. Berry (1987), A model predicting stomatal conductance and its contribution to the control of photosynthesis under different environmental conditions, Prog. Photosynthesis, 4, 221– 224.

Betts, R.A. P. M. Cox, S. E. Lee, and F. I. Woodward, (1997), Contrasting physiological and structural vegetation feedbacks in climate change simulations. Nature, 387:796-799.

Betts, R. A. (2000), Offset of the potential carbon sink from boreal forestation by decreases in surface albedo, Nature 408, 187-190, doi:10.1038/35041545.

Betts, R. A. (2001), Biogeophysical impacts of land use on present-day climate: near surface temperature and radiative forcing, Atmos. Sci. Lett., 1, doi:10.1006asle.2001.0023.

Betts, R. A., O. Boucher, M. Collins, P. M. Cox, P. D. Falloon, N. Gedney, D. L. Hemming, C. Huntingford, C. D. Jones, D. M. H. Sexton, and M. J. Webb (2007a), Projected increase in future river runoff through plant responses to carbon dioxide rise. Nature, 448: 1037-1042

Betts, R. A., P. D. Falloon, K. Klein Goldewijk, and N. Ramankutty (2007b), Biogeophysical effects of land use on climate: Model simulations of radiative forcing and large-scale temperature change, Agric. For. Meteor., 142, 216–233.

Bonan, G. B. (1999), Frost followed the plow: Impacts of deforestation on the climate of the United States. Ecological Applications 9:1305-1315.

Bonan, G. B. (2001), Observational evidence for reduction of daily maximum temperature by croplands in the Midwest United States. Journal of Climate 14:2430-2442.

Bonan, G. B. (2008a), Ecological Climatology: Concepts and Applications. 2nd edition. Cambridge University Press, Cambridge. 550 pp.

Bonan, G. B. (2008b), Forests and climate change: Forcings, feedbacks, and the climate benefits of forests, Science, 320, 1444–1449, doi:10.1126/science.1155121.

Bondeau, A., P. C. Smith, Z. Zaehle, S. Schaphoff, W. Lucht, W. Cramer, D. Gerten, H. Lotze-Campen, C. Müller, M. Reischtein, and B. Smith (2007), Modelling the role of agriculture for the 20th century global terrestrial carbon balance, Global Change Biol., 13(3), 679–706.

Bounoua, L., R. DeFries, G. J. Collatz, P. Sellers, and H. Khan (2002), Effects of land cover conversion on surface climate, Climatic Change, 52, 29–64.

Boucher, O., G. Myhre, and A. Myhre (2004), Direct human influence of irrigation on atmospheric water vapor and climate. Climate Dynamics, (22): pp. 597-603.

Bousquet, P., P. Peylin, P. Ciais, C. Le Quere, P. Friedlingstein, and P. P. Tans (2000), Regional changes in carbon dioxide fluxes of land and oceans since 1980, Science, 290, 1342-1346.

Brovkin, V., Ganopolski, A., Claussen, M., Kubatzki, C., and Petoukhov, V. (1999), Modelling climate response to historical land cover change. Global Ecology and Biogeography, 8(6), 509-517.

Brovkin, V., Sitch, S., von Bloh, W., Claussen, M., Bauer, E., Cramer, W. (2004), Role of land cover changes for atmospheric CO2 increase and climate change during the last 150 years. Global Change Biology 10, 1253–1266.

Brovkin, V., Claussen, M., Driesschaert, E., Fichefet, T., Kicklighter, D., Loutre, M.-F., Matthews, H. D., Ramankutty, N., Schaeffer, M., Sokolov, A. (2006), Biogeophysical effects of historical land cover changes simulated by six Earth system models of intermediate complexity, Climate Dynamics, doi: 10.1007/s00382-005-0092-6.

Buermann, W., B. R. Lintner, C. D. Koven, A. Angert, J. Pinzon, C. J. Tucker, and I. Fung (2007), The changing carbon cycle at Mauna Loa Observatory. Proceedings of the National Academy of Siences (USA), 104, 4249-4254.

Campbell J. E., Lobell D. B., Genova R. C., and Field C. B. (2008), The global potential of bioenergy on abandoned agriculture lands. Environ Sci Technol. 1;42(15):5791-4.

Canadell, J. G., Le Quere, C., Raupach, M. R., Field, C. B., Buitenhuis, E. T., Ciais, P., Conway, T. J., Gillett, N. P., Houghton, R. A. & Marland, G. (2007), Contributions to accelerating atmospheric CO2 growth from economic activity, carbon intensity, and efficiency of natural sinks. Proceedings of the National Academy of Sciences of the United States of America, 104, 18866-18870.

Chase, T. N., et al. (2000), Simulated impacts of historical land cover changes on global climate in northern winter. Clim. Dyn., 16, 93–105.

Christensen, J.H., B. Hewitson, A. Busuioc, A. Chen, X. Gao, I. Held, R. Jones, R.K. Koli, W.-T. Kwon, R. Laprise, V.M. Rueda, L. Mearns, C.G. Menéndez, J. Räisänen, A. Rinke, A. Sarr and P. Whetton (2007), Regional climate projections. Climate Change 2007: The Physical Science Basis. Contribution of Working Group I to the Fourth Assessment Report of the Intergovernmental Panel on Climate Change, S. Solomon, D. Qin, M. Manning, Z. Chen, M. Marquis, K.B. Averyt, M. Tignor and H.L. Miller, Eds., Cambridge University Press, Cambridge, 847-940.

Claussen M., Brovkin V., Ganopolski A. (2001), Biogeophysical versus biogeochemical feedbacks of large-scale land cover change, Geophys. Res. Lett., 28, 1011-1014.

Collatz, G., M. Ribas-Carbo, and J. Berry (1992), Coupled photosynthesisstomatal conductance model for leaves of C4 plants, Aust. J. Plant Physiol., 19, 519–538.

Collins, W.D., C. M. Bitz, M. L. Blackmon, G. B. Bonan, C. S. Bretherton, J. A. Carton, P. Chang, S. C. Doney, J. J. Hack, T. B. Henderson, J. T. Kiehl, W. G. Large, D. S. McKenna, B. D. Santer, and R. D. Smith (2006), The Community Climate System Model Version 3 (CCSM3), J. Climate, 19:2122-2143.

Cook, B.I., Bonan, G.B., Levis, S. (2006), Soil moisture feedbacks to precipitation in South Africa. J. Climate 19, 4198–4206.

Cox P.M, Betts R.A, Collins M, Harris P.P, Huntingford C, Jones C.D. (2004), Amazonian forest die-back under climate-carbon cycle projections for the 21st century. Theor. Appl. Climatol. 78:137–156. doi:10.1007/s00704-004-0049-4.

Coyle, W. (2007), The future of biofuels: A global perspective, Amber Waves, Vol. 5, Isuue 5, Economic

Research Service, Washington, D.C., http://www.ers.usda.gov/AmberWaves/November07/Features/Biofuels.htm.

D'Almeida C, Vorosmarty C, Hurtt G, Marengo J, Dingman S, Keim B (2007), The effects of deforestation on the hydrological cycle in Amazonia: a review on scale and resolution. Int J. Climatol 27(5):633–647.

Davin, E. L., N. de Noblet-Ducoudré, and P. Friedlingstein (2007), Impact of land cover change on surface climate: Relevance of the radiative forcing concept, Geophys. Res. Lett., 34, L13702, doi:10.1029/2007GL029678.

Davin, E. L., and N. de Noblet-Ducoudré (2010), Climatic Impact of Global-Scale Deforestation: Radiative versus Non radiative Processes, J. Climate, 23, 97–112.

Deardorff J. W. (1978), Efficient prediction of ground surface temperature and moisture with inclusion of a layer of vegetation. Journal of Geophysical Research 83: 1889–1903.

DeFries et al. (2002), Human modification of the landscape and surface climate in the next fifty years. In: Global Change Biology, 8: 438-458.

Denman, K. L., G. Brasseur, A. Chidthaisong, P. Ciais, P.M. Cox, R.E. Dickinson, D. Hauglustaine, C. Heinze, E. Holland, D. Jacob, U. Lohmann, S Ramachandran, P.L. da Silva Dias, S.C. Wofsy and X. Zhang, (2007), Couplings Between Changes in the Climate System and Biogeochemistry. In: Climate Change 2007: The Physical Science Basis. Contribution of Working Group I to the Fourth Assessment Report of the Intergovernmental Panel on Climate Change [Solomon, S., D. Qin, M. Manning, Z. Chen, M. Marquis, K.B. Averyt, M.Tignor and H.L. Miller (eds.)]. Cambridge University Press, Cambridge, United Kingdom and New York, NY, USA

De Noblet-Ducoudré, N. and A.J. Pitman (2007), LUCID – Land-Use and Climate, IDentification of robust impacts. iLEAPS Newsletter 4.

De Noblet-Ducoudré, N., J. P. Boisier, A. J. Pitman, G. B. Bonan, V. Brovkin, F. Cruz, C. Delire, V. Gayler, B. J. J. M. van den Hurk, P. J. Lawrence, M. K. van der Molen, C. Mueller, C. H. Reick, B. Strengers, and A. Voldoire (2012), Determining robust impacts of Land-Use induced Land-Cover Changes on surface climate over North America and Eurasia: Results from the first of LUCID experiments, J. Climate, 25, 3261–3281. doi: http://dx.doi.org/10.1175/JCLI-D-11-00338.1

Diamond, J. (1999), Guns, Germs, and Steel: The Fates of Human Societies. W. W. Norton & Company; 1 edition.

Dickinson RE, Henderson-Sellers A, Kennedy PJ, Wilson MF. (1986), Biosphere–Atmosphere Transfer Scheme (BATS) for the NCAR Community Climate Model. NCAR Technical Note TN-275 + STR.

Douglas, E. M., D. Niyogi, S. Frolking, J. B. Yeluripati, R. A. Pielke, Sr., N. Niyogi, C. J. Vörösmarty, and U. C. Mohanty (2006), Changes in moisture and energy fluxes due to agricultural land use and irrigation in the Indian Monsoon Belt. Geophysical Research Letters, 33, L14403.doi:10.1029/2006GL026550.

Ducoudré, N. I., K. Laval, and A. Perrier (1993), SECHIBA, a new set of parameterizations of the hydrologic exchanges at the land-atmosphere interface within the LMD atmospheric general circulation model, J. Clim., 6, 248– 273.

Dufresne J-L et al. (-), Climate change projections using the IPSL-CM5 Earth System Model: from CMIP3 to CMIP5. Submitted to Climate Dynamics.

Ellis, E. C. and N. Ramankutty (2008), Putting people in the map: anthropogenic biomes of the world. Frontiers in Ecology and the Environment 6:439-447

Ellis, E. C., K. Klein Goldewijk, S. Siebert, D. Lightman, and N. Ramankutty (2010), Anthropogenic transformation of the biomes, 1700 to 2000, Global Ecology and Biogeography. 19:589–606. doi:10.1111/j.1466-8238.2010.00540.x

Farquhar, G., S. von Caemmener, and J. Berry (1980), A biochemical model of photosynthesis CO2 fixation in leaves of C3 species, Planta, 149, 78– 90.

Fearnside, P. M. (2005), Deforestation in Brazilian Amazonia: History,rates and consequences. *Conservation Biology* 19(3): 680-688.

Feddema, J., K. Oleson, G. Bonan, L. Mearns, L. E. Buja, G. A. Meehl, and W. M. Washington (2005a), The importance of land-cover change in simulating future climates, Science, 310, 1674–1678.

Feddema, J., K. Oleson, G. Bonan, L. Mearns, W. Washington, G. Meehl, and D. Nychka (2005b), A comparison of a GCM response to historical anthropogenic land cover change and model sensitivity to uncertainty in present-day land cover representations, Climate Dyn., 25, 581–609.

Findell, K. L., E. Shevliakova, P. C. D. Milly, R. J. Stouffer (2007), Modeled Impact of Anthropogenic Land Cover Change on Climate. J. Climate, 20, 3621–3634.

Fischer G., and L. Schrattenholzer (2001), Global bioenergy potentials through 2050. Biomass Bioenergy 20(3):151–159

Forster, P., and Coauthors (2007), Changes in Atmospheric Constituents and in Radiative Forcing. In: Climate Change 2007: The Physical Science Basis. Contribution of Working Group I to the Fourth Assessment Report of the Intergovernmental Panel on Climate Change [Solomon, S., D. Qin, M. Manning, Z. Chen, M. Marquis, K.B. Averyt, M.Tignor and H.L. Miller (eds.)]. Cambridge University Press, Cambridge, United Kingdom and New York, NY, USA.

Friedlingstein, P. et al. (2010), Update on CO2 emissions. Nature Geoscience. 3: 811-812.

Fujino J, Nair R, Kainuma M, Masui T, Matsuoka Y (2006), Multi-gas mitigation analysis on stabilization scenarios using AIM global model. Energy J 27:343–353

Gao, F., Y. Jin, X. Li, C. Schaaf, and A. H. Strahler (2002), Bidirectional NDVI and Atmospherically Resistant BRDF Inversion for Vegetation Canopy, IEEE Trans. Geosci. Remote Sens., 40, 1269-1278.

Gash, J.H.C. and Nobre, C.A. (1997), Climatic effects of Amazonian deforestation: some results from ABRACOS. Bull. American Meteorol. Soc., 78, (5): 823-830.

Gedney, N. and P. J. Valdes (2000), The effect of Amazonian deforestation on the northern hemisphere circulation and climate, Geophys. Res. Lett., 27(19), 3053–3056, doi:10.1029/2000GL011794.

Gibbard, S., K. Caldeira, G. Bala, T. Phillips, and M. Wickett (2005), The effects of land cover changes on global climate, Geophys. Res. Lett., 32, doi:10.1029/2005GL024550.

Gordon, L. J., Steffen, W., Jonsson, B. F., Folke, C., Falkenmark, M., and Johannessen, A. (2005), Human modification of global water vapor flows from the land surface, Proc. Natl. Acad. Sci., 102, 7612–7617, doi:10.1073/pnas.0500208102.

Govindasamy, B., P. B. Duffy, and K. Caldeira (2001), Land use changes and Northern Hemisphere cooling, Geophys. Res. Lett., 28, 291–294.

Haddeland, I., Skaugen, T., and Lettenmaier, D. P. (2007), Hydrologic effects of land and water management in North America and Asia: 1700–1992, Hydrol. Earth Syst. Sc., 11, 1035–1045.

Hansen, J. E., M. Sato, A. Lacis, R. Ruedy, I. Tegen, and E. Mathews (1998), Climate forcings in the Industrial era, PNAS, 95:12,753–12,758, doi: 10.1073/pnas.95.22.12753.

Hansen, M. C., and Coauthors, (2008), Humid tropical forest clearing from 2000 to 2005 quantified by using multitemporal and multiresolution remotely sensed data. Proc. Natl. Acad. Sci. USA,105, 9439–9444.

Harris, N., L. et al. (2012), Baseline Map of Carbon Emissions from Deforestation in Tropical Regions. Science, Vol. 336 no. 6088 pp. 1573-1576. DOI: 10.1126/science.1217962.

Hibbard K *et al.* (2010). *International Journal of Climatology*, doi:10.1002/joc.2150.

Hirota, M., M. Holmgren, E. H. Van Nes ,and M. Scheffer (2011), Global Resilience of Tropical Forest and Savanna to Critical Transitions. Science. Vol. 334 no. 6053 pp. 232-235. DOI: 10.1126/science.1210657

Houghton, R.A. (2003), Revised estimates of the annual net flux of carbon to the atmosphere from changes in land use and land management 1850-2000. Tellus, 55B(2), 378–390.

Hourdin F., J-Y Grandpeix, C. Rio, S. Bony, A. Jam, F. Cheruy, N. Rochetin, L. Fairhead, A. Idelkadi, I. Musat, J-L Dufresne, M-P. Lefebvre, A. Lahellec, R. Roehrig (2012), LMDZ5B: the atmospheric component of the IPSL climate model with revisited parameterizations for clouds and convection. Climate Dynamics. pp. 1-30, doi:10.1007/s00382-012-1343-y

Hurtt, G. C., S. Frolking, M. G. Fearon, B. Moore III, E. Shevliakova, S. Malyshev, S. W. Pacala, R. A. Houghton (2006), The Underpinnings of Land-use History: Three Centuries of Global Gridded Land-Use Transitions, Wood Harvest Activity, and Resulting Secondary Lands, Global Change Biology, 12:1208-1229.

Hurtt G, Chini L, Frolking S, Betts R, Edmonds J, Feddema J, Fisher G, Goldewijk KK, Hibbard KA, Houghton R et al. (2011), Land use Change and earth system dynamics. Climatic Change. doi: 10.1007/s10584-011-0153-2.

Jin, Y, C. B. Schaaf, F. Gao, X. Li, A. H. Strahler, X. Zeng, and R. E. Dickinson (2002), How does snow impact the albedo of vegetated land surfaces as analyzed with MODIS data?, Geophys. Res. Lett., 29, 10, doi:10.1029/2001GL014132.

Kleidon, A., K. Fraedrich, and M. Heimann (2000), A green planet versus a desert world: estimating the maximum effect of vegetation on the land surface climate. Clim. Change, 44, 471–493.

Klein Goldewijk, K. (2001), Estimating global land use change over the past 300 years: The Hyde database, Global Biogeochem. Cycles, 15(2), 417–433.

Klein Goldewijk, K., A. Beusen, G. van Drecht, and M. de Vos (2011), The HYDE 3.1 spatially explicit database of human-induced global land-use change over the past 12,000 years, Global Ecology and Biogeography, 20:73–86. doi:10.1111/j.1466-8238.2010.00587.x

Koster, R. D., and P. C. D. Milly (1997), The Interplay between Transpiration and Runoff Formulations in Land Surface Schemes Used with Atmospheric Models, J. Climate, 10, 1578–1591. doi: 10.1175/1520-0442(1997)010<1578:TIBTAR>2.0.CO;2.

Koster, R. D., and Coauthors (2004), Regions of strong coupling between soil moisture and precipitation, Science, 305, 1138 – 1140, doi:10.1126/science.1100217.

Koster, R. D, and Coauthors (2006) GLACE: The Global Land–Atmosphere Coupling Experiment. Part I: Overview. J. Hydrometeor., 7, 590–610.

Krinner, G., N. Viovy, N. de Noblet-Ducoudré, J. Ogée, J. Polcher, P. Friedlingstein, P. Ciais, S. Sitch, and I.C. Prentice (2005), A dynamic global vegetation model for studies of the coupled atmosphere-biosphere system, Global Biogeochemical Cycles 19: GB1015. doi: 10.1029/2003GB002199.

Lawrence, P. J., Chase, T. N. (2007), Representing a new MODIS consistent land surface in the Community Land Model (CLM 3.0). J. Geophys. Res.-Biogeosci.: Vol. 112.

Lawrence, P. J., and T. N. Chase (2010), Investigating the climate impacts of global land cover change in the community climate system model, Int. J. Climatol., 30:2066-2087.

Lobell, D. B., C. Bonfils (2008), The Effect of Irrigation on Regional Temperatures: A Spatial and Temporal Analysis of Trends in California, 1934–2002. J. Climate, 21, 2063–2071.

Loveland, T., B. Reed, J. Brown, D. Ohlen, Z. Zhu, L. Yang, and J. Merchant (2000), Development of a global land cover characteristics database and IGBP DISCover from 1 km AVHRR data, Int. J. Remote Sens., 21, 1303– 1330.

Madec, G. (2008), NEMO ocean engine. Technical note, IPSL. Available at http://www.nemo1211ocean.eu/content/download/15482/73217/file/NEMO_book_v3_3.pdf.

Mahmood, R., S. A. Foster, T. Keeling, K. G. Hubbard, C. Carlson, and R. Leeper (2006), Impacts of irrigation on 20th century temperature in the northern Great Plains, Global Planet. Change 54:1–18.

Manabe S. (1969), Climate and the ocean circulation: 1, the atmospheric circulation and the hydrology of the Earth’s surface. Monthly Weather Review 97: 739–805.

Marengo J. A., W. R. Soares, C. Saulo, and M. Nicolini (2004), Climatology of the low level jet east of the Andes as derived from the NCEP-NCAR reanalyses: Characteristics and temporal variability. J. Climate, 17, 2261-2280.

Marti, O., Braconnot, P., Bellier, J., Benshila, R., Bony, S., Brockmann, P., Cadule, P., Caubel, A., Denvil, S., Dufresne, J-L., Fairhead, L., Filiberti, M-A., Foujols, M-A., T. Fichefet, T., Friedlingstein, P., Gosse, H., Grandpeix, J-Y., F. Hourdin, F., Krinner, G., Lévy, C., Madec, G., Musat, I., de Noblet, N., Polcher, J. and Talandier, C. (2006), The new IPSL climate system model: IPSL-CM4. France, Institut Pierre-Simon Laplace (IPSL), 84pp. (Note du Pole de Modélisation,(26)).

Marti, O., P. Braconnot, J. L. Dufresne, J. Bellier, R. Benshila, S. Bony, P. Brockmann, P. Cadule, A. Caubel, F. Codron, N. de Noblet-Ducoudré, S. Denvil, L. Fairhead, T. Fichefet, M. A. Foujols, P. Friedlingstein, H. Goosse, J. Y. Grandpeix, E. Guilyardi, F. Hourdin, G. Krinner, C. Lévy, G. Madec, J. Mignot, I. Musat, D. Swingedouw, and C. Talandier (2010), Key features of the IPSL ocean atmosphere model and its sensitivity to atmospheric resolution, Clim. Dyn., 34:1–26, DOI 10.1007/s00382-009-0640-6.

Matthews, H. D., A. J. Weaver, M. Eby, K. J. Meissner (2003), Radiative forcing of climate by historical land cover change, Geophys. Res. Lett. 30:1055. DOI 10.1029/2002GL01609.

Matthews, H.D., et al. (2004), Natural and anthropogenic climate change: Incorporating historical land cover change, vegetation dynamics and the global carbon cycle. Clim. Dyn., 22, 461–479.

McGregor, J. L., and M. R. Dix (2008), An updated description of the Conformal-Cubic Atmospheric Model.

High Resolution Simulation of the Atmosphere and Ocean, K. Hamilton and W. Ohfuchi, Eds., Springer, 51-76.

Meehl, G.A., Stocker, T.F., Collins, W.D., Friedlingstein, P., Gaye, A.T., Gregory, J.M., Kitoh, A., Knutti, R., Murphy, J.M., Noda, A., Raper, S.C.B., Watterson, I.G., Weaver, A.J. and Zhao, Z.-C. (2007), Global Climate Projections. In 'Climate Change 2007: The Physical Science Basis. Contribution of Working Group I to the Fourth Assessment Report of the Intergovernmental Panel on Climate Change'. (Eds S. Solomon, D. Qin, M. Manning, Z. Chen, M. Marquis, K.B. Averyt, M. Tignor and H.L. Miller). pp. 747-845. (Cambridge University Press: Cambridge, United Kingdom and New York, NY, USA).

Morton, D. C.; DeFries, R. S.; Shimabukuro, Y. E.; Anderson, L. O.; Arai, E.; Espirito-Santo, F. d. B.; Freitas, R. and Morisette, J. (2006), Cropland expansion changes deforestation dynamics in the southern Brazilian Amazon. Proceedings of the National Academy of Sciences 103(39): 14637-14641.

Moss, R.,H., Edmonds, J.,A., Hibbard, K.,A., Manning, M.,R., Rose, S.,K., van Vuuren, D.,P.,, Carter, T.,R., Emori, S., Kainuma, M., Kram, T., Meehl, G.,A., Mitchell, J.,F., Nakicenovic, N., Riahi, K., Smith, S.,J., Stouffer, R.,J., Thomson, A.,M., Weyant, J.,P., Wilbanks, T.J. (2010), The next generation of scenarios for climate change research and assessment. Nature. 463(7282):747-56.

Myhre, G., and A. Myhre (2003), Uncertainties in radiative forcing due to surface albedo changes caused by land-use changes, J. Climate, 16, 1511–1524.

Myhre, G., Kvalevåg, M. M., and Schaaf, C. B. (2005), Radiative forcing due to anthropogenic vegetation change based on MODIS surface albedo data, Geophys. Res. Lett., 32, L21410, doi:10.1029/2005GL024004.

Nabuurs, G.J., O. Masera, K. Andrasko, P. Benitez-Ponce, R. Boer, M. Dutschke, E. Elsiddig, J. Ford-Robertson, P. Frumhoff, T. Karjalainen, O. Krankina, W. Kurz, M. Matsumoto, W. Oyhantcabal, N.H. Ravindranath, M.S. Sanchez and X. Zhang, (2007), Forestry. Climate Change 2007: Mitigation. Contribution of Working Group III to the Fourth Assessment Report of the Intergovernmental Panel on Climate Change, B. Metz, O. Davidson, P. Bosch, R. Dave and L. Meyer, Eds., Cambridge University Press, UK.

Negri, A. J., R. F. Adler, L. Xu, J. Surratt (2004), The impact of Amazonian deforestation on dry season rainfall. Journal of Climate. 17(6):1306,Äì1319.

Nepstad, D.C.; Stickler, C.M.; Soares-Filho, B.; Merry, F. (2008), Interactions among Amazon land use, forests and climate: Prospects for a nearterm forest tipping point. Philos Trans R Soc Lond B Biol Sci. 363(1498): 1737–1746.

Oleson, K. W., G. B. Bonan, S. Levis, and M. Vertenstein (2004), Effects of land use change on North American climate: impact of surface datasets and model biogeophysics, Clim. Dyn., 23, 117–132, doi:10.1007/s00382-004-0426-9.

Oleson, K.W., G. Y. Niu, Z. L. Yang, D. M. Lawrence, P. E. Thornton, P. J. Lawrence, R. Stöckli, R. E. Dickinson, G. B. Bonan, S. Levis, A. Dai, and T. Qian (2008), Improvements to the Community Land Model and their impact on the hydrological cycle, J. Geophys. Res., 113, G01021, doi:10.1029/2007JG000563.

Oyama, M. D. and C. A. Nobre (2003), A new climate-vegetation equilibrium state for Tropical South America, Geophys. Res. Lett., 30(23), 2199, doi:10.1029/2003GL018600.

Pan Y. et al (2011), A Large and Persistent Carbon Sink in the World's Forests. Science, Vol. 333 no. 6045 pp. 988-993. DOI: 10.1126/science.1201609.

Pitman, A. J. and M. Zhao (2000), The relative impact of observed change in land cover and carbon dioxide as simulated by a climate model. Geophysical Research Letters, 27, 1267-1270.

Pitman, A. J. (2003), The evolution of, and revolution in, land surface schemes designed for climate models. International Journal of Climatology, 23, 479-510.

Pitman, A. J., N. de Noblet-Ducoudre, F. T. Cruz, E. L. Davin, G. B. Bonan, V. Brovkin, M. Claussen, C. Delire, L. Ganzeveld, V. Gayler, B. J. J. M. van den Hurk, P. J. Lawrence, M. K. van der Molen, C. Mueller, C. H. Reick, S. I. Seneviratne, B. Strengers, and A. Voldoire (2009), Uncertainties in climate responses to past land cover change: First results from the LUCID intercomparison study, Geophys. Res. Lett., 36, L14814, doi:10.1029/2009GL039076.

Pongratz, J., C. Reick, T. Raddatz, and M. Claussen (2008), A reconstruction of global agricultural areas and land cover for the last millennium, Global Biogeochem. Cycles, 22, GB3018, doi:10.1029/2007GB003153.

Pongratz, J., T. Raddatz, C. H. Reick, M. Esch, and M. Claussen (2009a), Radiative forcing from anthropogenic land cover change since A.D. 800, Geophys. Res. Lett., 36, L02709, doi:10.1029/2008GL036394.

Pongratz, J., C. H. Reick, T. Raddatz, and M. Claussen (2009b), Effects of anthropogenic land cover change on the carbon cycle of the last millennium, Global Biogeochem. Cycles, 23, GB4001, doi:10.1029/2009GB003488.

Puma, M. J., and B. I. Cook (2010), Effects of irrigation on global climate during the 20th century, J. Geophys. Res., 115, D16120, doi:10.1029/2010JD014122.

Raddatz, T., C. H. Reick, W. Knorr, J. Kattge, E. Roeckner, R. Schnur, K.-G. Schnitzler, P. Wetzel, and J. Jungclaus (2007), Will the tropical land biosphere dominate the climate-carbon cycle feedback during the twenty-first century?, Clim. Dyn., 29, 565-574

Ramankutty, N., and J. A. Foley (1999), Estimating historical changes in global land cover: Croplands from 1700 to 1992, Global Biogeochem. Cycles, 13, 997–1027.

Rayner, N. A., D. E. Parker, E. B. Horton, C. K. Folland, L. V. Alexander, D. P. Rowell, E. C. Kent, A. Kaplan (2003), Global analyses of sea surface temperature, sea ice, and night marine air temperature since the late nineteenth century, J. Geophys. Res., Vol. 108, No. D14, 4407 10.1029/2002JD002670.

Riahi, K., A. Gruebler, and N. Nakicenovic (2007), Scenarios of long-term socioeconomic and environmental development under climate stabilization. Greenhouse Gases - Integrated Assessment. Special Issue of Technological Forecasting and Social Change, 74(7):887–935, doi:10.1016/j.techfore.2006.05.026

Roeckner., E., R. Brokopf, M. Esch, M. Giorgetta, S. Hagemann, L. Kornblueh, E. Manzini, U. Schlese, U. Schulzweida (2006), Sensitivity of simulated climate to horizontal and vertical resolution in the ECHAM5 atmosphere model, J. Climate, 19, 3771–3791.

Ruimy, A., G. Dedieu, and B. Saugier (1996), TURC: A diagnostic model of continental gross primary productivity and net primary productivity, Global Biogeochem. Cycles, 10(2), 269–285, doi:10.1029/96GB00349.

Salas-Mélia, D., F. Chauvin, M. Déqué, H. Douville, J. F. Guérémy, P. Marquet, S. Planton, J. F. Royer, S. Tyteca (2005), Description and validation of the CNRM-CM3 global coupled climate model, Note de Centre du GMGEC N°103.

Sampaio, G., C. Nobre, M. H. Costa, P. Satyamurty, B. S. Soares-Filho, and M. Cardoso (2007), Regional climate change over eastern Amazonia caused by pasture and soybean cropland expansion, Geophys. Res. Lett., 34, L17709, doi:10.1029/2007GL030612.

Schimel, D., J. Melillo, H. Tian, A.D. McGuire, D. Kicklighter, T. Kittel, N. Rosenbloom, S. Running, P. Thornton, D. Ojima, W. Parton, R. Kelly, M. Sykes, R. Neilson, and B. Rizzo (2000), Contribution of increasing CO2 and climate to carbon storage by ecosystems of the United States. Science 287:2004-2006.

Sellers PJ, Mintz Y, Sud YC, Dalcher A. (1986), A Simple Biosphere model (SiB) for use within general circulation models. Journal of the Atmospheric Sciences 43: 505–531.

Sellers PJ, Dickinson RE, Randall DA, Betts AK, Hall FG, Berry JA, Collatz GJ, Denning AS, Mooney HA, Nobre CA, Sato N, Field CB, Henderson-Sellers A. (1997), Modelling the exchanges of energy, water and carbon between continents and the atmosphere. Science 275: 502–509.

Seneviratne, S. I., R. D. Koster, Z. Guo, P. A. Dirmeyer, E. Kowalczyk, D. Lawrence, P. Liu, D. Mocko, K. W. Oleson, D. Verseghy (2006), Soil Moisture Memory in AGCM Simulations: Analysis of Global Land–Atmosphere Coupling Experiment (GLACE) Data, J. Hydrometeor., 7, 1090–1112.

Seneviratne S. I., T. Corti, E. L. Davin, M. Hirschi, E. B. Jaeger, I. Lehner, B. Orlowsky, and A. J. Teuling (2010), Investigating soil moisture-climate interactions in a changing climate: A review, Earth-Science Reviews, Volume 99, Issues 3-4, Pages 125-161, ISSN 0012-8252, DOI: 10.1016/j.earscirev.2010.02.004

Seth, A., M. Rojas, and S. J. Rauscher (2010), CMIP3 projected changes in the annual cycle of the South American monsoon, Climatic Change. 98:331–357. DOI 10.1007/s10584-009-9736-6.

Shukla, J. and Y. Mintz (1982), The influence of land-surface evapotranspiration on the earth's climate. Science, 214, 1498-1501.

Sitch, S., Smith, B., Prentice, I., Arneth, A., Bondeau, A., Cramer, W., Kaplan, J. O., Levis, S., Lucht, W., Sykes, M., and Thonicke, K. (2003), Evaluation of ecosystem dynamics, plant geography and terrestrial carbon cycling in the LPJ dynamic global vegetation model, Glob. Change Biol., 9, 161–185.

Sitch, S., V. Brovkin, W. von Bloh, D. van Vuuren, B. Eickhout, and A. Ganopolski (2005), Impacts of future land cover changes on atmospheric CO2 and climate, Global Biogeochem. Cycles, 19, GB2013, doi:10.1029/2004GB002311.

Sitch, S., et al. (2008), Evaluation of the terrestrial carbon cycle, future plant geography and climate-carbon cycle feedbacks using 5 Dynamic Global Vegetation Models (DGVMs), Global Change Biol., 14, 1 – 25.

Snyder P. K., C. Delire, and J. A. Foley (2004), Evaluating the influence of different vegetation biomes on the global climate, Clim. Dyn., 23(3-4), 279-302.

Soares-Filho, B. S., D. Nepstad, L. Curran, E. Voll, G. Cerqueira, R.A.Garcia, C.A. Ramos, A. Mcdonald, P. Lefebvre, and P. Schlesinge (2006), Modelling conservation in the Amazon basin. Nature, 440, pp. 520-523.

Strengers B. J., C. Müller, M. Schaeffer, R. J. Haarsma, C. Severijns, D. Gerten, S. Schaphoff , R. van den Houdt, and R. Oostenrijk (2010), Assessing 20th century climate-vegetation feedbacks of land-use change and natural vegetation dynamics in a fully coupled vegetation-climate model, Int. J. Climatol., 30, 13, pp. 2055-2065, doi: 10.1002/joc.2132.

Swann, A. L. S., Fung, I. Y., and Chiang, J. C. H. (2011), Mid-latitude afforestation shifts general circulation and tropical precipitation, Proc. Nat. Aca. Sci., 109, 712–716, doi:10.1073/pnas.1116706108.

Taylor, Karl E., Ronald J. Stouffer, Gerald A. Meehl (2012), An Overview of CMIP5 and the Experiment Design. Bull. Amer. Meteor. Soc., 93, 485–498. doi: http://dx.doi.org/10.1175/BAMS-D-11-00094.1

Van den Hurk, B. J. J. M., P. Viterbo, A. C. M. Beljaars and A. K. Betts (2000), Offline validation of the ERA40 surface scheme; ECMWF Tech Memo 295 (http://www.ecmwf.int/publications/library/ecpublications.

Van der Molen M. K., B. J. J. M. van den Hurk, and W. Hazeleger (2011), A dampened land use change climate response towards the tropics, Clim. Dyn., doi: DOI 10.1007/s00382-011-1018-0.

Van Vuuren et al. (2011a), The Representative Concentration Pathways: An Overview. Climatic Change, 109 (1-2), 5-31.

Van Vuuren DP, Stehfest E, Den Elzen MGJ, Deetman S, Hof A, Isaac M, Klein Goldewijk K, Kram T, Mendoza Beltran A, Oostenrijk R et al (2011b) RCP2.6: Exploring the possibility to keep global mean temperature change below 2°C. Climatic Change. doi: 10.1007/s10584-011-0152-3

Vera, C., G. Silvestri, B. Liebmann, and P. Gonzalez (2006), Climate change scenarios for seasonal precipitation in South America from IPCC-AR4 models, Geophys. Res. Lett., 33, L13707, doi:10.1029/2006GL025759.

von Randow, C., Manzi, A.O., Kruijt, B., de Oliveira, P.J., Zanchi, F.B., Silva, R.L., Hodnett, M.G., Gash, J.H.C., Elbers, J.A., Waterloo, M.J., Cardoso, F.L. & Kabat, P. (2004), Comparative measurements and seasonal variations in energy and carbon exchange over forest and pasture in South West Amazonia. Theoretical and Applied Climatology, 78, 5-26.

Voldoire, A. (2006), Quantifying the impact of future land-use changes against increases in GHG concentrations, Geophys. Res. Lett., 33, L04701, doi:10.1029/2005GL024354.

Werth, D. and Avissar, R. (2005), The local and global effects of Southeast Asian deforestation, Geophys. Res. Lett., vol 32 no. 20, pp. 4 pp.

Williams, M. (2000), Dark ages and dark areas: global deforestation in the deep past. Journal of Historical Geography, vol. 26, no. 1, pp. 28-46.

Wise M. et al. (2009), Implications of Limiting CO2 Concentrations for Land Use and Energy. Science, Vol. 324 no. 5931 pp. 1183-1186. DOI: 10.1126/science.1168475.

Zhao, M., A. J. Pitman and T. Chase (2001), The impact of land cover change on the atmospheric circulation. Climate Dynamics, 17, 467-477.1.